

Late-Pleistocene Climate Evolution of the Southern Sub-Equatorial Tropics from East-Indonesian Speleothems

Michael Lindgren Griffiths

BSc (Geosci.), Msc (Geosci.)

A thesis submitted in fulfillment of the requirements for the degree of

DOCTOR OF PHILOSOPHY

at the University of Newcastle

August 2010

Statement of Originality

I declare this thesis contains no material which has been accepted for the award of any other degree or diploma in any university or other tertiary institution and, to the best of my knowledge and belief, contains no material previously published or written by another person, except where due reference has been made in the text. I give consent to this copy of my thesis, when deposited in the University Library, being made available for loan and photocopying subject to the provisions of the Copyright Act 1968.

Acknowledgement of Collaboration

I hereby certify that the work embodied in this thesis has been done in collaboration with other researchers, or carried out in other institution. Below I have outlined the extent of collaboration, with whom and under what auspices.

Linda Ayliffe and Michael Gagan, from the Australian National University, helped out with the stable isotope measurements presented in Chapter 2. Jian-xin Zhao, from the University of Queensland, and John Hellstrom, from the University of Melbourne, helped carry out U/Th dating presented in all chapters. Hubert Vonhof provided on-site training for the fluid-inclusion analysis carried out at Vrije Universiteit, Amsterdam; results from this are presented in Chapter 3. Ian Cartwright, from Monash University, carried out stable isotope analyses of rainwater samples presented in Chapters 2 and 3.

Acknowledgement of Authorship

I hereby certify that the work embodied in this thesis contains a published paper/s/scholarly work of which I am a joint author. I have included as part of the thesis a written statement, endorsed by my supervisor, attesting to my contribution to the joint publication/s/scholarly work.

I, Michael Griffiths, was the primary investigator and lead author of all papers presented in this thesis.

(Russell Neil Drysdale)

(Michael Lindgren Griffiths)

Dedication

To Jill and my parents for their unwavering support

Acknowledgements

This research was funded by a University of Newcastle Postgraduate Research Higher Degree scholarship and an Australian Research Council grant (DP0663274). I am indebted to my principal supervisor, Russell Drysdale, for his constant support and inspiration. There is no doubt in my mind that this thesis, along with the publications that were produced along the way, would not have eventuated without his guidance and knowledge of palaeoclimatology/geochemistry. His true passion for advancing our understanding of Earth's climate history is contagious and inspiring. Moreover, his impeccable writing ability has resulted in my own being greatly improved throughout my PhD. Russell has not only been an outstanding supervisor but also a great friend, and I am sure he will continue to be a supportive mentor for years to come. A great deal of thanks also goes to Silvia Frisia, whose vibrant approach to the advancement of science is truly motivating. Her vast geochemical knowledge and imagination was indispensable to this dissertation. Further, she has provided constant encouragement in all aspects of my studies. I am especially grateful to the staff and faculty within the department for their support and friendship over the years, namely: Judy Bailey, Richard Bale, Phil Gentry, Greg Hancock, Bill Landenberger, Janece McDonald, Robin Offler, Glen Phillips and anyone else who I may have missed.

I am deeply thankful to my external supervisor Mike Gagan [from the Research School of Earth Sciences (RSES), The Australian National University (ANU)] for his constant help and support. If not for his lengthy responses to my e-mail inquiries (regarding the Flores project) prior to me starting, I would never have been inspired to take on this project. Moreover, his invitation for me to help out with the challenging, yet very rewarding, caving fieldwork in Flores opened my eyes to the excitement of palaeoclimate research. Furthermore, his help with the final edits of all manuscripts arising from this dissertation profoundly improved the quality of the papers, and thus the quality of this dissertation. Linda Ayliffe also deserves a great deal of thanks for help with the stable isotope measurements from a replicated speleothem record provided in the *Nature Geoscience* paper, along with helpful discussion and feedback regarding the other two published papers.

I am very grateful to Jian-xin Zhao, from the University of Queensland, for his help with the U/Th dating and his insightful knowledge of geochemistry. In addition, he has always been a great support base, frequently offering words of wisdom and encouragement. John Hellstrom, from the University of Melbourne, also deserves a great deal of gratitude for the many U/Th dates and age-models he has run over the years.

Additional thanks go to Neil Anderson, Wahyoe S. Hantoro, Sophie Lewis, Jodie Rutledge, Garry Smith, Emma St. Pierre, Bambang W. Suwargadi and the Indonesian Institute of Sciences (LIPI) for logistical support and technical assistance with fieldwork. I also thank Heather Scott-Gagan, Joan Cowley and Joe Cali for laboratory assistance at the RSES (ANU) and Olivier Ray-Lescure (U.Newcastle) for help with some of the figures.

Table of Contents

1 Introduction.....	1
1.1 Background	1
1.2 Study area	2
1.3 Modern AISM dynamics	10
1.4 Speleothems as palaeoenvironmental archives: materials and methods	13
1.4.1 $^{230}\text{Th} - ^{234}\text{U}$ age dating	15
1.4.2 Stable isotope composition of speleothem calcite.....	15
1.4.2.1 Background	15
1.4.2.2 $\delta^{18}\text{O}$	17
1.4.2.3 $\delta^{13}\text{C}$	18
1.4.3 Stable isotopes of fluid inclusions	19
1.4.4 Trace elements	20
1.5 Objectives	20
1.6 Organisation of thesis	21
1.7 References	24
 2 Increasing Australian-Indonesian monsoon rainfall linked to early Holocene sea level rise	 31
Abstract	31
2.1 Introduction	31
2.2 Environmental setting.....	32
2.3 Sample description	36
2.4 Methods	39
2.4.1 Chronology	39
2.4.2 Stable isotopes	45
2.4.3 Assessment of equilibrium deposition.....	46
2.5 Results and Discussion	51
2.6 Conclusions	55
2.7 References	56
 3 Younger Dryas-Holocene temperature and rainfall history of southern Indonesia from $\delta^{18}\text{O}$ in speleothem calcite and fluid inclusions	 60
Abstract	60
3.1 Introduction and background.....	61
3.2 Regional setting.....	63
3.3 Methods	64
3.4 Results	68
3.5 Discussion	71
3.6 Conclusions	76
3.7 References	78
 4 Evidence for Holocene changes in Australian-Indonesian monsoon rainfall from stalagmite trace element and stable isotope ratios	 83
Abstract	83
4.1 Introduction and background.....	84
4.2 Study area and modern climatology	86
4.3 Methods	89
4.3.1 Sample collection and preparation.....	89
4.3.2 $^{230}\text{Th} - ^{234}\text{U}$ age dating.....	90
4.3.3 Stable isotope and trace element measurements	90
4.4 Results	91
4.4.1 Chronology.....	91
4.4.2 Stable isotopes	92
4.4.3 Trace elements and $[\text{}^{234}\text{U}/\text{}^{238}\text{U}]_1$	94
4.5 Discussion	97
4.5.1 Environmental controls on the trace elements and $[\text{}^{234}\text{U}/\text{}^{238}\text{U}]_1$	97

4.5.2 Climate signal of the $\delta^{18}\text{O}$ and trace elements	100
4.5.3 Centennial- to millennial-scale perturbations in the AISM-ITCZ	102
4.6 Conclusions	105
4.7 References	107
 5 Statistical “ramp-fitting” of Indonesian stalagmite record confirms early-Holocene resumption of monsoon system occurred within centuries	114
Abstract	114
5.1 Introduction	114
5.2 Study site and methods	115
5.3 Results and Discussion	116
5.3.1 Timing and structure of monsoon onset	116
5.3.2 Comparison with other records	119
5.3.3 Possible mechanisms	121
5.4 Conclusions	123
5.5 References	124
 6 Abrupt Indo-Pacific climate response to high-latitude warming during MIS 5a/b	127
Abstract	127
6.1 Introduction	128
6.2 Site description and climate setting	131
6.3 Materials and methods	133
6.3.1 Sample description and preparation	133
6.3.2 Chronology	133
6.3.3 Oxygen and carbon isotope measurements	134
6.3.4 Trace elements	135
6.4 Results	136
6.4.1 Chronology	136
6.4.2 Isotopic equilibrium precipitation	139
6.4.3 Stable isotopes	141
6.4.4 Trace elements	143
6.5 Discussion	147
6.5.1 Interpretation of the stable isotopes	147
6.5.1.1 $\delta^{18}\text{O}$	147
6.5.1.2 $\delta^{13}\text{C}$	149
6.5.2 Environmental controls on the trace elements	154
6.5.2.1 Magnesium and Strontium	154
6.5.2.2 Phosphorous and Yttrium	156
6.5.3 Summary of stable-isotope and trace-element results	158
6.5.4 Influence of GIS 21 in the southern Indo-Pacific	158
6.6 Conclusions	163
6.7 References	166
 7 Conclusions	176
7.1 Summary of thesis	176
7.1.1 Reconstruct the Holocene history of the AISM from $\delta^{18}\text{O}$ of coeval speleothems	176
7.1.2 Assessing the feasibility of using stable isotopes from speleothem fluid-inclusions to extract tropical palaeotemperatures	176
7.1.3 Utilising trace elements from a Holocene speleothem to validate oxygen isotope interpretations and provide additional palaeoenvironmental information	177
7.1.4 Explore a “snapshot” of Flores climate through MIS 5a/b and assess possible teleconnection patterns between the Indo-Pacific and high latitudes	179
7.2 Future directions	180
7.2.1 Exploring water-carbonate systematics in tropical cave systems	180
7.2.2 Extending the instrumental record back two millennia	180
7.2.3 Glacial/interglacial monsoon evolution	181
7.2.4 Integration of AISM reconstructions and palaeoclimate model simulations	182

7.3 Final comments	182
7.4 References	184

List of Figures

Figure 1.1 (a) Location of the east-Indonesian island of Flores (dashed box). The red arrows highlight the predominant NW surface-winds during the Austral-summer monsoon, which are being pulled in by the heat low (L) over northern Australia; (b) A Landsat image of western Flores showing the locations of Ruteng and the cave (Liang Luar) site; (c) Photo of the karst landscape surrounding the cave site. The white dashed line indicates the Wae Racang and the arrow shows the direction in which the river flows; (d) The volcanoes south of Ruteng and the cave site.....	3
Figure 1.2 Geological map of western Flores highlighting the lithology of the study region (map is taken from Hendaryono, 1999). The red circle indicates the cave site location. Lithological units are as follows: (1) Waihekang Formation–tuff-bearing clastic limestone; (2) Kiro Formation–breccia, lava, and tuff; (3) Nangapanda Formation–sandstone and limestone; (4) Miocene dykes/intrusions; (5) Bari Formation–limestone and sandy limestone; (6) Laka Formation–tuff with sandstone; (7) Older volcanic rocks; (8) coral-reef terrace; (9) Coastal terrace–alluvium; (10) Volcanoes.....	4
Figure 1.3 (a) A 1.5 km ² designated area around Liang Luar highlighting the morphology of the karst landscape. The concentric circles indicate karst cones while the open circles with hatch marks represent karst basins. Inset boxes show typical examples of karst cone and basin profiles. (b) A geomorphological map of the study area showing the four main cave systems in the region (colour coded). The pattern of cave dispersion highlights the interconnected nature of the cave systems throughout the karst region [figure modified after Westaway (2006)].	6
Figure 1.4 Plan view of Liang Luar Cave which stretches ~2 km in length. Orange dots show the positions of the stalagmites used in this thesis (survey map created by Garry K. Smith).	8
Figure 1.5 General circulation of the AISM at 200 hPa and 850 hPa (figure taken from Mitchell et al., 1994).	10
Figure 1.6 Monthly composites of NOAA satellite-observed outgoing long-wave radiation (OLR) and NCEP/NCAR Reanalysis 850-hPa wind vectors, based on data from 1979 to 2005. Low OLR values indicate cold cloud tops which are produced by precipitating cumulonimbus convection. OLR and wind vector data was retrieved from the following web address: http://www.esrl.noaa.gov/psd/cgi-bin/data/composites/printpage.pl	11
Figure 1.7 Schematic diagram displaying the links between the geochemical proxies preserved in the speleothem calcite and above-cave climate-environment parameters [figure taken from Frisia and Borsato (2010)].	14
Figure 2.1 Moisture-source trajectories and rainwater isotope ratios for Liang Luar Cave. Physiographic map showing location of Liang Luar and other study sites. Solid lines represent HYSPLIT (Draxler and Rolph, 2003) calculated 96-hour back-trajectories of dry season (red) and wet season (blue) air parcels that generated rainfall during September 2006 – April 2007. Inset shows $\delta^{18}\text{O}$ versus $\delta^2\text{H}$ for the same rain days during September 2006 – April 2007. Dry season (red dots) and wet season (blue dots) rainwater have amount-weighted average $\delta^{18}\text{O}$ values of -3.5‰ (V-SMOW) and -10.3‰, respectively. The dashed line represents the Global Meteoric Water Line (GMWL).	33
Figure 2.2 Rainfall climatology at Liang Luar from 1998 to 2008. Data is derived from NASA's satellite Tropical Rainfall Measuring Mission database (http://disc.sci.gsfc.nasa.gov/data/datapool/TRMM/01_Data_Products/02_Gridded/0_Monthly_Other_Data_Source_3B_43/index.html) centred at 8° 32'S, 120° 26'E with 0.25° resolution. Monthly values are expressed as the percentage of the mean annual total rainfall, which is 1200 mm for the 1998 to 2008 period.	34

- Figure 2.3** Scanned image of stalagmite LR06-B1 and photograph (top left) while *in situ* at the time of collection in June 2006. Black dots show the positions of the 33 U-Th ages. Section A (240 mm in length) was *in situ* at the time of collection while section B (1010 mm in length) had broken off 96 mm from the base ~1,500 years ago.37
- Figure 2.4** Same as Figure 2.3 but for stalagmite LR06-B3. Black dots show the positions of the 29 U-Th ages.38
- Figure 2.5** ^{230}Th depth-age models and 95% uncertainties are plotted for stalagmites a) LR06-B1 and b) LR06-B3. 95% uncertainty envelopes are indicated by blue shading. The symbols represent each U-Th age with 95% uncertainty shown by bars.40
- Figure 2.6** Hendy tests for ten individual growth laminae within stalagmite LR06-B1 for compact, translucent calcite. a(i) $\delta^{18}\text{O}$ and a(ii) $\delta^{13}\text{C}$ along individual calcite layers away from the central growth axis. Layers with $\delta^{18}\text{O}$ variability $< 0.5\text{‰}$ are assumed to have been deposited in isotopic equilibrium where the $\delta^{18}\text{O}$ reflects that of the drip-water, rather than kinetic fractionation. (b) Cross-plots of $\delta^{13}\text{C}$ and $\delta^{18}\text{O}$ along individual growth layers.48
- Figure 2.7** Same as Fig. 2.6 but for eight individual growth laminae for open, opaque calcite.49
- Figure 2.8** Same as Fig. 2.6 but for four individual growth laminae for stalagmite LR06-B3. In (b) it is evident that a number of layers display covariation between $\delta^{13}\text{C}$ and $\delta^{18}\text{O}$, however in all but one case (green diamonds) the covariation does not occur sequentially away from the central growth axis.50
- Figure 2.9** Liang Luar stalagmite $\delta^{18}\text{O}$ record and other palaeoclimate records. (a-d), Comparison of the Liang Luar $\delta^{18}\text{O}$ record (LR06-B1, blue; LR06-B3, pink) with stalagmite $\delta^{18}\text{O}$ records for Dongge Cave, China (Dykoski et al., 2005; Wang et al., 2005) (orange), Gunung Buda, Borneo (Partin et al., 2007) (red), and Botuverá Cave, Brazil (Wang et al., 2006) (green). Th/U ages for the Liang Luar records are shown (with 2σ errors) at top of figure. (e) Liang Luar $\delta^{18}\text{O}$ record adjusted for changes in Indo-Pacific Warm Pool sea-surface temperature (Stott et al., 2004) and global ice-volume (Siddall et al., 2003). (f) Sea-level reconstructions from the $\delta^{18}\text{O}$ of Red Sea benthic foraminifera (Siddall et al., 2003) (grey circles) with 5-point running mean (black line), and Barbados (Peltier and Fairbanks, 2006) (green triangles) and Tahiti (Bard et al., 1996) (yellow squares) coral reef studies. Dashed red lines highlight the concurrent increases in sea-level and AISM precipitation at Liang Luar. (g) December (austral summer) insolation at 20°S . The light brown shading indicates the timing of the Younger Dryas cooling in Greenland (EPICA members, 2006).52
- Figure 2.10** Comparison of palaeoclimate records between Flores, southern China, and northern South America during the Younger Dryas cooling. (a) A weakened East Asian summer monsoon recorded by the Dongge Cave, China, speleothem record (Dykoski et al., 2005) corresponds with (b) a southward displaced ITCZ over the Cariaco basin (Haug et al., 2001), (c) stronger outflow from the Asian winter monsoon (Yancheva et al., 2007), and (d) higher monsoon rainfall over Flores, as indicated by lower ice-volume (Siddall et al., 2003) and SST (Stott et al., 2004) adjusted $\delta^{18}\text{O}$ values. The light brown shading indicates a strong N-S inverse relationship during the time of the Younger Dryas cooling in Greenland (EPICA members, 2006).54
- Figure 3.1** Location of Liang Luar Cave, Flores, in the Australian-Indonesian summer monsoon domain. Shading represents monthly values of outgoing long-wave radiation (OLR) based on composites of NOAA satellite-observed OLR. Arrows show NCEP/NCAR Reanalysis 850-hPa wind direction based on data from 1979 to 2005 for the: (a) austral summer wet season (December-March) and (b) austral winter dry season (June-August). Low OLR values (dark shading) indicate cold cloud tops produced by precipitating cumulonimbus convection, which dominates the southern Indonesian region during the Australian-Indonesian summer monsoon. Also shown are the locations of marine sediment cores MD76 (Stott et al., 2004) and MD62 (Visser et al., 2003) and coral

records discussed in the text. OLR and wind vector data were retrieved from the following web address:
<http://www.esrl.noaa.gov/psd/cgi-bin/data/composites/printpage.pl>.....64

Figure 3.2 Plan of ~1km stretch (total length of cave is ~2km) of Liang Luar Cave, along with photographs taken from several sections of the cave. Symbols indicate the position of collection sites for drip and pool waters, and stalagmite LR06-B1.....65

Figure 3.3 Cross-plot of δD versus $\delta^{18}O$ for stalagmite LR06-B1 fluid-inclusion samples, cave drip waters (including the drip-water feeding stalagmite LR06-B1), and cave pool waters. Drip and pool waters were collected in May 2007. Also plotted are rainfall isotopes collected at the cave site between September 2006 and April 2007. The solid line indicates the Global Meteoric Water Line (GMWL) and the dashed line the Cave Meteoric Water Line. Error bars on the fluid inclusions represent the analytical reproducibility (1σ) of measurements on standard waters injected into the crusher. Error bars on the rainfall isotopes and cave drip and pool waters represent analytical precision (1σ) of replicate measurements on internal standards. The δD and $\delta^{18}O$ of the fluid inclusions display a trend that is parallel to the GMWL, and are in close agreement with the cave drip and pool waters. Furthermore, the fluid-inclusion $\delta^{18}O_f$ and δD_f values for the youngest calcite layers plot close to the field of modern drip water compositions thus confirming that the inclusion waters reflect the $\delta^{18}O$ and δD of the drip waters within the cave system. The gray shading highlights the ~0.9‰ enrichment in $\delta^{18}O$ of the fluid inclusions and cave drip and pool waters relative to the rainfall. I attribute this slight enrichment to evapotranspiration of the surface waters prior to reaching the cave interior.....70

Figure 3.4 Comparison of stalagmite LR06-B1 calcite $\delta^{18}O_c$ (black curve), fluid-inclusion $\delta^{18}O_f$ (circles), and fluid-inclusion δD_f (squares) records over the past 12.64 ka. U/Th ages used to construct the time-series are plotted along the top (dating and sampling errors are smaller than the symbols used). Error bars represent mean analytical (1σ) reproducibility of the standard waters injected into the crusher. The gray bar highlights the timing of the Younger Dryas climate anomaly. The $\delta^{18}O_f$ and δD_f trend towards lower values through the early- to mid-Holocene matches the trend in $\delta^{18}O_c$, thus confirming that the speleothem calcite $\delta^{18}O_c$ primarily reflects variations in the $\delta^{18}O$ of meteoric rainfall.....71

Figure 3.5 Comparison of ice-volume adjusted (Siddall et al., 2003) fluid-inclusion $\delta^{18}O_f$ (black circles) and reconstructed sea-level curves from the Red Sea (solid line; Siddall et al., 2003), Barbados (squares; Peltier and Fairbanks, 2006) and Tahiti (circles; Bard et al., 1996). Grey shading highlights the concurrent decrease in $\delta^{18}O_f$ and sea-level during the early to mid-Holocene reflecting intensification of Australian-Indonesian summer monsoon rainfall in response to eustatic sea-level rise and flooding of the Sunda Shelf.....73

Figure 3.6 (a) Comparison of reconstructed Liang Luar Cave palaeotemperatures (red circles) with reconstructions of IWP SSTs based on Mg/Ca in planktonic foraminifera in marine cores MD76 (black open circles; Stott et al., 2004) and MD62 (solid line; Visser et al., 2003), and coral Sr/Ca and U/Ca records from the tropical west and central Pacific (blue, Abram et al., 2009; gray, Asami et al., 2009; green, Castellaro et al., 1997; black, Corrège et al., 2004; purple, Gagan et al., 1998; orange, Gagan et al., 2000; white, McCulloch et al., 1996). Pink shading shows error envelope for palaeotemperatures calculated from fluid-inclusion $\delta^{18}O_f$ and calcite $\delta^{18}O_c$ [the combined analytical errors (1σ) for both measurements ($\pm 1.5^\circ C$)]. (b) $\delta^{18}O$ records from high-elevation tropical ice-cores from the Sajama (Bolivia; Thompson et al., 1998) and Huascarán (Peru; Thompson et al., 1995) ice caps. Green shading shows the Younger Dryas interval marked by ~5°C cooling on Flores and significant reduction in $\delta^{18}O$ of high-elevation ice caps in tropical South America.....75

Figure 4.1 Location map of Flores and other sites mentioned in the text. Liang Luar Cave lies ~550 m above sea level on the northern side of a volcanic mountain chain.....	86
Figure 4.2 Average monthly temperature and rainfall around Liang Luar Cave. Satellite derived average rainfall data are from NASA's Tropical Rainfall Measuring Mission (http://disc.sci.gsfc.nasa.gov/data/datapool/TRMM/01_Data_Products/02_Gridded/07_Monthly_Other_Data_Source_3B_43/index.html) from 1998 to 2007 (grey bars, left y-axis) centred at 8.45° S and 120.47° E with 0.25° resolution. Average annual rainfall for the area is 1200 mm. Average monthly temperature (black line) was calculated from NCEP/NCAR reanalysis data at the same grid-point as the precipitation.....	87
Figure 4.3 Photograph of stalagmite LR06-B1 at the time of collection in June 2006 and scanned images of separate calcite slabs. Black dots indicate the ages of the 33 uranium series dates. Section A (240 mm in length) of stalagmite LR06-B1 was <i>in situ</i> at the time of collection while section B (1010 mm in length) had broken off 96 mm from the base ~1.5 ka B.P.	89
Figure 4.4 Age versus depth (mm from top) model based on 33 U-Th dates for stalagmite LR06-B1. Black open dots and attached error bars are the U-Th ages and their 95% uncertainties.....	92
Figure 4.5 Time-series of (a) $\delta^{18}\text{O}$, (b) $\delta^{13}\text{C}$, (c) Mg/Ca, (d) Sr/Ca, and (e) $[\text{}^{234}\text{U}/\text{}^{238}\text{U}]_i$ for stalagmite LR06-B1. Additional $[\text{}^{234}\text{U}/\text{}^{238}\text{U}]_i$ values from a nearby stalagmite (LR06-B3), which were previously reported in Griffiths et al. (2009), are also shown in (e). The solid black lines represent 5-point running means.	93
Figure 4.6 Linear regression scatter plots of (a) $\delta^{13}\text{C}$ vs. $\delta^{18}\text{O}$, (b) Mg/Ca vs. Sr/Ca, (c) Mg/Ca vs. $\delta^{13}\text{C}$, (d) Sr/Ca vs. $\delta^{13}\text{C}$, (e) Mg/Ca vs. $\delta^{18}\text{O}$, and (f) Sr/Ca vs. $\delta^{18}\text{O}$. <i>r</i> -values and associated confidence intervals are shown in each box. Confidence intervals were calculated using the PearsonT computer program (Mudelsee 2003). Grey shading envelopes 95% prediction intervals.	96
Figure 4.7 Probability distribution functions (PDFs) for (a) $\delta^{13}\text{C}$, (b) Mg/Ca, (c) $\delta^{18}\text{O}$, and (d) Sr/Ca.....	97
Figure 4.8 (a) Time-series of the LR06-B1 Mg/Ca (green), Sr/Ca (orange) and $[\text{}^{234}\text{U}/\text{}^{238}\text{U}]_i$ (yellow circles) records. Also shown are the $[\text{}^{234}\text{U}/\text{}^{238}\text{U}]_i$ values for a nearby stalagmite (LR06-B3) (cyan circles), which were previously reported in Griffiths et al. (2009). (b) Comparison of stalagmite $\delta^{18}\text{O}$ records from Liang Luar Cave (Flores) and Gunung Buda National Park (northern Borneo; Martin et al., 2007). There is a significant correlation between the two records [$r=0.50$ with 95% confidence interval (0.40; 0.58)]. The colour-coded arrows highlight the opposing $\delta^{18}\text{O}$ trends during the mid-Holocene interval from 4 to 6 ka. (c) Austral summer insolation at 20° S. (d) Average $\delta^{18}\text{O}_{\text{sw}}$ time-series for the IPWP reconstructed from stacked planktonic foraminifer $\delta^{18}\text{O}$ records (Stott et al., 2004). Grey shading highlights the timing of the Younger-Dryas climate anomaly (~12.8-11.5 ka) and the mid-Holocene interval from 4 to 6 ka.....	101
Figure 4.9 Comparison of Holocene palaeoclimate records from China, Indonesia, and east Africa. (a) Speleothem $\delta^{18}\text{O}$ records from Dongge cave, China (Wang et al., 2005), and (b) Liang Luar, Flores. (c) SST anomalies reconstructed from corals taken from the Mentawai (black circles) and Muschu/Koil (grey circles) islands (Abram et al., 2009; Fig. 4.1). The grey bars highlight increases in IPWP SSTs and the AISM coincident (within dating error) with decreases in the ASM at ~6.3 and ~4.2 ka. This indicates a southward displacement of the ITCZ. (d) An ice-core $\delta^{18}\text{O}$ record from Mt. Kilimanjaro (Thompson et al., 2002) shows air temperature trends in east Africa. Periods of cooler (warmer) air temperatures in east Africa correspond with higher (lower) IPWP SSTs and a stronger (weaker) AISM, indicating that the IOD may have been responsible for much of the Holocene variability in the AISM.....	105

- Figure 5.1** Location of Flores and other sites mentioned in the text. Mean summer (DJF) 96-hour back trajectory moisture path is shown (thick dashed line) for the period 1960-2000. HYSPLIT (Draxler and Rolph, 2003) was used to calculate moisture-source back-trajectories starting at an elevation of 1000 m (approximate cloud base height in the tropics). Gray shading shows the approximate position of the shoreline at 10 ka calculated from reconstructed gridded sea-level data (http://geochange.er.usgs.gov/pub/data/sea_level/). 116
- Figure 5.2** Multi-proxy records for stalagmite LR06-B1 over the period 0 to 12.7 ka B.P. (a) Time series of stalagmite $\delta^{18}\text{O}$, Sr/Ca, and Mg/Ca. (b) Rampfit regression model applied to the $\delta^{18}\text{O}$, Sr/Ca, and Mg/Ca time series over the period 8.65 ka to 10.15 ka. Gray shading highlights the duration of the shift in mean values for all three proxies. 118
- Figure 5.3** Comparison of the (b) first multi-proxy principal component (PCA1), extracted from the LR06-B1 $\delta^{18}\text{O}$, Sr/Ca, and Mg/Ca stalagmite records, with (a) charcoal and (c) PCA1 from rainforest pollen taxa from Lake Euramoo, Atherton Tablelands (Haberle, 2005). The red line shows a 10-point running mean. The open circles and dashed line in (b) shows the rampfit regression results, indicating the short duration of the monsoon transition which is also evident in the PCA1 of rainforest pollen taxa (yellow shading). Colour coded analytical uncertainties for the dates through the sharp transition in the stalagmite and pollen records are shown along the bottom. The gray shading highlights the timing of the Younger Dryas, which is characterised by increased AISM rainfall coeval with a periodic expansion of rainforest in northeast Australia. 120
- Figure 5.4** Comparison of the (a) LR06-B1 PCA1 record with other proxy data over the period 12.64 ka to present. Red line shows a 10-point running mean. (b) Sea-level reconstruction based on marine sediments from the Red Sea (Siddall et al., 2003). (c) Sea-surface temperature (SST) reconstructions from planktonic foraminifera marine cores MD76 (black circles; (Stott et al., 2004) and MD62 (solid line; (Visser et al., 2003), and coral records from the tropical west Pacific (blue, Abram et al., 2009; orange, Beck et al., 1997; pink, Castellaro et al., 1997; purple, McCulloch et al., 1996). Blue dashed line shows a 3-point running mean between all fossil coral records. Gray shading envelopes the 95% confidence interval around the running mean. (d) Summer (DJF) insolation at 20° S. The blue box surrounds the common change in the LR06-B1 PCA1, sea-level and coral-inferred SSTs. 122
- Figure 6.1** The location of Liang Luar Cave, Flores, Indonesia, from where stalagmites LR07-A8 and LR07-A9 were collected. Contour lines show average SST anomalies during the 1975/76, 1988/89 and 1998/99 La Niña events (Smith et al., 2008). Inset: The GISP2 $\delta^{18}\text{O}$ (blue) (Groote and Stuiver, 1997) and CH_4 (red) (Blunier and Brook, 2001) profiles plotted against Northern Hemisphere summer insolation (gray) (Berger and Loutre, 1991). The yellow shading is the time period of interest, with GIS 21 labelled. The gray box indicates the approximate timing of the MIS5a-5b transition. The GISP2 records were synchronised to the most recent EPICA time-scale (Lemieux-Dudon et al., 2010). 130
- Figure 6.2** Scanned images of stalagmites LR07-A8 and LR07-A9. Blue dots indicate the positions of the 19 U/Th ages. Yellow dashed lines show the positions and names of the nine Hendy tests conducted along individual laminae. Red dashed lines show the 1-mm resolution drill-hole tracks used for the stable isotopes. Black boxes indicate the micro-milled sections used for high-resolution (0.25 mm) analysis of stable isotopes and trace elements. Also indicated is the approximate mid-point position of GIS 21. 134
- Figure 6.3** Age-depth models for stalagmites LR07-A8 (upper) and LR07-A9 (lower). The symbols each date along with its respective 2σ uncertainty. The red line indicates the derived age model, while the green shading represents 1σ and 2σ error envelopes. The two anomalous ages (blue diamonds) were not included in the age-model calculations. 139

- Figure 6.4** Hendy tests conducted on nine individual growth laminae throughout stalagmites LR07-A8 and LR07-A9. Colour coded symbols represent the names of each laminae corresponding to their longitudinal positions indicated in Fig. 6.2. Laminae with $\delta^{18}\text{O}$ variability $\leq 0.5\text{‰}$ are assumed to have been deposited in isotopic equilibrium where the $\delta^{18}\text{O}$ reflects that of the drip-water, rather than non-equilibrium fractionation (Hendy, 1971)..... 141
- Figure 6.5** Comparison of the combined $\delta^{18}\text{O}$ and $\delta^{13}\text{C}$ records with the growth rate curves for stalagmites LR07-A8 (red) and LR07-A9 (blue). The positions of the U/Th ages used to construct the age models and growth rates are shown along the bottom. The gray shading highlights two isotopic excursions that coincide with start of increased growth rates. These intervals are examined in finer detail in the next section..... 143
- Figure 6.6** (a) Comparison of the $\delta^{18}\text{O}$ and $\delta^{13}\text{C}$ records for the spliced time-series of stalagmites LR07-A8 and LR07-A9. The spliced record was obtained by averaging the stable-isotope values for the period of overlap (i.e. $\sim 88 - 89$ ka). Both records were also detrended to highlight the decadal- to centennial-scale coherence between the two records. The detrended $\delta^{18}\text{O}$ ($\Delta\delta^{18}\text{O}$) and $\delta^{13}\text{C}$ ($\Delta\delta^{13}\text{C}$) records have a significant correlation coefficient ($r = 0.43$). (b) High-resolution analysis of stable isotopes and trace elements through TS1 (85.7 – 86.3 ka) and (c) TS2 (89.4 – 90.2 ka). Trace elements have been smoothed with a 5-point running mean. 145
- Figure 6.7** Comparison of stalagmite $\delta^{18}\text{O}$ records between (a) Liang Luar Cave, Flores, (b) Boutevera Cave, Brazil (Cruz et al., 2005; Wang et al., 2007), and (c) Sanbao Cave, China (Wang et al., 2008). The gray curves represent summer insolation at the respective cave latitudes. The y-axis for the $\delta^{18}\text{O}$ curves in (a) and (b) have been inverted for clarity. The open circles in (a) show a 3-point running mean. Colour-coded error bars for the U/Th ages used to constrain the isotopes for each record are also shown. 149
- Figure 6.8** Comparison of the Liang Luar stalagmite $\delta^{13}\text{C}$ record (c), with (a) CH_4 (Grachev et al., 2007) and (b) $\delta^{18}\text{O}$ (Grootes and Stuiver 1997) concentrations from the GISP2 ice-core, (d) CO_2 (Ahn and Brook, 2008) and $\delta^{18}\text{O}$ records from the Byrd ice core, and (f) dD from the EPICA ice core record (Members, 2006). The gray shading highlights the abrupt negative shift in stalagmite $\delta^{13}\text{C}$ values coincident with the abrupt CH_4 and $\delta^{18}\text{O}$ excursions during the onset of GIS 21. The positions of the speleothem radiometric ages are shown along the bottom (red dots). All ice-core records have been placed on the most up-to-date EPICA time-scale (Lemeux-Dudon et al., 2010), which employed a stratigraphic marker (i.e. a tephra layer) at 92.5 ± 2 ka. All ice-core records were subsequently synchronised to the new EPICA time-scale by linearly interpolating between the ‘old’ and ‘new’ EPICA time-scale and then applying these adjustment factors to the GISP2 CH_4 and $\delta^{18}\text{O}$ ice-core records and the Byrd CO_2 and $\delta^{18}\text{O}$ ice-core records. This resulted in all records being shifted back in time by ~ 2 ka. The Byrd time-scale was on the GISP2 time-scale prior to adjustment..... 152
- Figure 6.9** Age-uncertainty-versus-age plot for stalagmite LR07-A9 calculated from the U/Th age-model - see Drysdale et al. (2005, 2007) for details of the methods used to calculate this plot. The gray bar brackets GIS 21 in Liang Luar while the dashed line shows the commencement of this event as highlighted in Figure 6. 10. Note the minimal uncertainty in the speleothem chronology during GIS 21 owing to the high concentration of U/Th ages throughout this interval. The timing of the event is thus extremely well constrained..... 159
- Figure 6.10** Comparison of GISP2 (a) CH_4 (Grachev et al., 2007) and (b) $\delta^{18}\text{O}_{\text{ice}}$ (Grootes and Stuiver 1997) with (c) $\delta^{13}\text{C}$, (d) growth rate (e) $\delta^{18}\text{O}$ and (f) the first principal component (PC1) of the trace elements from stalagmite LR07-A9 for the period 85-87 ka. PC1 was obtained from the elements Mg, Sr, Y, and P and explains 50% of the variance. The coloured lines in (c) and (e) represent the high-resolution (0.25 mm) stable-isotope measurements while the gray circles show the lower resolution (1 mm) analyses. The gray shading highlights the duration of the transition of each proxy into

GIS 21. The dashed vertical lines indicate the approximate timing of GIS 21, and the isotopic anomaly just prior-to, in the CH₄, $\delta^{18}\text{O}_{\text{ice}}$, and stalagmite $\delta^{13}\text{C}$. Black dots at the bottom of the figure show radiometric ages for LR07-A9.....161

List of Tables

Table 2.1 Oxygen ($\delta^{18}\text{O}$) and hydrogen isotope ($\delta^2\text{H}$) compositions of rainfall collected near Liang Luar Cave during the September 2006 – April 2007 period. Delta values are reported as the per mil (‰) difference between the sample and Vienna Standard Mean Ocean Water (VSMOW).	35
Table 2.2 Summary of TIMS U-Th age data for stalagmites LR06-B1 and LR06-B3 from Liang Luar Cave. Ratios in brackets are activity ratios calculated from the atomic ratios, using decay constants in Edwards et al. (1987). 2σ errors for the uncorrected (uncorr.) ages were propagated directly from the uncertainties in the ($^{230}\text{Th}/^{238}\text{U}$) and ($^{234}\text{U}/^{238}\text{U}$) ratios. The corrected (corr.) ^{230}Th ages were calculated using equation 1 of Hellstrom (2006) using half-lives specified in Cheng et al. (2000). BP = before present (present = A.D. 1950).	41
Table 2.3 Summary of MC-ICP-MS U-Th age data for stalagmites LR06-B1 and LR06-B3 from Liang Luar Cave. “U ng g ⁻¹ ” is uranium content of the sample. Activity ratios were determined by the methods described in Hellstrom (2003) and the supplementary materials of Drysdale et al. (2005). The corrected (corr.) ^{230}Th ages were calculated using the equation 1 of Hellstrom (2006) using half-lives specified in Cheng et al. (2000). BP = before present (present = A.D. 1950).	43
Table 3.1 Summary of fluid-inclusion δD_f (VSMOW) and $\delta^{18}\text{O}_f$ (VSMOW), and speleothem calcite $\delta^{18}\text{O}_c$ (VPDB) shown in Figs 3.3-3.5. Depth is the mid-point distance (in mm) from the top of stalagmite LR06-B1 where the calcite prisms were extracted for fluid inclusion analyses. Ages (ka) are from the published age-depth model of Griffiths et al. (2009). Speleothem calcite formation temperatures shown in Fig. 3.6 were calculated using the Craig (1965) equation. ΔT represents the difference in temperature relative to the modern cave average of 25°C.	67
Table 3.2 Summary of the $\delta^{18}\text{O}$ (VSMOW) and δD (VSMOW) values for the drip waters (D-W) and cave pool waters (P-W) displayed in Figs 3.2-3.3. D-W1 represents the modern drip-water feeding stalagmite LR06-B1 used in this study.	68
Table 4.1 Summary of Pearson correlation coefficients (r -values) between the trace element and stable isotope ratios. All values are significant at the 95%-level.	95
Table 6.1 Summary of MC-ICP-MS U-Th age data (ka) for stalagmites LR07-A8 and LR07-A9 from Liang Luar Cave. “U ng g ⁻¹ ” is uranium content of the sample. Activity ratios were determined by the methods described in Hellstrom (2003) and the supplementary materials of Drysdale et al. (2005). The corrected (corr.) ^{230}Th ages were calculated using equation 1 of Hellstrom (2006) using half-lives specified in Cheng et al., 2000.	137
Table 6.2 Correlation matrix of the stable isotope and trace element transects through (a) TS1 (89.4 – 90.2 ka; $n=260$) and (b) TS2 (89.4 – 90.2 ka; $n=252$). Prior to analysis, trace element profiles were interpolated to the same depth scale (0.25 mm resolution) as the stable isotopes. All series were detrended prior to analysis. Bold values are significant at the $P < 0.01$ level.	146

Publications arising from this thesis

Peer-reviewed Publications

- Griffiths, M.L.**, R.N. Drysdale, M.K. Gagan, J.C. Hellstrom, W.S. Hantoro, L.K. Ayliffe, S. Frisia, B.W. Suwargadi, *in preparation*. Abrupt Indo-Pacific climate response to high-latitude warming during MIS 5a/b. *Nature Geoscience*.
- Griffiths, M.L.**, R. N. Drysdale, H.B. Vonhof, M.K. Gagan, J.-x. Zhao, L.K. Ayliffe, W.S. Hantoro, J.C. Hellstrom, I. Cartwright, S. Frisia, B.W. Suwargadi, 2010. Younger Dryas-Holocene temperature and rainfall history of southern Indonesia from $\delta^{18}\text{O}$ in speleothem calcite and fluid inclusions. *Earth and Planetary Science Letters* 295, 30-36.
- Griffiths, M.L.**, R.N. Drysdale, M.K. Gagan, L.K. Ayliffe, S. Frisia, J.-x. Zhao, J.C. Hellstrom, M.J. Fischer, W. S. Hantoro, Y. -x. Feng, B.W. Suwargadi, 2010. Evidence for Holocene changes in Australian-Indonesian monsoon rainfall from stalagmite trace element and stable isotope ratios. *Earth and Planetary Science Letters* 292, 27-38.
- Griffiths, M.L.**, R.N. Drysdale, M. K. Gagan, J.-xin Zhao, L.K. Ayliffe, J.C. Hellstrom, W. S. Hantoro, S. Frisia, Y. -x. Feng, I. Cartwright, E. St. Pierre, M.J. Fischer, B.W. Suwargadi, 2009. Increasing Australian-Indonesian monsoon rainfall linked to early Holocene sea-level rise. *Nature Geoscience*, 2, 636-639.

Conference Proceedings

- Griffiths, M.L.**, R. Drysdale, S. Frisia, M. Gagan, J.-x. Zhao, M. Fischer, L. Ayliffe, Y.-x. Feng, J. Hellstrom, E. St Pierre, W. Hantoro, B. Suwargadi. Post-Glacial Climate Evolution of the Southern Sub-equatorial Tropics From Speleothems in Flores, Indonesia. *Past Global Changes (PAGES) 1st Young Scientists Meeting and Open Science Meeting, Oregon State University, Corvallis, Oregon, U.S.A., July 6-11, 2009*.
- Lewis, S., M. Gagan, L. Ayliffe, A. LeGrande, M. Kelley, G. Schmidt, J.-x. Zhao, **M. Griffiths**, R. Drysdale, W. Hantoro. Water isotope records of palaeomonsoon dynamics over the last ~30 kyr: integrating speleothem reconstructions and GCM results. *Past Global Changes (PAGES) 1st Young Scientists Meeting and Open Science Meeting, Oregon State University, Corvallis, Oregon, U.S.A., July 6-11, 2009*.
- Griffiths, M.L.**, R. Drysdale, M. Gagan, J.-x. Zhao, L. Ayliffe, J. Hellstrom, W. Hantoro, S. Frisia, Y.-x. Feng, I. Cartwright, E. St Pierre, M. Fischer, B. Suwargadi. Post-glacial coupling of the Australasian monsoon and teleconnections to the North Atlantic: New insights from Indonesian speleothems. *Past Climates Meeting, Wellington, New Zealand, May 15-17, 2009*.
- Griffiths, M.L.**, R. Drysdale, S. Frisia, M. Gagan, J.-x. Zhao, M. Fischer, L. Ayliffe, Y.-x. Feng, E. St Pierre, W. Hantoro, B. Suwargadi. Multi-proxy Evidence of Australian Summer Monsoon Variability During the Holocene: Links to the East-Asian Monsoon and the North Atlantic. *American Geophysical Union (AGU) Fall Meeting, San Francisco, U.S.A., Dec. 15-19, 2008*.
- Lewis, S., M.K. Gagan, L.K. Ayliffe, J.-x. Zhao, **M.L. Griffiths**, R.N. Drysdale, W.S. Hantoro. Speleothem reconstructions of palaeomonsoon dynamics from Flores, Indonesia over the last 24 kyr. *Goldschmidt, Vancouver, Canada, Jul. 13-18, 2008*.
- Griffiths, M.L.**, R. Drysdale, S. Frisia, M. Gagan, L. Ayliffe, J.-x. Zhao, E. St Pierre, Yue-xing Feng, W. Hantoro, B. Suwargadi. Post-glacial evolution of tropical monsoon precipitation from east Indonesian speleothems. *European Geosciences Union (EGU) general assembly, Vienna, Austria, Apr. 13-18, 2008*.
- Griffiths, M.L.**, S. Frisia, R. Drysdale, M. Gagan, L. Ayliffe, J.-x. Zhao, E. St Pierre, Yue-xing Feng, W. Hantoro, B. Suwargadi. Holocene Australasian monsoon intensity recorded in speleothems from Flores, Indonesia. *DAPHNE workshop, Heidelberg, Germany, Feb. 26-28, 2008*.
- Griffiths, M.L.**, R. Drysdale, M. Gagan, L. Ayliffe, J. X- Zhao, E. St Pierre, W. Hantoro, B. Suwargadi. A Holocene record of monsoon intensity from speleothems in Flores, Indonesia. *American Geophysical Union (AGU) Fall Meeting, San Francisco, Dec. 10-14, 2007*.

Griffiths, M.L., R. Drysdale, M. Gagan, L. Ayliffe, J. X- Zhao, E. St Pierre, W. Hantoro, B. Suwargadi.
A 12,800 year palaeomonsoon record from a stalagmite in Flores, Indonesia. *XVII IN QUATERNARY CONGRESS, Cairns, Australia, Jul. 28 – Aug. 3, 2007.*

Abstract

The climate evolution of the southern sub-equatorial tropics during marine isotope stage (MIS) 5a/b and the Holocene is explored using geochemical tracers from speleothems on Flores island, Indonesia. Oxygen isotope measurements from two precisely-dated stalagmites reveal that the Australian-Indonesian monsoon increased during the Younger Dryas (YD) cooling event, when Atlantic meridional overturning circulation was relatively weak. Monsoon precipitation intensified even more rapidly from 11 to 7 ka ago, when the Indonesian continental shelf was flooded by global sea-level rise.

Analysis of oxygen ($\delta^{18}\text{O}$) and hydrogen (δD) isotope ratios from speleothem fluid inclusions shows that inclusion- $\delta^{18}\text{O}$ values vary in phase with speleothem calcite $\delta^{18}\text{O}$ during the Holocene, confirming that calcite $\delta^{18}\text{O}$ primarily reflects variations in the $\delta^{18}\text{O}$ of meteoric rainfall. Cave drip-water temperatures, reconstructed from coupled measurements of $\delta^{18}\text{O}$ in speleothem calcite and fluid inclusions, remained relatively constant through the Holocene but were significantly cooler during the YD, consistent with the high northern latitudes.

To help confirm the stable isotope records, trace elements were used to reconstruct the position of the austral summer inter-tropical convergence zone and east Indonesian rainfall variability during the Holocene. Mg/Ca and Sr/Ca ratios correlate significantly with one another, and with $\delta^{18}\text{O}$ and $\delta^{13}\text{C}$, throughout the record suggesting that the trace element ratios were dominated by prior calcite precipitation, a process whereby degassing in the vadose zone during periods of low recharge causes deposition of calcite and disproportionate loss of Ca^{2+} ions (relative to Mg^{2+} and Sr^{2+}) ‘upstream’ of the stalagmite. Comparison of speleothem $\delta^{18}\text{O}$ time-series from Flores and Borneo shows that they vary in unison for much of the Holocene. However, there is an exception during the mid-Holocene when a distinct anomaly in $\delta^{18}\text{O}$ in the Borneo record, possibly caused by a change in the circulation of the Australian-Indonesian summer monsoon (AISM) in response to a period of positive IOD-like conditions in the eastern Indian Ocean, occurred between the two regions.

A stalagmite reconstruction of Indo-Pacific climate through the interval 84 - 91 ka shows that the lower-frequency oxygen isotope trend indicates that the AISM was largely controlled by local summer insolation during this time, while the carbon isotopes show a pattern that is closer linked with northern polar-latitude ice-core records. Most notably, an abrupt decrease in the temperature-controlled $\delta^{13}\text{C}$ values at the MIS 5a/b transition occurs in parallel with GIS 21 in the GISP2 $\delta^{18}\text{O}$ and CH_4 records highlighting the strong connection between the IPWP and North Atlantic during the last glacial period.

1 Introduction

1.1 Background

The modern climate of southern Australasia is orchestrated by the strength of the Australian-Indonesian summer monsoon (AISM), which is among the largest monsoon systems on Earth and accounts for ~70-80% of the region's annual precipitation. Gaining a clearer understanding of how this climatic phenomenon has varied through time is paramount to improved monsoon predictions and timely adaptation measures, especially given the uncertainties still evident in climate model projections under enhanced greenhouse-gas forcing (IPCC, 2007).

The AISM system delivers life-giving moisture to the millions of people who reside on the Indonesian archipelago, a region of rapid population growth and resource exploitation. Variations in the strength and/or timing of the monsoon can have catastrophic effects on the agricultural practises and industries of the population, hence greatly affecting the economy and livelihood of vulnerable communities. The AISM also adversely influences fragile ecosystems within the continental interior of the Australian land-mass, specifically the Lake Eyre Basin. During periods of strong summer rains (e.g. during La Niña events), the drainage from sub-catchments to the north flows southward through the "Channel Country" and, if the monsoon is strong enough, into the Lake Eyre Basin. This lake filling can permit life to flourish, as was the case following the strong summer monsoon season of 2008-2009 when Lake Eyre filled a depth of ~1.5 m. This was its deepest level since 1974 (when the depth reached ~6 m) and resulted in the return of many bird and fish species that had largely been absent for decades. Given the large influence of the AISM system on weather in Indonesia/northern Australia, its behaviour affects all aspects of the region's social, economic, and biological activity. Thus, it is critical that we gain a firmer handle on the factors controlling its variability over different time-scales so that we are better placed to make more accurate predictions.

Palaeoclimate proxy records and climate model experiments show that the dominant mechanism controlling orbital-scale variations in tropical monsoon behaviour is changes in the intensity of summer insolation (Ruddiman, 2006). However, in the region affected by the AISM system there is still some disagreement. Traditionally, it has been proposed that the AISM was generally stronger during warmer phases and weaker during cooler phases of the late-Quaternary (Kershaw, 1986; Kershaw and Nanson,

1993). Evidence from lake-level records suggest that AISM activity was reduced during the last glacial maximum (LGM) and became re-established during the late Glacial-to-Holocene transition (Magee et al., 2004; Miller et al., 2005; Wyrwoll and Miller, 2005); caution should be exercised when interpreting these records, however, given the inherent uncertainties in their chronologies and the fact that these lakes may reflect processes operating at a large drainage-basin scale. These authors attribute this change to boreal-winter insolation and its inherent influence on the AISM through the cross-equatorial flow of air from the semi-permanent Siberian high-pressure system. In contrast, some palaeoclimate model simulations have shown that increased local summer insolation can lead to stronger monsoon activity over northern Australia (Chappell and Sýktus, 1996; Wyrwoll and Valdes, 2003), effectively cancelling out the inference of a reduced monsoon during the LGM. These ambiguities highlight the need for more accurately dated regional to local-scale records from within the AISM domain because, hitherto, coral (Abram et al., 2007), lake (Magee et al., 2004) and deep sea-sediment (Stott et al., 2004) records provide only low-resolution and/or fragmentary information on past monsoon behaviour for the region.

This thesis aims to address these discrepancies by reconstructing the environmental-monsoon history of southern Australasia. It seeks to identify, for the first time, significant climate turning points during recent Earth history by utilising absolute-dated, highly-resolved, and environmentally sensitive geochemical tracers from speleothems on Flores island (southeastern Indonesia).

1.2 Study area

The study site is situated in the western portion of the east Indonesian island of Flores (namely the Manggarai province), which resides between latitudes 8°4' and 8°58' south and longitudes 119° 48' and 123° 1' 30'' east. The island extends over a length of 360 kilometres and lies to the northwest of Australia (Fig. 1.1a). Thus, it belongs to the southeastern islands of the Indonesian archipelago (Nusa Tenggara province) which includes the islands of Timor and Sumba. Flanked to the north by the Flores Sea and to the south by the Sawu Sea, Flores is volcanically active with at least 13 active volcanoes.

The Indonesian archipelago was formed from the tectonic collision and subduction of plate margins. The shifting of tectonic plates in the region created a convergent plate boundary, where the Indian Plate was subducted beneath the Eurasian Plate (Simandjuntak and Barber, 1996). This caused submarine volcanism and the subsequent emergence of new crust (Hall, 1996), and resulted in the

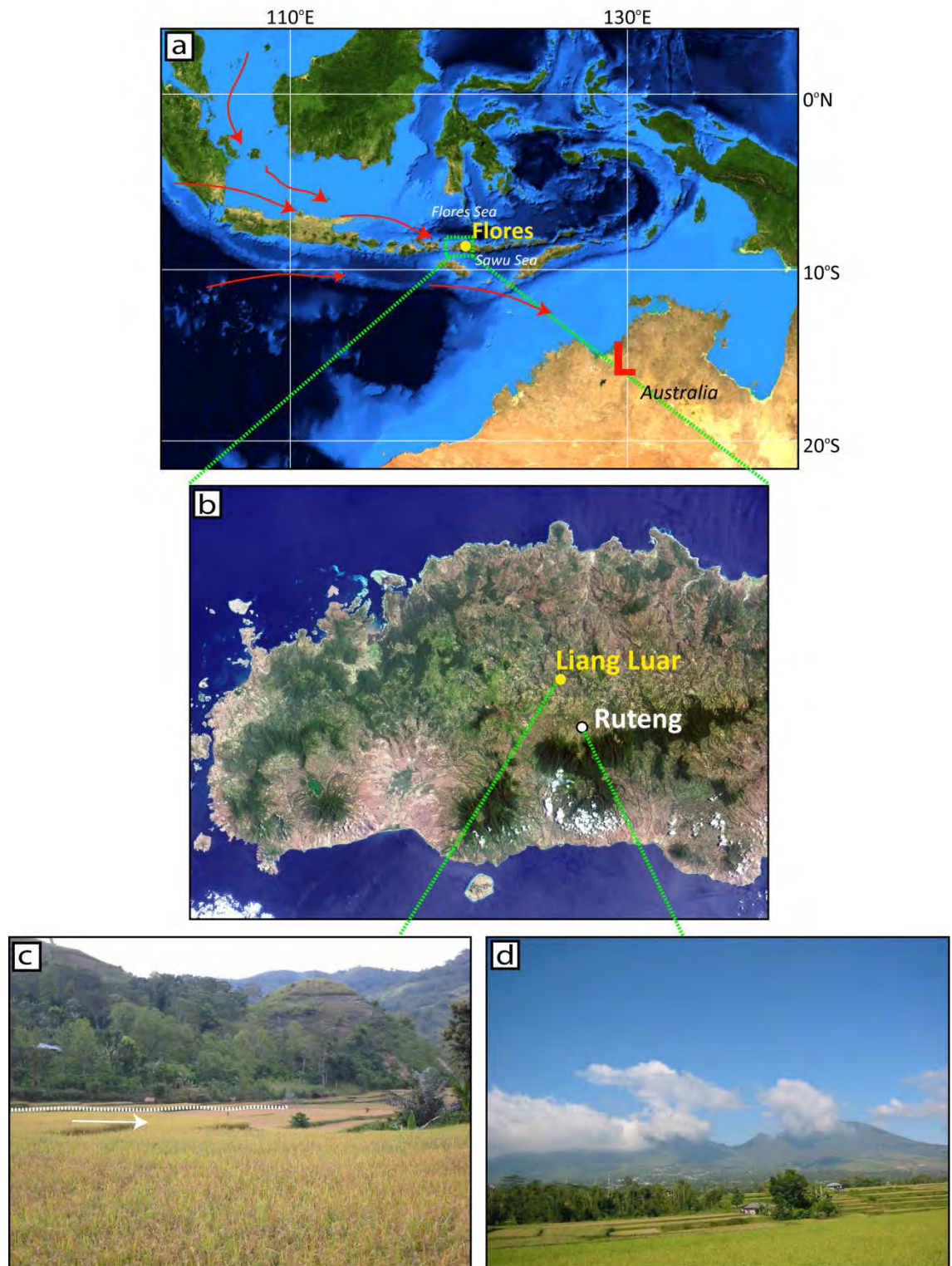
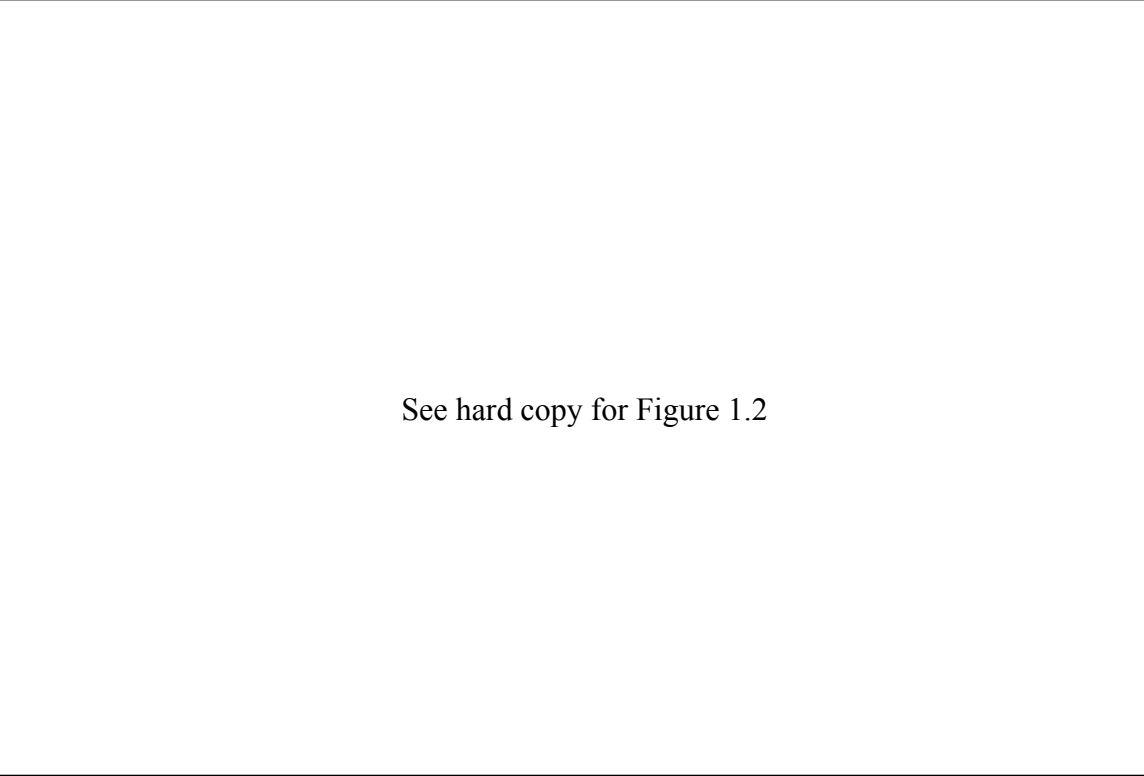


Figure 1.1 (a) Location of the east-Indonesian island of Flores (dashed box). The red arrows highlight the predominant NW surface-winds during the Austral-summer monsoon, which are being pulled in by the heat low (L) over northern Australia; (b) A Landsat image of western Flores showing the locations of Ruteng and the cave (Liang Luar) site; (c) Photo of the karst landscape surrounding the cave site. The white dashed line indicates the Wae Racang and the arrow shows the direction in which the river flows; (d) The volcanoes south of Ruteng and the cave site.

formation of the Banda Volcanic Arc and the volcanic islands that make up the Indonesian archipelago (Bellwood, 1997).

The speleothems used in this thesis were collected from Liang Luar Cave, located ~14 km north of Ruteng and ~25 km from the north coast (Fig. 1.1b). Liang Luar has developed within reefal (mainly built by corals) carbonates of Late Miocene-Early Pliocene age, which are mantled in part by volcanics of Quaternary age (Monk et al., 1997; van Bemmelen, 1949). The initial uplift of the reefal limestone surrounding the volcanic arc was the result of early submarine volcanism that formed the island (Burrett et al., 1991). The limestone deposit hosting Liang Luar Cave (i.e. the Waihekeng Formation; Fig. 1.2) contains folded strata that dip between 10 and 25° (Westaway, 2006) and is composed of a tuff-bearing clastic limestone with a sandy composition (van Bemmelen, 1949). It overlies the Nangapanda (sandstone



See hard copy for Figure 1.2

Figure 1.2 Geological map of western Flores highlighting the lithology of the study region (map is taken from Hendaryono, 1999). The red circle indicates the cave site location. Lithological units are as follows: (1) Waihekeng Formation–tuff-bearing clastic limestone; (2) Kiro Formation–breccia, lava, and tuff; (3) Nangapanda Formation–sandstone and limestone; (4) Miocene dykes/intrusions; (5) Bari Formation–limestone and sandy limestone; (6) Laka Formation–tuff with sandstone; (7) Older volcanic rocks; (8) coral-reef terrace; (9) Coastal terrace–alluvium; (10) Volcanoes.

and limestone) and Kiro (breccia) formations, and is bordered to the south by older volcanics (Figs 1.1d and 1.2). The thickness of the deposit is ~700 m. It contains fragments of orange chert and fossils, suggestive that deposition occurred within a deep-sea environment (Koesoemadinata et al., 1994). Despite its thickness, the limestone is minimally compact and porous, making it particularly susceptible to rapid karstification (Westaway et al., 2009). During the Middle Miocene, sandstone and limestones were deposited within the surrounding basins, and volcanic activity produced widespread breccias (Kiro formation). The Mangari province of western Flores represents an advanced cone karst landscape which can be classified as polygonal karst, although features characterised by residual cone karst can also be observed (Haryono and Day, 2004; Westaway, 2006) (Fig. 1.3a).

By the Late Miocene-Early Pliocene, the younger limestones [including the Waihekang formation (Fig. 1.2)] containing volcanic material had been deposited. Since the early Pleistocene, the limestone beds of western Flores have been periodically uplifting, rejuvenating an old Miocene coral bed to form its current relief (Koesoemadinata et al., 1994). It is this uplift process that is a governing force in shaping the geological and geomorphological landscape in the region. For example, tectonic uplift has resulted in: raised coral beds, river incision, valley deepening, terrace formation, stacked cave features, and accelerated karstification (Westaway et al., 2009). Evidence for this uplift is apparent from the raised coral-reef terraces of the northern and southern coast of Flores, and on the neighbouring islands of Sumba, Timor, Atauro, and Alor. A 1 Ma uranium-series dated coral-reef terrace record from Cape Laundi, Sumba Island (located 95 km south of Ruteng) provides an estimated uplift rate of between 0.2 and 0.5 mm/yr. (Bard et al., 1996; Pirazzoli et al., 1991, 1993).

See hard copy for Figure 1.3

Figure 1.3 (a) A 1.5 km² designated area around Liang Luar highlighting the morphology of the karst landscape. The concentric circles indicate karst cones while the open circles with hatch marks represent karst basins. Inset boxes show typical examples of karst cone and basin profiles. (b) A geomorphological map of the study area showing the four main cave systems in the region (colour coded). The pattern of cave dispersion highlights the interconnected nature of the cave systems throughout the karst region [figure modified after Westaway (2006)].

Liang Luar is a ~2 km-long cave, formed within a river-cut valley and overlain by ~30-50 m of bedrock. The soil is relatively thin above the cave and likely represents only the top ~1-2 m of the soil-bedrock profile. The cave is situated ~550 m above mean sea-level (a.m.s.l.), which is the approximate elevation of the highest three alluvial terraces deposited by the Wae Racang river (Fig. 1.1c) located in the wide Wae Racang valley (Westaway, 2006). The area is characterised by a dense network of cave systems with distinct morphologies, creating a honeycomb effect within the rounded limestone mountains. Tectonic uplift in the region has resulted in the descending of palaeowater tables, the abandonment of large dissolution chambers and the subsequent downward extension of the cave system via phreatic tubes and sinkholes (Westaway, 2006). As a result of this process, the area has four known major systems of interconnected caves spanning a horizontal distance of ~3 km (Fig. 1.3b).

The first ~100 m of Liang Luar is characterised by a small entrance, followed by a narrow passageway that is met by a ~5-7 m pitch over a rock fall (Fig. 1.4). It has a single (predominant) elliptical passageway that appears to have been formed via phreatic processes (Ford and Williams, 2004). At a distance of ~600-800 m from the cave entrance (where the speleothems were collected), the average temperature is ~25 °C (closely resembling the mean annual surface temperature) and a relative humidity of ~100%. The vegetation cover above the cave is dominated by tropical forest regrowth and coffee plantations.

See hard copy for Figure 1.4

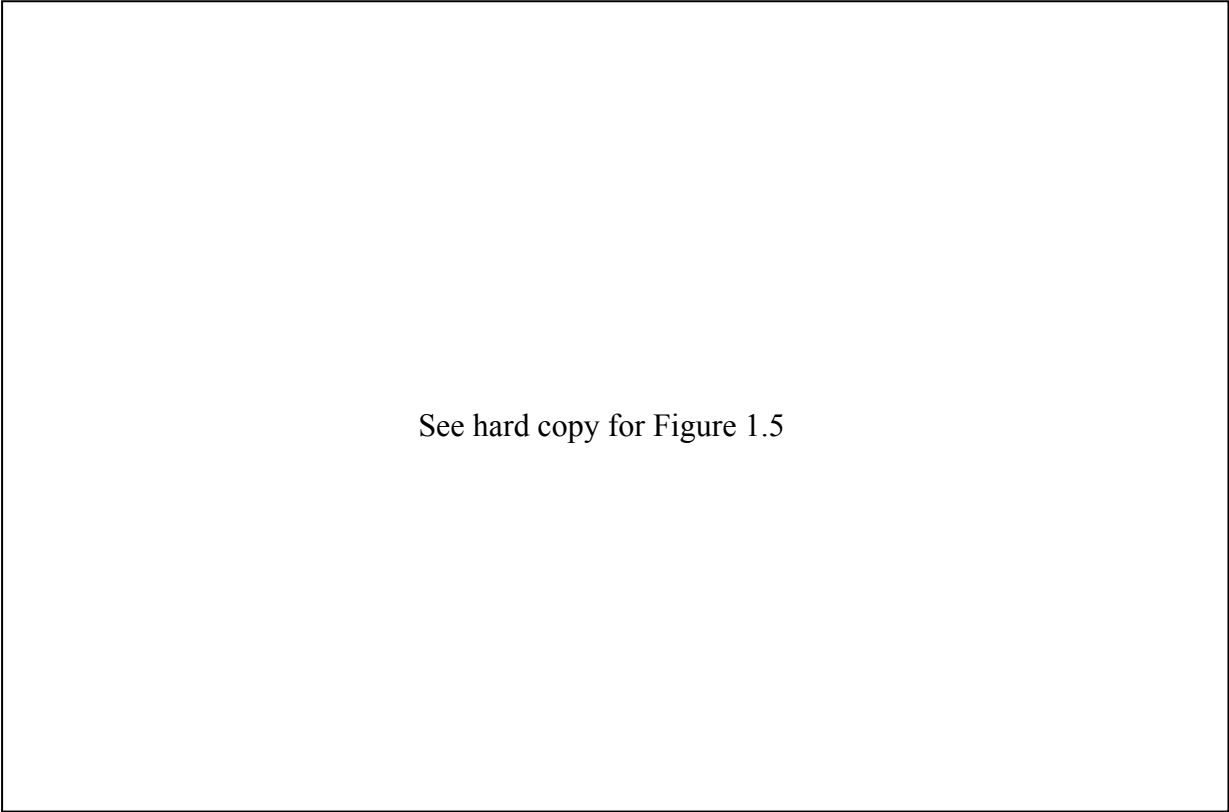
Figure 1.4 Plan view of Liang Luar Cave which stretches ~2 km in length. Orange dots show the positions of the stalagmites used in this thesis (survey map created by Garry K. Smith).

See hard copy for Figure 1.4

Figure 1.4 (continued)

1.3 Modern AISM dynamics

The Australian-Indonesian summer monsoon is one of the larger monsoon systems on Earth, affecting much of northern Australia, Indonesia, Malaysia, Papua New Guinea and the Solomon Islands (Fig. 1.5). A distinct feature of this system is that it is much weaker than its Asian counterpart. This is linked to the absence of intense mid- and upper-level atmospheric heating, due to the lack of a large topographic feature similar to that of the Tibetan plateau (Wyrwoll and Miller, 2001).



See hard copy for Figure 1.5

Figure 1.5 General circulation of the AISM at 200 hPa and 850 hPa (figure taken from Mitchell et al., 1994).

The mean seasonal cycle of the region affected by the Australian monsoon is characterised by a reversal in lower tropospheric winds and a marked change in rainfall. A close examination of Figure 1.6 reveals these seasonal changes in 850-hPa winds (representing lower tropospheric winds) and satellite-observed Outgoing Long-wave Radiation (OLR) (representing cloud tops of rain-producing convective systems).

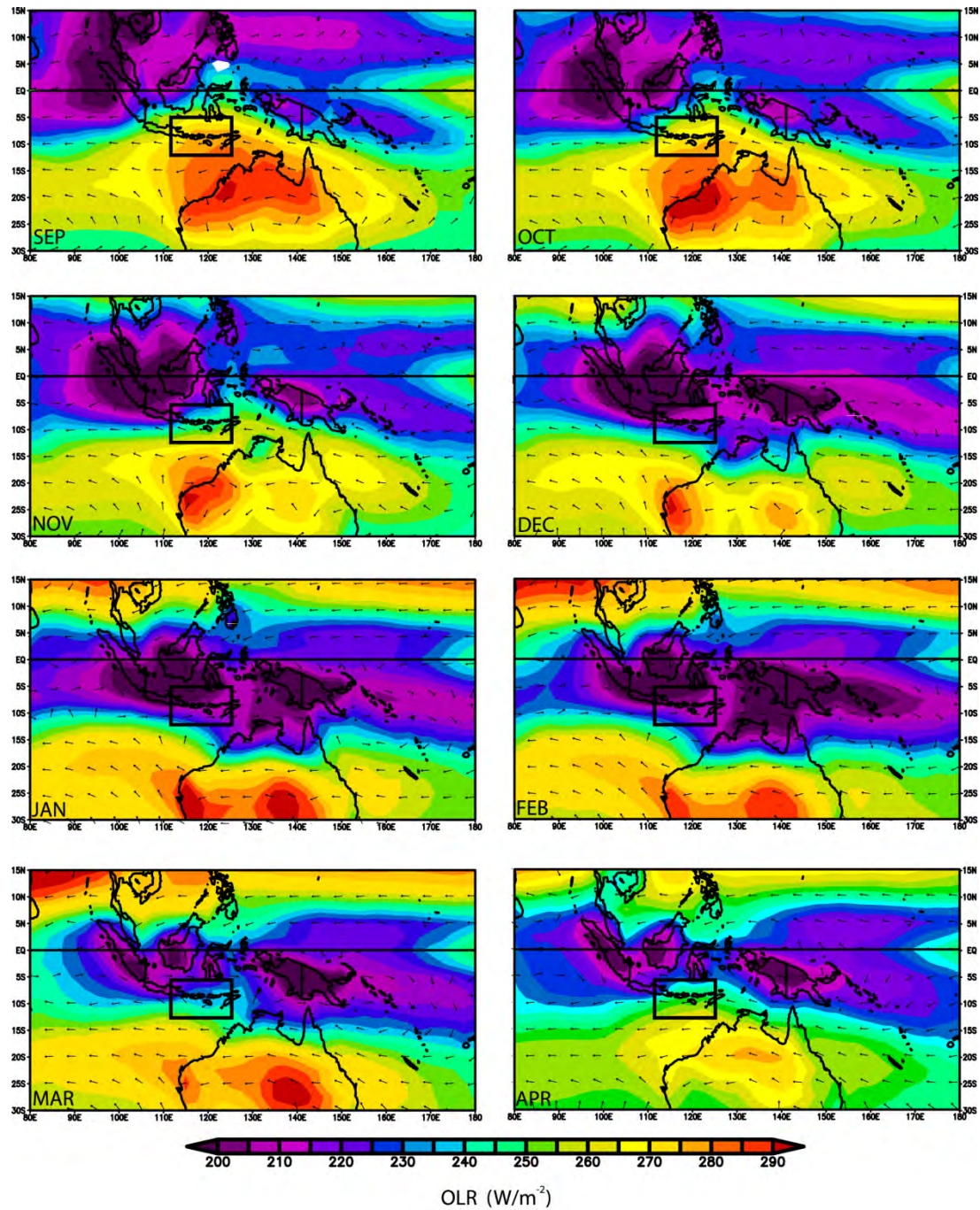


Figure 1.6 Monthly composites of NOAA satellite-observed outgoing long-wave radiation (OLR) and NCEP/NCAR Reanalysis 850-hPa wind vectors, based on data from 1979 to 2005. Low OLR values indicate cold cloud tops which are produced by precipitating cumulonimbus convection. OLR and wind vector data was retrieved from the following web address: <http://www.esrl.noaa.gov/psd/cgi-bin/data/composites/printpage.pl>.

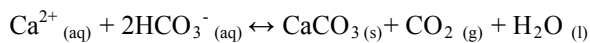
The seasonal cycle of the Australian summer monsoon may thus be summarised as follows (Wheeler and McBride 2005):

- In September, the prevailing mean 850-hPa winds across Indonesia are southeasterly trade winds originating from the subtropical ridge lying approximately 25°S . During this time, the strongest convective activity (OLR less than 220 W m^{-2}) is restricted to the north of the equator. This intense convective activity is associated with the northern hemisphere summer monsoon still being active, with the line of convection (low OLR) indicating the location of the Inter-tropical Convergence Zone (ITCZ). As the cycle progresses into the months of October and November, the low level easterlies decrease with a southeastward shift in the focus of strongest convective activity.
- By December, a continuous line of convective activity has been created along the region centred near 5°S , representing the southward movement of the ITCZ. As the ITCZ continues to intensify in the region south of the equator, westerly winds begin to appear between the equator and 10°S , while the easterly trades retreat southwards over the Australian continent.
- By January to February, the Southern Hemisphere convective activity has peaked with the tropical latitudes of Indonesia and northern Australia having a strong westerly flow with wind speeds up to 9 m s^{-1} . During this time the easterly trades strengthen across the central Australian continent, which consequently results in a well defined monsoon shear line along the region centred between $10^{\circ}\text{S} - 15^{\circ}\text{S}$.

Hence, the overall sequence of the ASM system in the Indonesia/Northern Australia region is a replacement of the dry easterlies with the convective westerlies for the months of October through February. Similar to other monsoon systems, the seasonal nature of the monsoon is thought to occur as a result of the land-sea thermal contrast which, in this case, is a result of the location of the off-equatorial Australian continent (Webster et al., 1998). However, additional Austral-summer forcing mechanisms have also been identified, including: (i) the seasonal incursion of warm sea-surface temperatures (SST's) south of the equator (Yano and McBride, 1998); and (ii) a southward movement of the Southern Hemisphere subtropical jet and subsequent increase in upper-level easterlies around Darwin (Troup, 1961).

1.4 Speleothems as palaeoenvironmental archives: materials and methods

Speleothems are secondary mineral deposits formed in caves. They consist of sparitic (crystalline) calcite or aragonite (Frisia and Borsato, 2010) and are widely used for palaeoclimate investigations (e.g. Burns et al., 2001; Fairchild et al., 2006; Fleitmann et al., 2003). The most common sparitic speleothems are stalactites (deposits hanging from the ceiling), stalagmites (growing from the floor upwards) and flowstones (deposits formed by stacked crystals commonly elongated perpendicular to the surface). Microbial activity in the soil zone produces carbon dioxide that dissolves in infiltration waters commonly generated from rainfall, and gives rise to the weak carbonic acid which dissolves the carbonate bedrock. The partial pressure of CO₂ in the seepage waters is higher than that of the cave air, resulting in the transfer of CO₂ from the drip water to the cave gas phase; this process is referred to as degassing (McDermott, 2004; McDermott et al., 2006). The pH of the solution increases and as such becomes supersaturated with respect to either calcite or aragonite. The precipitation of calcium carbonate on the growing surface of a speleothem is described by the following equation:



Given their direct dependency on climate-environmental parameters, the use of speleothems for paleoenvironmental reconstruction has been ever increasing over the past four decades since the early works of Hendy and colleagues on the isotopic composition of cave carbonates (Hendy and Wilson, 1968; Hendy, 1971). The recent exponential growth of speleothem studies has been facilitated by the development of thermal ionization mass spectrometry (TIMS) and multi-collector inductively coupled plasma mass spectrometry (MC-ICP-MS), which can provide accurate uranium series ages (Edwards et al., 1987; Eggins et al., 2005; Richards and Dorale, 2003; Shen et al., 2002). In addition, there have been improved techniques for high resolution sampling and analysis using laser ablation (LA)-ICP-MS, improved micromilling techniques using a lathe attached to a moving stage, ion microprobes and micro X-ray fluorescence scanners (Baldini et al., 2002; Kolodny et al., 2003), and synchrotron-radiation based ultra-high resolution micro X-ray fluorescence mapping (Borsato et al., 2007; Frisia et al., 2005). Hence, using these improved techniques, speleothems have the ability to record key aspects of climate variability such as mean annual temperature, rainfall variability, atmospheric circulation changes and vegetation

response in a variety of measurable parameters which include (Fig. 1.7) (McDermott, 2004):

1. Stable isotope ratios of calcite ($\delta^{18}\text{O}$ and $\delta^{13}\text{C}$)
2. Stable isotope analysis of fluid inclusions (δD and $\delta^{18}\text{O}$)
3. Variations in trace elements (e.g. Mg, Sr, P, S, U)
4. Inter-annual thickness variations of growth layers
5. Organic acid content

Most published speleothem studies, particularly from monsoon dominated regions, have used the $\delta^{18}\text{O}$ composition of the calcite to reconstruct past climate without the support of additional proxies. While this approach has proven successful in reconstructing higher-amplitude and lower-frequency climate changes, it is less robust at detecting the more subtle changes in climate. Hence, a multi-proxy (i.e. using multiple indicators of environmental change) approach is desirable as it provides complementary information from the same archive that may be used to support the oxygen isotope record. Thus, this thesis employs a multi-proxy approach by utilising parameters one, two and three, to reconstruct Indo-Pacific climate.

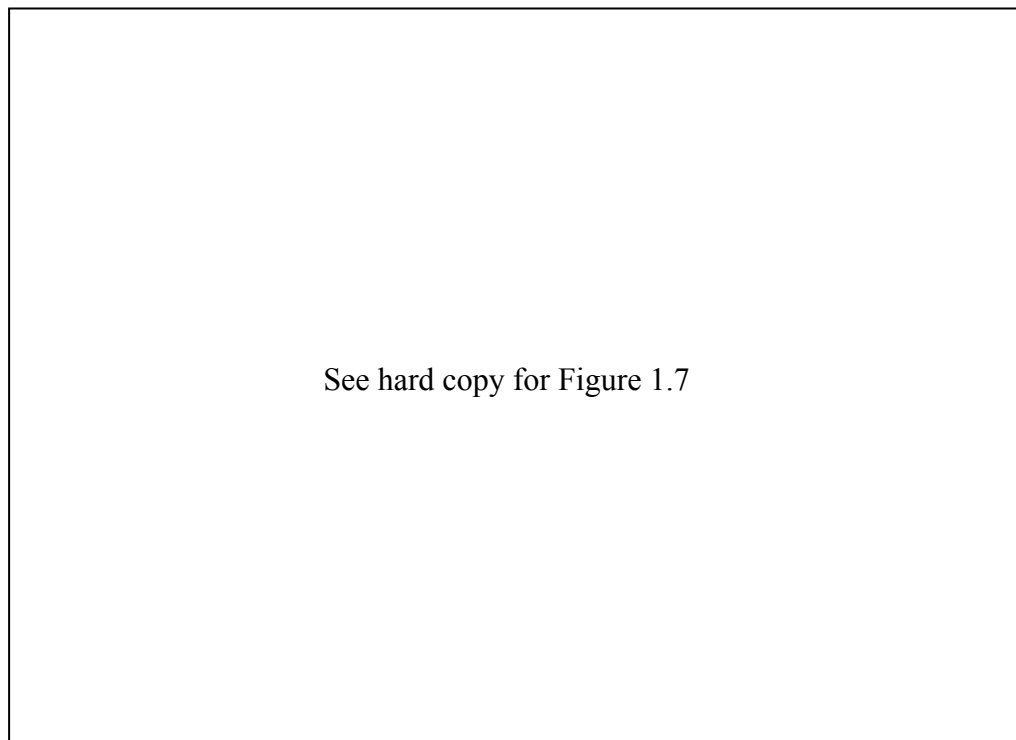


Figure 1.7 Schematic diagram displaying the links between the geochemical proxies preserved in the speleothem calcite and above-cave climate-environment parameters [figure taken from Frisia and Borsato (2010)].

1.4.1 ^{230}Th - ^{234}U age dating

An advantage of using speleothems to examine palaeoclimates is that they can be dated, with minimal error, using uranium series methods. Using the ^{230}Th dating technique, stalagmites can be dated between decades (i.e. <100 years) to around 500 ka with a typical age error of 1 to 3 % of the absolute age. Uranium isotopes leached from the carbonate bedrock are co-precipitated as uranyl carbonate with the calcite of the speleothems or, in some cases, incorporated as extra-lattice compounds associated with organic molecules/colloids. Normally, the precipitating solution contains no ^{230}Th because thorium ions are either absorbed onto clay minerals or remain in place as insoluble hydrolysates. Thus, providing the speleothem contains no clay or other insoluble materials which are carriers of detrital thorium, and assuming the initial $^{234}\text{U}/^{238}\text{U}$ ratio is known, we can use the initial activity ratio of ^{234}U to its decay product ^{230}Th to determine the sample age (Richards and Dorale, 2003).

Ground waters typically contain 0.1 to 3 parts per billion (ppb) of uranium, whereas thorium is insoluble in cave waters. As a result, newly formed speleothems have an initial concentration of parent ^{234}U , whereas the daughter ^{230}Th is absent. Speleothems generally have an initial uranium concentration of between 0.01 to several hundred parts per million, with the average value being around 0.5 ppm (Schwartz, 1986). After deposition, the number of ^{230}Th atoms increases as the ^{234}U atoms decay, until the rate of production of ^{230}Th comes into equilibrium with the rate of decay of ^{234}U . An important advantage of using this method is that the ^{230}Th ages are absolute ages and no significant correction factor is needed, except for samples with relatively high detrital contamination.

In this thesis, the ^{230}Th dating was performed on a TIMS at the Centre for Microscopy and Microanalysis, University of Queensland, Australia, under the supervision of Associate Professor Jian-xin Zhao. Additional samples were dated using a MC-ICP-MS at the University of Melbourne, Australia, under the supervision of Dr. John C. Hellstrom.

1.4.2 *Stable isotope composition of speleothem calcite*

1.4.2.1 *Background*

The most commonly used stable isotopes in speleothem paleoenvironmental research are C and O. These elements are an essential ingredient in the dissolution and deposition of calcium carbonate. Their chemical behaviour is not affected by the isotopic configuration, but rather the isotopic fractionation between different physical phases. The heavier isotopes tend to have a greater abundance in

the denser phases, such as in the liquid compared to the gas phase (Ford and Williams, 2007). Fractionation in chemical transformations or between physical phases is expressed by the fractionation factor (α). This fractionation factor is the proportion of isotope ratios for the reactant relative to the product:

e.g. $\text{H}_2\text{O}_{\text{water}} \leftrightarrow \text{H}_2\text{O}_{\text{vapour}}$

$$\alpha_{\text{water-vapour}} = \frac{R_{\text{reactant}}}{R_{\text{product}}}$$

$$\alpha^{18}\text{O}_{\text{water-vapour}} = \frac{(^{18}\text{O}/^{16}\text{O})_{\text{water}}}{(^{18}\text{O}/^{16}\text{O})_{\text{vapour}}}$$

The concentrations of isotopes are described as the ratio of the heavier, rare isotopes per thousand relative to the light isotope in a molecule. The standard unit of isotope ratio measurements is the “delta” (δ) value, given in per mil (‰). The results are expressed as a departure in parts per thousand from international standards (Hoefs, 1987):

$$\delta \text{ in } \text{‰} = \frac{R_{\text{(sample)}} - R_{\text{(standard)}}}{R_{\text{(standard)}}} \times 1000$$

For different elements a convenient “working standard” is used in each laboratory. However, all values measured relative to the “working standard” are reported in the literature relative to a universal standard (Hoefs, 1987). The common standard used to measure oxygen and carbon isotope ratios of carbonates is Vienna Pee Dee Belemnite (VPDB) and oxygen and hydrogen isotope ratios of water are measured using Vienna Standard Mean Ocean Water (VSMOW).

The use of stable isotope ratios has proven to be the most important proxy for speleothem-based environmental reconstructions and has formed the major type of geochemical investigation in speleothems (Fairchild et al., 2006; McDermott, 2004). Amongst other things, stable isotopes can provide information about the isotopic composition of precipitation ($\delta^{18}\text{O}_{\text{calcite}}$), type of vegetation and/or extent of soil microbial activity ($\delta^{13}\text{C}$) and cave air temperature on long time scales.

In this thesis, stable-isotope analyses were conducted on calcite powders drilled (1-mm resolution) and micro-milled (250- μm resolution) from four speleothem samples using a Taig CN C micromilling lathe. The isotopes were analysed from a gas-source isotope ratio mass spectrometer at the University of Newcastle, Australia (GV Instruments GV2003), and also a mass spectrometer at the Australian National University (Finnigan MAT-251).

1.4.2.2 $\delta^{18}\text{O}$

Thermal equilibrium between the bedrock temperature and that of the air in the cave is established when air and water movement in a cave is relatively slow; this thermal equilibrium approximates the mean annual surface temperature. As calcite precipitates from meteoric water as CO_2 is degassed, fractionation of oxygen isotopes occurs, which is dependent on the temperature of deposition ($-0.24\text{‰ }^{\circ}\text{C}^{-1}$ at 25°C ; O'Neil et al., 1969). Rozanski et al. (1993) examined the long-term changes in the oxygen isotopic composition of precipitation over the mid- to high latitudes and calculated an average modern-day $d\delta^{18}\text{O}_p/dT$ of $\sim 0.6\text{‰ }^{\circ}\text{C}^{-1}$. This suggests that, in theory, oxygen isotopes should provide a proxy for surface air temperature.

This theory, however, which was the goal of some earlier speleothem studies (e.g. Gascoyne et al., 1980), has proven inaccurate due to the number of other factors (besides air temperature) that can potentially influence the $\delta^{18}\text{O}$ signature of the cave drip-waters and hence that of the precipitated calcite (McDermott, 2004). Provided the speleothem was deposited in isotopic equilibrium with the parent water (Hendy, 1971), the $\delta^{18}\text{O}$ of the calcite may reflect source-moisture variations in: latitude, altitude (“altitude effect”), distance from the sea (“continental effect”), and rainfall amount (“amount effect”) (Rozanski et al., 1993). Moreover, on decadal to millennial time scales factors controlling the $\delta^{18}\text{O}$ of meteoric waters include changes in the $\delta^{18}\text{O}$ of the ocean (“ice volume effect”), changes in the seasonality of precipitation and shifts in the source of moisture and/or storm tracks (e.g., Bar-Matthews et al., 2003; Burns et al., 2001; Fleitmann et al., 2003). Hence, one must consider all these influences when interpreting speleothem oxygen isotopes in terms of palaeoclimate and, ideally, should seek the support of independent proxies (Fairchild et al., 2007).

Liang Luar provides an ideal environment for the use of $\delta^{18}\text{O}$ in palaeoclimate reconstruction for two reasons:

1. the small and single cave entrance restricts air-flow and as such the temperature remains relatively constant (typically $\sim 25^\circ\text{C}$) throughout the cave passages. Therefore, temperature dependent fractionation of $\delta^{18}\text{O}$ on short timescales (i.e. 1 to 100 years) is likely to be minimal.
2. humidity levels in most cave systems are high, including Liang Luar, which typically has a relative humidity level of between 95 and 99%. Hence, kinetic fractionation due to evaporation would have minor (if any) effects on the isotopic composition of drip waters. As such, the $\delta^{18}\text{O}$ values of the speleothems should reflect the isotopic composition of cave drip waters.

1.4.2.3 $\delta^{13}\text{C}$

Although carbon isotopic composition in speleothem calcite is an additional important palaeoenvironment proxy, interpreting changes in $\delta^{13}\text{C}$ can be a challenge (e.g. Baker et al., 1997; Fairchild et al., 2007). Non-climatic effects such as isotopic fractionation due to rapid CO_2 degassing can have a significant impact on $\delta^{13}\text{C}$ and thus alter the environmental signal. Regardless, many studies on speleothems from areas of different climatic settings have shown that $\delta^{13}\text{C}$ often reflects the changes in vegetation cover (e.g. C_3 versus C_4 plants) and the degree of soil microbial activity as related to climate (Genty et al, 2003, 2006). Generally, higher biogenic activity and /or higher proportion of C_3 vegetation (trees and shrubs) results in more negative $\delta^{13}\text{C}$ calcite values.

The Dissolved Inorganic Carbon (DIC) in drip waters is mainly derived from three sources (Fairchild et al., 2006):

1. atmospheric CO_2
2. soil CO_2 – type of surface vegetation
3. dissolution of the karst host rock

The evolution of DIC and $\delta^{13}\text{C}_{\text{DIC}}$ begins with the uptake of CO_2 , the isotopic component of which has decreased during the last 100 years from pre-industrial values of -6.4‰ to -7.8‰ (Friedli et al., 1986). The $\delta^{13}\text{C}$ composition of soil CO_2 is dependent on the photosynthetic pathway of the overlying plant material and the degree of microbial activity which is controlled by temperature. Generally the $\delta^{13}\text{C}$

values of respired soil CO_2 of C_3 -type plants (trees and shrubs) adapted to cold, wet climates range between -26 and -20‰ while that of C_4 -type plants (drought adapted grasses) between -16 and -10‰ (Cerling, 1984).

Under open system conditions, continuous equilibration occurs between the seepage water and an infinite reservoir of soil CO_2 . This drives a steady increase in bicarbonate content as the water progressively acquires more solutes in the unsaturated zone. Under this scenario, the $\delta^{13}\text{C}_{\text{DIC}}$ reflects the isotopic composition of the soil CO_2 , with reduced contribution from the host-rock (McDermott, 2004). In contrast, under closed system conditions the percolating water becomes isolated from the soil CO_2 reservoir as soon as carbonate dissolution commences. Since the carbonation reaction ($\text{H}_2\text{O} + \text{CO}_2 \leftrightarrow \text{H}_2\text{CO}_3$) consumes CO_2 , the extent of limestone dissolution is limited by the finite CO_2 reservoir. Under these conditions the isotopic composition of the carbonate host-rock influences the isotopic composition of the DIC (Hendy, 1971; Salomons and Mook, 1986) and as such the $\delta^{13}\text{C}_{\text{DIC}}$ becomes more enriched with longer water/host-rock interaction times.

1.4.3 Stable isotopes of fluid inclusions

A unique feature of certain speleothems is the presence of fluid inclusions, which are trapped residues of fossil cave drip-water that originally fell as rainfall above the cave (Schwarcz, 1976). Since the $\delta^{18}\text{O}$ and δD values of the drip waters feeding speleothems reflect those of the recharge precipitation, inclusion waters provide an additional proxy for regional rainfall and temperature reconstructions (McDermott et al., 2006). Traditionally, researchers have avoided analysing the $\delta^{18}\text{O}$ of fluid inclusions, mainly because of the widely held assumption that fluid inclusions may have exchanged oxygen isotopes with the host calcite through time, and thus the fluid-inclusion $\delta^{18}\text{O}$ may not reflect the pore-water composition at the time of entrapment (Schwarcz, 1976). However, recent studies have shown that post-depositional ^{18}O - ^{16}O exchange is negligible in Holocene stalagmites on the premise that the fluid-inclusion data plotted on (or close to) the GMWL, and are consistent with modern cave drip waters (Dennis et al., 2001; Dublyansky et al., 2009; van Breukelen et al., 2008).

Prisms of calcite were extracted from the longitudinal axis of one Holocene speleothem from Liang Luar, where the samples were then crushed (using a newly designed crushing device) and the liberated water analysed for $\delta^{18}\text{O}$ ($\delta^{18}\text{O}_f$) and δD (δD_f) using a Thermo-Finnigan TC-EA pyrolysis furnace housed at Vrije Universiteit, Amsterdam.

1.4.4 Trace elements

Trace element chemistry of speleothems has increasingly become an important proxy for palaeoclimate studies due to its ability to respond to changes in environmental conditions. As a speleothem continues to grow, it incorporates trace elements (e.g. Mg, Sr, Ba, Ca, U, Na, P) into its crystal structure, where the ratios of these elements are thought to correlate with changes in environmental conditions at the time of deposition, particularly temperature and rainfall at the surface. The interest in using trace elements as a palaeoenvironmental proxy in speleothems is largely attributed to the recent advancements in analytical measurement techniques such as secondary ionization mass spectrometry (SIMS), laser ablation inductively-coupled plasma mass spectrometry (LA-ICPMS) and synchrotron radiation based micro X-ray fluorescence (Borsato et al., 2007; Kuczumow et al., 2003).

Studies performed on speleothems from different environmental settings reveal that both hydrological (e.g. amount of precipitation, ground-water residence time) and/or growth related processes can affect trace element concentrations (e.g. Fairchild et al., 2001; Treble et al., 2003). While continued research on trace elements is needed, Mg, Sr, P, U, Y and Na appear to be the most reliable palaeohydrological indicators (Treble et al., 2003; Roberts et al., 1998; Borsato et al., 2007). However, the relationship between trace element concentrations and environmental-climatic conditions can vary amongst cave sites due to differences in the thickness and chemical composition of bedrock, groundwater movement, and soil processes. Therefore, a degree of caution is required when interpreting these elemental concentrations in terms of palaeoenvironmental processes.

Trace element concentrations of the stalagmites were measured on a Varian Liberty 4000 inductively coupled plasma atomic emission spectrometer (ICP-AES) at the University of Newcastle, Australia, and on a LA-ICP-MS at the University of Melbourne, Australia.

1.5 Objectives

This thesis aims to examine the AISM-environmental history of southern Indonesia during the Late-Pleistocene and explore possible teleconnections to other parts of the global climate system. The specific objectives of this thesis are:

1. To reconstruction the history of the AISM during the Holocene from the $\delta^{18}\text{O}$ composition of coeval stalagmites.

2. To explore the possibility of using stable isotopes of speleothem fluid inclusions to extract tropical palaeotemperatures (through coupled $\delta^{18}\text{O}$ of calcite and inclusion water) through the Holocene.
3. To utilise the trace-element composition of Liang Luar speleothems to help confirm the interpretation of the stable isotope records obtained from objectives one and two, and provide additional information as to the environmental fluctuations above the cave during the Holocene.
4. Explore a “snapshot” of Flores climate during MIS 5 a/b, with the specific goal of assessing possible teleconnection patterns between the Indo-Pacific and high latitudes.

1.6 Organisation of thesis

This thesis is arranged as a series of manuscripts that are either published, submitted or in preparation. Owing to this style, some sections (e.g. methods) within each chapter will appear slightly repetitive. However, I feel that this format permits a more effective and streamlined presentation of the main findings of the research.

Chapter 2 utilises the oxygen isotope composition of two exceptionally-well dated stalagmites from Liang Luar to reconstruct the history of the AISM from 12.4 ka to present. The main finding of this chapter was that the large increase in AISM intensity during the end of the deglaciation occurred at a time of rapid sea-level rise over the Sunda Shelf, the moisture source-region that fuels the local summer monsoon. Moreover, the Younger Dryas (YD) cold stage was characterised by increased monsoon precipitation, attributed to a southward shift in the ITCZ. Results of this chapter have been published in the journal *Nature Geoscience* (Griffiths et al., 2009).

Chapter 3 explores the use of stalagmite fluid inclusions to reconstruct AISM variability and cave palaeotemperatures based on the combined $\delta^{18}\text{O}$ composition of the fossil pore-water and host calcite. I find that the Holocene trend in fluid-inclusion $\delta^{18}\text{O}$ matches that of the host-calcite presented in Chapter 2, supporting the idea that the calcite $\delta^{18}\text{O}$ preserves the isotopic composition of the drip-water. Moreover, reconstructed cave palaeotemperatures demonstrate relative stability through much of the Holocene, consistent with IPWP marine sediments. However, there is a noticeable disparity during the YD where cave temperatures were $\sim 5^\circ\text{C}$ cooler than present; this finding is in agreement with fossil coral reconstructions. This chapter has been published in the journal *Earth and Planetary Science Letters* (Griffiths et al., 2010b).

Chapters 4 and 5 investigate the use of trace element variability (i.e. Mg and Sr) and initial $^{234}\text{U}/^{238}\text{U}$ activity ratios ($[^{234}\text{U}/^{238}\text{U}]_i$) as a potential proxy for palaeohydrology in a Holocene stalagmite. Here I find that the dominant environmental factors controlling the trace elements and $[^{234}\text{U}/^{238}\text{U}]_i$ are likely to be linked with hydrological processes above the cave system. These proxies thus provide independent support for the previous oxygen isotope interpretation and subsequently indicate that the early Holocene was somewhat drier than the mid-to-late Holocene in Flores. A unique feature of chapter 4 is the strong coherence of Liang Luar stalagmite- $\delta^{18}\text{O}$ and IPWP fossil-coral SST reconstructions (Abram et al., 2009) since the mid-Holocene. Specifically, I find that a weaker mid-Holocene AISM is synchronous with a slightly contracted IPWP (inferred from corals) and higher western Indian Ocean air temperatures [inferred from Kilimanjaro ice cores (Thompson et al., 2002.)]. Similar to previous interpretations, I attribute these patterns to “positive IOD-like” conditions during this time. Chapter 5 builds upon the findings of Chapter 4 by demonstrating that when the oxygen isotopes are combined with the moisture-sensitive trace elements, the merged records indicate that the early-Holocene monsoon onset may have occurred more abruptly than indicated from the oxygen isotopes alone. Chapter 4 has been published in the journal *Earth and Planetary Science Letters* (Griffiths et al., 2010a) while Chapter 5 has been submitted to *Journal of Quaternary Research*.

Chapter 6 examines Flores palaeoclimate during MIS 5a/b. The high-resolution record, which covers the interval 84 - 91 ka, is composed of two precisely-dated stalagmites. The lower-frequency oxygen isotope trend indicates that the AISM was largely controlled by local summer insolation during this time, while the carbon isotopes show a pattern that is more closely linked with northern polar-latitude ice-core records. Most notably, an abrupt decrease in Liang Luar $\delta^{13}\text{C}$ values at the MIS 5a/b transition occurs at the same time (within dating uncertainties) as GIS 21 in the GISP2 $\delta^{18}\text{O}$ and CH_4 records. In contrast, the Liang Luar $\delta^{18}\text{O}$ and trace elements show minor variability through this interval, suggesting that there was no significant shift in the monsoon. It is argued that this shift in $\delta^{13}\text{C}$ represents an abrupt increase in southern Indo-Pacific air temperatures, which would increase soil microbial activity and, hence, result in lower stalagmite $\delta^{13}\text{C}$ values. This occurred in sync with increased atmospheric methane concentrations and high northern-latitude air temperatures. This implies that changes in tropical air temperatures do not necessarily occur simultaneously with changes in monsoon rainfall. A direct causal mechanism for this equator-to-pole temperature connection during GIS 21 is a reduction in the Hadley circulation due to a weaker meridional temperature gradient, which resulted in a weakening of the trades

and hence reduced upwelling around the southern IPWP. This pattern of variability resembles conditions experienced during a La Niña phase. This chapter is currently in preparation for submission to *Nature Geoscience*.

1.7 References

- Abram, N.J., McGregor, H.V., Gagan, M.K., Hantoro, W.S. and Suwargadi, B.W., 2009. Oscillations in the southern extent of the Indo-Pacific Warm Pool during the mid-Holocene. *Quaternary Science Reviews* 28, 2794-2803.
- Abram, N.J., Gagan, M.K., Liu, Z.Y., Hantoro, W.S., McCulloch, M.T. and Suwargadi, B.W., 2007. Seasonal characteristics of the Indian Ocean Dipole during the Holocene epoch. *Nature* 445, 299-302.
- Baker, A., Ito, E., Smart, P.L. and McEwan, R.F., 1997. Elevated and variable values of C-13 in speleothems in a British cave system. *Chemical Geology* 136, 263-270.
- Baldini, J.U.L., McDermott, F. and Fairchild, I.J., 2002. Structure of the 8200-year cold event revealed by a speleothem trace element record. *Science* 296, 2203-2206.
- Bard, E., Jouanneau, C., Hamelin, B., Pirazzoli, P.A., Arnold, M., Faure, G., Somoosastro, P. and Syaefudin, I. 1996. Pleistocene sea levels and tectonic uplift based on dating corals from Sumba island, Indonesia. *Geophysical Research Letters* 23, 1473-1476.
- Bar-Matthews, M., Ayalon, A., Gilmour, M., Matthews, A. and Hawkesworth, C.J., 2003. Sea-land oxygen isotopic relationships from planktonic foraminifera and speleothems in the Eastern Mediterranean region and their implication for paleorainfall during interglacial intervals. *Geochimica et Cosmochimica Acta* 67, 3181-3199.
- Bellwood, P., 1997. The prehistory of Indonesian Malaysian Archeology. University of Hawaii Press, Honolulu, pp. 373.
- Borsato, A., Frisia, S., Fairchild, I.J., Somogyi, A. and Susini, J., 2007. Trace element distribution in annual stalagmite laminae mapped by micrometer-resolution X-ray fluorescence: Implications for incorporation of environmentally significant species. *Geochimica et Cosmochimica Acta* 71, 1494-1512.
- Burns, S.J., Fleitmann, D., Matter, A., Neff, U. and Mangini, A., 2001. Speleothem evidence from Oman for continental pluvial events during interglacial periods. *Geology* 29, 623-626.
- Burret, C., Berry, D.R., and Varne, R., 1991. Asian and South-western Pacific continental terranes derived from Gondwana, and their biogeographic. *Australian Systematic Botany* 4, 13-24.
- Cerling, T.E., 1984. The stable isotopic composition of soil carbonate and its relationship to climate. *Earth and Planetary Science Letters* 71, 229-240.

- Chappell, J., and Syktus, J., 1996. Palaeoclimate modelling: a western Pacific perspective. In: *Climate Change: Developing Southern Hemisphere Perspectives*. Eds. Giamblluca, T.W., and Henderson-Sellers, A. Chichester, Wiley, pp. 175-194.
- Climate Change 2007: The Physical Science Basis. Contribution of Working Group I to the Fourth Assessment Report of the Intergovernmental Panel on Climate Change. Eds. Solomon, S., D. Qin, M. Manning, Z. Chen, M. Marquis, K.B. Averyt, M. Tignor and H.L. Miller. Cambridge University Press, Cambridge.
- Dennis, P.F., Rowe, P.J. and Atkinson, T.C., 2001. The recovery and isotopic measurement of water from fluid inclusions in speleothems. *Geochimica et Cosmochimica Acta* 65, 871-884.
- Dublyansky, Y.V. and Spötl, C., 2009. Hydrogen and oxygen isotopes of water from inclusions in minerals: design of a new crushing system and on-line continuous-flow isotope ratio mass spectrometric analysis. *Rapid Communications in Mass Spectrometry* 23, 2605-2613.
- Edwards, R.L., Chen, J.H. and Wasserburg, G.J., 1987. U-238 U-234-Th-230-Th-232 Systematics and the Precise Measurement of Time over the Past 500000 Years. *Earth and Planetary Science Letters* 81, 175-192.
- Eggins, S.M., Grun, R., McCulloch, M.T., Pike, A.W.G., Chappell, J., Kinsley, L., Mortimer, G., Shelley, M., Murray-Wallace, C.V., Spötl, C. and Taylor, L., 2005. In situ U-series dating by laser-ablation multi-collector ICPMS: new prospects for Quaternary geochronology. *Quaternary Science Reviews* 24, 2523-2538.
- Fairchild, I.J., Baker, A., Borsato, A., Frisia, S., Hinton, R.W., McDermott, F. and Tooth, A.F., 2001. Annual to sub-annual resolution of multiple trace-element trends in speleothems. *Journal of the Geological Society* 158, 831-841.
- Fairchild, I.J., Smith, C.L., Baker, A., Fuller, L., Spötl, C., Matthey, D., McDermott, F. and Eimp, 2006. Modification and preservation of environmental signals in speleothems. *Earth-Science Reviews* 75, 105-153.
- Fairchild, I.J., Frisia, S., Borsato, A., Tooth, A., 2007. Speleothems. In: *Geochemical Sediments and Landscapes*. Eds. Nash, D.J., and McLaren, S.J., Blackwell Publishing, Oxford, pp. 200-245.
- Fleitmann, D., Burns, S.J., Neff, U., Mangini, A. and Matter, A., 2003. Changing moisture sources over the last 330,000 years in Northern Oman from fluid-inclusion evidence in speleothems. *Quaternary Research* 60, 223-232.

- Ford, D.C., and Williams, P., 2007. Karst Hydrogeology and Geomorphology. Wiley, West Sussex, England
- Friedli, H., Lotscher, H., Oeschger, H., Siegenthaler, U. and Stauffer, B., 1986. Ice core record of the $^{13}\text{C}/^{12}\text{C}$ ratio of atmospheric CO_2 in the past two centuries. *Nature* 324, 237-238.
- Frisia, S., Borsato, A., Fairchild, I.J. and Susini, J., 2005. Variations in atmospheric sulphate recorded in stalagmites by synchrotron micro-XU and XANES analyses. *Earth and Planetary Science Letters* 235, 729-740.
- Frisia, S., and Borsato, A., 2010. Karst. In: *Developments in sedimentology*, vol. 61. Ed. Van Loon, A.J. Doorwerth, The Netherlands, Elsevier, pp. 269-318.
- Gascoyne, M., Schwarcz, H.P., Ford, D.C., 1980. A palaeotemperature record for the mid-Wisconsin in Vancouver Island. *Nature* 285, 474-476.
- Genty, D., Blamart, D., Ouahdi, R., Gilmour, M., Baker, A., Jouzel, J. and Van-Exter, S., 2003. Precise dating of Dansgaard-Oeschger climate oscillations in western Europe from stalagmite data. *Nature* 421, 833-837.
- Genty, D., Blamart, D., Ghaleb, B., Plagnes, V., Causse, C., Bakalowicz, M., Zouari, K., Chkir, N., Hellstrom, J., Wainer, K. and Bourges, F., 2006. Timing and dynamics of the last deglaciation from European and North African delta C-13 stalagmite profiles - comparison with Chinese and South Hemisphere stalagmites. *Quaternary Science Reviews* 25, 2118-2142.
- Griffiths, M.L., Drysdale, R.N., Gagan, M.K., Zhao, J.X., Ayliffe, L.K., Hellstrom, J.C., Hantoro, W.S., Frisia, S., Feng, Y.X., Cartwright, I., Pierre, E.S., Fischer, M.J. and Suwargadi, B.W., 2009. Increasing Australian-Indonesian monsoon rainfall linked to early Holocene sea-level rise. *Nature Geoscience* 2, 636-639.
- Griffiths, M.L., Drysdale, R.N., Gagan, M.K., Ayliffe, L.K., Frisia, S., Zhao, J.-x., Hellstrom, J.C., Fischer, M.J., Hantoro, W.S., Feng, Y.-x., Suwargadi, B.W., 2010a. Evidence for Holocene changes in Australian-Indonesian monsoon rainfall from stalagmite trace element and stable isotope ratios. *Earth and Planetary Science Letters* 292, 27-38.
- Griffiths, M.L., Drysdale, R.N., Vonhof, H.B., Gagan, M.K., Zhao, J.-x., Ayliffe, L.K., Hantoro, W.S., Hellstrom, J.C., Cartwright, I., Frisia, S., Suwargadi, B.W., 2010b. Younger Dryas-Holocene temperature and rainfall history of southern Indonesia from $\delta^{18}\text{O}$ in speleothem calcite and fluid inclusions. *Earth and Planetary Science Letters* 295, 30-36.

- Hall, R., 1996. Reconstructing Cenozoic SE Asia. In: Tectonic Evolution of Southeast Asia. Eds. Hall, R. et al. Geological Society special publication, London, pp. 153-184.
- Haryono, E., and Day, M., 2004. Landform differentiation within the Gunung Kidul karst, Java, Indonesia. *Journal of Cave and Karst Studies* 66, 62-69.
- Hendaryono, 1999. Etude géologique de l'île de Florès—Apports à la connaissance de l'archipel indonésien oriental. PhD thesis, Département des Sciences de la Terre, Université de Savoie, Campus de Technolac, Le Bourget du Lac cedex, France.
- Hendy, C.H. and Wilson, A.T., 1968. Palaeoclimatic data from speleothems. *Nature* 219, 48-51.
- Hendy, C.H., 1971. The isotopic geochemistry of speleothems: The calculations of the effects of different modes of formation on the isotopic composition of speleothems and their applicability as palaeoclimate indicators. *Geochimica et Cosmochimica Acta* 35, 801-824.
- Hoefs, J., 1987. *Stable Isotope Geochemistry*. 3rd Edition, Springer-Verlag Berlin, pp. 241.
- Kershaw, A.P., 1986. Climatic-Change and Aboriginal Burning in Northeast Australia during the Last 2 Glacial Interglacial Cycles. *Nature* 322, 47-49.
- Kershaw, A.P. and Nanson, G.C., 1993. The Last Full Glacial Cycle in the Australian Region. *Global and Planetary Change* 7, 1-9.
- Koesoemadinata, S., Noya, Y., and Kadarisman, D., 1994. Geological Map of the Ruteng Quadrangle, Nusatenggara. Geological Research and Development Centre, Bandung.
- Kolodny, Y., M. Bar-Matthews, et al. 2003. A high spatial resolution $\delta^{18}\text{O}$ profile of a speleothem using an ion microprobe. *Chemical Geology* 197, 21-28.
- Kuczumow, A., Genty, D., Chevallier, P., Nowak, J. and Ro, C.U., 2003. Annual resolution analysis of a SW-France stalagmite by X-ray synchrotron microprobe analysis. *Spectrochimica Acta Part B-Atomic Spectroscopy* 58, 851-865.
- Magee, J.W., Miller, G.H., Spooner, N.A. and Questiaux, D., 2004. Continuous 150 ky monsoon record from Lake Eyre, Australia: Insolation-forcing implications and unexpected Holocene failure. *Geology* 32, 885-888.
- McDermott, F., 2004. Palaeo-climate reconstructions from stable isotope variations in speleothems: a review. *Quaternary Science Reviews* 23, 901-918.

- McDermott, F., Schwarcz, H.P., Harmon, R.S., Thompson, P. and Ford, D.C., 2006. Isotopes in speleothems. In: *Isotopes in Palaeoenvironmental Research. Developments in Palaeoenvironmental Research*. Ed. Leng, M.J. Springer, Dordrecht, the Netherlands, pp. 185–225.
- Miller, G., Mangan, J., Pollard, D., Thompson, S., Felzer, B., and Magee, J., 2005. Sensitivity of the Australian Monsoon to insolation and vegetation: Implications for human impact on continental moisture balance. *Geology* 33, 65-68.
- Mitchell, C.D., Hennessy, K.J., Pittock, A.B., 1994. Regional impact of the enhanced Greenhouse Effect on the Northern Territory. CSIRO Annual Report, 1992–1993.
- Monk, K.A., De Fretes, V., and Eksodiharjo-Lilley, G., 1997. The Ecology of Nusa Tenggara and Maluku. *The Ecology of Indonesia Series, Volume V*. Periplus Editions, Singapore.
- O'Neil, J.R., Clayton, R.N., Mayeda, T.K., 1969. Oxygen isotope fractionation in divalent metal carbonates. *Journal of Chemical Physics* 51, 1-10.
- Pirazzoli, P.A., Radtke, U., Hantoro, W.S., Jouannic, C., Hoang, C.T., Causse, C., Borel Best, M., 1991. Quaternary raised coral-reef terraces on Sumba Island, Indonesia. *Science* 252, 1834-1836.
- Pirazzoli, P.A., Radtke, U., Hantoro, W.S., Jouannic, C., Hoang, C.T., Causse, C., Borel Best, M., 1993. A one million-year-long sequence of marine terraces on Sumba Island, Indonesia. *Marine Geology* 109, 221–236.
- Richards, D.A. and Dorale, J.A., 2003. Uranium-series chronology and environmental applications of speleothems. *Uranium-Series Geochemistry* 52, 407-460.
- Rozanski, K., Aragulas-Aragulas, L., Gonfiantini, R., 1993. Isotopic patterns in modern precipitation. In: *Climate Change in Continental Isotopic Records, Geophysical Monograph 78*. Eds. Swart, P.K., Lohmann, K.C., McKenzie, J., Savin, S. American Geophysical Union, Washington, DC, pp. 1–36.
- Ruddiman, W.F., 2006. What is the timing of orbital-scale monsoon changes? *Quaternary Science Reviews* 25, 657-658.
- Roberts, M.S., Smart, P.L. and Baker, A., 1998. Annual trace element variations in a Holocene speleothem. *Earth and Planetary Science Letters* 154, 237-246.
- Salomons, W., Mook, W.G., 1986. Isotope geochemistry of carbonates in the weathering zone. In: *Handbook of Environmental Isotope Geochemistry, Vol. 2*. Eds. Fritz, P., Fontes, C.J. The Terrestrial Environment, B. Elsevier, Amsterdam, pp. 239–270.

- Schwarcz, H.P., Harmon, R.S., Thompson, P. and Ford, D.C., 1976. Stable isotope studies of fluid inclusions in speleothems and their paleoclimatic significance. *Geochimica et Cosmochimica Acta* 40, 657-665.
- Schwarcz, H.P.a.F., D.C., 1986. Geochronology and isotopic geochemistry of speleothems. In: *Handbook of Environmental Isotope Geochemistry*. Ed. Fontes, P.F.a.J.C. Elsevier, Amsterdam, pp. 271-303.
- Shen, C.-C., Edwards, R. L., Cheng, H., Dore, J.A., Thomas, R.B., Moran, S.B., Weinstein, S.E., Edmonds, H.N., 2002. Uranium and thorium isotopic concentration measurements by magnetic sector inductively coupled plasma mass spectrometry. *Chemical Geology* 185, 165-178.
- Simandjuntak, T.O., Barber, A.J., 1996. Contrasting tectonic styles in the Neogene orogenic belts of Indonesia. In: *Tectonic Evolution of Southeast Asia*. Eds. Hall, R., Blundell, D.J. Geological Society Special Publication, No. 106. The Geological Society, London, pp. 185–201.
- Stott, L., Cannariato, K., Thunell, R., Haug, G.H., Koutavas, A. and Lund, S., 2004. Decline of surface temperature and salinity in the western tropical Pacific Ocean in the Holocene epoch. *Nature* 431, 56-59.
- Thompson, L.G., Mosley-Thompson, E., Davis, M.E., Henderson, K.A., Brecher, H.H., Zagorodnov, V.S., Mashiotta, T.A., Lin, P.N., Mikhalev, V.N., Hardy, D.R., Beer, J., 2002. Kilimanjaro ice core records: evidence of Holocene climate change in tropical Africa. *Science* 298, 589–593.
- Treble, P., Shelley, J.M.G. and Chappell, J., 2003. Comparison of high resolution sub-annual records of trace elements in a modern (1911-1992) speleothem with instrumental climate data from southwest Australia. *Earth and Planetary Science Letters* 216, 141-153.
- Troup, A.J., 1961. Variations in upper tropospheric flow associated with the onset of the Australian summer monsoon. *Indian Journal of Meteorology and Geophysics* 12, 217-230.
- van Bemmelen, R.W., (1949). *The Geology of Indonesia*. General Geology of Indonesia and Adjacent Archipelagos, Volume 1A. Government Printing Office, The Hague.
- van Breukelen, M.R., Vonhof, H.B., Hellstrom, J.C., Wester, W.C.G. and Kroon, D., 2008. Fossil dripwater in stalagmites reveals Holocene temperature and rainfall variation in Amazonia. *Earth and Planetary Science Letters* 275, 54-60.
- Webster, P.J., Magaña, V.O., Palmer, T.N., Shukla, J., Tomas, R.A., Yanai, M., and Yasunari, T., 1998. Monsoons: Processes, predictability, and the prospects for prediction. *Journal of Geophysical Research* 103, 14451-14510.

- Westaway, K.E., 2006. Reconstructing the Quaternary landscape evolution and climate history of western Flores: an environmental and chronological context for an archaeological site. Unpublished PhD thesis, The University of Wollongong, Australia.
- Westaway, K.E., Roberts, R.G., Sutikna, T., Morwood, M.J., Drysdale, R.N., Zhao, J.-x., Chivas, A.R., 2009. The evolving landscape and climate of western Flores: an environmental context for the archaeological site of Liang Bua. *Journal of Human Evolution* 57, 450-464.
- Wheeler, M.C., and J.L. McBride, 2005. Australian-Indonesian Monsoon. In: *Intraseasonal Variability in the Atmosphere-Ocean Climate System*. Eds. Lau, W.K.M, and Waliser, D.E. Praxis Publishing, pp. 125-173.
- Wyrwoll, K.H. and Miller, G.H., 2001. Initiation of the Australian summer monsoon 14,000 years ago. *Quaternary International* 83-5, 119-128.
- Wyrwoll, K. H., and Valdes, P., 2003. Insolation forcing of the Australian monsoon as a control of Pleistocene mega-lake events. *Geophysical Research Letters* 30, 2279, doi:10.1029/2003GL018486.
- Yano, J.I., and McBride, J.L., 1998. An aqua planet monsoon. *Journal of Atmospheric Science* 55, 1373-1399.

2 Increasing Australian-Indonesian monsoon rainfall linked to early Holocene sea level rise

Abstract

The Australian–Indonesian summer monsoon affects rainfall variability and hence agricultural productivity in the densely populated tropical Indo–Pacific region. It has been proposed that the main control of summer monsoon precipitation on millennial timescales is local insolation (Holbourn et al., 2005; Kershaw et al., 2003; Wyrwoll et al., 2007), but unravelling the mechanisms that have influenced monsoon variability and teleconnections has proven difficult owing to the lack of high-resolution records of past monsoon behaviour. Here I present a precisely dated reconstruction of monsoon rainfall over the past 12,000 years, based on oxygen isotope measurements from two stalagmites collected in southeast Indonesia. I show that the summer monsoon precipitation increased during the Younger Dryas cooling event, when Atlantic meridional overturning circulation was relatively weak (McManus et al., 2004). Monsoon precipitation intensified even more rapidly from 11,000 to 7,000 years ago, when the Indonesian continental shelf was flooded by global sea-level rise (Bard, 1996; Peltier and Fairbanks, 2006; Siddall et al., 2003). I suggest that the intensification during the Younger Dryas cooling was caused by enhanced winter monsoon outflow from Asia and a related southward migration of the intertropical convergence zone (Yancheva et al., 2007). However, the early Holocene intensification of monsoon precipitation was driven by sea level rise, which increased the supply of moisture to the Indonesian archipelago.

2.1 Introduction

Improved knowledge of Australian-Indonesian Summer Monsoon (AISM) dynamics, particularly the factors that cause secular variability in monsoon strength, is critical to the sustainability of agricultural practices and life in the densely populated regions of the tropical Indo-Pacific. Palaeoclimate model experiments (Wyrwoll et al., 2007), palaeoproductivity data (Holbourn et al., 2005) and pollen records (Kershaw et al., 2003), suggest that variations in Southern Hemisphere summer insolation influence AISM rainfall at orbital time scales. In contrast, other studies suggest that the dominant AISM forcing is the strength of the East Asian Winter Monsoon (EAWM) (Miller et al., 2005), which is

governed by the strength of air outflowing from the semi-permanent high-pressure system over Siberia (the Siberian High). Through the Holocene, the mechanisms that drive shorter-term millennial- to centennial-scale AISM variations are poorly known, largely because existing coral records (Abram et al., 2007; Tudhope et al., 2001) and deep-sea sediments (Stott et al., 2004; Visser et al., 2003) provide only fragmentary or low-resolution information. Changes in the tropical Pacific zonal sea-surface temperature (SST) gradient (Stott et al., 2004) are thought to be important over this timescale for regions north of the equator (Haug et al., 2001; Partin et al., 2007; Wang et al., 2005), as are teleconnections with the high northern latitudes, but no detailed study has evaluated these influences south of the equator.

2.2 Environmental setting

Tropical speleothems have proven fruitful in recording Holocene variations in the intensity of the Asian monsoon (Dykoski et al., 2005; Partin et al., 2007; Wang et al., 2005) where information about rainfall amount and air-mass transport is captured by the oxygen isotope ratios ($\delta^{18}\text{O}$) of speleothem calcite (Rozanski et al., 1992). For this study, I investigated the Holocene history of the AISM through analysis of $\delta^{18}\text{O}$ in two stalagmites (LR06-B1, LR06-B3) collected from Liang Luar Cave in western Flores, Indonesia (8°32'S, 120°26'E; 550 m above sea level; Fig. 2.1). Liang Luar is ideally located to investigate past variations in the AISM because of its strong seasonal cycle of winds and precipitation. Mean annual rainfall at the cave site is 1,200 mm, with ~69% falling during the summer monsoon season (Dec–Mar) and only ~5% falling during the winter dry season (June–Sep) (Fig. 2.2). The rainfall maximum on Flores is linked to the lower tropospheric flow of moisture from the northwest during the southward progression of the intertropical convergence zone in the austral summer. The mean winds on Flores then shift from northwesterly to southeasterly trade winds in the austral winter dry season.

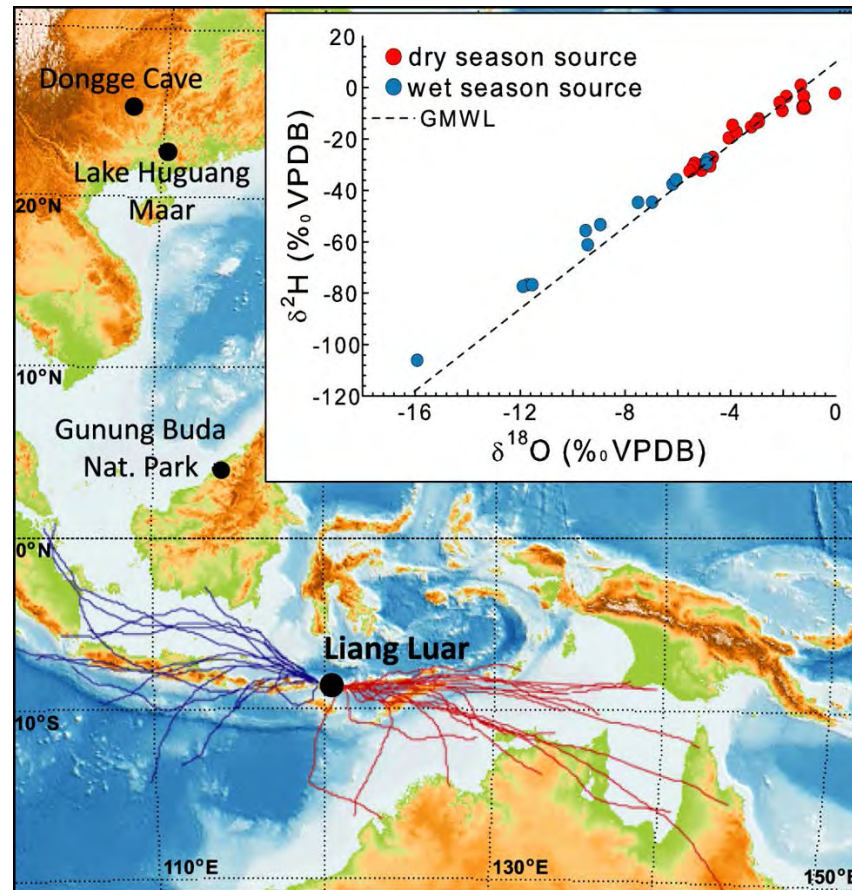


Figure 2.1 Moisture-source trajectories and rainwater isotope ratios for Liang Luar Cave. Physiographic map showing location of Liang Luar and other study sites. Solid lines represent HYSPLIT (Draxler and Rolph, 2003) calculated 96-hour back-trajectories of dry season (red) and wet season (blue) air parcels that generated rainfall during September 2006 – April 2007. Inset shows $\delta^{18}\text{O}$ versus $\delta^2\text{H}$ for the same rain days during September 2006 – April 2007. Dry season (red dots) and wet season (blue dots) rainwater have amount-weighted average $\delta^{18}\text{O}$ values of -3.5‰ (V-SMOW) and -10.3‰ , respectively. The dashed line represents the Global Meteoric Water Line (GMWL).

The strong seasonality of precipitation amount at Liang Luar is recorded by variations in the $\delta^{18}\text{O}$ of local rainwater (Fig. 2.1, Table 2.1). Comparisons of modern rainfall $\delta^{18}\text{O}$ values using back trajectory analysis of moisture-source regions reveal that monsoon season rainwater is depleted in ^{18}O (-10.3‰ for amount-weighted average $\delta^{18}\text{O}$) relative to dry season rainwater (-3.5‰ for amount-weighted average $\delta^{18}\text{O}$), with both seasonal sources plotting close to the Global Meteoric Water Line. This isotopic difference is related primarily to the stronger convergence and uplift of water vapour over the southern Indonesian maritime continent during austral summer.

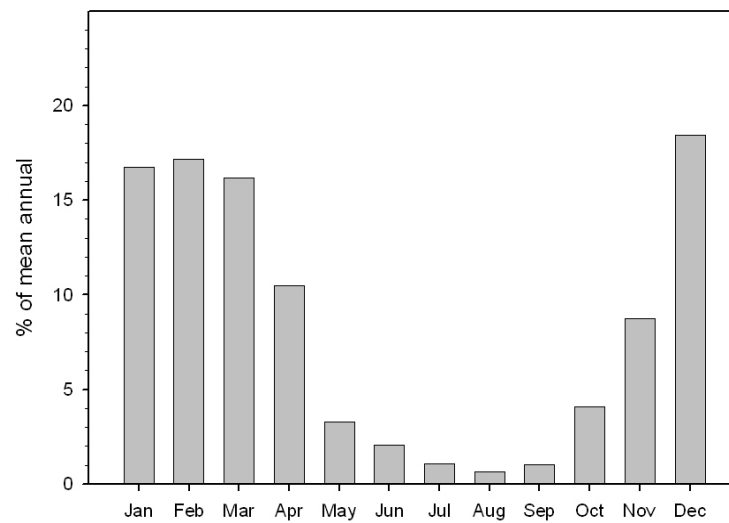


Figure 2.2 Rainfall climatology at Liang Luar from 1998 to 2008. Data is derived from NASA's satellite Tropical Rainfall Measuring Mission database (http://disc.sci.gsfc.nasa.gov/data/datapool/TRMM/01_Data_Products/02_Gridded/0_Monthly_Other_Data_Source_3B_43/index.html) centred at 8° 32'S, 120° 26'E with 0.25° resolution. Monthly values are expressed as the percentage of the mean annual total rainfall, which is 1200 mm for the 1998 to 2008 period.

Table 2.1 Oxygen ($\delta^{18}\text{O}$) and hydrogen isotope ($\delta^2\text{H}$) compositions of rainfall collected near Liang Luar Cave during the September 2006 – April 2007 period. Delta values are reported as the per mil (‰) difference between the sample and Vienna Standard Mean Ocean Water (VSMOW).

Date	Rainfall Amount	$\delta^{18}\text{O}$	$\delta^2\text{H}$
Southeasterly (dry season) source	mm	‰	‰
10/09/2006	3.5	-5.1	-32
14/09/2006	15.5	-2.0	-9
19/09/2006	4	-1.2	-7
11/10/2006	17.5	-1.3	1
13/10/2006	19.5	-1.2	-7
15/10/2006	22	-1.2	-3
23/10/2006	12.5	-1.2	-8
29/10/2006	27.5	-1.2	-8
3/11/2006	32.5	-3.2	-15
5/11/2006	40.5	-1.2	-8
8/11/2006	3.5	-2.9	-12
13/11/2006	11.5	-2.9	-13
17/11/2006	5.5	-3.0	-14
21/11/2006	14.5	-4.7	-27
22/11/2006	6	-4.8	-31
6/12/2006	32	-4.1	-20
10/12/2006	8.5	-1.9	-3
15/12/2006	27	-3.8	-17
20/12/2006	21.5	-5.1	-30
26/01/2007	13	0.0	-2
18/02/2007	3.5	-2.1	-6
21/02/2007	52.5	-3.9	-15
3/04/2007	15	-5.4	-30
4/04/2007	5.5	-5.5	-32
5/04/2007	11.5	-5.4	-31
8/04/2007	118.5	-5.6	-33
Amount-weighted average		-3.5	-21.6
Northwesterly (monsoon) source			
1/01/2007	42	-15.9	-106
3/01/2007	22	-8.9	-53
3/02/2007	23	-4.9	-28
23/02/2007	5	-6.2	-38
27/02/2007	21	-11.7	-77
1/03/2007	89	-11.9	-77
2/03/2007	278	-11.5	-77
6/03/2007	63.5	-7.0	-45
7/03/2007	53.5	-6.1	-36
14/03/2007	23	-7.5	-45
15/03/2007	10	-4.9	-30
17/03/2007	8.5	-9.5	-56
30/03/2007	13	-9.4	-61
Amount-weighted average		-10.3	-63.7
Total amount-weighted average		-7.2	-44.7

2.3 Sample description

Stalagmites LR06-B1 and LR06-B3 were collected from a large chamber located ~800 m from the single entrance of Liang Lue, a limestone cave underlying ~30-50 m of soil and bedrock. The chamber has a high humidity (close to 100% in June 2006 and May 2007) and stable mean annual temperature of ~25 °C, which closely resembles the temperature at the ground surface.

Stalagmite LR06-B1 (Fig. 2.3), which measures 1.25 m in length, was cut obliquely and embedded in clear casting resin and then microdrilled at 1 mm resolution along the central growth axis using a Taig CNC micromilling lathe. Stalagmite LR06-B3 is 1.6 m in length with Holocene material preserved above a sharp unconformity located 1.5 m below the actively growing upper surface (Fig. 2.4). Similar to LR06-B1, the specimen was cut into sections with ends angled at ~45° relative to the growth axis (to allow for sample overlap across the cuts). The lengths of the sections were determined to ensure that a 20 mm-thick longitudinal slab would definitely include the central growth axis in each section, thus accommodating movement of the growth axis in any direction. Shorter sections were cut where stalagmite growth was relatively complex, and vice versa. Contiguous low-resolution samples were then milled at ~10 mm increments (average 70 year resolution). The sample cross-section was large (5 mm x 5 mm) to allow the samples to extend into the central part of the slab (including the main growth axis) and provide sufficient material for initial U-series dating.

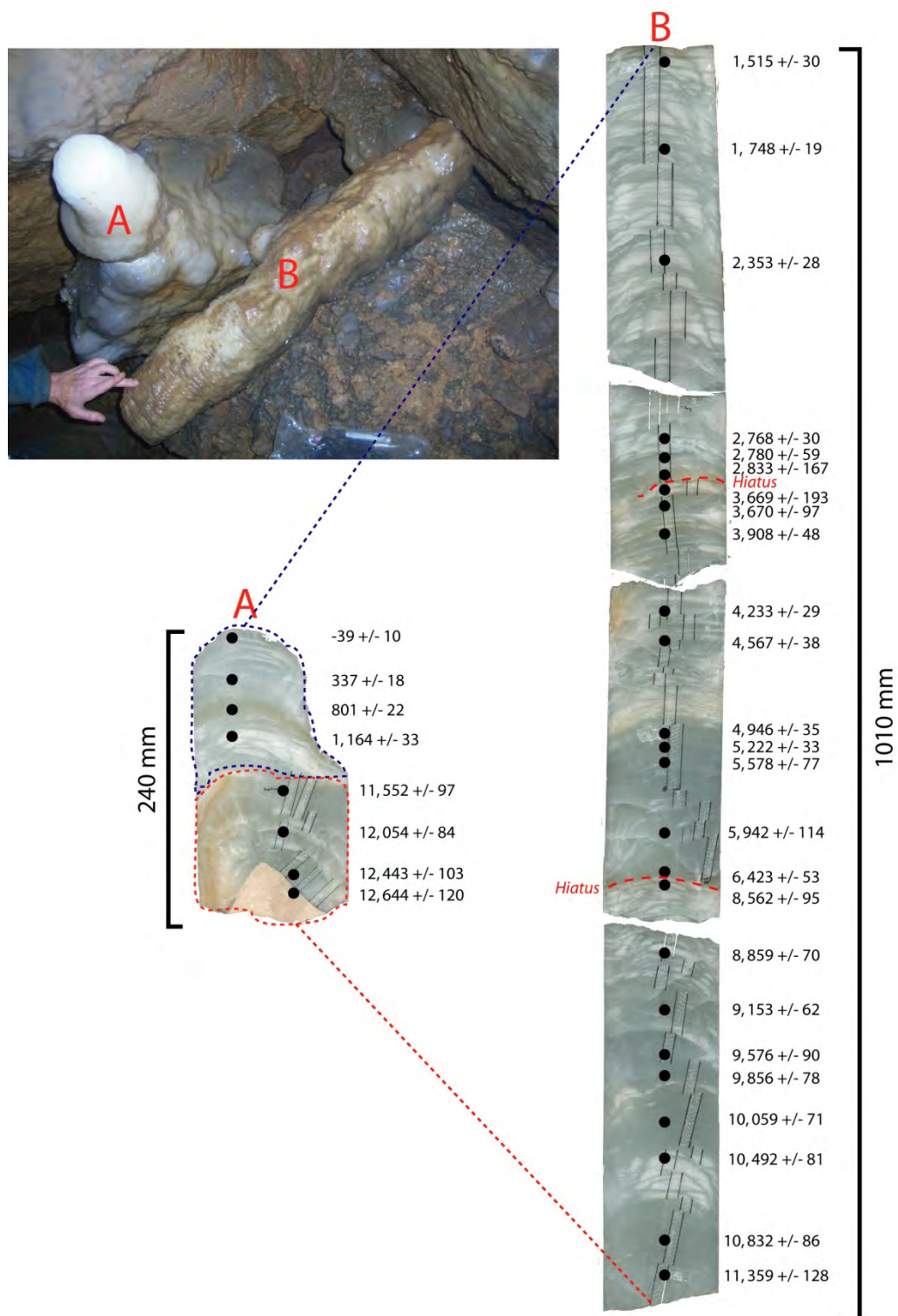


Figure 2.3 Scanned image of stalagmite LR06-B1 and photograph (top left) while *in situ* at the time of collection in June 2006. Black dots show the positions of the 33 U-Th ages. Section A (240 mm in length) was *in situ* at the time of collection while section B (1010 mm in length) had broken off 96 mm from the base ~1,500 years ago.

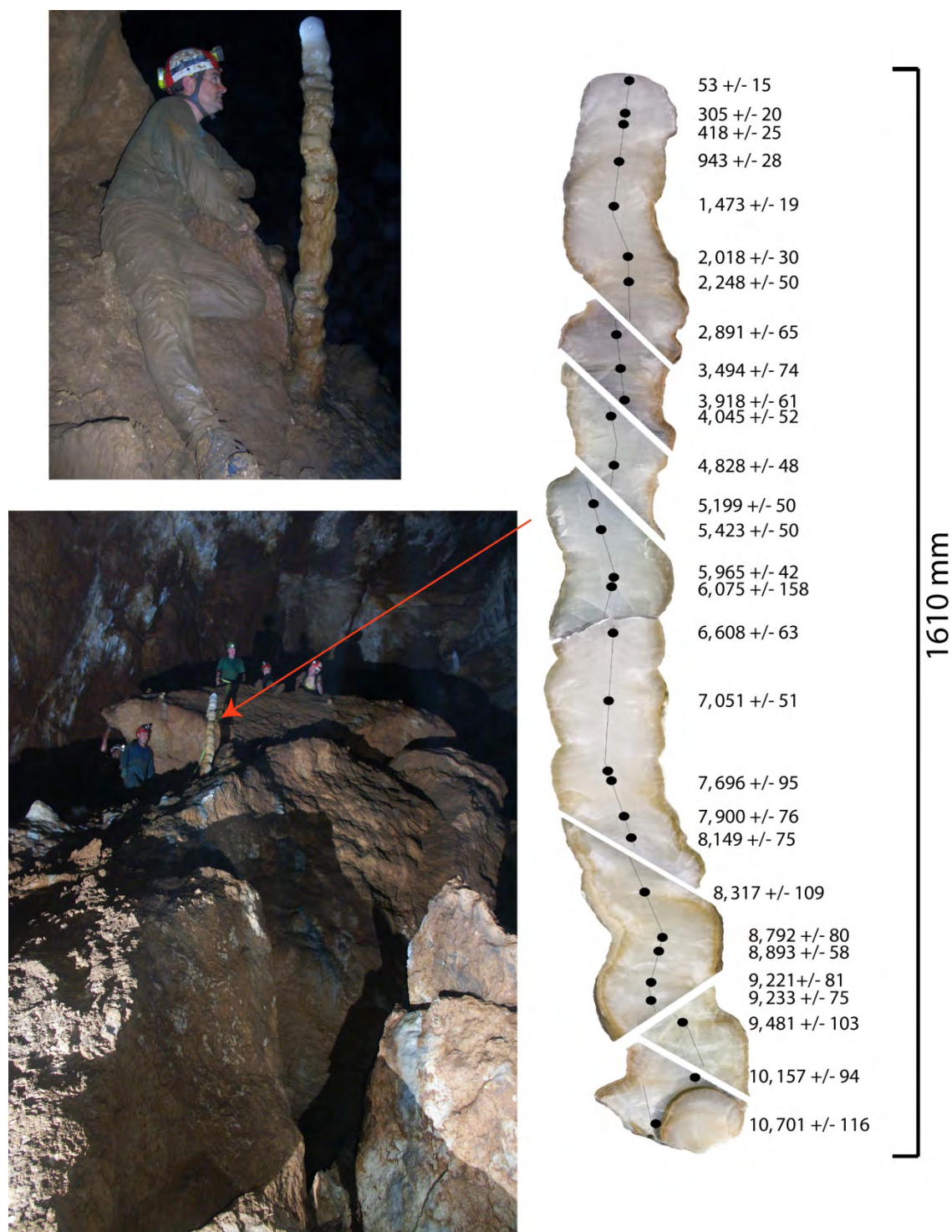


Figure 2.4 Same as Figure 2.3 but for stalagmite LR06-B3. Black dots show the positions of the 29 U-Th ages.

2.4 Methods

2.4.1 Chronology

The chronologies for stalagmites LR06-B1 and LR06-B3 were constructed from 62 U/Th dates using thermal ionisation mass spectrometry (TIMS) at the Centre for Microscopy and Microanalysis, University of Queensland, and a multi-collector coupled plasma mass spectrometer (MC-ICP-MS) at the University of Melbourne (Fig. 2.5; Table 2.2 and 2.3). The TIMS analyses were conducted on small pieces of calcite or splits of sample powders (covering ~5 – 10 mm of vertical growth) and weighing between 200 and 700 mg using a Fisons VG Sector 54 - 30 mass spectrometer equipped with a WARP filter and a ni on-counting Daly detector; see Yu et al. (2006) for a full description of the methods employed. The MC-ICP-MS analyses were performed on calcite samples weighing between 12 and 40 mg; refer to Hellstrom (2003, 2006) for a full description of the methods. The $[^{230}\text{Th}/^{232}\text{Th}]_i$ values for both specimens were determined to be 7 ± 2 (using the method of Hellstrom, 2006), which is within the range of values reported for tropical stalagmites (e.g. Partin et al., 2007). All U-Th ages have been corrected using this value and eqn. 1 of Hellstrom (2006) using the half-lives of Cheng et al. (2000).

The age models were constructed using a Bayesian-Monte Carlo approach using Wavemetrics *Igor Pro* software. A full description of the technique can be found in Drysdale et al. (2005, 2007). Based on these age-models, LR06-B1 grew in two phases: 12.6 ± 0.12 to 8.5 ± 0.09 thousand years before the present (ka; the data are calibrated to the ^{14}C age scale where “present” is defined as 1950 A.D.) and 6.5 ± 0.05 ka to the time of collection in June 2006. Both specimens experienced similar growth rates through time with LR06-B1 having an average growth rate of $0.12 \text{ mm year}^{-1}$ since 12.6 ka while LR06-B3 had an growth rate of $0.13 \text{ mm year}^{-1}$ since 10.7 ka.

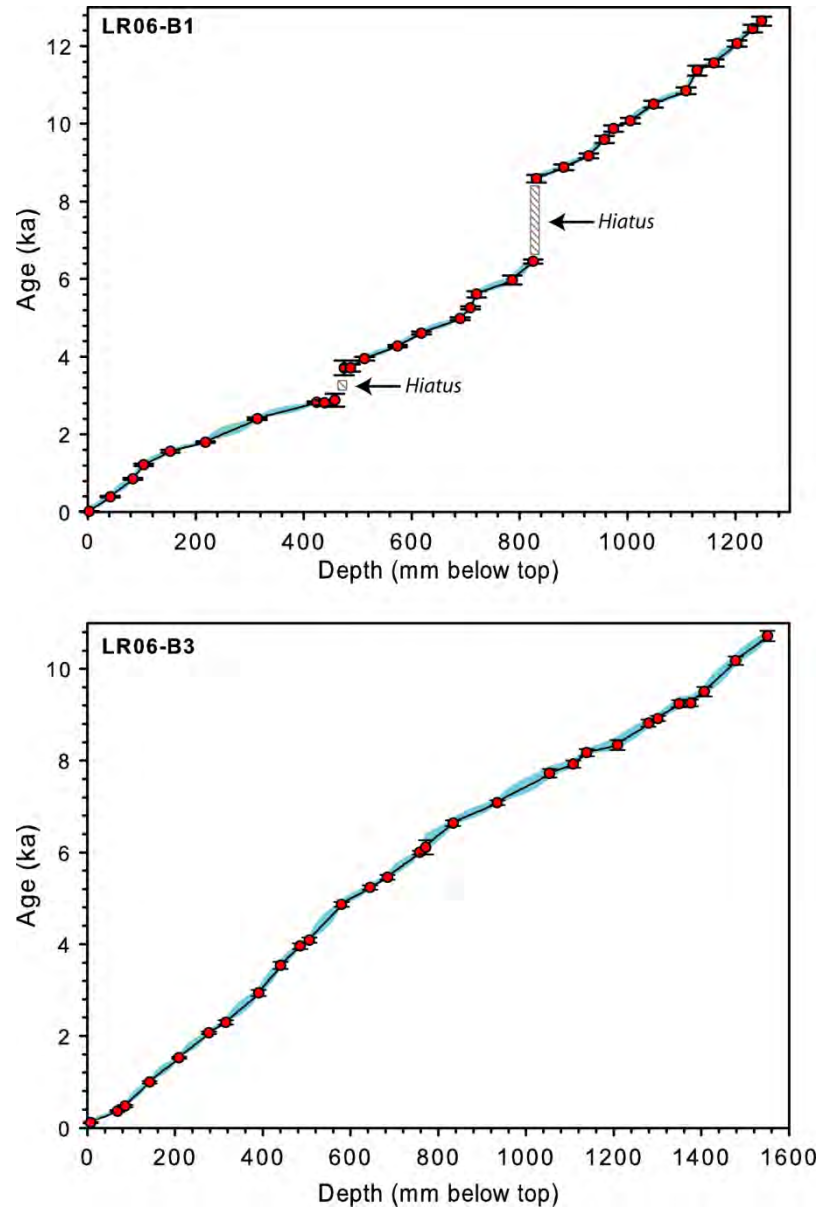


Figure 2.5 ^{230}Th depth-age models and 95% uncertainties are plotted for stalagmites a) LR06-B1 and b) LR06-B3. 95% uncertainty envelopes are indicated by blue shading. The symbols represent each U-Th age with 95% uncertainty shown by bars.

Table 2.2 Summary of TIMS U-Th age data for stalagmites LR06-B1 and LR06-B3 from Liang Luar Cave. Ratios in brackets are activity ratios calculated from the atomic ratios, using decay constants in Edwards et al. (1987). 2σ errors for the uncorrected (uncorr.) ages were propagated directly from the uncertainties in the $(^{230}\text{Th}/^{238}\text{U})$ and $(^{234}\text{U}/^{238}\text{U})$ ratios. The corrected (corr.) ^{230}Th ages were calculated using equation 1 of Hellstrom (2006) using half-lives specified in Cheng et al. (2000). BP = before present (present = A.D. 1950).

Sample I.D.	Depth (mm)	U (ppm)	^{232}Th (ppb)	$\pm 2\sigma$	$[^{230}\text{Th}/^{232}\text{Th}]$	$[^{230}\text{Th}/^{238}\text{U}]$	$\pm 2\sigma$	$[^{234}\text{U}/^{238}\text{U}]$	$\pm 2\sigma$	Uncorr. ^{230}Th age (yr)	Corr. ^{230}Th age (yr ago)	Corr. ^{230}Th age (yr BP)	Corr. initial $[^{234}\text{U}/^{238}\text{U}]$	$\pm 2\sigma$	$\pm 2\sigma$
B1/0003	3	0.2922	0.050	0.000	10.9	0.00061	0.00004	1.2526	0.0019	53	19	-39	1.2545	10	0.0018
B1/0042	42	0.2761	0.042	0.001	97.6	0.00492	0.00018	1.2660	0.0014	423	396	337	1.2682	18	0.0014
B1/0084	84	0.2285	0.024	0.000	288.5	0.01001	0.00024	1.2471	0.0015	876	859	801	1.2496	22	0.0016
B1/0107	107	35.481	4.354	0.082	349.1	0.01410	0.00036	1.2414	0.0012	1242	1222	1164	1.2441	33	0.0012
B1/0156	156	0.5405	0.182	0.001	162.3	0.01801	0.00024	1.2058	0.0029	1636	1573	1515	1.2086	30	0.0029
B1/0220	220	0.3639	0.038	0.000	591.5	0.02047	0.00020	1.2327	0.0019	1820	1806	1748	1.2357	19	0.0019
B1/0317	317	0.3690	0.064	0.001	490.2	0.02776	0.00030	1.2522	0.0030	2437	2412	2353	1.2559	28	0.0030
B1/0423	423	0.4507	0.060	0.000	735.6	0.03212	0.00032	1.2394	0.0027	2854	2838	2780	1.2433	30	0.0027
B1/0486	486	0.1295	0.089	0.001	194.7	0.04423	0.00103	1.2712	0.0017	3847	3728	3670	1.2760	97	0.0017
B1/0510	510	0.2667	0.050	0.001	740.8	0.04585	0.00051	1.2723	0.0027	3986	3966	3908	1.2774	48	0.0027
B1/0574	574	0.3283	0.081	0.000	593.2	0.04841	0.00027	1.2404	0.0011	4324	4291	4233	1.2452	29	0.0011
B1/0612	612	0.2372	0.087	0.001	433.2	0.05222	0.00033	1.2382	0.0021	4680	4625	4567	1.2433	38	0.0021
B1/0690	690	0.2688	0.043	0.000	1059.2	0.05542	0.00034	1.2278	0.0025	5016	5004	4946	1.2329	35	0.0026
B1/0709	709	0.2413	0.050	0.001	856.3	0.05848	0.00031	1.2274	0.0020	5301	5280	5222	1.2326	33	0.0020
B1/0718	718	0.2183	0.083	0.001	498.8	0.06243	0.00079	1.2227	0.0022	5691	5636	5578	1.2282	77	0.0022
B1/0786	786	0.3274	0.068	0.000	1006.7	0.06845	0.00118	1.2697	0.0098	6015	6000	5942	1.2764	114	0.0099
B1/0812	812	0.2329	0.075	0.001	656.6	0.06952	0.00049	1.1926	0.0026	6522	6481	6423	1.1980	53	0.0027
B1/0831	831	0.2496	0.158	0.001	448.0	0.09341	0.00088	1.2105	0.0020	8714	8620	8562	1.2175	95	0.0020
B1/0882	882	0.2783	0.044	0.000	1939.9	0.10162	0.00075	1.2877	0.0013	8913	8918	8859	1.2971	70	0.0014
B1/0928	928	0.2929	0.056	0.000	1726.3	0.10803	0.00064	1.3262	0.0023	9210	9212	9153	1.3368	62	0.0024
B1/0957	957	0.2164	0.060	0.000	1277.3	0.11733	0.00103	1.3771	0.0020	9647	9634	9576	1.3896	90	0.0020
B1/0974	974	0.2332	0.035	0.000	2371.1	0.11658	0.00085	1.3348	0.0021	9902	9915	9856	1.3464	78	0.0021
B1/1005	1005	0.2519	0.030	0.000	2965.8	0.11634	0.00076	1.3075	0.0018	10099	10117	10059	1.3183	71	0.0018
B1/1048	1048	0.3977	0.150	0.002	976.7	0.12104	0.00082	1.3014	0.0020	10578	10550	10492	1.3125	81	0.0021
B1/1108	1108	0.2316	0.090	0.000	964.5	0.12348	0.00088	1.2878	0.0019	10922	10890	10832	1.2988	86	0.0020
B1/1129	1129	0.2783	0.067	0.000	1634.5	0.12898	0.00138	1.2892	0.0019	11420	11417	11359	1.3007	128	0.0020

Table 2.2 (continued)

Sample I.D.	Depth (mm)	U (ppm)	^{232}Th (ppb)	$\pm 2\sigma$	$[\frac{^{230}\text{Th}}{^{232}\text{Th}}]$	$[\frac{^{230}\text{Th}}{^{238}\text{U}}]$	$\pm 2\sigma$	$[\frac{^{234}\text{U}}{^{238}\text{U}}]$	$\pm 2\sigma$	Uncorr. ^{230}Th age (yr)	Corr. ^{230}Th age (yr ago)	Corr. ^{230}Th age (yr BP)	$\pm 2\sigma$	Corr. initial $[\frac{^{234}\text{U}}{^{238}\text{U}}]$	$\pm 2\sigma$
B1/1160	1160	0.3857	0.098	0.000	1589.1	0.13245	0.00102	1.3029	96	11612	11610	11552	97	1.3150	0.0021
B1/1203	1203	0.4267	0.115	0.001	1512.2	0.13375	0.00083	1.2641	81	12116	12112	12054	84	1.2753	0.0019
B1/1235	1235	0.3626	0.119	0.001	1356.7	0.14644	0.00110	1.3416	103	12511	12501	12443	103	1.3560	0.0030
B1/1249	1249	0.3741	0.476	0.001	365.9	0.15325	0.00111	1.3662	102	12873	12695	12636	120	1.3816	0.0028
B3/A-AB-a1	7.8	0.3354	0.073	0.001	25.6	0.00183	0.00009	1.2744	8	156	111	53	15	1.2745	0.0021
B3/B-AB-a12	484.9	0.3014	0.047	0.001	919.6	0.04743	0.00046	1.3142	39	3992	3976	3918	61	1.3177	0.0023
B3/E-AB-b12	1138.1	0.3336	0.064	0.002	1483.1	0.09409	0.00055	1.2905	51	8211	8208	8149	75	1.2973	0.0026
B3/H-AB-c1	1550.2	0.4067	0.104	0.002	1422.5	0.11951	0.00081	1.2639	78	10767	10759	10701	116	1.2720	0.0021

Table 2.3 Summary of MC-ICP-MS U-Th age data for stalagmites LR06-B1 and LR06-B3 from Liang Luar Cave. ^{238}U ng g $^{-1}$ is uranium content of the sample. Activity ratios were determined by the methods described in Hellstrom (2003) and the supplementary materials of Drysdale et al. (2005). The corrected (corr.) ^{230}Th ages were calculated using the equation 1 of Hellstrom (2006) using half-lives specified in Cheng et al. (2000). BP = before present (present = A.D. 1950).

Sample I.D.	U ng g $^{-1}$	Depth (mm)	$^{230}\text{Th}/^{238}\text{U}$	$\pm 2\sigma$	$^{234}\text{U}/^{238}\text{U}$	$\pm 2\sigma$	$^{232}\text{Th}/^{238}\text{U}$	$\pm 2\sigma$	$^{230}\text{Th}/^{232}\text{Th}$	Corr. ^{230}Th age (yr ago)	Corr. ^{230}Th (yr BP)	$\pm 2\sigma$	Corr. initial $^{234}\text{U}/^{238}\text{U}$	$\pm 2\sigma$
B1/437	248	439	0.0323	0.0006	1.2281	0.0024	0.000133	0.000006	243.7	2826	2768	59	1.2299	0.0024
B1/455	265	458	0.0376	0.0005	1.2100	0.0025	0.000876	0.000046	43.0	2892	2833	167	1.2117	0.0025
B1/475	354	475	0.0479	0.0005	1.2186	0.0021	0.001032	0.000004	46.4	3727	3669	193	1.2209	0.0021
B3-101	332	68.3	0.0047	0.0002	1.2901	0.0022	0.000058	0.000002	80.0	363	305	20	1.2904	0.0022
B3-102	332	86.3	0.0059	0.0003	1.3147	0.0026	0.000025	0.000002	235.4	476	418	25	1.3151	0.0025
B3-103	345	141.8	0.0126	0.0003	1.3242	0.0022	0.000074	0.000003	171.7	1001	943	28	1.3251	0.0021
B3-104	405	208.8	0.0180	0.0002	1.2737	0.0023	0.000037	0.000001	482.0	1531	1473	19	1.2749	0.0023
B3-105	237	276.9	0.0244	0.0003	1.2646	0.0022	0.000083	0.000002	293.9	2076	2018	30	1.2662	0.0021
B3-106	281	315.4	0.0263	0.0004	1.1967	0.0022	0.000186	0.000001	141.5	2306	2248	50	1.1980	0.0022
B3-107	255	390.2	0.0325	0.0007	1.2070	0.0032	0.000047	0.000001	688.6	2949	2891	65	1.2087	0.0033
B3-108	214	440.5	0.0437	0.0009	1.3488	0.0029	0.000069	0.000003	628.7	3552	3494	74	1.3523	0.0029
B3-109	251	506.0	0.0477	0.0006	1.2870	0.0027	0.000027	0.000001	1800.3	4103	4045	52	1.2903	0.0028
B3-110	233	579.4	0.0531	0.0005	1.2076	0.0025	0.000026	0.000002	2065.7	4886	4828	48	1.2105	0.0025
B3-111	247	644.4	0.0552	0.0005	1.1673	0.0019	0.000041	0.000001	1347.8	5257	5199	50	1.1698	0.0020
B3-112	263	684.2	0.0568	0.0005	1.1561	0.0029	0.000023	0.000002	2502.7	5481	5423	50	1.1585	0.0029
B3-113	236	757.3	0.0627	0.0004	1.1638	0.0023	0.000025	0.000001	2474.1	6023	5965	42	1.1666	0.0024
B3-D-SS-2	215	771.6	0.0643	0.0016	1.1638	0.0037	0.000091	0.000006	704.3	6133	6075	158	1.1667	0.0038
B3-E-SS-3	184	833.7	0.0699	0.0006	1.1718	0.0027	0.000051	0.000001	1369.5	6667	6608	63	1.1750	0.0028
B3-E-SS-4	313	934.2	0.0775	0.0005	1.2225	0.0027	0.000037	0.000001	2121.4	7109	7051	51	1.2270	0.0027
B3-114	226	1053.6	0.0892	0.0010	1.2901	0.0027	0.000084	0.000001	1061.4	7754	7696	95	1.2965	0.0028
B3-E-SS-6	285	1107.6	0.0900	0.0008	1.2735	0.0024	0.000032	0.000001	2856.4	7959	7900	76	1.2798	0.0025
B3-F-SS-7	265	1208.3	0.0949	0.0011	1.2626	0.0026	0.000215	0.000001	441.8	8375	8317	109	1.2689	0.0027

Table 2.3 (continued)

Sample I.D.	U ng g ⁻¹	Depth (mm)	²³⁰ Th/ ²³⁸ U]	±2σ	[²³⁴ U/ ²³⁸ U]	±2σ	[²³² Th/ ²³⁸ U]	±2σ	[²³⁰ Th/ ²³² Th]	Corr. ²³⁰ Th age (yr ago)	Corr. ²³⁰ Th (yr BP)	±2σ	Corr. initial [²³⁴ U/ ²³⁸ U]	±2σ
B3-F-SS-8	211	1279.2	0.0959	0.0008	1.2236	0.0028	0.000056	0.000001	1705.3	8850	8792	80	1.2293	0.0028
B3-115	226	1300.7	0.0978	0.0006	1.2371	0.0022	0.000029	0.000001	3420.1	8952	8893	58	1.2432	0.0022
B3-116	291	1348.7	0.1094	0.0009	1.3353	0.0028	0.000042	0.000002	2617.0	9279	9221	81	1.3441	0.0029
B3-117	302	1375.1	0.1082	0.0008	1.3144	0.0025	0.000098	0.000004	1101.1	9291	9233	75	1.3228	0.0026
B3-118	128	1406.4	0.1084	0.0009	1.2649	0.0028	0.000360	0.000019	301.0	9539	9481	103	1.2722	0.0028
B3-119	186	1477.8	0.1183	0.0009	1.3060	0.0037	0.000196	0.000007	604.3	10216	10157	94	1.3150	0.0039

2.4.2 *Stable isotopes*

Measurements of $\delta^{18}\text{O}$ and $\delta^{13}\text{C}$ (1240 samples) for stalagmite LR06-B1 were performed on calcite powders weighing $\sim 1\text{ mg}$ (average 8 year resolution). The isotopes were analysed for CO_2 produced by reaction of the powders with 105% H_3PO_4 at 70°C using a continuous-flow GV2003 gas-source isotope ratio mass spectrometer at the University of Newcastle, Australia. Results are shown as the per mil (‰) difference between the sample and Vienna Pee Dee Belemnite (VPDB) using internal working standards of Carrara Marble (New1), which were cross-checked with National Bureau of Standards NBS18 and NBS19 calcite. Mean analytical precision for $\delta^{18}\text{O}$ was 0.08‰ and 0.05‰ for $\delta^{18}\text{O}$ and $\delta^{13}\text{C}$, respectively.

Measurements of $\delta^{18}\text{O}$ and $\delta^{13}\text{C}$ for stalagmite LR06-B3 were conducted on an automated individual-carbonate reaction Kiel device coupled to a Finnigan MAT-251 dual-inlet stable isotope mass spectrometer at the Research School of Earth Sciences, Australian National University. The powdered calcite samples were homogenised and replicate 180–220 μg aliquots of each sample were reacted with anhydrous 103% H_3PO_4 at 90°C to liberate CO_2 for isotopic analysis. The results have been normalised on the VPDB scale such that NBS19 yields $\delta^{18}\text{O}_{\text{VPDB}}$ (-2.20‰) and $\delta^{13}\text{C}_{\text{VPDB}}$ (+1.95‰), and NBS18 yields $\delta^{18}\text{O}_{\text{VPDB}}$ (-23.0‰) and $\delta^{13}\text{C}_{\text{VPDB}}$ (-5.0‰). The measurement precision for NBS19 ($n = 105$) within the mass spectrometer runs was $\pm 0.06\text{‰}$ for $\delta^{18}\text{O}$ (2σ) and $\pm 0.03\text{‰}$ for $\delta^{13}\text{C}$ (2σ). The average standard error of the mean for replicate measurements of the stalagmite samples ($n = 154$ pairs) was 0.02‰ and 0.01‰ for $\delta^{18}\text{O}$ and $\delta^{13}\text{C}$, respectively. In some cases, additional aliquots of a sample were measured until the standard error of the mean $\delta^{18}\text{O}$ value fell below 0.10‰ to ensure that even subtle changes in the speleothem $\delta^{18}\text{O}$ record could be accurately discerned.

To assess interlaboratory performance, 143 replicate samples from stalagmite LR06-B1 were run on the GV2003 (at the University of Newcastle) and the Finnigan MAT-251 (at the Australian National University). The average difference between the measurements was less than 0.07‰ for $\delta^{18}\text{O}$ and $\delta^{13}\text{C}$, indicating good analytical agreement between the two laboratories.

$\delta^{18}\text{O}$ and $\delta^2\text{H}$ values were determined for modern rainwater samples collected at the cave site between September 2006 and April 2007. The $\delta^{18}\text{O}$ values were measured at Monash University, Australia, via equilibration with CO_2 at 32°C for 24–48 hours in a Finnigan MAT Gas Bench and analysed using a continuous-flow technique on a Finnigan MAT 252 mass spectrometer. $\delta^2\text{H}$ measurements were conducted via reaction with Cr at 850°C using an automated Finnigan MAT

H/Device. $\delta^{18}\text{O}$ and $\delta^2\text{H}$ values were measured relative to internal standards (TAP $\delta^{18}\text{O} = -5.7\text{‰}$, $\delta^2\text{H} = -33.9\text{‰}$; LTP $\delta^{18}\text{O} = -14.5\text{‰}$, $\delta^2\text{H} = -102.5\text{‰}$) that were calibrated using the International Atomic Energy Agency (IAEA) Standard Mean Ocean Water (SMOW), Greenland Ice Sheet Project (GISP), and Standard Light Antarctic Precipitation (SLAP) standards. All isotopic data are reported as per mil (‰) deviations relative to Vienna Standard Mean Ocean Water (VSMOW) where $\delta^{18}\text{O}$ and $\delta^2\text{H}$ values of SLAP are -55.5‰ and -428‰ , respectively. Analytical precision (1σ) for replicate measurements of the internal standards was $\pm 0.1\text{‰}$ for $\delta^{18}\text{O}$ and $\pm 1\text{‰}$ for $\delta^2\text{H}$.

2.4.3 Assessment of equilibrium deposition

Prior to making environmentally based interpretations of speleothem stable isotopes, it is essential that we eliminate the possibility that the calcite was subjected to non-equilibrium deposition with respect to the cave drip-waters. Non-equilibrium calcite fractionation can occur if the degassing of CO_2 is too rapid for the stable isotopes to equilibrate with the bicarbonate ion (Hendy, 1971). This can lead to Rayleigh fractionation of the isotopes, generating higher values than those expected from equilibrium precipitation at the same temperature and drip-water $\delta^{18}\text{O}$.

Based on a series of ‘Hendy tests’ and petrographic observations, stalagmites LR06-B1 and LR06-B3 appear to have been deposited in or close to quasi-isotopic equilibrium, enabling variations in $\delta^{18}\text{O}$ of the speleothem calcite to be interpreted primarily as changes in the $\delta^{18}\text{O}$ of regional rainfall. First, both stalagmites were collected from deep within the cave system (~800 m from the single cave entrance) where evaporation would be minimal due to poor ventilation and high humidity levels (close to 100%). It can thus be assumed that any fractionation effects due to evaporation inside this part of the cave are negligible (Fairchild et al., 2006). Second, Hendy tests (Hendy, 1971) were performed on calcite powders drilled along a total of twenty-two individual growth layers to assess whether samples LR06-B1 and LR06-B3 were deposited in isotopic equilibrium. For LR06-B1, eight of the tests were conducted on open columnar calcite while ten were conducted on compact columnar calcite. Isotopic values are plotted as distances away from the central growth axis (Figs 2.6 – 2.8). Non-equilibrium fractionation during deposition may have occurred if there is a positive correlation between $\delta^{18}\text{O}$ and $\delta^{13}\text{C}$ values and if $\delta^{18}\text{O}$ along single growth layers varies by more than 0.5‰ (Hendy, 1971). Our results indicate that $\delta^{18}\text{O}$ values have not varied by more than 0.5‰ along the majority of tested growth layers with little covariation between the $\delta^{18}\text{O}$ and $\delta^{13}\text{C}$ (Figs 2.6-2.8). Lastly, the $\delta^{18}\text{O}$ profile of stalagmite LR06-B1 has a similar

structure to stalagmite LR06-B3 (Fig. 2.9); it is highly unlikely that two speleothems that formed under non-equilibrium conditions would produce similar isotopic profiles.

Calcite fabrics provide a rather useful tool for establishing equilibrium deposition during speleothem formation with respect to their dependence on hydrology and growth rates (Frisia et al., 2000). Stalagmites LR06-B1 and LR06-B3 are composed mostly of translucent, columnar calcite with well-developed rhombohedra and flat-faced terminations. Rhombohedra terminations indicate that crystals developed within a thin water film, creating a persistently submerged environment at the top of the speleothem (Frisia et al., 2000). Successive crystal terminations preserved at a mean lateral spacing of ca. 100 μm within adjacent columns may be the result of periodic changes in the physical and chemical parameters of the drip water. I infer that each visible layer, characterised by well developed crystal terminations, may represent a monsoon cycle. The predominant columnar fabric indicates calcite formation in quasi-equilibrium conditions under relatively constant drip rates throughout the year. This corroborates the inference of low degassing rates and suggests that kinetic effects manifested as disequilibrium isotope fractionation should only be related to external environmental (vis-à-vis cave-specific) factors.

The above tests and observations lead us to believe that stalagmites LR06-B1 and LR06-B3 were deposited at or close to quasi-isotopic equilibrium suggesting that the slow degassing of CO_2 from drip waters maintained isotopic equilibrium among the aqueous species. I thus conclude that the oxygen isotope ratios of LR06-B1 and LR06-B3 primarily record changes in the $\delta^{18}\text{O}$ of the drip water from which the speleothem was formed.

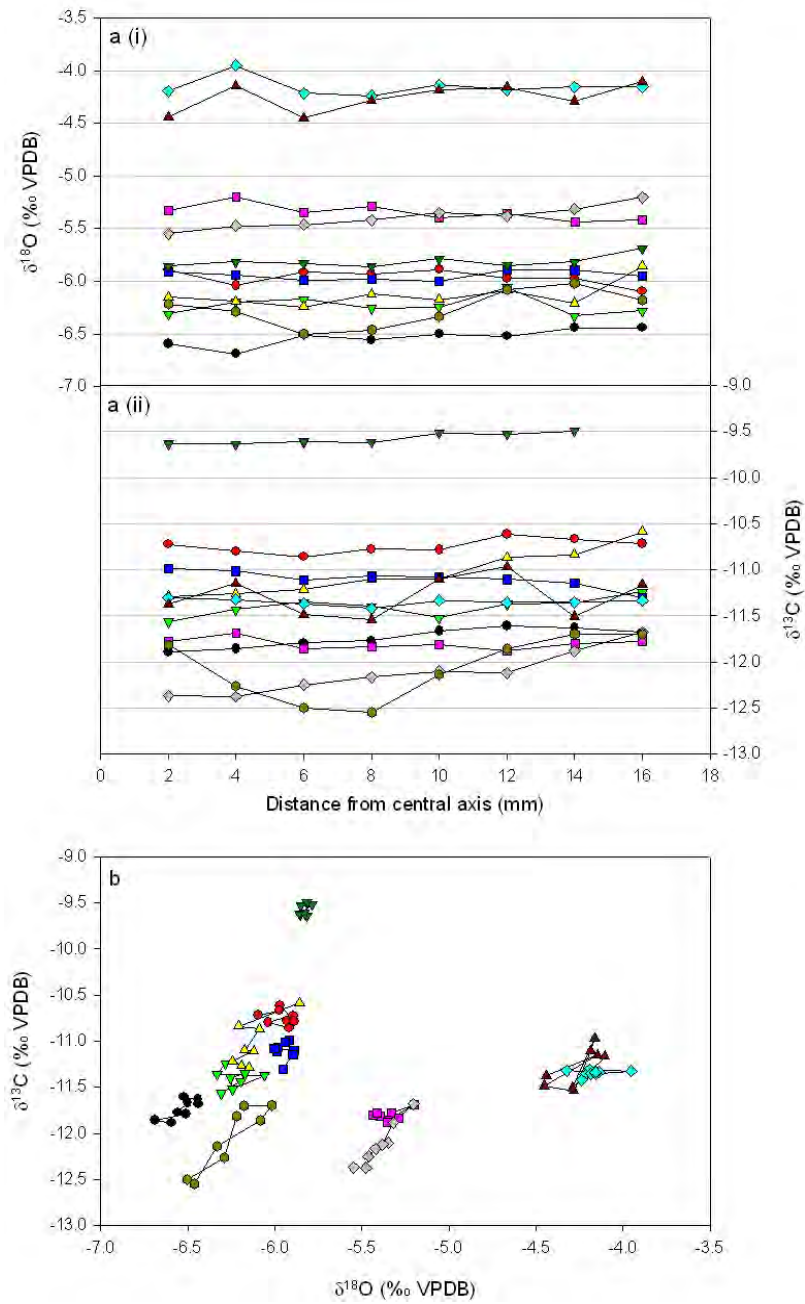


Figure 2.6 Hendy tests for ten individual growth laminae within stalagmite LR06-B1 for compact, translucent calcite. a(i) $\delta^{18}\text{O}$ and a(ii) $\delta^{13}\text{C}$ along individual calcite layers away from the central growth axis. Layers with $\delta^{18}\text{O}$ variability $< 0.5\text{‰}$ are assumed to have been deposited in isotopic equilibrium where the $\delta^{18}\text{O}$ reflects that of the drip-water, rather than kinetic fractionation. (b) Cross-plots of $\delta^{13}\text{C}$ and $\delta^{18}\text{O}$ along individual growth layers.

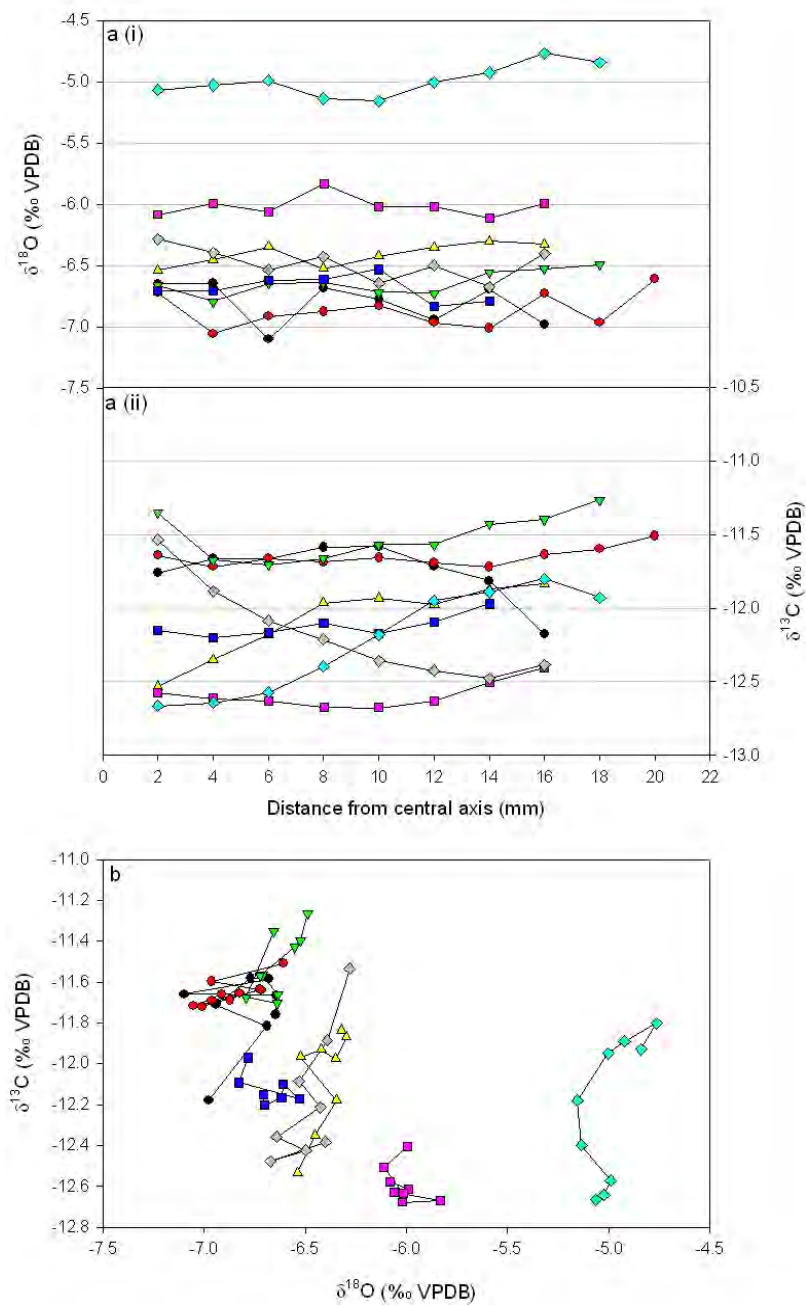


Figure 2.7 Same as Fig. 2.6 but for eight individual growth laminae for open, opaque calcite.

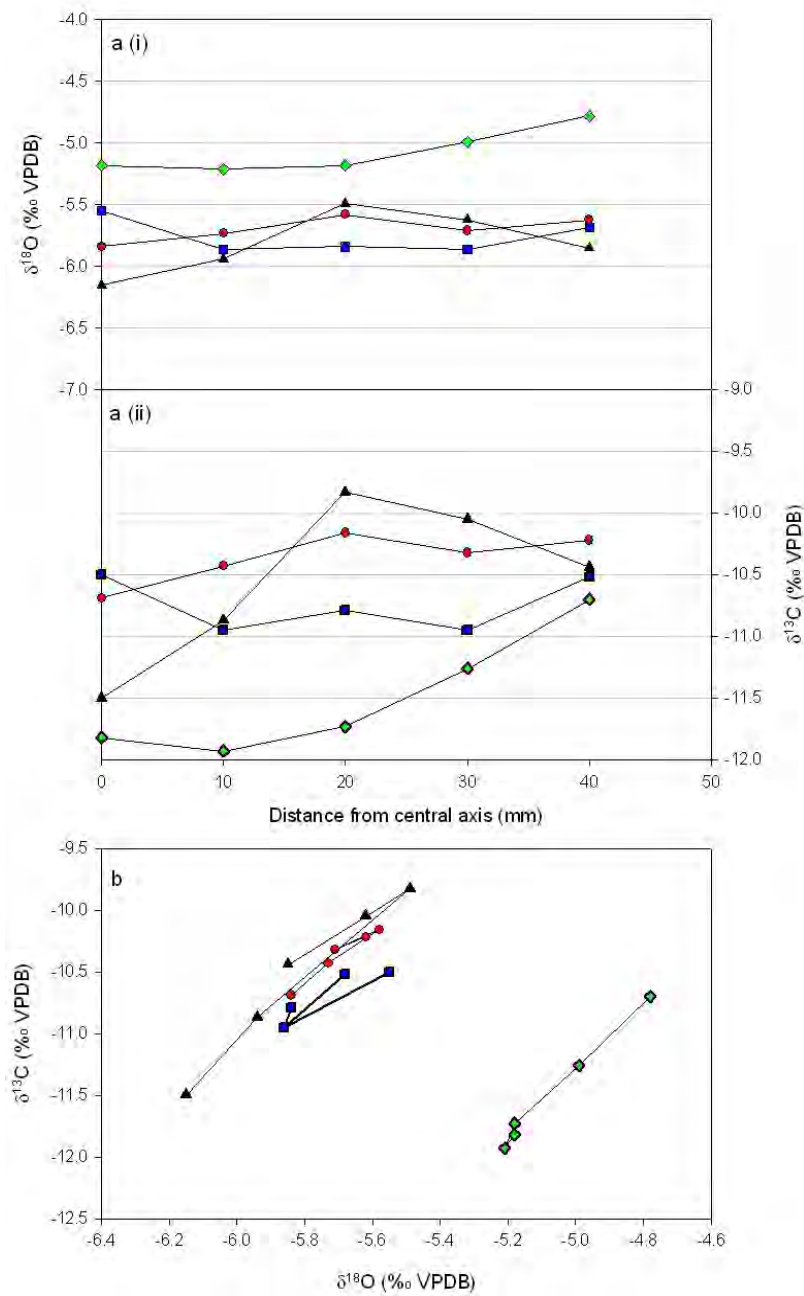


Figure 2.8 Same as Fig. 2.6 but for four individual growth laminae for stalagmite LR06-B3. In (b) it is evident that a number of layers display covariation between $\delta^{13}\text{C}$ and $\delta^{18}\text{O}$, however in all but one case (green diamonds) the covariation does not occur sequentially away from the central growth axis.

2.5 Results and Discussion

The $\delta^{18}\text{O}$ values in the LR06-B1 record range from -4.05‰ to -6.92‰ (Fig. 2.9c), and reflect the combined effects of changes in global ice volume, air temperature, rainfall amount, and moisture source area on stalagmite $\delta^{18}\text{O}$ over the past 12.6 ka. Lower $\delta^{18}\text{O}$ values are observed in the recent part of the record, with the mean value for the late Holocene (3-0 ka) 1.65‰ lower relative to the 12.6-10.0 ka period. Part of this shift reflects a $\sim 1^\circ\text{C}$ post-glacial warming of the tropical western Pacific (Stott et al., 2004; Visser et al., 2003) (accounting for $\sim 0.23\text{‰}$ in $\delta^{18}\text{O}$) and a $\sim 0.5\text{‰}$ decrease in the $\delta^{18}\text{O}$ of sea water due to the global ice-volume effect (Schrage et al., 1996). However, the combined effects of temperature and ice volume only account for $\sim 0.7\text{‰}$ of the 1.65‰ Holocene shift, suggesting that the trend in stalagmite $\delta^{18}\text{O}$ values cannot be explained by these factors alone.

To remove these effects from the records, I adjusted the LR06-B1 and LR06-B3 $\delta^{18}\text{O}$ series for changes in Indo-Pacific Warm Pool (IPWP) sea-surface temperature (Stott et al., 2004) (closely coupled to tropical air temperature) and global ice-volume (Siddall et al., 2003) (Fig. 2.9e) during the late glacial/Holocene. After adjustment, a $\sim 1\text{‰}$ decrease in the $\delta^{18}\text{O}$ is observed through the early to middle Holocene which may be indicative of changes in the $\delta^{18}\text{O}$ of monsoonal rainfall. Several factors may have contributed to this decrease, including: 1) variations in rainfall amount related to the intensity and/or positioning of the intertropical convergence zone; 2) changes in the seasonal balance of summer versus winter rainfall; and 3) changes in the frequency and/or intensity of ENSO events.

The prominent feature of the adjusted Holocene $\delta^{18}\text{O}$ curve is the sharp decrease in values from 11 to 7 ka (Fig. 2.9e). This inferred early Holocene trend towards wetter conditions culminates at the end of the deglaciation when eustatic sea-level rise had levelled off (Fig. 2.9f). Indeed, while higher $\delta^{18}\text{O}$ values coincide with lower insolation during the early Holocene, the fastest decrease in $\delta^{18}\text{O}$ occurred between 11 and 9 ka, preceding the sharpest rise in insolation (Fig. 2.9g). Moreover, the southern hemisphere summer insolation trend through the middle to late Holocene is not evident in the Liang Luar $\delta^{18}\text{O}$ record. Therefore, in contrast to other monsoon-dominated regions, such as northern Borneo (Partin et al., 2007) (Fig. 2.9b), southern Brazil (Wang et al., 2006) (Fig. 2.9d), and southern China (Dykoski et al., 2005; Wang et al., 2005) (Fig. 2.9a), I find little evidence for insolation being responsible for the Holocene change in AISM rainfall and instead suggest that sea-level rise is a more important regional forcing mechanism. Two complementary possibilities may explain this sea-level influence: (1) assuming monsoon moisture trajectories were broadly similar to the present, a large proportion of the summer

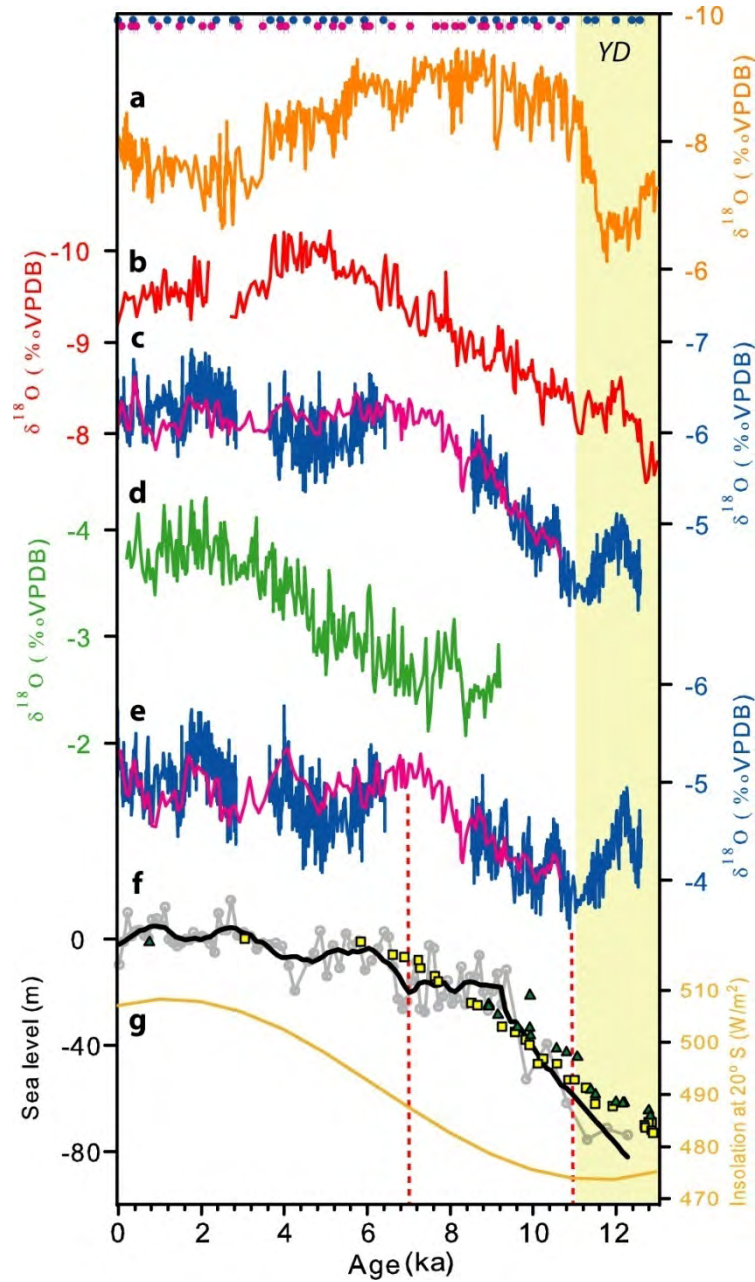


Figure 2.9 Liang Luar stalagmite $\delta^{18}\text{O}$ record and other palaeoclimate records. (a-d), Comparison of the Liang Luar $\delta^{18}\text{O}$ record (LR06-B1, blue; LR06-B3, pink) with stalagmite $\delta^{18}\text{O}$ records for Dongge Cave, China (Dykoski et al., 2005; Wang et al., 2005) (orange), Gunung Buda, Born eo (Partin et al., 2007) (red), and Botuverá Cave, Brazil (Wang et al., 2006) (green). Th/U ages for the Liang Luar records are shown (with 2σ errors) at top of figure. (e) Liang Luar $\delta^{18}\text{O}$ record adjusted for changes in Indo-Pacific Warm Pool sea-surface temperature (Stott et al., 2004) and global ice-volume (Siddall et al., 2003). (f) Sea-level reconstructions from the $\delta^{18}\text{O}$ of Red Sea benthic foraminifera (Siddall et al., 2003) (grey circles) with 5-point running mean (black line), and Barbados (Peltier and Fairbanks, 2006) (green triangles) and Tahiti (Bard et al., 1996) (yellow squares) coral reef studies. Dashed red lines highlight the concurrent increases in sea-level and AISM precipitation at Liang Luar. (g) December (austral summer) insolation at 20°S . The light brown shading indicates the timing of the Younger Dryas cooling in Greenland (EPICA members, 2006).

monsoon trajectory path would have been occupied by either land surface or extremely shallow seas during the early Holocene. Thus, a lower surface area of ocean water along the dominant air-mass trajectory would have limited the availability of source moisture fuelling the monsoon; (2) sea-level rise plus northern hemisphere insolation-induced heating of the South China Sea (Kienast et al., 2001) may have resulted in the migration of warmer waters into the Sunda area, thus resulting in higher evaporation over the source region.

The close coupling of rainfall variability in the northern and southern low latitudes with temperature fluctuations in the North Atlantic during the last glacial cycle has long been documented (Haug et al., 2001; Turney et al., 2004; Wang et al., 2005; Wang et al., 2006;). However, the degree to which these meridional connections extend into the southern sector of the Indo-Pacific during the late glacial–Holocene interval has not been previously observed. Superimposed upon the LR06-B1 $\delta^{18}\text{O}$ trend are a number of significant isotopic excursions of centennial- and millennial-scale duration. Most notable is the prominent $\delta^{18}\text{O}$ depletion event between ~12.7 and ~11.5 ka (Fig. 2.10d) that occurred concurrently with the Younger Dryas cooling in the North Atlantic (EPICA members, 2006).

The more depleted $\delta^{18}\text{O}$ values of LR06-B1 during the Younger Dryas cooling reflect a stronger monsoon on Flores (Fig. 2.10d). This pattern of southern Indonesian rainfall correlates with high $\delta^{18}\text{O}$ values at Dongge cave (Dykoski et al., 2005), inferred to reflect a weakened East Asian summer monsoon (Fig. 2.10a). Moreover, the higher rainfall event on Flores correlates with lower titanium counts from the Cariaco basin (Haug et al., 2001) which are interpreted as lower rainfall intervals (Fig. 2.10b), and travertine growth phases in northeast Brazil (Wang et al., 2004), indicative of higher rainfall. Thus, a stronger AISM during the Younger Dryas cooling is in parallel with higher rainfall over the southern tropics (Cruz et al., 2005; Wang et al., 2004) and lower rainfall over the northern tropics (Dykoski et al., 2005; Haug et al., 2001).

A likely explanation for these observed phase relationships, in particular between the Australian-Indonesian and East Asian summer monsoons, is an abrupt southward shift in the mean summer location of the ITCZ. The Younger Dryas cooling is thought to be the result of a marked reduction in meridional overturning circulation (McManus et al., 2004) due to a major release of meltwater into the North Atlantic (Broecker, 2003). Modelling experiments indicate that these periods of reduced North Atlantic overturning highly favour the southward displacement of the ITCZ in the tropical Pacific (Zhang and Delworth, 2005).

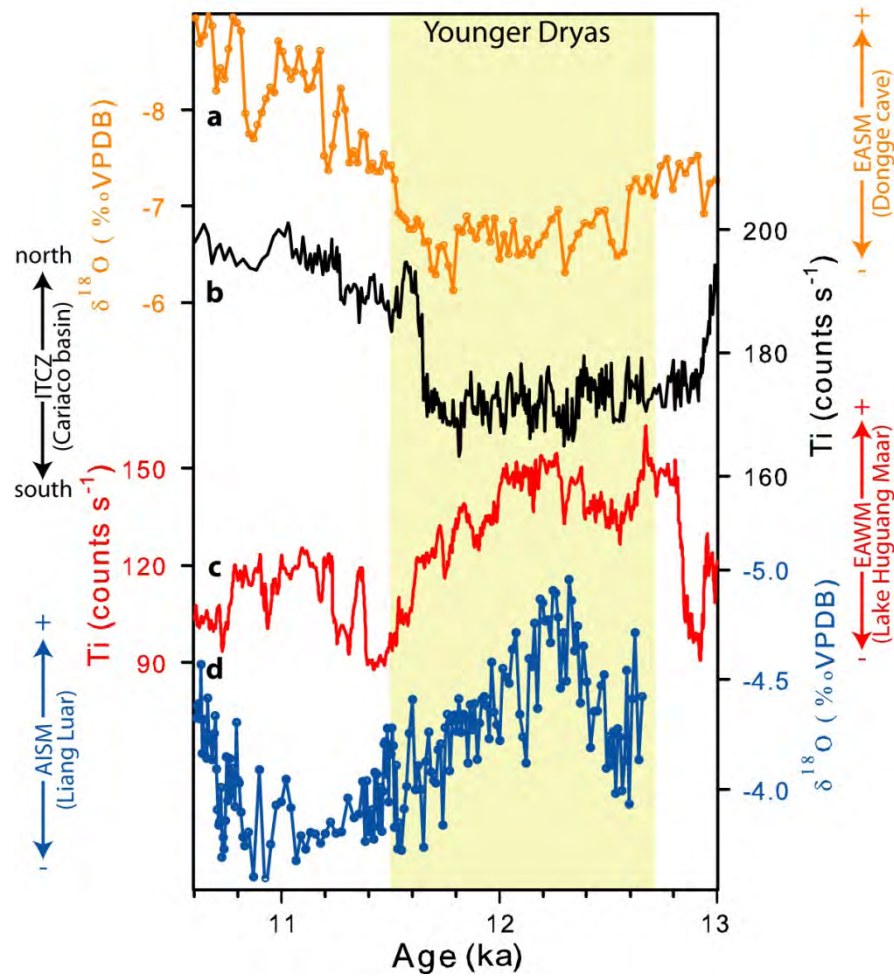


Figure 2.10 Comparison of palaeoclimate records between Flores, southern China, and northern South America during the Younger Dryas cooling. (a) A weakened East Asian summer monsoon recorded by the Dongge Cave, China, speleothem record (Dykoski et al., 2005) corresponds with (b) a southward displaced ITCZ over the Cariaco basin (Haug et al., 2001), (c) stronger outflow from the Asian winter monsoon (Yancheva et al., 2007), and (d) higher monsoon rainfall over Flores, as indicated by lower ice-volume (Siddall et al., 2003) and SST (Stott et al., 2004) adjusted $\delta^{18}\text{O}$ values. The light brown shading indicates a strong N-S inverse relationship during the time of the Younger Dryas cooling in Greenland (EPICA members, 2006).

A more direct link between the AISM, and the North Atlantic and associated migration of the ITCZ during the Younger Dryas, may be the influence of the East Asian winter monsoon. Comparison of the titanium content of Lake Huguang Maar (Fig. 2.10c), regarded as a proxy for the strength of East Asian winter monsoon winds (Yancheva et al., 2007), with the $\delta^{18}\text{O}$ of LR06-B1 reveals a strong positive relationship. This correspondence supports previous suggestions that the AISM is largely controlled by a ‘push-pull’ relationship between the Australasian monsoon systems and hence corroborates cross-equatorial linkages between the two regions.

Noteworthy is the absence of a Younger Dryas signal in the nearby monsoon speleothem records from northern Borneo (Partin et al., 2007), which lies in stark contrast to the Liang Luar and Dongge Cave records (Dykoski et al., 2005). A possible explanation for this mismatch may be related to the geographical location of northern Borneo and its lack of seasonality. Because Dongge Cave and Liang Luar are positioned at the northern and southern limits of the summer ITCZ belt respectively, slight adjustments in meridional positioning are likely to have a greater influence on seasonal rainfall at those sites compared with northern Borneo.

2.6 Conclusions

Results of this study show that southern hemisphere summer insolation was not the most important driver of AISM rainfall during the late glacial-Holocene interval in SE Indonesia. Reduced North Atlantic overturning circulation led to a progressive southward displacement of the Austral-summer ITCZ and thus wetter conditions in southern Indonesia at the time of the Younger Dryas. However, the most sustained decrease in speleothem $\delta^{18}\text{O}$, indicative of increasing monsoon rainfall, coincided with the sharpest eustatic sea-level rise, which increased moisture availability. More precisely dated high-resolution proxy records of AISM strength will be required to determine whether the patterns observed in SE Indonesia are synchronous across the region, particularly over the north Australian land mass where the epicentre of the AISM system lies.

2.7 References

- Abram, N.J., Gagan, M.K., Liu, Z.Y., Hantoro, W.S., McCulloch, M.T. and Suwargadi, B.W., 2007. Seasonal characteristics of the Indian Ocean Dipole during the Holocene epoch. *Nature* 445, 299-302.
- Bard, E., Hamelin, B., Arnold, M., Montaggioni, L., Cabioch, G., Faure, G., and Rougerie, F., 1996. Deglacial sea-level record from Tahiti corals and the timing of global meltwater discharge. *Nature* 382, 241-244.
- Broecker, W. S., 2003. Does the trigger for abrupt climate change reside in the ocean or in the atmosphere? *Science* 300, 1519-1522.
- Cheng, H., Edwards, R.L., Hoff, J., Gallup, C.D., Richards, D.A. and Asmerom, Y., 2000. The half-lives of uranium-234 and thorium-230. *Chemical Geology* 169, 17-33.
- Cruz, F.W., Burns, S.J., Karmann, I., Sharp, W.D., Vuille, M., Cardoso, A.O., Ferrari, J.A., Dias, P.L.S. and Viana, O., 2005. Insolation-driven changes in atmospheric circulation over the past 116,000 years in subtropical Brazil. *Nature* 434, 63-66.
- Draxler, R.R. and Rolph, G.D., 2003. HYSPLIT (Hybrid Single-Particle Lagrangian Integrated Trajectory) Model access via NOAA ARL READY Website (<http://www.arl.noaa.gov/ready/hysplit4.html>). NOAA Air Resources Laboratory, Silver Spring, MD.
- Drysdale, R.N., Zanchetta, G., Hellstrom, J.C., Fallick, A.E. and Zhao, J.X., 2005. Stalagmite evidence for the onset of the Last Interglacial in southern Europe at 129 +/- 1 ka. *Geophysical Research Letters* 32, L24708, doi:10.1029/2005GL024658.
- Drysdale, R.N., Zanchetta, G., Hellstrom, J.C., Fallick, A.E., McDonald, J. and Cartwright, I., 2007. Stalagmite evidence for the precise timing of North Atlantic cold events during the early last glacial. *Geology* 35, 77-80.
- Dykoski, C.A., Edwards, R.L., Cheng, H., Yuan, D.X., Cai, Y.J., Zhang, M.L., Lin, Y.S., Qing, J.M., An, Z.S. and Revenaugh, J., 2005. A high-resolution, absolute-dated Holocene and deglacial Asian monsoon record from Dongge Cave, China. *Earth and Planetary Science Letters* 233, 71-86.
- Edwards, R.L., Chen, J.H. and Wasserburg, G.J., 1987. U-238/U-234-Th-230-Th-232 Systematics and the Precise Measurement of Time over the Past 500,000 Years. *Earth and Planetary Science Letters* 81, 175-192.

- EPICA members, 2006. One-to-one coupling of glacial climate variability in Greenland and Antarctica. *Nature* 444, 195-198.
- Fairchild, I.J., Smith, C.L., Baker, A., Fuller, L., Spötl, C., Matthey, D., McDermott, F. and Eimp, 2006. Modification and preservation of environmental signals in speleothems. *Earth-Science Reviews* 75, 105-153.
- Frisia, S., Borsato, A., Fairchild, I.J. and McDermott, F., 2000. Calcite fabrics, growth mechanisms, and environments of formation in speleothems from the Italian Alps and southwestern Ireland. *Journal of Sedimentary Research* 70, 1183-1196.
- Haug, G.H., Hughen, K.A., Sigman, D.M., Peterson, L.C. and Rohl, U., 2001. Southward migration of the intertropical convergence zone through the Holocene. *Science* 293, 1304-1308.
- Hellstrom, J., 2003. Rapid and accurate U/Th dating using parallel ion-counting multi-collector ICP-MS. *Journal of Analytical Atomic Spectrometry* 18, 1346-1351.
- Hellstrom, J. C., 2006. U-Th dating of speleothems with high initial ^{230}Th using stratigraphical constraint. *Quaternary Geochronology* 1, 289-295.
- Hendy, C.H., 1971. The isotopic geochemistry of speleothems: The calculations of the effects of different modes of formation on the isotopic composition of speleothems and their applicability as palaeoclimate indicators. *Geochimica et Cosmochimica Acta* 35, 801-824.
- Holbourn, A., Kuhnt, W., Kawamura, H., Jian, Z.M., Grootes, P., Erlenkeuser, H. and Xu, J., 2005. Orbitally paced paleoproductivity variations in the Timor Sea and Indonesian Throughflow variability during the last 460 kyr. *Paleoceanography* 20, doi:10.1029/2004PA001094.
- Kershaw, A.P., van der Kaars, S. and Moss, P.T., 2003. Late Quaternary Milankovitch-scale climatic change and variability and its impact on monsoonal Australasia. *Marine Geology* 201, 81-95.
- Kienast, M., Steinke, S., Stattegger, K. and Calvert, S.E., 2001. Synchronous tropical South China Sea SST change and Greenland warming during deglaciation. *Science* 291, 2132-2134.
- McManus, J.F., Francois, R., Gherardi, J.M., Keigwin, L.D. and Brown-Leger, S., 2004. Collapse and rapid resumption of Atlantic meridional circulation linked to deglacial climate changes. *Nature* 428, 834-837.
- Miller, G., Mangan, J., Pollard, D., Thompson, S., Felzer, B. and Magee, J., 2005. Sensitivity of the Australian Monsoon to insolation and vegetation: Implications for human impact on continental moisture balance. *Geology* 33, 65-68.

- Partin, J.W., Cobb, K.M., Adkins, J.F., Clark, B. and Fernandez, D.P., 2007. Millennial-scale trends in west Pacific warm pool hydrology since the Last Glacial Maximum. *Nature* 449, 452-455.
- Peltier, W.R. and Fairbanks, R.G., 2006. Global glacial ice volume and Last Glacial Maximum duration from an extended Barbados sea level record. *Quaternary Science Reviews* 25, 3322-3337.
- Rozanski, K., Araguasaraguas, L. and Gonfiantini, R., 1992. Relation between Long-Term Trends of O-18 Isotope Composition of Precipitation and Climate. *Science* 258, 981-985.
- Schrag, D.P., Hampt, G. and Murray, D.W., 1996. Pore fluid constraints on the temperature and oxygen isotopic composition of the glacial ocean. *Science* 272, 1930-1932.
- Siddall, M., Rohling, E.J., Almogi-Labin, A., Hemleben, C., Meischner, D., Schmelzer, I. and Smeed, D.A., 2003. Sea-level fluctuations during the last glacial cycle. *Nature* 423, 853-858.
- Stott, L., Cannariato, K., Thunell, R., Haug, G.H., Koutavas, A. and Lund, S., 2004. Decline of surface temperature and salinity in the western tropical Pacific Ocean in the Holocene epoch. *Nature* 431, 56-59.
- Tudhope, A.W., Chilcott, C.P., McCulloch, M.T., Cook, E.R., Chappell, J., Ellam, R.M., Lea, D.W., Lough, J.M. and Stahmied, G.B., 2001. Variability in the El Niño - Southern oscillation through a glacial-interglacial cycle. *Science* 291, 1511-1517.
- Turney, C.S.M., Kershaw, A.P., Clemens, S.C., Branch, N., Moss, P.T. and Field, L.K., 2004. Millennial and orbital variations of El Niño/Southern Oscillation and high-latitude climate in the last glacial period. *Nature* 428, 306-310.
- Visser, K., Thunell, R. and Stott, L., 2003. Magnitude and timing of temperature change in the Indo-Pacific warm pool during deglaciation. *Nature* 421, 152-155.
- Wang, X.F., Auler, A.S., Edwards, R.L., Cheng, H., Cristalli, P.S., Smart, P.L., Richards, D.A. and Shen, C.C., 2004. Wet periods in northeastern Brazil over the past 210 kyr linked to distant climate anomalies. *Nature* 432, 740-743.
- Wang, X.F., Auler, A.S., Edwards, R.L., Cheng, H., Ito, E. and Solheid, M., 2006. Interhemispheric anti-phasing of rainfall during the last glacial period. *Quaternary Science Reviews* 25, 3391-3403.
- Wang, Y.J., Cheng, H., Edwards, R.L., He, Y.Q., Kong, X.G., An, Z.S., Wu, J.Y., Kelly, M.J., Dykoski, C.A. and Li, X.D., 2005. The Holocene Asian monsoon: Links to solar changes and North Atlantic climate. *Science* 308, 854-857.

- Wyrwoll, K.H., Liu, Z.Y.S., Chen, G., Kutzbach, J.E. and Liu, X.D., 2007. Sensitivity of the Australian summer monsoon to tilt and precession forcing. *Quaternary Science Reviews* 26, 3043-3057.
- Yancheva, G., Nowaczyk, N.R., Mingram, J., Dulski, P., Schettler, G., Negendank, J.F.W., Liu, J.Q., Sigman, D.M., Peterson, L.C. and Haug, G.H., 2007. Influence of the intertropical convergence zone on the East Asian monsoon. *Nature* 445, 74-77.
- Yu, K.F., Zhao, J.X., Shi, Q., Chen, T.G., Wang, P.X., Collerson, K.D. and Liu, T.S., 2006. U-series dating of dead *Porites* corals in the South China sea: Evidence for episodic coral mortality over the past two centuries. *Quaternary Geochronology* 1, 129-141.
- Zhang, R. and Delworth, T.L., 2005. Simulated tropical response to a substantial weakening of the Atlantic thermohaline circulation. *Journal of Climate* 18, 1853-1860.

3 Younger Dryas-Holocene temperature and rainfall history of southern Indonesia from $\delta^{18}\text{O}$ in speleothem calcite and fluid inclusions

Abstract

We have applied a new technique to analyze the oxygen ($\delta^{18}\text{O}$) and hydrogen (δD) isotope ratios in speleothem fluid inclusions to reconstruct the temperature and rainfall history of southern Indonesia during the Younger Dryas (YD) event and the Holocene. The 12,640-year speleothem record, anchored by 33 uranium-series dates, shows that fluid-inclusion $\delta^{18}\text{O}$ varies in phase with speleothem calcite $\delta^{18}\text{O}$ during the Holocene, suggesting that the speleothem calcite $\delta^{18}\text{O}$ primarily reflects variations in the $\delta^{18}\text{O}$ of local rainfall. Significant early to mid-Holocene decreases in both $\delta^{18}\text{O}$ series are interpreted as an intensification of Australian-Indonesian summer monsoon rainfall in response to deglacial eustatic sea-level rise and flooding of the Sunda Shelf.

Cave drip-water temperatures reconstructed from coupled measurements of $\delta^{18}\text{O}$ in speleothem calcite and fluid inclusions remained relatively constant through the Holocene. This is consistent with reconstructions of Indo-Pacific sea-surface temperature (SST) based on analysis of Mg/Ca in planktonic foraminifera. However, during the YD event, drip-water (i.e. cave) temperature was $\sim 5^\circ\text{C}$ cooler than modern, which is substantially cooler than SSTs inferred from foraminiferal Mg/Ca, but consistent with coral Sr/Ca reconstructions of SST and terrestrial evidence for high-elevation snow-line depressions. Lower fluid-inclusion $\delta^{18}\text{O}$ during the YD indicates that the cooling was accompanied by increased monsoon rainfall. Taken together, the results suggest that the southerly penetration of the intertropical convergence zone (ITCZ) was largely influenced by the cross-equatorial temperature gradient, rather than local SSTs (and air temperatures). These results provide new evidence for a rapid cooling of deep tropical air temperatures and repositioning of the ITCZ during the YD event.

3.1 Introduction and background

The Indo-Pacific Warm Pool (IPWP) plays a critical role in the global climate system. It provides a source of heat and moisture that is distributed both zonally between the Indian and Pacific Ocean basins and to higher latitudes. Within the southern sector of the IPWP, including northern Australia and Indonesia, rainfall variability is dominated by the Australian-Indonesian Summer Monsoon (AISM), which accounts for ~69% of the annual precipitation. Variations in the strength and/or timing of AISM rainfall can have catastrophic consequences for the millions of people who reside in the Indonesian archipelago. Therefore, it is critical to improve our understanding of the parameters that control AISM variability over the recent past (e.g. the Holocene).

Compared to the last glacial period, high latitude ice-core records demonstrate that air temperatures were relatively stable (i.e. temperature range of $\sim 3^{\circ}\text{C}$) through much of the Holocene (EPICA members, 2006; NGRIP members, 2004; Vinther et al., 2009). Sea-surface temperature (SST) reconstructions from the tropical west Pacific indicate a similar pattern (Brijker et al., 2007; Lea et al., 2000; Stott et al., 2004; Visser et al., 2003), highlighting the relative stability of tropical and high-latitude regions over the past ~ 10 thousand years (ka). In contrast, major hydrological variations have occurred during this time, particularly in the low and mid-latitudes (Mayewski et al., 2004). However, the lack of continental palaeotemperature records from the tropics precludes a full understanding of the low-latitude response to high-latitude temperature fluctuations, particularly during major climate transitions (e.g. last glacial maximum). Here I aim to bridge this knowledge gap by reconstructing temperature and rainfall trends from coupled measurements of $\delta^{18}\text{O}$ in speleothem calcite and fluid inclusions.

Speleothems (i.e. stalagmites and flowstones) are excellent terrestrial palaeoclimate archives because of their sensitivity to climate variability and the relative ease with which their age profiles can be constrained via high-precision (typically $<1\%$ age-error) uranium-series dating. An additional feature of speleothems is the presence of fluid inclusions, which are trapped residues of fossil cave drip-water that originally fell as rainfall above the cave (Schwarcz et al., 1976). Since the $\delta^{18}\text{O}$ and δD values of the drip waters feeding speleothems reflect those of the recharge precipitation, inclusion waters provide an additional proxy for regional rainfall reconstructions (McDermott et al., 2006).

Provided the speleothem grew in isotopic equilibrium (Hendy, 1971), coupled measurements of $\delta^{18}\text{O}$ in fluid inclusions and the host calcite can be used to determine independent speleothem growth temperatures, by subtracting the effect of changes in the $\delta^{18}\text{O}$ of rainfall from the calcite $\delta^{18}\text{O}$ signal.

There are two important caveats, however, which must be considered. First, most calcite-water palaeotemperature equations (e.g. Kim and O'Neil, 1997) tend to underestimate palaeotemperatures (on the order of ~2-3 °C) for speleothems (e.g. McDermott et al. 2006; van Breukelen et al. 2008). Second, a widely held assumption is that fluid inclusions may have exchanged oxygen isotopes with the host calcite through time, and thus the fluid-inclusion $\delta^{18}\text{O}$ may not reflect the pore-water composition at the time of entrapment (Schwarcz et al., 1976). Consequently, most fluid-inclusion studies (Fleitmann et al., 2003; Zhang et al., 2008) measure δD and use the δD - $\delta^{18}\text{O}$ relationship determined by the Global Meteoric Water Line (GMWL) to estimate the inclusion $\delta^{18}\text{O}$ value because hydrogen does not exchange with the calcite phase. However, recent studies have shown that post-depositional ^{18}O - ^{16}O exchange is negligible in Holocene stalagmites on the premise that the fluid-inclusion data plotted on (or close to) the GMWL and / or shared a similar slope, and are consistent with modern cave drip waters (Dennis et al., 2001; Dublyansky and Spötl, 2009; van Breukelen et al., 2008).

Earlier studies on speleothem fluid inclusions involved an off-line preparation of pore-water extraction using: (i) crushing techniques at various temperatures; or (ii) thermal decrepitation at much higher temperatures with varying degrees of calcite decomposition. Thermal decrepitation was, until recently, certainly the favoured technique for off-line extraction because it yielded larger water quantities than crushing. However, a caveat of this method was that the measured δD values tended to have an approximate 20-30‰ offset relative to that of the cave seepage water (Matthews et al., 2000; McGarry et al., 2004). This apparent offset was attributed to analytical error (Matthews et al., 2000; McGarry et al., 2004) and/or contamination of the signal through the presence of small isotopically-fractionated inclusion waters on crystal boundaries (McDermott et al., 2006). Given these ambiguities the previously reported 'crushing technique' was re-investigated by Dennis et al. (2001), whose findings demonstrated that prior difficulties associated with fluid-inclusion δD - $\delta^{18}\text{O}$ analyses were caused by the incomplete injection of waters into the mass-spectrometer. To circumvent this problem they suggested heating the crushing-cell and attached vacuum line to 150 °C to reduce the likelihood of waters being adsorbed onto surfaces within the system. An additional advance in the application of fluid-inclusion analysis to palaeoclimate studies has been the advent of on-line pyrolysis techniques, which have permitted the acquisition of δD and $\delta^{18}\text{O}$ from a single, sub-microlitre aliquot of water. This has allowed much higher sampling throughput because it avoids time-consuming data reductions and off-line gas conversion steps (Vonhof et al., 2006; Dublyansky and Spötl, 2009).

In this study, I employ this recently developed continuous-flow pyrolysis technique to speleothem $\delta^{18}\text{O}$ - δD fluid-inclusions from a precisely dated, 12.64 k a-long record from Flores, east Indonesia. Following successful pioneering studies of fluid inclusions in a speleothem from tropical Amazonia (van Breukelen et al., 2008), I have applied the same novel technique of Vonhof et al. (2006, 2007) to my speleothem record from Indonesia. Results of these analyses are used to estimate the temperature and rainfall variability in the southern sector of the AISM region from the Younger Dryas (YD) event to the present.

3.2 Regional setting

The fluid-inclusion $\delta^{18}\text{O}$ and δD data were obtained from a 1.25 m tall actively growing stalagmite (LR06-B1) collected from a large chamber within Liang Luar (8° 32' N, 120° 26' E), a cave located on the east Indonesian island of Flores (Fig. 3.1). The sampling site (550 m.a.s.l.) is located ~30-50 m below the ground surface and ~800 m in from the cave entrance (Fig. 3.2). The chamber currently has a mean annual temperature (MAT) of ~25 °C, which closely resembles the surface MAT. The cave receives ~69% (~800 mm) of its annual recharge from the summer monsoon between December and March, most of which infiltrates the highly porous karst terrain. This highly seasonal pattern of rainfall in Flores is linked to low-level north-westerly flow of moisture from the AISM and the southward displacement of the inter-tropical convergence zone (ITCZ) during the austral summer (Fig. 3.1).

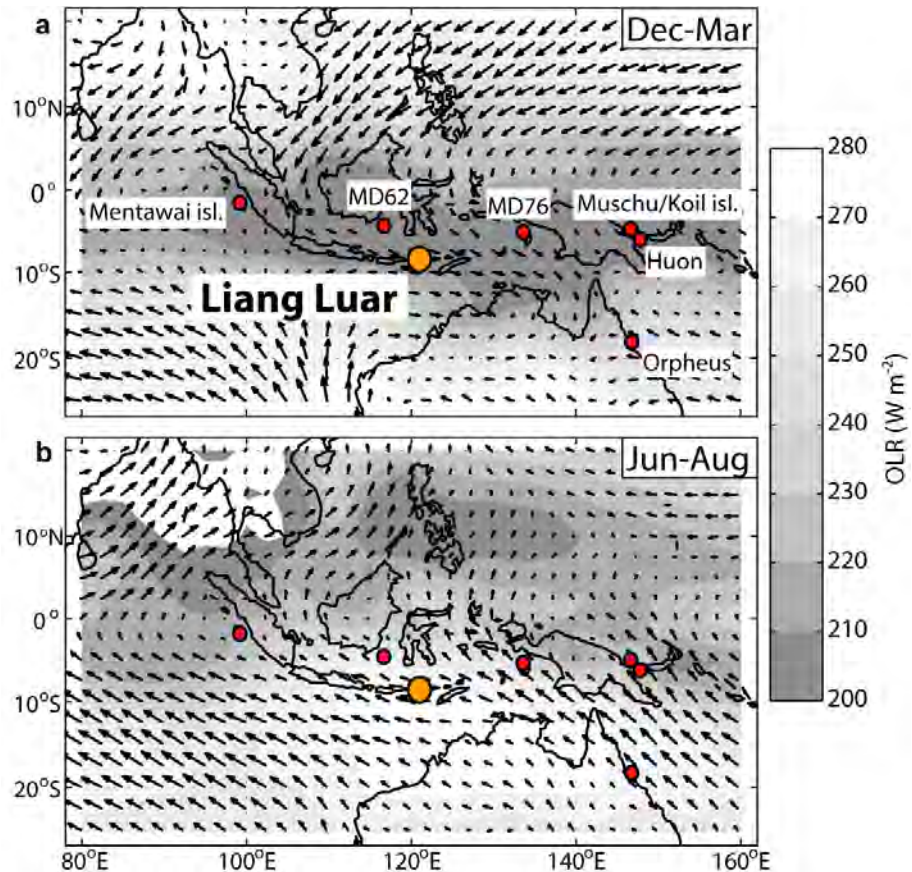


Figure 3.1 Location of Liang Luar Cave, Flores, in the Australian-Indonesian summer monsoon domain. Shading represents monthly values of outgoing long-wave radiation (OLR) based on composites of NOAA satellite-observed OLR. Arrows show NCEP/NCAR Reanalysis 850-hPa wind direction based on data from 1979 to 2005 for the: (a) austral summer wet season (December-March) and (b) a austral winter dry season (June-August). Low OLR values (dark shading) indicate cold cloud tops produced by precipitating cumulonimbus convection, which dominates the southern Indonesian region during the Australian-Indonesian summer monsoon. Also shown are the locations of marine sediment cores MD76 (Stott et al., 2004) and MD62 (Visser et al., 2003) and coral records discussed in the text. OLR and wind vector data were retrieved from the following web address: <http://www.esrl.noaa.gov/psd/cgi-bin/data/composites/printpage.pl>.

3.3 Methods

The depth-age model of stalagmite LR06-B1 was constructed from 33 U/Th dates (Griffiths et al., 2009) performed using both thermal ionisation mass-spectrometry (Yu et al. 2006) and multi-collector inductively coupled plasma mass spectrometry (Hellstrom, 2003, 2006). Microsampling for analysis of $\delta^{18}\text{O}$ in calcite ($\delta^{18}\text{O}_c$) was performed at 1 mm increments along the vertical axis of polished sections of LR06-B1 using a milling lathe. The $\delta^{18}\text{O}_c$ values for 1240 calcite powders were determined on a GV2003 continuous-flow stable isotope ratio mass spectrometer at the University of Newcastle, Australia. Results are reported using the standard δ notation in per mil (‰) relative to the Vienna Pee Dee

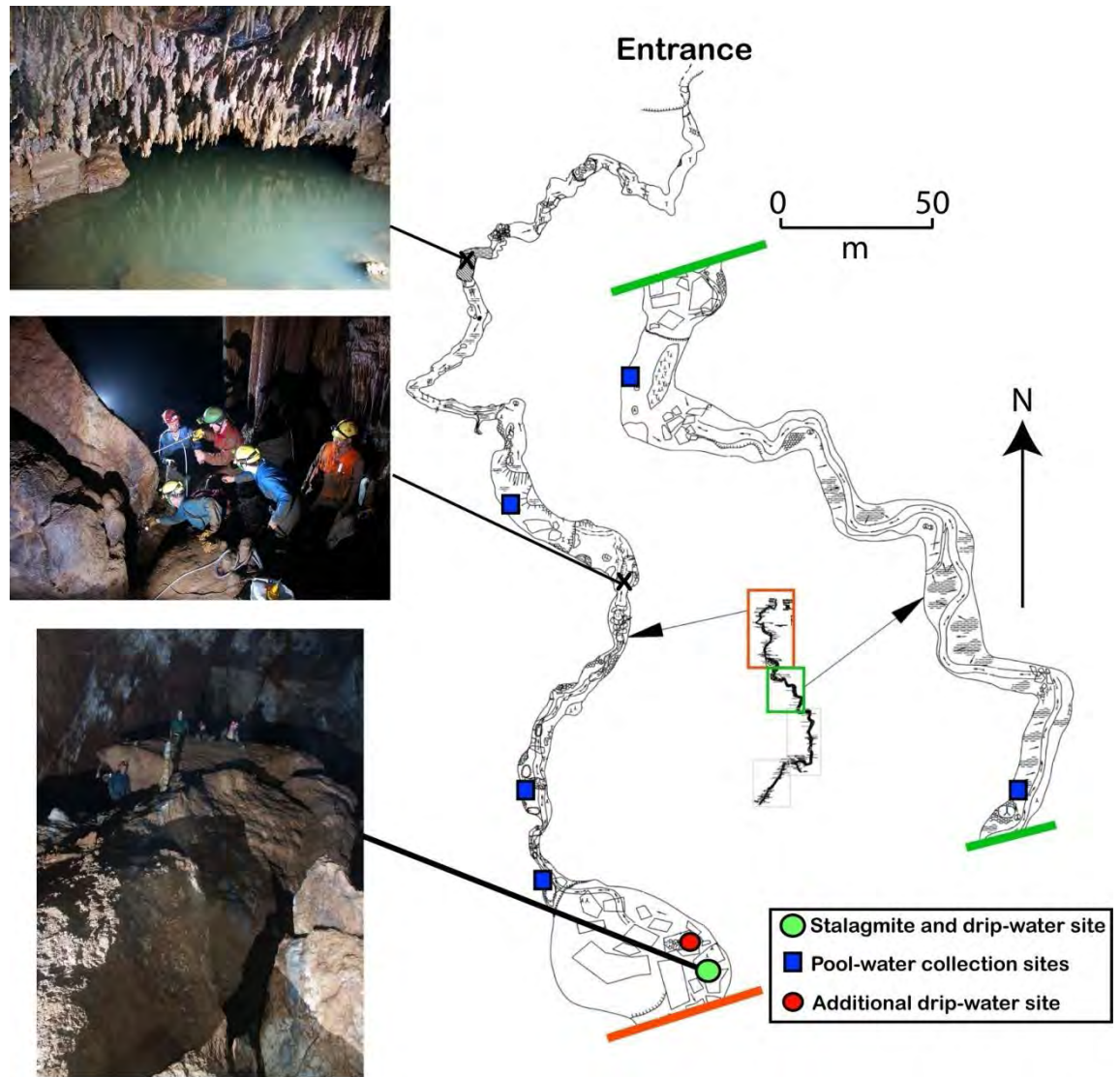


Figure 3.2 Plan of ~1km stretch (total length of cave is ~2km) of Liang Luar Cave, along with photographs taken from several sections of the cave. Symbols indicate the position of collection sites for drip and pool waters, and stalagmite LR06-B1.

Belemnite (VPDB) scale using an internal working standard of Carrara Marble (New1), which was calibrated using the international standards, NBS18 and NBS19. The analytical uncertainty (2σ) of in-run measurements of Carrara Marble (New1) was 0.08‰ for $\delta^{18}\text{O}$.

The fluid inclusion analyses were conducted on what has been termed the ‘Amsterdam Device’, which comprises a newly modified crushing device attached to a continuous-flow Thermo-Finnigan TC-EA pyrolysis furnace housed at Vrije Universiteit, Amsterdam (see Vonhof 2006, 2007). This device consists of a manual crushing apparatus made from a modified 8BG vacuum valve. The valve plunger is

fitted with a hardened steel piston, which is lowered into the crushing chamber by turning the valve handle. The crushing chamber has a total volume of 1.5 cm^3 , which permits calcite cubes of up to $\sim 1 \text{ g}$ to be crushed. The crusher is fitted with a septum port that allows the direct injection of sub-microlitre amounts of water into the crushing chamber using a small syringe. The crusher is mounted on a small oven containing a 250 W plate heater, while a second 250 W plate heater is inserted in the base plate of the crusher. With an insulating cover placed over the crusher, the heaters can generate temperatures of 30–200 °C within 15 minutes for the whole system. Inside the oven, the crusher is connected to the He carrier flow and the TC-EA via a cold trap unit, which comprises a 0.75 mm i.d. annealed stainless steel capillary and Swagelok connectors. At the top of the TC-EA reactor, the device is connected to a standard inlet of He carrier gas controlled by four valves that can be switched between two modes. The *default mode* is the bypass mode for conventional automatic analysis on the TC-EA system, while the *crusher mode* allows a 90 mL/min flow of He to pass through the crushing chamber once the cube of calcite has been crushed. This flow of He carries water from the crusher into the cold trap unit, where it is cryogenically trapped in a 1 m coiled 0.75 mm i.d. stainless steel capillary tube immersed in liquid N_2 for a period of ~ 2 minutes. Following this, the cold trap unit is flash heated to release the water in a short pulse into the TC-EA for analysis.

Fifteen prisms of speleothem calcite, each weighing $\sim 300 \text{ mg}$ and measuring 3–5 mm longitudinally, were extracted from the central growth axis of stalagmite LR06-B1. The prisms were then crushed and the liberated water analysed for $\delta^{18}\text{O}$ ($\delta^{18}\text{O}_f$) and δD (δD_f) using the method described above. Four of the crushed samples had water yields that either exceeded the range of detection or were too low for an accurate signal to be obtained by the TC-EA. These samples were subsequently omitted from the final analysis, leaving a total of eleven samples for the Holocene reconstruction. Owing to the complex crystallographic structure of speleothem LR07-B1, it was extremely difficult to assess the optimal sample mass required for signal detection in the ‘Amsterdam Device’. Hence, the process of fluid inclusion extraction from this speleothem was a little ‘hit and miss’, largely because of the longitudinal changes in calcite petrography throughout the specimen. Notwithstanding this, LR06-B1 was a favourable specimen for this type of work given that it contained plenty of water within the inclusions (typically $>0.25 \mu\text{L}$), a result that is somewhat of a rarity in speleothem fluid-inclusion studies. A reason for these large and abundant inclusions being preserved in this speleothem is possibly related to the fact that the region experiences abundant rainfall each year (via the summer monsoon), resulting in the fast growth and hence

effective entrapment of tiny inclusion waters. However, this observable process may be restricted to this cave system and/or speleothem.

The $\delta^{18}\text{O}_f$ and δD_f of the waters are reported with reference to Vienna Standard Mean Ocean Water (VSMOW). Mean analytical reproducibility (1σ) of standard waters injected into the crusher was 1.5‰ for δD and 0.3‰ for $\delta^{18}\text{O}$. The stable isotope ratios of the fluid inclusions and host calcite were tied to a Monte Carlo-derived age-depth model previously described by Drysdale et al. (2005, 2007), and are summarised in Table 3.1.

Table 3.1 Summary of fluid-inclusion δD_f (VSMOW) and $\delta^{18}\text{O}_f$ (VSMOW), and speleothem calcite $\delta^{18}\text{O}_c$ (VPDB) shown in Figs 3.3-3.5. Depth is the mid-point distance (in mm) from the top of stalagmite LR06-B1 where the calcite prisms were extracted for fluid inclusion analyses. Ages (ka) are from the published age-depth model of Griffiths et al. (2009). Speleothem calcite formation temperatures shown in Fig. 3.6 were calculated using the Craig (1965) equation. ΔT represents the difference in temperature relative to the modern cave average of 25 °C.

Sample I.D	Depth (mm)	Age (ka)	δD_f (VSMOW)	$\delta^{18}\text{O}_f$ (VSMOW)	$\delta^{18}\text{O}_c$ (VPDB)	Calcite formation T (°C)	ΔT (°C relative to modern)
E1-1	1204	12.07	-30.7	-4.70	-4.96	18.0	-7.0
D1-2	1130	11.37	-25.7	-3.42	-4.28	20.6	-4.4
D1-3	1007	10.08	-30.2	-3.49	-4.71	22.2	-2.8
D1-4	937	9.29	-31.3	-4.00	-5.57	23.8	-1.2
C1-5	832	8.57	-33.9	-4.39	-5.98	23.9	-1.1
C2-6	797	6.10	-39.2	-4.76	-6.55	24.8	-0.2
C2-7	675	4.86	-36.0	-5.20	-6.36	22.0	-3.0
B1-8	531	4.01	-40.6	-5.27	-6.56	22.5	-2.5
A1-9	286	2.17	-35.2	-4.75	-6.32	23.8	-1.2
A1-10	218	1.75	-33.9	-5.00	-6.75	24.5	-0.5
E2-11	44	0.36	-38.6	-5.00	-6.69	24.4	-0.6

$\delta^{18}\text{O}$ and δD values were determined for modern cave drip- and pool-water samples collected in May 2007 from various locations in Liang Luar Cave (Fig. 3.2). In addition, $\delta^{18}\text{O}$ and δD were measured on modern rainfall samples collected from the cave site between September 2006 and April 2007 [refer to chapter 2 or supplementary material of Griffiths et al., (2009) for rainfall isotope data]. The $\delta^{18}\text{O}$ values were measured at Monash University, Australia, via equilibration with CO_2 at 32 °C for 24–48 h in a Finnigan MAT Gas Bench and analysed using a continuous-flow technique on a Finnigan MAT 252 mass

spectrometer. δD measurements were conducted via reaction with Cr at $850^{\circ}C$ using an automated Finnigan MAT H/Device. $\delta^{18}O$ and δD values were measured relative to internal standards that were calibrated using the International Atomic Energy Agency (IAEA) S MOW, Greenland Ice Sheet Precipitation (GISP) and Standard Light Antarctic Precipitation (SLAP) standards. All isotopic data are reported as per mil (‰) deviations relative to VSMOW where $\delta^{18}O$ and δD values of SLAP are -55.5% and -428% , respectively. Analytical precision (1σ) for replicate measurements of the internal standards was $\pm 0.1\%$ for $\delta^{18}O$ and $\pm 1\%$ for δD . The cave drip- and pool-water results are summarised in Table 3.2.

Table 3.2 Summary of the $\delta^{18}O$ (VSMOW) and δD (VSMOW) values for the drip waters (D-W) and cave pool waters (P-W) displayed in Figs 3.2-3.3. D-W1 represents the modern drip-water feeding stalagmite LR06-B1 used in this study.

Sample I.D	δD (VSMOW)	$\delta^{18}O$ (VSMOW)
P-W1	-39	-5.4
P-W2	-36	-5.4
P-W3	-38	-5.6
P-W4	-35	-5.5
P-W5	-40	-5.6
D-W1	-38	-5.5
D-W2	-38	-5.4

3.4 Results

The accuracy of the fluid-inclusion $\delta^{18}O_f$ and δD_f values, in terms of recording drip-water isotope composition, can be checked by comparing the results with the GMWL and the isotopic composition of the cave drip and pool waters (Fig. 3.3). The $\delta^{18}O_f$ and δD_f values of the fluid inclusions display a trend that is parallel to the GMWL, and are in close agreement with the cave drip and pool waters. Furthermore, the fluid-inclusion $\delta^{18}O_f$ and δD_f values for the youngest calcite layers plot close to the field of modern drip water compositions. The result confirms that modern inclusions in stalagmite LR06-B1 preserve a quasi-pristine record of the $\delta^{18}O$ and δD of the cave drip waters. Noteworthy is the $\sim 1\%$ enrichment in $\delta^{18}O$ of the fluid inclusions, and cave drip and pool waters, relative to the rainfall collected from the cave site (Fig. 3.3). Given the extreme relative humidity of the cave environment

(close to 100% - Griffiths et al. 2009), I interpret this enrichment to reflect evapotranspiration in the epikarst, particularly during the dry season when percolating waters may become stagnant or slow moving through the soil-bedrock profile due to the lower hydrostatic pressure induced by lower rainfall. This process would produce higher $\delta^{18}\text{O}$ waters permeating the karst and entering the cave due to the preferential loss of ^{16}O to the vapour phase. The area surrounding Liang Luar Cave is conducive to these evaporative processes because the highly seasonal climate is characterised by strong summer heating (i.e. the dry season), followed by a rapid increase in precipitation (i.e. the wet season) enabling the transport of isotopically-enriched surface water to the lower vadose zone and cave interior (Fairchild et al., 2006).

Throughout the Holocene the $\delta^{18}\text{O}_f$ values range from -3.4‰ to -5.3‰ (ave. -4.5‰), while the δD_f ranges from -26‰ to -41‰ (ave. -34‰). The $\delta^{18}\text{O}_f$ and δD_f records trend towards lower values through much of the early to mid-Holocene, in phase with the $\delta^{18}\text{O}$ trend of the host calcite (Fig. 3.4). The coupled measurements of $\delta^{18}\text{O}_f$ and $\delta^{18}\text{O}_c$ provide an independent means of reconstructing cave air temperature (stalagmite growth temperature) by removal of the water $\delta^{18}\text{O}$ component of the calcite $\delta^{18}\text{O}_c$ record. This was achieved by averaging the $\delta^{18}\text{O}_c$ measurements over the same temporal resolution (3-5 mm) as the extracted adjacent calcite prisms used for fluid inclusion analysis. Here I assume that the $\delta^{18}\text{O}_c$ of the calcite prisms are the same as that of the temporally-averaged 1 mm-resolution calcite powders. In the first instance, the equilibrium palaeotemperature equation of Kim and O'Neil (1997) produced a growth temperature for the most recently deposited calcite of $\sim 22^\circ\text{C}$, which is $\sim 3^\circ\text{C}$ cooler than the average modern cave temperature. An offset of similar magnitude for cave palaeotemperature reconstructions has been noted in other speleothem fluid-inclusion studies (e.g. McDermott et al., 2006; van Breukelen et al., 2008; Zhang et al., 2008). However, the equation of Craig (1965) yielded speleothem growth temperatures ranging from 18.6 to 25.3°C (Table 3.1), with an average of $\sim 24^\circ\text{C}$ during the Holocene. The calculated average cave temperature of $\sim 24^\circ\text{C}$ is in good agreement with the modern cave temperature of $\sim 25^\circ\text{C}$ and the tropical air temperature expected at a site 550 m.a.s.l, given an environmental lapse rate of $\sim 0.6^\circ\text{C}$ per 100 m altitude and an average SST around Flores of 28.5°C . Further, Holocene temperatures are likely to be $\sim 1^\circ\text{C}$ lower than today's $\sim 25^\circ\text{C}$ average, given the $\sim 0.7^\circ\text{C}$ of recent global warming.

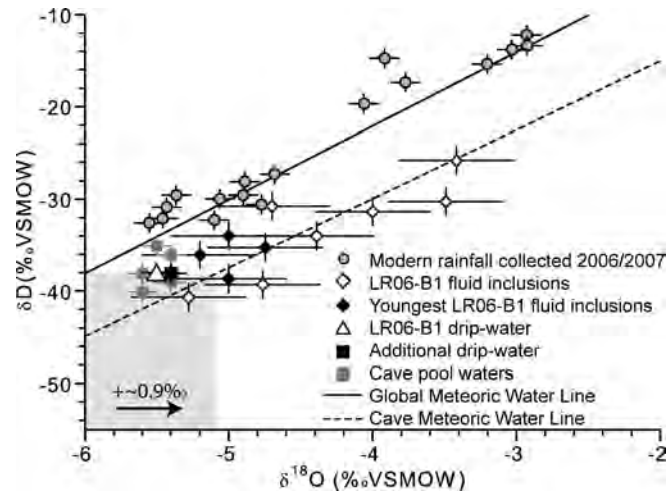


Figure 3.3 Cross-plot of δD versus $\delta^{18}O$ for stalagmite LR06-B1 fluid-inclusion samples, cave drip waters (including the drip-water feeding stalagmite LR06-B1), and cave pool waters. Drip and pool waters were collected in May 2007. Also plotted are rainfall isotopes collected at the cave site between September 2006 and April 2007. The solid line indicates the Global Meteoric Water Line (GMWL) and the dashed line the Cave Meteoric Water Line. Error bars on the fluid inclusions represent the analytical reproducibility (1σ) of measurements on standard waters injected into the crusher. Error bars on the rainfall isotopes and cave drip and pool waters represent analytical precision (1σ) of replicate measurements on internal standards. The δD and $\delta^{18}O$ of the fluid inclusions display a trend that is parallel to the GMWL, and are in close agreement with the cave drip and pool waters. Furthermore, the fluid-inclusion $\delta^{18}O_f$ and δD_f values for the youngest calcite layers plot close to the field of modern drip water compositions thus confirming that the inclusion waters reflect the $\delta^{18}O$ and δD of the drip waters within the cave system. The gray shading highlights the $\sim 0.9\text{‰}$ enrichment in $\delta^{18}O$ of the fluid inclusions and cave drip and pool waters relative to the rainfall. I attribute this slight enrichment to evapotranspiration of the surface waters prior to reaching the cave interior.

The calculated late Holocene cave temperature of $\sim 24\text{ °C}$ provides a well-calibrated modern “anchor point” for the Younger Dryas-Holocene palaeotemperature reconstruction. During the YD event, reconstructed cave air temperatures were, on average, $\sim 5\text{ °C}$ cooler than modern values. Since $\sim 10\text{ ka}$, cave air temperatures were much more stable, remaining within $\pm 2\text{ °C}$ of the Holocene average of $\sim 24\text{ °C}$.

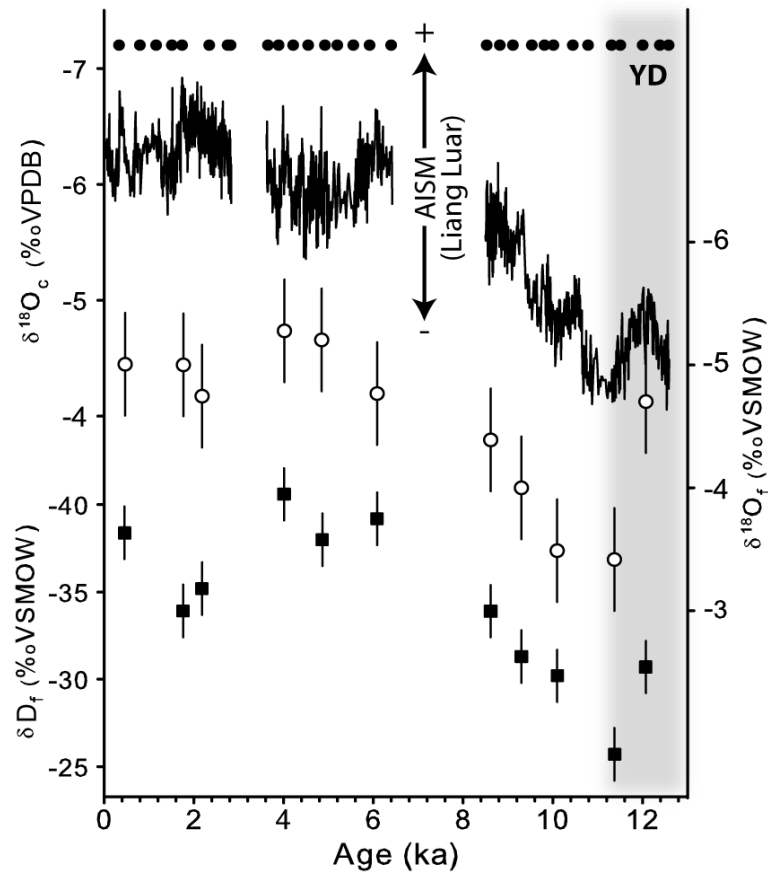


Figure 3.4 Comparison of stalagmite LR06-B1 calcite $\delta^{18}\text{O}_c$ (black curve), fluid-inclusion $\delta^{18}\text{O}_f$ (circles), and fluid-inclusion δD_f (squares) records over the past 12.64 ka. U/Th ages used to construct the time-series are plotted along the top (dating and sampling errors are smaller than the symbols used). Error bars represent mean analytical (1σ) reproducibility of the standard waters injected into the crusher. The gray bar highlights the timing of the Younger Dryas climate anomaly. The $\delta^{18}\text{O}_f$ and δD_f trend towards lower values through the early- to mid-Holocene matches the trend in $\delta^{18}\text{O}_c$, thus confirming that the speleothem calcite $\delta^{18}\text{O}_c$ primarily reflects variations in the $\delta^{18}\text{O}$ of meteoric rainfall.

3.5 Discussion

In Griffiths et al. (2009), we concluded that the calcite $\delta^{18}\text{O}_c$ values of stalagmite LR06-B1 were largely dependent upon the intensity of the monsoon (rather than changes in temperature), whereby higher (lower) rainfall amounts correspond with lower (higher) $\delta^{18}\text{O}_c$ values in the tropics. This interpretation can be verified by comparing the LR06-B1 calcite $\delta^{18}\text{O}_c$ record with the new fluid-inclusion $\delta^{18}\text{O}_f$ record, which directly records the $\delta^{18}\text{O}$ of monsoon rainfall at Flores (Fig. 3.4). The results show that fluid-inclusion $\delta^{18}\text{O}_f$ varies in phase with calcite $\delta^{18}\text{O}_c$, and both records define a prominent $\sim 2\%$ decrease in $\delta^{18}\text{O}$ during the early-middle Holocene. The good agreement between the calcite $\delta^{18}\text{O}_c$ record and the new fluid-inclusion $\delta^{18}\text{O}_f$ record eliminates the possibility of changes in cave drip-water temperature

(calcite formation temperature) as a potential driver of the early-middle Holocene shift in $\delta^{18}\text{O}$. Moreover, only ~25% of the ~2‰ shift in $\delta^{18}\text{O}_f$ and $\delta^{18}\text{O}_c$ can be due to the early-middle Holocene decrease in global ice volume (Siddall et al., 2003), which decreased the $\delta^{18}\text{O}$ of seawater, and hence the $\delta^{18}\text{O}$ of rainfall (Fig. 3.5). Therefore, a significant decrease in the $\delta^{18}\text{O}$ of AISM precipitation during air-mass transport must account for the remaining ~75% (~1.5‰) of the early-middle Holocene isotopic shift observed in LR06-B1.

Based on these results, I interpret the early-middle Holocene decrease in $\delta^{18}\text{O}_c$ and $\delta^{18}\text{O}_f$ to reflect a sharp intensification of the AISM until ~6 ka, followed by relative stability until the present. In contrast to other low-latitude monsoon records (e.g. Dykoski et al., 2005; van Breukelen et al., 2008; Wang et al., 2005), the absence of a prominent mid-late Holocene trend in the $\delta^{18}\text{O}_c$ and $\delta^{18}\text{O}_f$ records suggests that the impact of local summer insolation on monsoon air-mass transport to Flores (Fig. 3.5) was minimal. Our previous interpretation (see previous chapter and/or Griffiths et al., 2009) was that the early Holocene increase in the AISM was largely driven by the effect of deglacial inundation of the Sunda Shelf on monsoon moisture availability. Like the $\delta^{18}\text{O}_c$ record, the decreasing trend in the new $\delta^{18}\text{O}_f$ record resembles the eustatic sea-level curve (Bard et al., 1996; Peltier and Fairbanks, 2006; Siddall et al., 2003; Fig. 3.5), thus confirming the potential role of Sunda Shelf inundation in controlling the postglacial onset of the AISM.

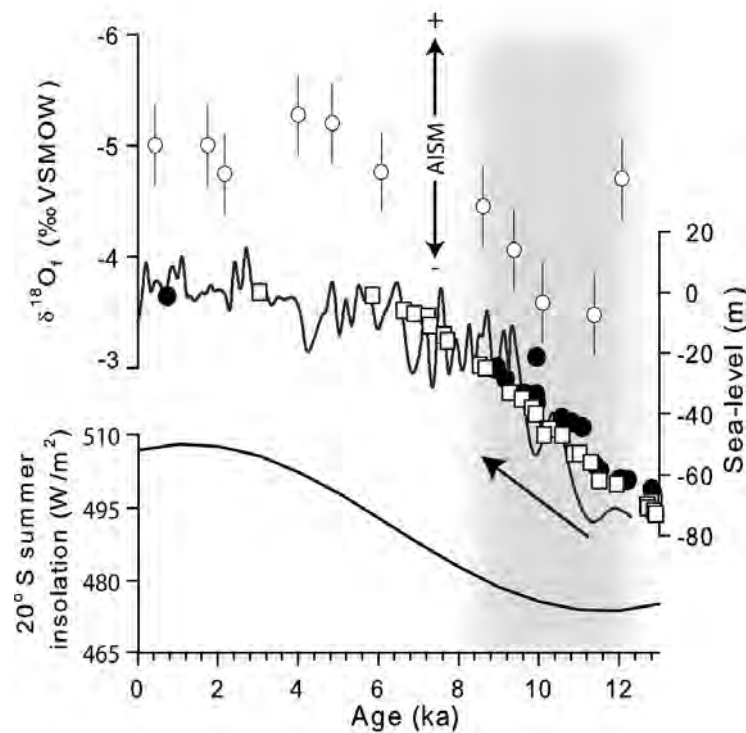


Figure 3.5 Comparison of ice-volume adjusted (Siddall et al., 2003) fluid-inclusion $\delta^{18}\text{O}_f$ (black circles) and reconstructed sea-level curves from the Red Sea (solid line; Siddall et al., 2003), Barbados (squares; Peltier and Fairbanks, 2006) and Tahiti (circles; Bard et al., 1996). Grey shading highlights the concurrent decrease in $\delta^{18}\text{O}_f$ and sea-level during the early to mid-Holocene reflecting intensification of Australian-Indonesian summer monsoon rainfall in response to eustatic sea-level rise and flooding of the Sunda Shelf.

The paired fluid-inclusion $\delta^{18}\text{O}_f$ and calcite $\delta^{18}\text{O}_c$ records from Flores provide new insights into the history of tropical air temperature in the IPWP region. Figure 3.6 shows that air temperatures inside Liang Luar Cave remained relatively stable over the past ~ 10 ka (ave. $\sim 24^\circ\text{C}$). The result is in good agreement with stable Holocene SSTs ($\pm 1^\circ\text{C}$) reconstructed for the IPWP (Briker et al., 2007; Lea et al., 2000; Stott et al., 2004; Visser et al., 2003), based on the analysis of Mg/Ca in planktonic foraminifera. Stable tropical air temperatures during the Holocene were also inferred from fluid inclusions in stalagmites from Peruvian Amazonia (van Breukelen et al., 2008), highlighting the strong zonal synchrony in Holocene temperatures between the eastern and western tropical Pacific. Taken together, the results support the interpretation that the early-middle Holocene onset of the AISM is related primarily to deglacial flooding of the Sunda Shelf, rather than changes in local SST (and air temperature).

Close inspection of Figure 3.6, however, shows that there are millennial-scale structural patterns in Liang Luar Cave air temperature through the Holocene. Several of these excursions in air temperature

are synchronous with excursions in coral Sr/Ca-SST reconstructions for the southern sector of the IPWP (Abram et al., 2009). For example, cooling of coral-inferred SSTs from ~4-6 ka is mirrored by a cooling trend in Liang Luar. This trend is followed by an increase in SST and cave temperatures to modern values. Therefore, on millennial-timescales, it appears that (like today) local changes in tropical SST and air temperature were tightly coupled in the IPWP region.

Before ~10 ka, the Liang Luar record shows significantly cooler cave air temperatures with maximum cooling (~5 °C cooler than modern) during the YD climate anomaly (Fig. 3.6a). About 0.4-0.5 °C of the ~5 °C cooling during the YD can be explained by the 60-80 m increase in altitude caused by lower eustatic sea levels during the YD (assuming a lapse rate of 0.6 °C 100⁻¹ m altitude). This still leaves a significant ~4.5 °C reduction in southern IPWP air temperature during the YD. The ~4.5 °C cooling is consistent with numerous coral Sr/Ca-SST reconstructions, which indicate ~2-5 °C reduction in southern IPWP SSTs during the YD (e.g. Castellaro et al., 1997; Corrège et al., 2004; Gagan et al., 2000), and hence suggest a similar magnitude of cooling. However, the Mg/Ca-inferred SST records from planktonic foraminifera (Stott et al., 2004; Visser et al., 2003) indicate only ~1 °C cooling in the IPWP region during this time (Fig. 3.6a). Possible explanations for these discrepancies include: (i) diagenetic alteration of fossil corals and/or marine sediment foraminifera; and/or (ii) differences in climate sensitivity of air versus sea-surface temperatures.

Comparison of the Liang Luar temperature record with high-elevation tropical ice-core records from Sajama, Bolivia (Thompson et al., 1998) and Huascarán, Peru (Thompson et al., 1995) reveals strong zonal synchronicity between the two regions during the YD (Fig. 3.6b). The negative $\delta^{18}\text{O}$ excursions observed for the YD interval in the ice cores have been inferred to reflect cooler temperatures and lower snowlines associated with higher accumulation rates (Thompson et al., 1998). The cooler YD temperatures observed on both sides of the Pacific demonstrate that terrestrial temperatures cooled substantially during the YD event in both low-elevation and high-elevation tropical environments. Taken together, the results contribute to the growing body of evidence for a close equator-to-pole link between the North Atlantic and deep tropics during the YD event.

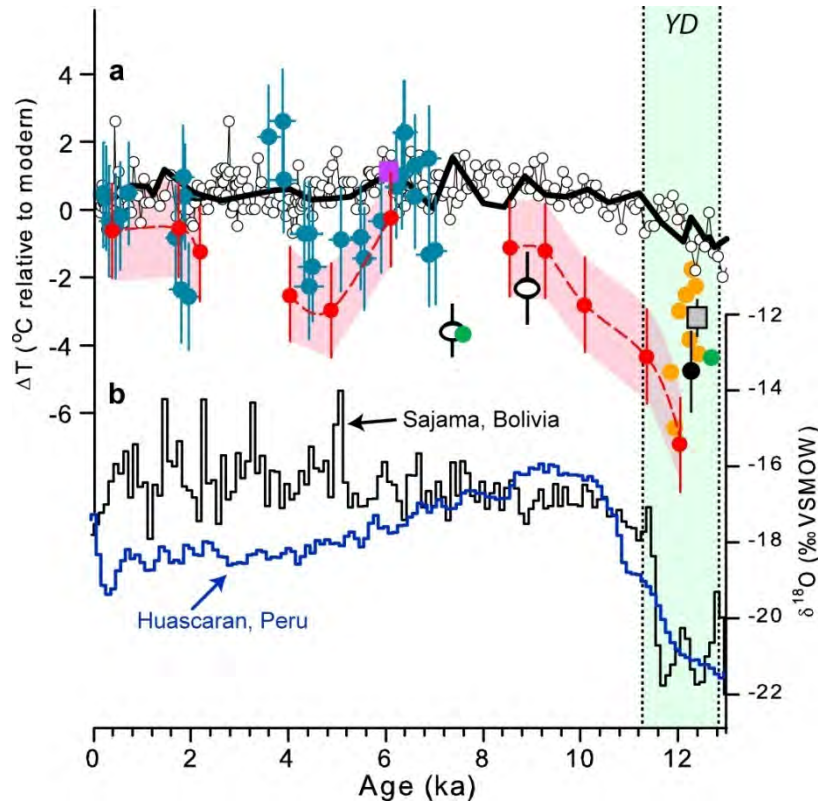


Figure 3.6 (a) Comparison of reconstructed Liang Luar Cave palaeotemperatures (red circles) with reconstructions of IPWP SSTs based on Mg/Ca in planktonic foraminifera in marine cores MD76 (black open circles; Stott et al., 2004) and MD62 (solid line; Visser et al., 2003), and coral Sr/Ca and U/Ca records from the tropical west and central Pacific (blue, Abram et al., 2009; gray, Asami et al., 2009; green, Castellaro et al., 1997; black, Corrège et al., 2004; purple, Gagan et al., 1998; orange, Gagan et al., 2000; white, McCulloch et al., 1996). Pink shading shows error envelope for palaeotemperatures calculated from fluid-inclusion $\delta^{18}\text{O}_f$ and calcite $\delta^{18}\text{O}_c$ [the combined analytical errors (1σ) for both measurements ($\pm 1.5^\circ\text{C}$)]. (b) $\delta^{18}\text{O}$ records from high-elevation tropical ice-cores from the Sajama (Bolivia; Thompson et al., 1998) and Huascarán (Peru; Thompson et al., 1995) ice caps. Green shading shows the -Younger Dryas interval marked by $\sim 5^\circ\text{C}$ cooling on Flores and significant reduction in $\delta^{18}\text{O}$ of high-elevation ice caps in tropical South America.

As previously noted by Griffiths et al. (2009), the LR06-B1 calcite $\delta^{18}\text{O}_c$ values were significantly lower during the YD event indicating that, despite the cooler air temperatures, monsoon rainfall intensity may have been greater. The new fluid-inclusion $\delta^{18}\text{O}_f$ record confirms that the average $\delta^{18}\text{O}$ value of monsoon rainfall in Flores was substantially lower during the YD. Taking into account the positive relationship observed between air temperature and $\delta^{18}\text{O}$ of rainfall in the tropics (the “air temperature effect”, $\sim 0.1\text{‰ }^\circ\text{C}^{-1}$) (Gat and Gouffier, 1981), and the negative relationship between $\delta^{18}\text{O}$ of calcite and drip-water temperature (the “cave temperature effect”, $\sim -0.24\text{‰ }^\circ\text{C}^{-1}$) (O’Neil et al., 1969), a $\sim 5^\circ\text{C}$ cave temperature increase through the YD-Holocene transition would account for the observed $\sim 0.7\text{‰}$ change. That is, a $\sim 1.2\text{‰}$ change caused by the cave temperature effect is partially countered by a

$\sim +0.5\text{‰}$ change due to the air temperature effect, producing the net decrease of $\sim -0.7\text{‰}$ in the stalagmite $\delta^{18}\text{O}$. The speleothem $\delta^{18}\text{O}$ signature therefore suggests a significantly drier early Holocene relative to the YD; this finding has been corroborated independently from trace elements (Mg/Ca and Sr/Ca) and $\delta^{234}\text{U}$ activity ratios from the same stalagmite (see chapters 4 and 5), which indicate lower Mg/Ca, Sr/Ca, and $\delta^{234}\text{U}$ values during the YD interpreted to reflect higher infiltration rates (and hence higher rainfall) through the soil-bedrock profile. I attribute this isotopic excursion to increased convective activity associated with a southward migration of the average position of the AISM-ITCZ. Modelling results suggest that increased meridional SST gradients during the YD cold interval would have favoured the southward migration of the ITCZ (Chiang et al., 2003), leading to dry northern and wet southern low latitudes (Haug et al., 2001; van Breukelen et al., 2008). Together, the results imply that the positioning of the ITCZ has little to do with local SST (and air temperature), as has been suggested by a recent foraminiferal Mg/Ca reconstruction for the IPWP showing cool SSTs and high rainfall in the IPWP during the Little Ice Age (Oppo et al., 2009).

3.6 Conclusions

The oxygen and hydrogen isotopic composition of Indonesian palaeorainfall was determined by extracting fluid inclusions from stalagmite LR06-B1 from Liang Luar Cave, Flores, in the southern sector of the IPWP and AISM climate domains. The results demonstrate that the fluid-inclusion $\delta^{18}\text{O}_f$ record varies in phase with $\delta^{18}\text{O}_c$ of the speleothem calcite through the Holocene, confirming that the $\delta^{18}\text{O}$ of LR06-B1 is representative of variations in the $\delta^{18}\text{O}$ of meteoric rainfall. Given this, parallel trends towards lower $\delta^{18}\text{O}_f$ and $\delta^{18}\text{O}_c$ values through the early- to mid-Holocene are interpreted to reflect intensification of the AISM in response to postglacial eustatic sea-level rise and flooding of the Sunda Shelf.

It has been shown that coupled measurements of $\delta^{18}\text{O}$ in speleothem fluid inclusions and host calcite can be used to reconstruct terrestrial palaeotemperatures in tropical settings based on the relationship between $\delta^{18}\text{O}$ of the calcite and formation drip water. The general stability of air temperatures in Liang Luar during the Holocene epoch is in good agreement with the SST history for the IPWP. In contrast, the YD climate anomaly is characterised by a $\sim 5^\circ\text{C}$ cooling of cave air temperature. The speleothem-inferred paleotemperatures are in good agreement with YD temperatures given by coral Sr/Ca and tropical ice-core records, while foraminiferal Mg/Ca ratios for the IPWP only indicate a $\sim 1^\circ\text{C}$

cooling during the YD event. The speleothem fluid-inclusion $\delta^{18}\text{O}_f$ record also indicates that local SSTs (and air temperatures) had little influence on the positioning of the ITCZ because cooling of the southern IPWP during the YD was accompanied by higher rainfall in the AISM climate domain.

3.7 References

- Abram, N.J., McGregor, H.V., Gagan, M.K., Hantoro, W.S., Suwargadi, B.W., 2009. Oscillations in the southern extent of the Indo-Pacific Warm Pool during the mid-Holocene. *Quaternary Science Reviews* 28, 2794-2803.
- Asami, R., Felis, T., Deschamps, P., Hanawa, K., Iryu, Y., Bard, E., Durand, N., and Murayama, M., 2009. Evidence for tropical South Pacific climate change during the Younger Dryas and the Bolling-Allerod from geochemical records of fossil Tahiti corals, *Earth and Planetary Science Letters* 288, 96-107.
- Bard, E., Hamelin, B., Arnold, M., Montaggioni, L., Cabioch, G., Faure, G., and Rougerie, F., 1996. Deglacial sea-level record from Tahiti corals and the timing of global meltwater discharge. *Nature* 382, 241-244.
- Brijker, J.M., Jung, S.J.A., Ganssen, G.M., Bickert, T. and Kroon, D., 2007. ENSO related decadal scale climate variability from the Indo-Pacific Warm Pool. *Earth and Planetary Science Letters* 253, 67-82.
- Castellaro, C., Ribaud-Laurenti, A., Claverie, K., Cabioch, G., Hamelin, B., Bard, E., Montaggioni, L., J. Recy, 1997. Variabilite de climat tropical a l'holocene: Enregistrements Sr/Ca et U/Ca dans les coraux de Nouvelle-Caledonia, de Tahiti, et des Seychelles (Indo-Pacifique). 6 Congres Francais de la Chronologie Lion des Resumes, Publication ASF, Paris, 293 pp. 47-48.
- Chiang, J.C.H., Biasutti, M. and Battisti, D.S., 2003. Sensitivity of the Atlantic Intertropical Convergence Zone to Last Glacial Maximum boundary conditions. *Paleoceanography* 18, 1094, doi: 10.1029/2003PA000916.
- Correge, T., Gagan, M.K., Beck, J.W., Burr, G.S., Cabioch, G. and Le Cornec, F., 2004. Interdecadal variation in the extent of South Pacific tropical waters during the Younger Dryas event. *Nature* 428, 927-929.
- Craig, H., 1965. The measurement of oxygen isotope palaeotemperatures. In: E. Tongiorgi (Ed.), *Stable isotopes in oceanographic studies and palaeotemperatures*. Consiglio Nazionale delle Ricerche Laboratorio di Geologia Nucleare, Pisa, pp. 166-182.
- Dennis, P.F., Rowe, P.J. and Atkinson, T.C., 2001. The recovery and isotopic measurement of water from fluid inclusions in speleothems. *Geochimica et Cosmochimica Acta* 65, 871-884.

- Drysdale, R.N., Zanchetta, G., Hellstrom, J.C., Fallick, A.E. and Zhao, J.X., 2005. Stalagmite evidence for the onset of the Last Interglacial in southern Europe at 129 +/- 1 ka. *Geophysical Research Letters* 32, L24708, doi:10.1029/2005GL024658.
- Drysdale, R.N., Zanchetta, G., Hellstrom, J.C., Fallick, A.E., McDonald, J. and Cartwright, I., 2007. Stalagmite evidence for the precise timing of North Atlantic cold events during the early last glacial. *Geology* 35, 77-80.
- Dublyansky, Y.V. and Spötl, C., 2009. Hydrogen and oxygen isotopes of water from inclusions in minerals: design of a new crushing system and on-line continuous-flow isotope ratio mass spectrometric analysis. *Rapid Communications in Mass Spectrometry* 23, 2605-2613.
- Dykoski, C.A., Edwards, R.L., Cheng, H., Yuan, D.X., Cai, Y.J., Zhang, M.L., Lin, Y.S., Qing, J.M., An, Z.S. and Revenaugh, J., 2005. A high-resolution, absolute-dated Holocene and deglacial Asian monsoon record from Dongge Cave, China. *Earth and Planetary Science Letters* 233, 71-86.
- EPICA members, 2006. One-to-one coupling of glacial climate variability in Greenland and Antarctica. *Nature* 444, 195-198.
- Fairchild, I.J., Smith, C.L., Baker, A., Fuller, L., Spötl, C., Matthey, D., McDermott, F. and Eimp, 2006. Modification and preservation of environmental signals in speleothems. *Earth-Science Reviews* 75, 105-153.
- Fleitmann, D., Burns, S.J., Neff, U., Mangini, A. and Matter, A., 2003. Changing moisture sources over the last 330,000 years in Northern Oman from fluid-inclusion evidence in speleothems. *Quaternary Research* 60, 223-232.
- Gagan, M.K., Ayliffe, L.K., Hopley, D., Cali, J.A., Mortimer, G.E., Chappell, J., McCulloch, M.T., Head, M.J., 1998. Temperature and surface-ocean water balance of the mid-Holocene tropical western Pacific. *Science* 279, 1014-1018.
- Gagan, M.K., Ayliffe, L.K., Beck, J.W., Cole, J.E., Druffel, E.R.M., Dunbar, R.B., Schrag, D.P., 2000. New views of tropical paleoclimates from corals. *Quaternary Science Reviews* 19, 45-64.
- Gat, J.R., Gonfiantini, R., 1981. Stable isotope hydrology: Deuterium and oxygen-18 in the water cycle. IAEA Technical Report Series No. 210, International Atomic Energy Agency, Vienna, pp. 339.

- Griffiths, M.L., Drsydale, R.N., Gagan, M.K., Zhao, J.-x., Ayliffe, L.K., Hellstrom, J.C., Hantoro, W.S., Frisia, S., Feng, Y.-x., Cartwright, I., St. Pierre, E., Fischer, M.J., Suwargadi, B.W., 2009. Increasing Australian-Indonesian monsoon rainfall linked to early Holocene sea-level rise. *Nature Geoscience* 2, 636-639.
- Haug, G.H., Hughen, K.A., Sigman, D.M., Peterson, L.C. and Rohl, U., 2001. Southward migration of the intertropical convergence zone through the Holocene. *Science* 293, 1304-1308.
- Hellstrom, J., 2003. Rapid and accurate U/Th dating using parallel ion-counting multi-collector ICP-MS. *Journal of Analytical Atomic Spectrometry* 18, 1346-1351.
- Hellstrom, J.C., 2006. U-Th dating of speleothems with high initial ^{230}Th using stratigraphical constraint. *Quaternary Geochronology* 1, 289-295.
- Hendy, C.H., 1971. The isotopic geochemistry of speleothems: The calculations of the effects of different modes of formation on the isotopic composition of speleothems and their applicability as palaeoclimate indicators. *Geochimica et Cosmochimica Acta* 35, 801-824.
- Kim, S.T. and O'Neil, J.R., 1997. Equilibrium and nonequilibrium oxygen isotope effects in synthetic carbonates. *Geochimica et Cosmochimica Acta* 61, 3461-3475.
- Lea, D.W., Pak, D.K. and Spero, H.J., 2000. Climate impact of late Quaternary equatorial Pacific sea surface temperature variations. *Science* 289, 1719-1724.
- Matthews, A., Ayalon, A. and Bar-Matthews, M., 2000. D/H ratios of fluid inclusions of Soreq cave (Israel) speleothems as a guide to the Eastern Mediterranean Meteoric Line relationships in the last 120 ky. *Chemical Geology* 166, 183-191.
- Mayewski, P.A., Rohling, E.J., Stager, J.C., Karlen, W., Maasch, K.A., Meeker, L.D., Meyerson, E.A., Gasse, F., van Krevelend, S., Holmgren, K., Lee-Thorp, J., Rosqvist, G., Rack, F., Staubwasser, M., Schneider, R.R. and Steig, E.J., 2004. Holocene climate variability. *Quaternary Research* 62, 243-255.
- McCulloch, M.T., Mortimer, G., Esat, T., Xianhua, L., Pillans, B., Chappell, J., 1996. High resolution windows into early Holocene climate: Sr/Ca coral records from the Huon Peninsula. *Earth and Planetary Science Letters* 138, 169-178.
- McDermott, F., Schwarcz, H.P., Harmon, R.S., Thompson, P. and Ford, D.C., 2006. Isotopes in speleothems. In: M.J. Leng (Ed.), *Isotopes in Palaeoenvironmental Research. Developments in Palaeoenvironmental Research*. Springer, Dordrecht, the Netherlands, pp. 185-225.

- McGarry, S., Bar-Matthews, M., Matthews, A., Vaks, A., Schilman, B. and Ayalon, A., 2004. Constraints on hydrological and paleotemperature variations in the Eastern Mediterranean region in the last 140 ka given by the δD values of speleothem fluid inclusions. *Quaternary Science Reviews* 23, 919-934.
- NGRIP members, 2004. High-resolution record of Northern Hemisphere climate extending into the last interglacial period. *Nature* 431, 147-151.
- O'Neil, J. R., Clayton, R. N., Mayeda, T. K., 1969. Oxygen isotope fractionation in divalent metal carbonates. *Journal of Chemical Physics* 51, 1-10.
- Oppo, D. W., Rosenthal, Y. and Linsley, B.K., 2009. 2,000-year-long temperature and hydrology reconstructions from the Indo-Pacific warm pool. *Nature* 460, 1113-1116.
- Peltier, W.R. and Fairbanks, R.G., 2006. Global glacial ice volume and Last Glacial Maximum duration from an extended Barbados sea level record. *Quaternary Science Reviews* 25, 3322-3337.
- Schwarcz, H. P., Harmon, R. S., Thompson, P. and Ford, D. C., 1976. Stable isotope studies of fluid inclusions in speleothems and their paleoclimatic significance. *Geochimica et Cosmochimica Acta* 40, 657-665.
- Siddall, M., Rohling, E.J., Almogi-Labin, A., Hemleben, C., Meischner, D., Schmelzer, I., and Smeed, D.A., 2003. Sea-level fluctuations during the last glacial cycle. *Nature* 423, 853-858.
- Stott, L., Cannariato, K., Thunell, R., Haug, G.H., Koutavas, A. and Lund, S., 2004. Decline of surface temperature and salinity in the western tropical Pacific Ocean in the Holocene epoch. *Nature* 431, 56-59.
- Thompson, L.G., Mosley-Thompson, E., Davis, M.E., Lin, P.N., Henderson, K.A., Cole, D.J., Bolzan, J.F., Liu, K.B., 1995. Late Glacial Stage and Holocene tropical ice core records from Huscarán, Peru. *Science* 269, 46-50.
- Thompson, L.G., Davis, M.E., Mosley-Thompson, E., Sowers, T.A., Henderson, K.A., Zagorodnov, V.S., Lin, P.N., Mikhalev, V.N., Campen, R.K., Bolzan, J.F., Cole-Dai, J. and Francou, B., 1998. A 25,000-year tropical climate history from Bolivian ice cores. *Science* 282, 1858-1864.
- van Breukelen, M. R., Vonhof, H. B., Hellstrom, J. C., Wester, W.C.G. and Kroon, D., 2008. Fossil dripwater in stalagmites reveals Holocene temperature and rainfall variation in Amazonia. *Earth and Planetary Science Letters* 275, 54-60.

- Vinther, B. M., Buchardt, S. L., Clausen, H. B., Dahl-Jensen, D., Johnsen, S. J., Fisher, D. A., Koerner, R. M., Raynaud, D., Lipenkov, V., Andersen, K. K., Blunier, T., Rasmussen, S. O., Steffensen, J. P. and Svensson, A. M., 2009. Holocene thinning of the Greenland ice sheet. *Nature* 461, 385-388.
- Visser, K., Thunell, R. and Stott, L., 2003. Magnitude and timing of temperature change in the Indo-Pacific warm pool during deglaciation. *Nature* 421, 152-155.
- Vonhof, H.B., van Breukelen, M.R., Postma, O., Rowe, P.J., Atkinson, T.C. and Kroon, D., 2006. A continuous-flow crushing device for on-line delta H-2 analysis of fluid inclusion water in speleothems. *Rapid Communications in Mass Spectrometry* 20, 2553-2558.
- Vonhof, H.B., Atkinson, T.C., van Breukelen, M.R., Postma, O., 2007. Fluid inclusion hydrogen and oxygen isotope analyses using the "Amsterdam Device": a progress report. *Geophysical Research Abstracts* 9, 05702.
- Wang, Y.J., Cheng, H., Edwards, R.L., He, Y.Q., Kong, X.G., An, Z.S., Wu, J.Y., Kelly, M.J., Dykoski, C.A. and Li, X.D., 2005. The Holocene Asian monsoon: Links to solar changes and North Atlantic climate. *Science* 308, 854-857.
- Yu, K.F., Zhao, J.X., Shi, Q., Chen, T.G., Wang, P.X., Collerson, K.D. and Liu, T.S., 2006. U-series dating of dead Porites corals in the South China sea: Evidence for episodic coral mortality over the past two centuries. *Quaternary Geochronology* 1, 129-141.
- Zhang, R., Schwarcz, H. P., Ford, D.C., Schroeder, F.S. and Bédows, P.A., 2008. An absolute paleotemperature record from 10 to 6 ka inferred from fluid inclusion D/H ratios of a stalagmite from Vancouver Island, British Columbia, Canada. *Geochimica et Cosmochimica Acta* 72, 1014-1026.

4 Evidence for Holocene changes in Australian-Indonesian monsoon rainfall from stalagmite trace element and stable isotope ratios

Abstract

Trace element and stable isotope ratios from an active stalagmite (LR06-B1) recovered from Liang Luar Cave on the island of Flores (eastern Indonesia), are used to reconstruct the position of the austral summer inter-tropical convergence zone and Australian-Indonesian summer monsoon variability during the Holocene. Uranium-series dating of the stalagmite shows that it commenced growth at 12,640 years ago, with hiatuses spanning 8,560 to 6,420 and 3,670 to 2,780 years ago. Stalagmite Mg/Ca and Sr/Ca ratios correlate significantly with one another, and with $\delta^{18}\text{O}$ and $\delta^{13}\text{C}$, throughout the record. This suggests that the Mg/Ca and Sr/Ca ratios are dominated by prior calcite precipitation, a process whereby degassing in the vadose zone during periods of low recharge causes deposition of calcite and disproportionate loss of Ca^{2+} ions (relative to Mg^{2+} and Sr^{2+}) 'upstream' of the stalagmite. The degree of initial $^{234}\text{U}/^{238}\text{U}$ disequilibrium also appears to have been controlled by recharge to the overlying aquifer. Together with the Mg/Ca, Sr/Ca, and $\delta^{18}\text{O}$ values, the initial uranium isotope activity ratios ($[^{234}\text{U}/^{238}\text{U}]_i$) imply a generally drier early Holocene, coincident with a lower sea level and lower Southern Hemisphere summer insolation.

Comparison of speleothem $\delta^{18}\text{O}$ time-series from Flores and Borneo shows that they vary in unison for much of the Holocene. However, there is a significant decrease in the Borneo $\delta^{18}\text{O}$ record ~6,000 to 4,000 years ago that does not occur in the Flores record. This anomaly may be related to a change in the Australian-Indonesian summer monsoon circulation in response to a protracted positive phase of the Indian Ocean Dipole. Under this scenario, stronger upwelling off of western Indonesia would, based on present-day effects, result in reduced summer convective activity over Flores and a subsequent northward shift of the intertropical convergence zone.

4.1 Introduction and background

Rainfall in eastern Indonesia is largely controlled by the strength of the Australian-Indonesian Summer Monsoon (AISM), which is one of the largest monsoon systems on Earth. The AISM impacts most significantly on southeast Asia, a region of rapid population growth and escalating resource exploitation. It is therefore important that we gain a clearer understanding of the parameters that control variations in AISM intensity if we are to accurately predict future changes to this populous region under conditions of future greenhouse warming.

AISM variability over Milankovitch time scales is thought to be broadly paced by the growth and decay of ice-sheets (Kershaw et al., 2003) and associated orbital forcing related to Earth's axial tilt and precession (Wyrwoll et al., 2007). It has been postulated that the AISM was generally strongest during warm phases and weakest during cool phases of the Late Quaternary (Kershaw, 1986; Kershaw and Nanson, 1993). For example, evidence of monsoon variability from low resolution lake-level records suggests that the AISM activity was reduced during the last glacial maximum (LGM), then experienced a marked strengthening during late glacial-early Holocene times (Magee et al., 2004; Wyrwoll and Miller, 2001).

While records of broader-scale changes in AISM behaviour already exist, finer-scale fluctuations in the monsoon are yet to be fully explored. This is because coral (e.g. Abram et al., 2007), lake (Magee et al., 2004) and deep-sea sediment records (e.g. Stott et al., 2004) have hitherto provided only fragmentary or low resolution information on past climate variability in the region. This study aims to fill this knowledge gap by assembling a detailed record of AISM dynamics during the Holocene based on a suite of climate proxies from an Indonesian speleothem, and exploring the possible teleconnections between the AISM region and the higher latitudes of the Northern Hemisphere.

In recent years, speleothems have emerged as an important source for reconstructing past climate changes over a variety of time scales (e.g. Burns et al., 2002; Cruz et al., 2005). Stable isotope ratios ($\delta^{18}\text{O}$ and $\delta^{13}\text{C}$) have been widely used as proxies for palaeorainfall (e.g. Burns et al., 1998; Drysdale et al., 2005; Wang et al., 2005), and less commonly as a proxy for palaeotemperature (e.g. Gascoyne, 1992; Williams et al., 2005). By contrast, the use of speleothem trace element ratios (e.g. Mg/Ca and Sr/Ca) as palaeoclimate indicators has not been explored as extensively. Most studies on the trace element composition of speleothems have focused on annual to decadal time scales over the late Holocene (e.g. Borsato et al., 2007; Kuczumow et al., 2003, 2005; Treble et al., 2003). Here, the processes behind the

incorporation of trace elements into speleothem calcite are relatively well understood, particularly when coupled with modern drip-water surveys and detailed microstratigraphy (e.g. Borsato et al., 2007; Fairchild et al., 2001; Frisia et al., 2005; Johnson et al., 2006; Treble et al., 2003). Few studies, however, have documented trace element changes over longer time scales (e.g. centennial to millennial scale, glacial-interglacial scale) (Cruz et al., 2007; Drysdale et al., 2006; Goede and Vogel, 1994; Li et al., 2005; Veyheiden et al., 2000), even though they are capable of providing supporting data for interpretation of stable isotope records (Cruz et al. 2007; Drysdale et al. 2006).

The trace element geochemistry of speleothems has become increasingly important as a palaeoclimate proxy due to its ability to record high-resolution changes in environmental (in particular hydrological) processes (Fairchild & Treble, 2009). Trace elements (such as Mg, Sr, Ba, U, and P) may be incorporated into speleothems via the calcite lattice, extra-lattice sites (Borsato et al., 2007) or even as co-precipitated micro-phases (Mason et al., 2007). In the case of Mg and Sr, it is believed that these elements are mostly incorporated into the crystal structure where they substitute for Ca in the lattice. The degree to which Mg and Sr concentrations are present in the calcite phase relative to that of the coexisting parent water, is referred to as the partition coefficient (Gascoyne, 1983). This value varies with temperature, growth rate, and crystal form (Morse & Bender, 1990; Paquette and Reeder, 1990). Because Mg and Sr incorporation in speleothem calcite is well understood and mostly dictated by the theoretical partition coefficient, most studies have focused on the variability of these elements through time. While earlier studies interpreted variations in Mg/Ca and Sr/Ca as reflecting changes in temperature – given the temperature-dependency of the partition coefficient (Gascoyne, 1992; Goede, 1991) – more recent studies have emphasized the importance of palaeohydrology (Fairchild et al., 2000; Fairchild and Treble, 2009; Roberts, 1998) and growth rate (e.g. Borsato et al., 2007). This is largely due to the increased knowledge gained from experimental studies (Gabitov and Watson, 2006) and field values (Huang and Fairchild, 2001).

Most speleothem studies based in the tropics have interpreted $\delta^{18}\text{O}$ in terms of rainfall amount (e.g. Dykoski et al., 2005; Wang et al., 2005), without the support of other proxies from the same specimen [e.g. trace elements, initial uranium isotope activity ratios (i.e. $[^{234}\text{U}/^{238}\text{U}]_i$), fluorescence, petrography etc.]. In this study I shed new light on tropical climate variability by employing multiple proxies to test the interpretation of oxygen isotope variability. This record not only presents a new multi-

proxy speleothem reconstruction of Indonesian rainfall, but also gives clues as to how trace elements record environmental processes in the tropics.

4.2 Study area and modern climatology

Liang Luar is a ~2-km long cave located on the east-Indonesian island of Flores (8° 32'S, 120° 26'E; Fig. 4.1). The cave lies in the western portion of the island (Manggarai Province), and has formed in porous and permeable reef carbonates of late Miocene age. The carbonates are mantled by volcanics extruded during the Quaternary (Monk, 1997).

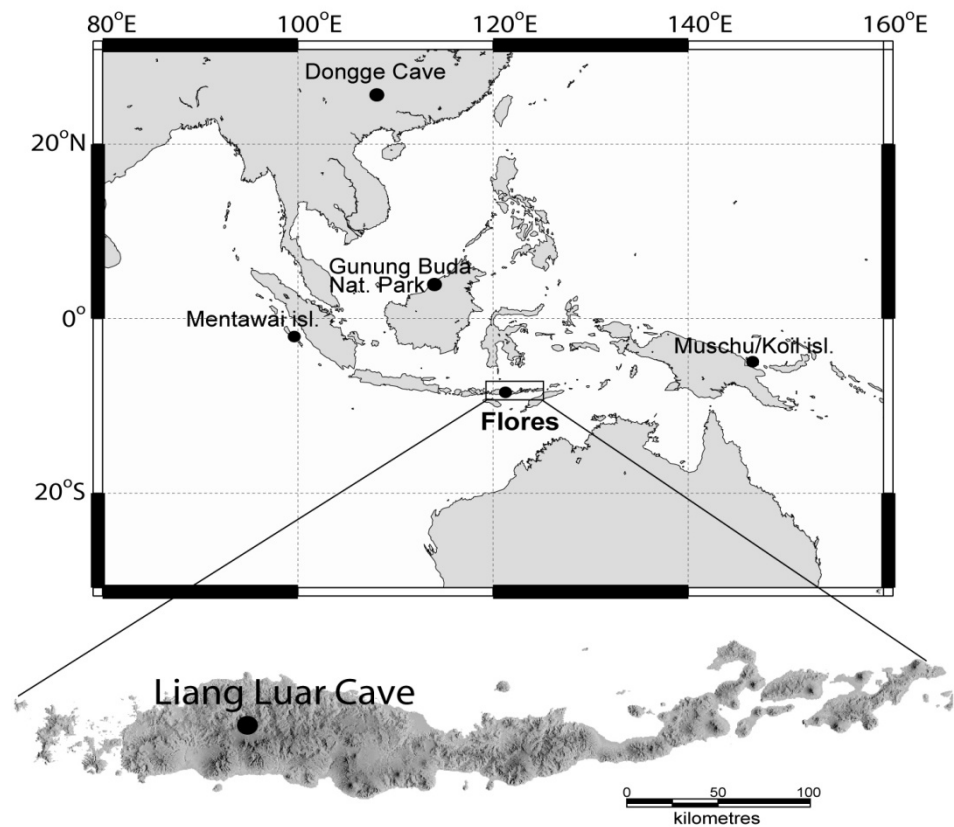


Figure 4.1 Location map of Flores and other sites mentioned in the text. Liang Luar Cave lies ~550 m above sea level on the northern side of a volcanic mountain chain.

Stalagmite LR06-B1 formed in a large chamber situated 550 m above mean sea level (a.m.s.l.) and ~800 m from the cave entrance, beneath ~30-50 m of bedrock. The chamber has a high relative humidity (close to 100%) and a temperature of ~25 °C. Because the study region lacks accurate temperature records, I used NCEP/NCAR reanalysis data to calculate average monthly temperature over the 1948 to 2005 period for the nearest grid point to the cave. This data shows that the average monthly temperature closely follows the seasonal variations in precipitation, with average summer temperatures of 27.7 °C corresponding to higher rainfall, and average winter temperatures of 25.4 °C corresponding to lower rainfall (Fig. 4.2). Thus, cave temperature closely approximates mean annual temperature at the surface.

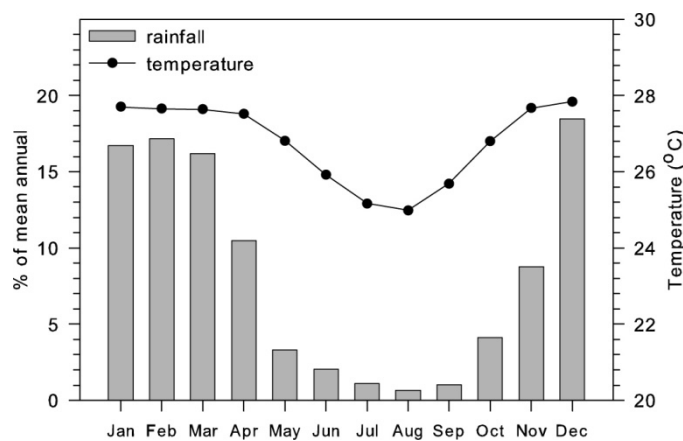


Figure 4.2 Average monthly temperature and rainfall around Liang Luar Cave. Satellite derived average rainfall data are from NASA's Tropical Rainfall Measuring Mission (http://disc.sci.gsfc.nasa.gov/data/datapool/TRMM/01_Data_Products/02_Gridded/07_Monthly_Other_Data_Source_3B_43/index.html) from 1998 to 2007 (grey bars, left y-axis) centred at 8.45° S and 120.47° E with 0.25° resolution. Average annual rainfall for the area is 1200 mm. Average monthly temperature (black line) was calculated from NCEP/NCAR reanalysis data at the same grid-point as the precipitation.

The mean annual precipitation at the cave site is 1200 mm, with ~800 mm (~69% of average annual precipitation) falling during the summer monsoon season (Dec – Mar) and ~60 mm (~5% of average annual precipitation) during the winter dry season (June – Sep) (Fig. 4.2). This seasonal pattern of rainfall on Flores is linked to the low-level northwesterly flow of moisture from the AISM and the southward progression of the intertropical convergence zone (ITCZ) during the austral summer. The overall sequence of the AISM system in the Indo-Australia region is a replacement of the low-level dry

winter easterlies with the low-level convective westerlies for the November to March period. Similar to other monsoon systems, the seasonal nature of the AISM is thought to occur as a result of the land-sea thermal contrast, which in this case is a result of the location of the off-equatorial Australian continent (Webster et al., 1998).

In addition to the above-mentioned influence of the summer land-sea thermal contrast, other forcing mechanisms, such as the incursion of warm surface-ocean waters during summer (Yano and McBride, 1998) and the occurrence of El Niño/Southern Oscillation (ENSO) (Dai and Wigley, 2000) and Indian Ocean Dipole (IOD) (Saji et al., 1999; Webster et al., 1999) events, are known to have a large impact on inter-annual tropical west-Pacific circulation patterns. Numerous studies have reported markedly reduced rainfall anomalies over Indonesia during ENSO (e.g. McBride et al., 2003; Ropelewski et al., 1987; Webster et al., 1998) and positive IOD (Saji et al., 1999; Webster et al., 1999) events. ENSO events are characterised by an eastward shift of warm Indo-Pacific sea-surface temperatures (SSTs) and the associated atmospheric Walker circulation, which reduces convection (and increases subsidence) over Indonesia and thus leads to drier conditions. Intimately linked to the ENSO phenomenon (Meyers et al., 2007; Saji et al., 1999; Webster et al., 1999), the positive phase of the IOD is characterised by enhanced easterly trade winds across the equatorial Indian Ocean which drives strong upwelling of ocean waters off of the Sumatran coastline. This upwelling can reduce SSTs in western Indonesia by more than 4 °C (Saji et al., 1999; Webster et al., 1999), which again decreases convection and thus leads to reduced rainfall over much of Indonesia. Comparison of observational stable isotope data with model simulations shows that $\delta^{18}\text{O}$ of precipitation over Indonesia is tightly coupled with the IOD mode: stronger zonal winds over the equatorial Indian Ocean (thus positive IOD mode) correspond with lighter $\delta^{18}\text{O}$ values of precipitation over much of Indonesia (Vuille et al., 2005).

The isotope values preserved in east-Indonesian stalagmites are potentially sensitive to change because the region is strategically positioned on a strong spatial gradient in the $\delta^{18}\text{O}$ of mean rainfall (Aggarwal et al., 2004). The position of this gradient reflects the southern extent of the ITCZ, and thus the balance between summer (northwesterly sourced - “Asian”) and winter (southeasterly sourced - “Pacific”) rainfall domains (Aggarwal et al., 2004). Comparisons of modern rainfall isotopes with 96-hour back-trajectory analyses starting at an elevation of 1000 m (approximate cloud base height in the tropics) (Griffiths et al., 2009) reveal that monsoon precipitation is isotopically light (amount-weighted average of -10.3‰) relative to the dry season rainfall (-3.5‰) that originates southeast of Flores. This

isotopic difference cannot be explained by source-water variations alone, which are less than 1‰ across the Indo-Pacific Warm Pool (Brown et al., 2006), and are likely a result of strong convective activity that occurs over the region during the Austral summer. This strong seasonal isotopic behaviour also illustrates that the phenomenon of the “amount effect” (Rozanski et al., 1992), whereby higher (lower) rainfall amounts correspond with lower (higher) $\delta^{18}\text{O}$ values, has a dominant influence on the $\delta^{18}\text{O}$ signal at the site.

4.3 Methods

4.3.1 Sample collection and preparation

LR06-B1 is a 125-cm tall stalagmite (Fig. 4.3) that was actively growing at the time of collection in 2006. Most of the stalagmite is contained in a single segment that broke at a point ~96 mm above the base around 1,500 years ago. The active part of the stalagmite accumulated *in situ* over the fracture surface produced from this breakage (Fig. 4.3).

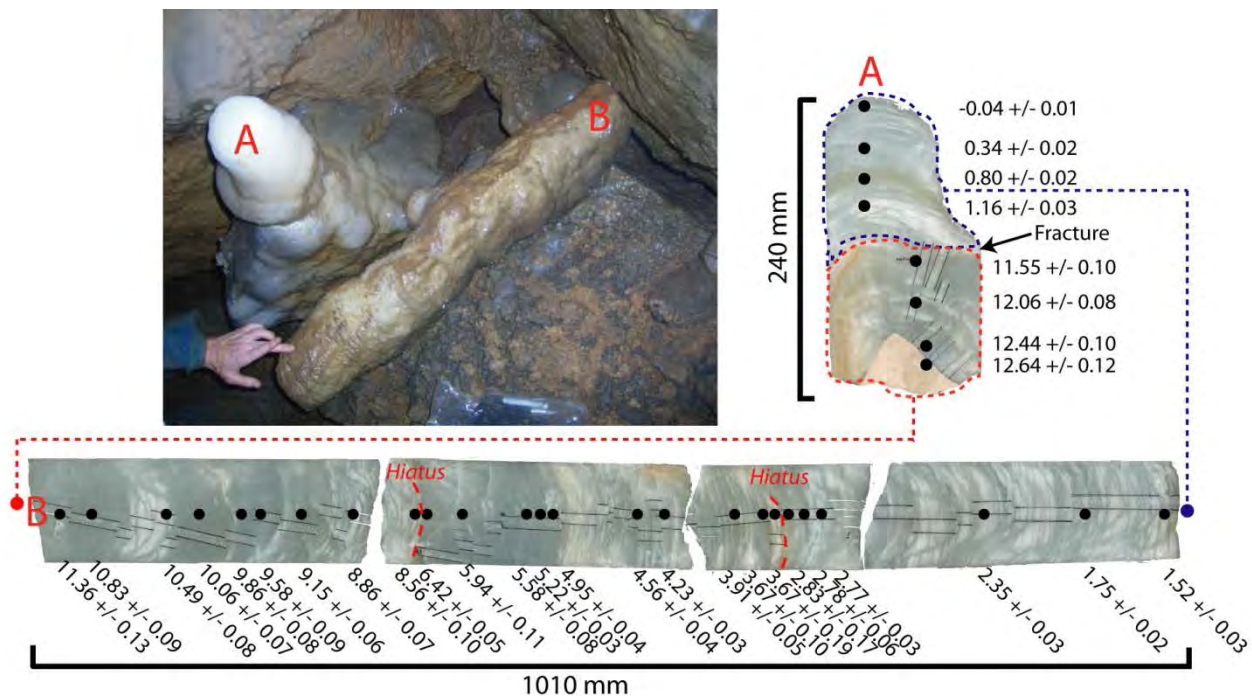


Figure 4.3 Photograph of stalagmite LR06-B1 at the time of collection in June 2006 and scanned images of separate calcite slabs. Black dots indicate the ages of the 33 uranium series dates. Section A (240 mm in length) of stalagmite LR06-B1 was *in situ* at the time of collection while section B (1010 mm in length) had broken off 96 mm from the base ~1.5 ka B.P.

Owing to its irregular external morphology, LR06-B1 was cut into four oblique segments, from each of which a slab was cut. Each slab was embedded in clear casting resin and the surfaces polished so that individual calcite layers could be identified by visual inspection. A complete sequence of overlapping thin sections was prepared along the vertical growth axis of the entire sample for petrographic analysis.

4.3.2 ^{230}Th - ^{234}U age dating

Uranium-series dating of stalagmite LR06-B1 was performed on a thermal ionization mass spectrometer (TIMS) at the Centre for Microscopy and Microanalysis, University of Queensland, and a multi-collector inductively coupled plasma mass spectrometer (MC-ICPMS) at the University of Melbourne. The TIMS analyses were conducted on pieces of calcite weighing from 200 to 700 mg. The MC-ICPMS analyses were performed on samples weighing between 12 and 40 mg. All samples were extracted from the central growth axis using an Air Line Kit air drill fitted with a dental bur. TIMS ^{230}Th dates were determined using a Fisons VG Sector 54 - 30 mass spectrometer equipped with a WARP filter and an ion-counting Daly detector. A detailed description of the analytical TIMS technique can be found in Yu et al. (2006). MC-ICPMS ^{230}Th dates were determined using a Nu Instruments Plasma mass spectrometer. Full details of the MC-ICPMS methods can be found in Hellstrom, (2003, 2006).

4.3.3 Stable isotope and trace element measurements

The stable isotope analyses (1240 samples) were conducted on ~1 mg calcite powders extracted at continuous 1 mm increments (~8-year resolution) along the vertical growth axis using a 1 mm carbide dental burr. Each speleothem slab was mounted to a stage where it was drilled using a Taig CNC micromilling lathe. Additional samples were drilled from individual growth layers to determine whether the isotopic composition of the stalagmite calcite was affected by kinetic fractionation (Hendy, 1971).

Stable isotope analysis was performed on CO_2 produced by reaction of the calcite powder with 105% phosphoric acid at 70 °C. Isotope ratios ($\delta^{18}\text{O}$ and $\delta^{13}\text{C}$) were measured using a GV2003 continuous-flow isotope ratio mass spectrometer at the University of Newcastle, Australia. The results are expressed in per mil (‰) relative to the VPDB scale using an internal working standard of Carrara Marble (New1), which was calibrated using the international standards, NBS18 and NBS19. The analytical uncertainty (2σ) of in-run measurements of Carrara Marble (New1) was 0.08‰ and 0.05‰ for $\delta^{18}\text{O}$ and $\delta^{13}\text{C}$, respectively.

Elemental concentrations of Mg, Sr, and Ca were measured on the digest produced from the stable isotope analysis. The digest was diluted to 1:7000 with Specpure concentrated HNO₃ and analysed on a Varian Liberty 4000 inductively coupled plasma atomic emission spectrometer (ICP-AES). Molar concentrations of the elements were calculated from ICP-AES intensities using four internal working standards of known concentration, and a blank, with concentrations expressed as ratios to Ca. Instrumental drift of the machine was monitored by running a multi-element standard every 10 samples. Acid blank corrections were applied to both sample and standards data prior to conversion of the data to ratios. The relative standard deviation of replicate standards of Ca, Mg, and Sr was 1.5%, 1.6%, and 2.4%, respectively.

4.4 Results

4.4.1 Chronology

The 33 corrected ²³⁰Th ages of stalagmite LR06-B1 range from -0.04 to 12.64 thousand years before present (ka; where “present” is defined as 1950 A.D.) and increase systematically with depth from the top (see Tables 2.2 and 2.3 in Chapter 2). The average U concentration throughout the stalagmite is 0.3 ppm (±0.003), excluding the unusually high value of 35 (ppm) at 1.2 ka. The analytical error of the ages (expressed as 2σ) ranges from 0.62% (0.033 ka) at 5.22 ka to 5.8% (0.167 ka) at 2.83 ka, excluding the youngest [-0.04 ± 0.01 (52%)] date.

The age model was constructed using a Bayesian-Monte Carlo approach implemented in two stages using Wavemetrics *Igor Pro* software. A full description of the technique can be found in Drysdale et al. (2005, 2007). From the depth-age plot (Fig. 4.4) it is evident that speleothem LR06-B1 was deposited in three phases. The first phase (12.64 to 8.56 ka) experienced a mean growth rate of 91 μm year⁻¹, while the second (6.42 to 3.67 ka) and third (2.78 ka to present) phases represent growth rates of 113 and 146 μm year⁻¹, respectively. The growth hiatuses (8.56 - 6.42 ka and 3.67 - 2.78 ka) are marked by a distinct abrupt change in calcite fabric and colour.

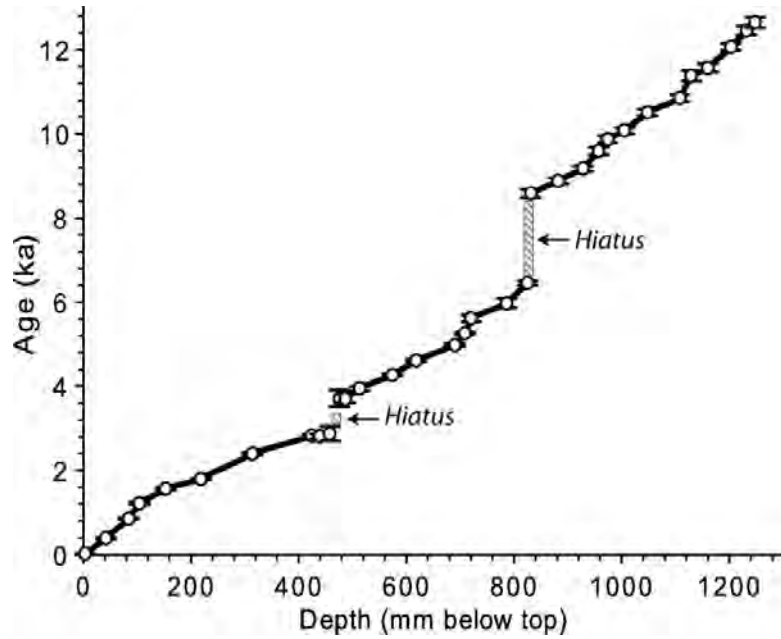


Figure 4.4 Age versus depth (mm from top) model based on 33 U-Th dates for stalagmite LR06-B1. Black open dots and attached error bars are the U-Th ages and their 95% uncertainties.

4.4.2 Stable isotopes

The $\delta^{18}\text{O}$ and $\delta^{13}\text{C}$ of LR06-B1 share similar structural features at the decadal to centennial time-scale, while displaying different trends at the millennial to multi-millennial scale. Throughout the Holocene, $\delta^{18}\text{O}$ values (Fig. 4.5a) averaged -5.8‰ and ranged from -6.9‰ to -4.0‰ , while the $\delta^{13}\text{C}$ values (Fig. 4.5b) averaged -11.7‰ and ranged from -13.4‰ to -8.6‰ . The oxygen isotopes during the early Holocene (averaged over the 10 – 12.6 ka interval) were 1.5‰ (25%) heavier than those during the mid to late Holocene (averaged over the 0 – 6 ka interval). The low-frequency trend in the $\delta^{18}\text{O}$ profile displays a decrease from the beginning of the record until ~ 2 ka, from where the values generally increase, with present-day values of $\sim -6.3\text{‰}$.

While the progression towards lighter $\delta^{18}\text{O}$ values is the dominant low-frequency signal in the record, shorter-term trends are also present. For example, the mid-Holocene is characterised by a brief increase in $\delta^{18}\text{O}$ values from ~ 6.5 to ~ 4.8 ka, followed by a decrease until ~ 2 ka. In addition, numerous abrupt shifts in the $\delta^{18}\text{O}$, spanning decades to millennia, are superimposed on the longer-term trends. For example, the Younger Dryas climate anomaly (~ 12.8 – 11.5 ka) is characterised by a shift towards lighter values, reaching a minimum at ~ 12 ka, indicative of wetter conditions during this time.

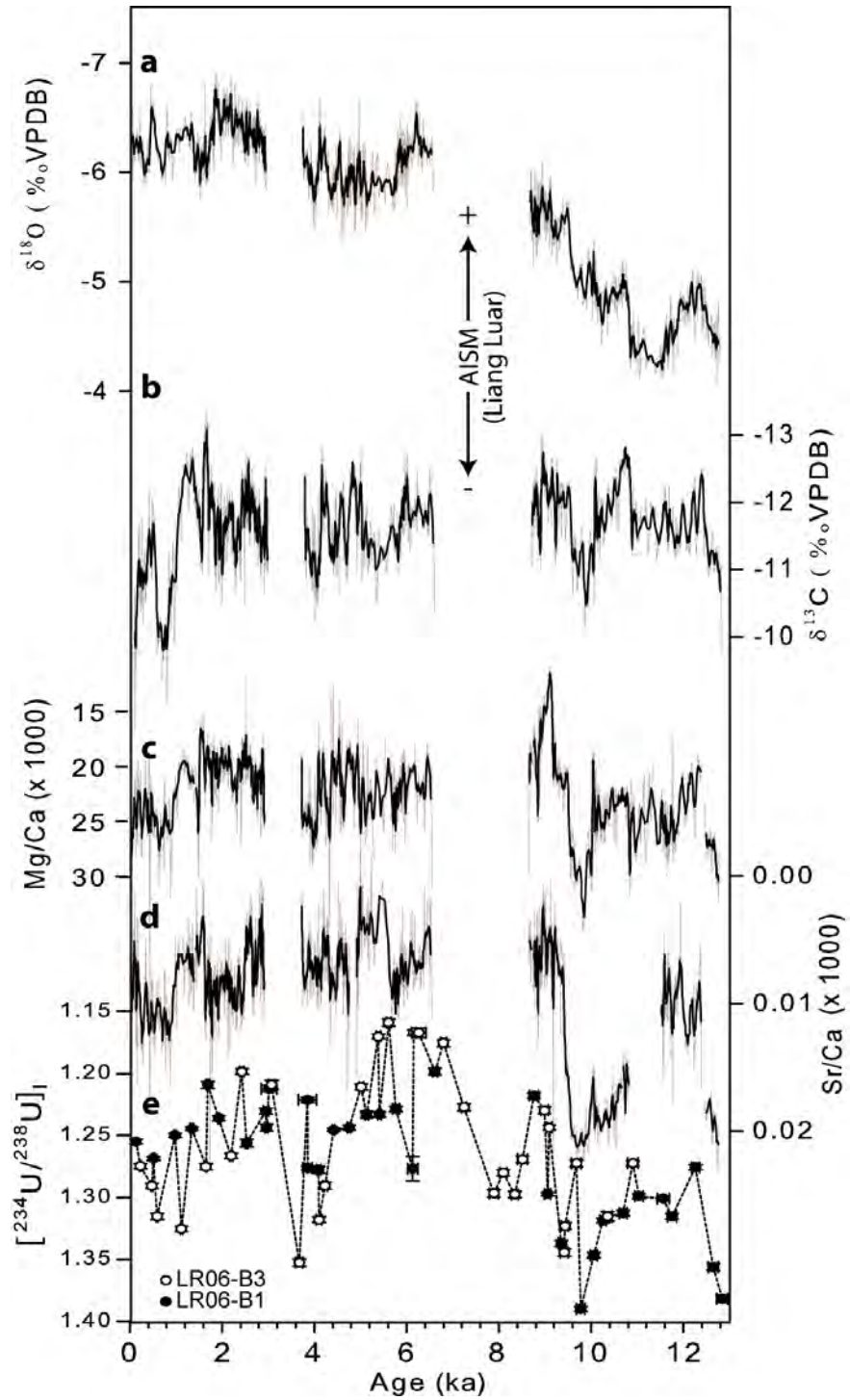


Figure 4.5 Time-series of (a) $\delta^{18}\text{O}$, (b) $\delta^{13}\text{C}$, (c) Mg/Ca , (d) Sr/Ca , and (e) $[\text{}^{234}\text{U}/\text{}^{238}\text{U}]_i$ for stalagmite LR06-B1. Additional $[\text{}^{234}\text{U}/\text{}^{238}\text{U}]_i$ values from a nearby stalagmite (LR06-B3), which were previously reported in Griffiths et al. (2009), are also shown in (e). The solid black lines represent 5-point running means.

Examination of the $\delta^{13}\text{C}$ record reveals that the dominant low-frequency trend present in the $\delta^{18}\text{O}$ profile is absent. While the $\delta^{18}\text{O}$ time-series displays a general decrease through much of the Holocene, the $\delta^{13}\text{C}$ remains relatively stable from the beginning of the record until ~ 12.2 ka (averaging 11.8‰). Noteworthy, is the sharp increase from ~ 12.2 ka to the present, with modern-day values $\sim 2\text{‰}$ higher than the Holocene average (averaged over the period 12.6 to 1.2 ka). While displaying dissimilar trends, millennial- to centennial-scale variations in the $\delta^{13}\text{C}$ (Fig. 4.5b) match those of the $\delta^{18}\text{O}$ (Fig. 4.5a). Moreover, the $\delta^{13}\text{C}$ and $\delta^{18}\text{O}$ records display a significant correlation [$r = 0.39$ with 95% confidence interval (0.27; 0.49)¹] after both records were detrended and the autocorrelation preserved (Table 4.1; Fig. 4.6a). The positive correlation suggests that similar or linked processes controlled the higher-frequency variability in both the $\delta^{18}\text{O}$ and $\delta^{13}\text{C}$ during the Holocene.

4.4.3 Trace elements and $[^{234}\text{U}/^{238}\text{U}]_i$

Time-series of the LR06-B1 Mg/Ca and Sr/Ca ratios are plotted in Fig. 4.5 and associated regressions with stable isotopes displayed in Fig. 4.6 and Table 4.1. Mg/Ca ratios ($\times 10^3$) range from 10.7 to 40.5, with an average of 22.2, while Sr/Ca ratios ($\times 10^3$) range from 0.0001 to 0.02, with an average of 0.009. Similar to the $\delta^{18}\text{O}$ record, average Mg/Ca (Fig. 4.5c) and Sr/Ca (Fig. 4.5d) values were higher (12% and 49%, respectively) during the Younger Dryas-early Holocene (12.6 to 10 ka) compared with the middle to late Holocene (6.4 ka to present). There are, however, some notable differences in the long-term variability between the $\delta^{18}\text{O}$ and trace element profiles throughout the early and late Holocene. For example, in contrast to the gradual decline in the $\delta^{18}\text{O}$ through the early to middle Holocene, the Sr/Ca (and the Mg/Ca to a lesser extent) displays a gradual decline from 12.6 to ~ 9.5 ka followed by an abrupt transition to lower mean values.

The pattern of Holocene changes in $[^{234}\text{U}/^{238}\text{U}]_i$ (Fig. 4.5e), for stalagmites LR06-B1 and LR06-B3 (see Griffiths et al., 2009), show significant structural similarities to the trace elements. The period from 12.6 to ~ 9.5 ka contains a sharp decrease in $[^{234}\text{U}/^{238}\text{U}]_i$ values from 12.6 to 11.8 ka (during the Younger Dryas climate anomaly) followed by a sharp increase from 11.8 to 9.5 ka. The $[^{234}\text{U}/^{238}\text{U}]_i$ then displays a major step change beginning ~ 9.5 ka and ending ~ 8.8 ka, with the $[^{234}\text{U}/^{238}\text{U}]_i$ values having an average of 1.32 during the early Holocene and an average value of 1.24 during the middle to late

¹Statistical significance of r -values throughout this chapter was validated using the PearsonT computer program, developed by Mudelsee (2003), which calculates accurate confidence intervals for time-series affected by serial dependence based on a non-parametric stationary bootstrap method.

Holocene. These shifts are synchronous with trace element changes, with higher (lower) $[^{234}\text{U}/^{238}\text{U}]_i$ values corresponding to higher (lower) Mg/Ca (Fig. 4.5c) and Sr/Ca (Fig. 4.5d) values.

Table 4.1 Summary of Pearson correlation coefficients (r -values) between the trace element and stable isotope ratios. All values are significant at the 95%-level.

	Mg/Ca	Sr/Ca	$\delta^{18}\text{O}$	$\delta^{13}\text{C}$
Mg/Ca	—	0.50	0.51	0.71
Sr/Ca		—	0.27	0.25
$\delta^{18}\text{O}$			—	0.39
$\delta^{13}\text{C}$				—

The Mg/Ca and Sr/Ca ratios have a significant positive correlation [$r=0.50$ with 95% confidence interval (0.39; 0.62); Fig. 4.6b] with one another and display a pattern that is coherent with the $\delta^{13}\text{C}$ values; the $\delta^{13}\text{C}$ profile has a strong positive correlation with the Mg/Ca [$r=0.71$ with 95% confidence interval (0.64; 0.76); Fig. 4.6c] and to a lesser extent with the Sr/Ca [$r=0.25$ with 95% confidence interval (0.14; 0.36); Fig. 4.6d]. Similarly, the $\delta^{18}\text{O}$ profile displays a significant positive correlation with the Mg/Ca [$r=0.51$ with 95% confidence interval (0.44; 0.61); Fig. 4.6e], and to a lesser extent with the Sr/Ca [$r=0.27$ with 95% confidence interval (0.14; 0.39); Fig. 4.6f]. These consistent relationships suggest that similar or linked forcing mechanisms dominated, at least, the higher-frequency variability of all four proxies during the Holocene. Of particular note, is the weaker correlation observed between the Sr/Ca and both the $\delta^{13}\text{C}$ and $\delta^{18}\text{O}$ (as compared with the Mg/Ca), which may be related to the added kinetic influences on Sr incorporation, such as speleothem growth rate (Huang and Fairchild, 2001).

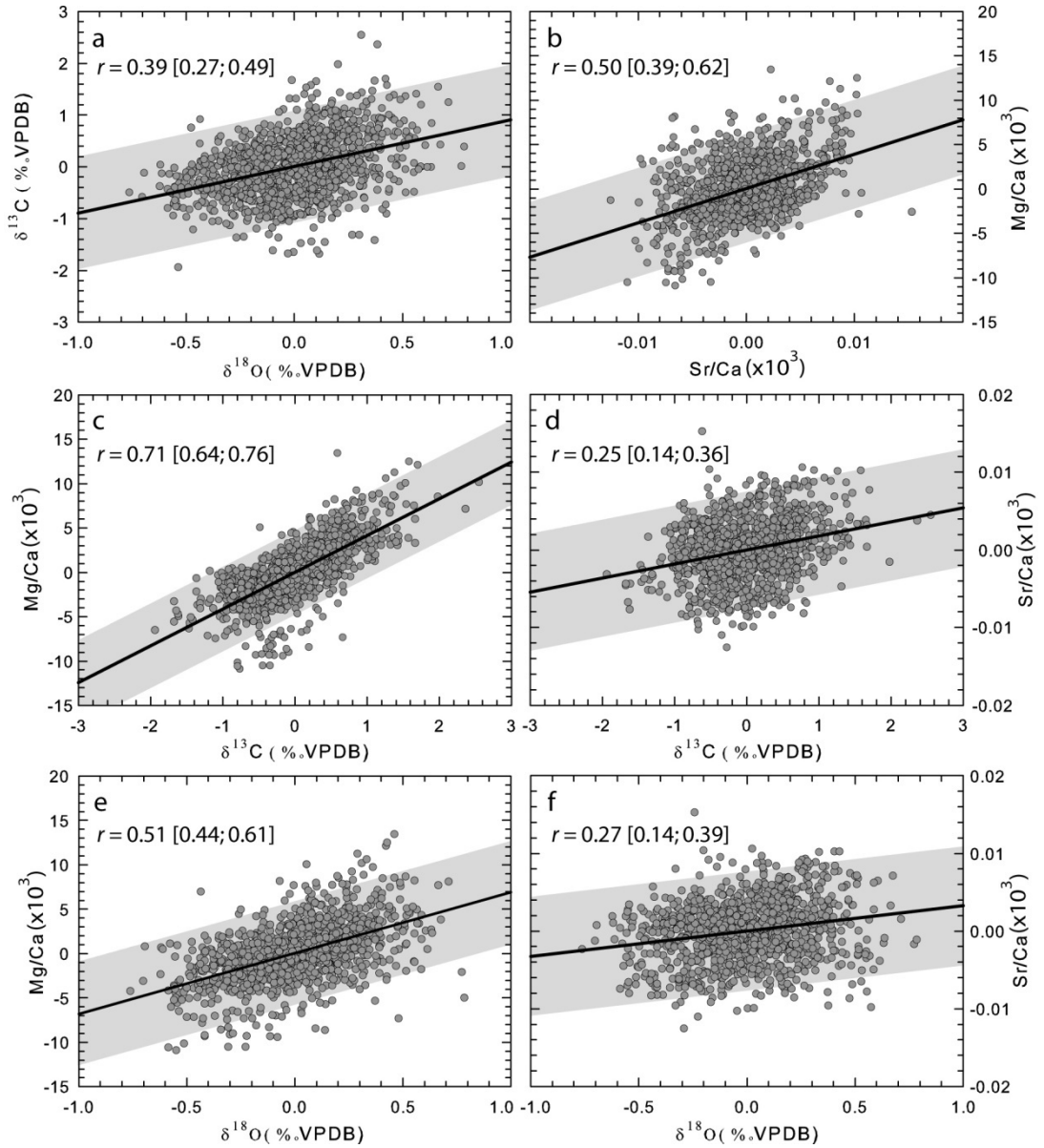


Figure 4.6 Linear regression scatter plots of (a) $\delta^{13}\text{C}$ vs. $\delta^{18}\text{O}$, (b) Mg/Ca vs. Sr/Ca , (c) Mg/Ca vs. $\delta^{13}\text{C}$, (d) Sr/Ca vs. $\delta^{13}\text{C}$, (e) Mg/Ca vs. $\delta^{18}\text{O}$, and (f) Sr/Ca vs. $\delta^{18}\text{O}$. r -values and associated confidence intervals are shown in each box. Confidence intervals were calculated using the PearsonT computer program (Mudelsee 2003). Gray shading envelopes 95% prediction intervals.

To help visualize the relative distribution of trace element and stable isotope values through the Holocene, we examined probability distribution functions (PDFs) for the $\delta^{18}\text{O}$, $\delta^{13}\text{C}$, Mg/Ca , and Sr/Ca records (Fig. 4.7). It is evident that while the $\delta^{13}\text{C}$ and Mg/Ca PDFs show a predominantly Gaussian distribution (Figs 4.7a and 4.7b), the $\delta^{18}\text{O}$ and Sr/Ca PDFs display more of a bimodal pattern (Figs 4.7c and 4.7d), possibly representing a system with two distinct states (i.e. an early and a mid-late Holocene

state); these bimodal features are also evident in the $[^{234}\text{U}/^{238}\text{U}]_i$, with values shifting from one state to another at ~ 9.5 ka (Fig. 4.5e).

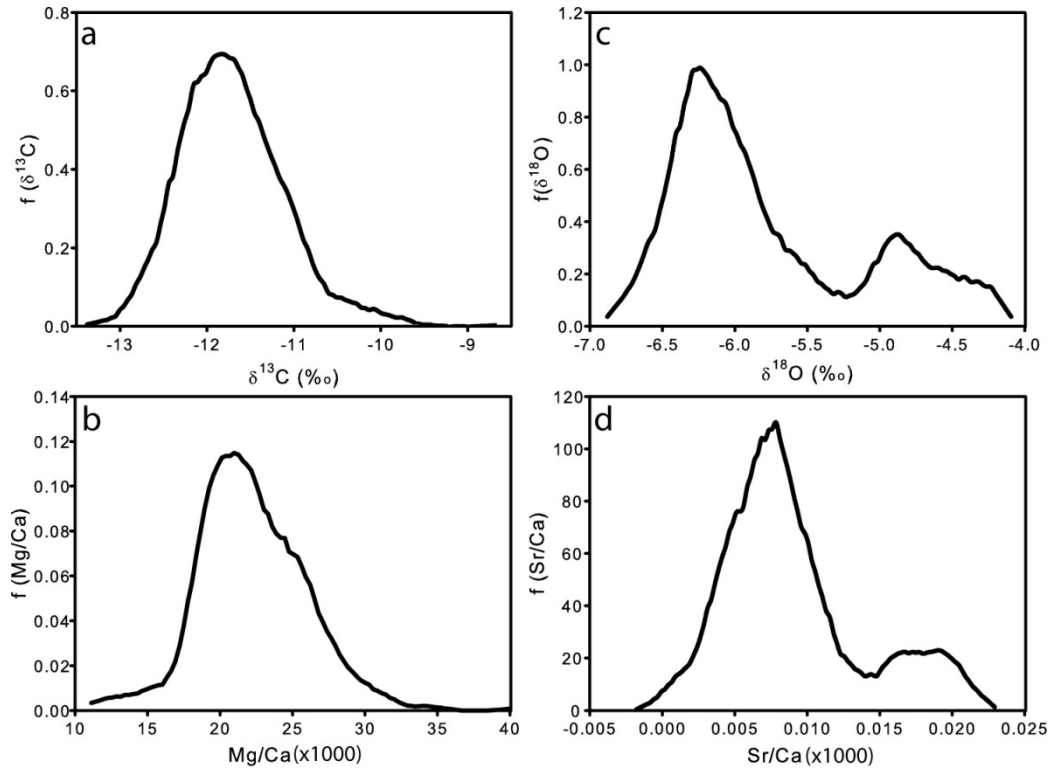


Figure 4.7 Probability distribution functions (PDFs) for (a) $\delta^{13}\text{C}$, (b) Mg/Ca , (c) $\delta^{18}\text{O}$, and (d) Sr/Ca .

4.5 Discussion

4.5.1 Environmental controls on the trace elements and $[^{234}\text{U}/^{238}\text{U}]_i$

Many recent studies have compared annual to sub-annual changes in speleothem trace element composition to changes in climate, or environmental parameters including hydrology (e.g. Borsato et al., 2007; Fairchild et al., 2001; Johnson et al., 2006; Treble et al., 2003, 2005). However, extrapolating, or up-scaling, these processes over longer time scales has proven to be more difficult (Fairchild et al., 2006). Mg/Ca and Sr/Ca in speleothems are controlled by a number of variables that probably operate at different time scales, including the composition of the parent water, cave air temperature, and growth

rates (Huang and Fairchild, 2001; Treble et al., 2003). Huang and Fairchild (2001) noted that, in addition to drip-water chemistry, the partition coefficients for Sr (D_{Sr}) and Mg (D_{Mg}) were controlled by speleothem growth rate and temperature, respectively. In terms of Mg, the temperature of Liang Luar Cave has a constant mean annual temperature (MAT) that closely resembles the external MAT throughout the year and has likely remained relatively stable throughout the Holocene, based on minimal cave palaeotemperature fluctuations reconstructed from combined calcite and fluid inclusion $\delta^{18}\text{O}$ (see previous chapter). Therefore, the Mg/Ca variations in LR06-B1 are likely to have been controlled primarily by drip-water composition changes through the Holocene. Worth noting, some of the Mg/Ca variability during the YD-Holocene transition may be explained by the $\sim 5^\circ\text{C}$ lower cave palaeotemperature. Hence, after the Mg-temperature relationship has been factored in (Gascoyne, 1983), the YD-early Holocene Mg/Ca values may have a closer resemblance to the Sr/Ca values then observed in Fig. 4.5.

The significant positive correlations observed between the Mg/Ca and Sr/Ca, and $\delta^{13}\text{C}$ values, suggests that all three proxies are being controlled by similar processes. Based on these systematic covariations, we interpret the Mg/Ca, Sr/Ca and $\delta^{13}\text{C}$ values to reflect changes in meteoric infiltration rates in the vadose zone (Fairchild et al., 2000; McDonald et al., 2004; Tooth and Fairchild, 2003), which are influenced by hydrological changes at the surface. Under drier conditions, decreased water storage and flow in the vadose zone can enhance ventilation within the karst fracture network and trigger CO_2 degassing in the roof pores and stalactite tips, which promotes calcium carbonate precipitation ‘upstream’ of the stalagmite. This phenomenon, known as ‘prior calcite precipitation’ (PCP) (Fairchild et al., 2000), is enhanced during dry phases when aerated zones become important within the aquifer, and results in higher Mg/Ca and Sr/Ca ratios in the seepage waters and higher $\delta^{13}\text{C}$ in the dissolved inorganic carbon (DIC). Because the incorporation of both Mg and Sr into calcite is influenced by partition coefficients that are much less than one, covariation of Mg and Sr is a strong indicator that PCP is the dominant mechanism (Johnson et al., 2006). Hellstrom and McCulloch (2000) argued for a residence time effect on Mg variations in a New Zealand flowstone, in part because of the absence of a relationship between Mg and Sr. Moreover, Johnson et al. (2006) noted that PCP and drip-water CO_2 degassing have a dominant influence on the Mg/Ca and Sr/Ca ratios of Chinese stalagmites, based on the strong positive relationship between these trace elements and $\delta^{13}\text{C}$.

These results strongly argue for PCP being the dominant mechanism controlling the trace elements and $\delta^{13}\text{C}$ values in stalagmite LR06-B1. Therefore, the trace element and $\delta^{13}\text{C}$ variations can be related to the degree of dewatering in the soil, epikarst and aquifer overlying the cavern, which would be directly dependent upon the local rainfall. However, this process would be less effective during periods of higher recharge because the amount of PCP is limited by the degree of ventilation in the vadose zone. In such cases, a threshold is reached where Mg/Ca is minimized because the lower end member is constrained by the bedrock Mg/Ca , DMg, and the calcite precipitation temperature (Fairchild et al., 2000). This may be one of the factors responsible for the slight trend differences in the trace elements compared with the $\delta^{18}\text{O}$ (Fig. 4.8): during periods of high recharge, a ‘floor’ is reached in the Mg/Ca where no more PCP can occur. An additional reason for the slight mismatch in the long-term trace element– $\delta^{18}\text{O}$ trends is the fact that the $\delta^{18}\text{O}$ is controlled by a greater number of factors (e.g. cave altitude, moisture trajectories, seasonal variations, vapour source regions etc.) compared with the Mg and Sr , which are primarily controlled by dissolution and re-precipitation processes within the vadose zone, and therefore local hydrology.

Another useful proxy used to infer palaeohydrological conditions in karst systems is the extent of uranium isotope disequilibrium at the time of calcite precipitation, measured as $[\text{}^{234}\text{U}/\text{}^{238}\text{U}]_i$ (Richards and Dorale, 2003). Since uranium isotopes are not thought to be fractionated by natural processes, such as calcite precipitation from seepage waters, the $[\text{}^{234}\text{U}/\text{}^{238}\text{U}]_i$ of any speleothem should reflect that of the percolation water from which it was formed (Hellstrom and McCulloch, 2000).

The uranium content of the waters can be controlled by the dissolution of limestone and the acquisition of the ^{234}U isotope in the waters by alpha recoil (Ayalon et al., 1999). If the groundwater becomes enriched in ^{234}U by this process, then residence time is an important factor, with relatively fast percolation rates (i.e. higher rainfall) causing a decrease in the $[\text{}^{234}\text{U}/\text{}^{238}\text{U}]_i$ and vice versa. Decreased $[\text{}^{234}\text{U}/\text{}^{238}\text{U}]_i$ values, for example, can be observed during periods of increased speleothem growth, which can reflect the palaeohydrology above the cave system (Plagnes et al., 2002). An alternative ^{234}U -enriching mechanism involves the preferential leaching of ^{234}U from crystal lattice sites disrupted by alpha decay. This process is related to the dissolution rate, with relatively aggressive waters resulting in lower $[\text{}^{234}\text{U}/\text{}^{238}\text{U}]_i$ values for the dissolved uranium (Hellstrom and McCulloch, 2000).

The observed higher $[\text{}^{234}\text{U}/\text{}^{238}\text{U}]_i$ values during the early Holocene (12.6 ka to ~9.5 ka) are consistent with the trace elements results, indicating reduced precipitation and dissolution rates (Fig.

4.8a). Based on this coherent relationship with the Sr/Ca and Mg/Ca values, I conclude that variations in $[^{234}\text{U}/^{238}\text{U}]_i$ are primarily influenced by groundwater hydrology, which is governed by rainfall amounts at the surface. Studies analysing $[^{234}\text{U}/^{238}\text{U}]_i$ measurements from other cave systems have shown similar climate-related variations; Ayalon et al. (1999) show a rapid fall in $[^{234}\text{U}/^{238}\text{U}]_i$, synchronous with $\delta^{18}\text{O}$, at ~17 ka from Soreq Cave (Israel), which they interpret to reflect a dramatic increase in precipitation in the eastern Mediterranean as the climate began to shift from glacial to interglacial conditions. Hellstrom and McCulloch (2000) noted a strong temporal relationship between $[^{234}\text{U}/^{238}\text{U}]_i$ and trace elements, stable isotopes and luminescence intensity from Nettlebed Cave (New Zealand), which they relate to changes in effective moisture and vegetation density from the last glacial maximum to the present.

4.5.2 Climate signal of the $\delta^{18}\text{O}$ and trace elements

There were a number of possible factors responsible for the ~2‰ decline in $\delta^{18}\text{O}$ of LR06-B1 during the Holocene (Fig. 4.8b). These include: cave air-temperature, in-cave kinetic effects (e.g. evaporation due to cave ventilation), and $\delta^{18}\text{O}$ of the source (sea-water), which is expected to control that of the precipitation. With the exception of the YD-Holocene transition, temperature effects can likely be ruled out as a dominant influence given the relative stability of cave-air palaeotemperatures during the Holocene (see Chapter 3 and Griffiths et al., 2010). In addition, I have previously demonstrated that LR06-B1 was deposited in quasi-isotopic equilibrium (see Chapter 2 and Griffiths et al., 2009), thus eliminating the possibility of kinetic fractionation being responsible for the $\delta^{18}\text{O}$ trends. Together, these lines of evidence suggest that the Holocene shift in LR06-B1 $\delta^{18}\text{O}$ (Fig. 4.8b) was dominated by variations in the $\delta^{18}\text{O}$ of the recharge rainfall.

The rainfall- $\delta^{18}\text{O}$ signal preserved in LR06-B1 represents the combined effects of ocean-source fluctuations (related to the global ice-volume effect) and mean changes in the isotopic fractionation of moist air between the site of evaporation and the cave site. However, only ~0.5‰ (25%) of this shift can be attributed to a decrease in global ice-volume (Siddall et al., 2003), which decreased the $\delta^{18}\text{O}$ of the seawater and hence AISM rainfall. Therefore, the significant decrease in the $\delta^{18}\text{O}$ of AISM precipitation during air-mass transport must account for the remaining ~75% (~1.5‰) of the early-middle Holocene isotopic shift observed in LR06-B1.

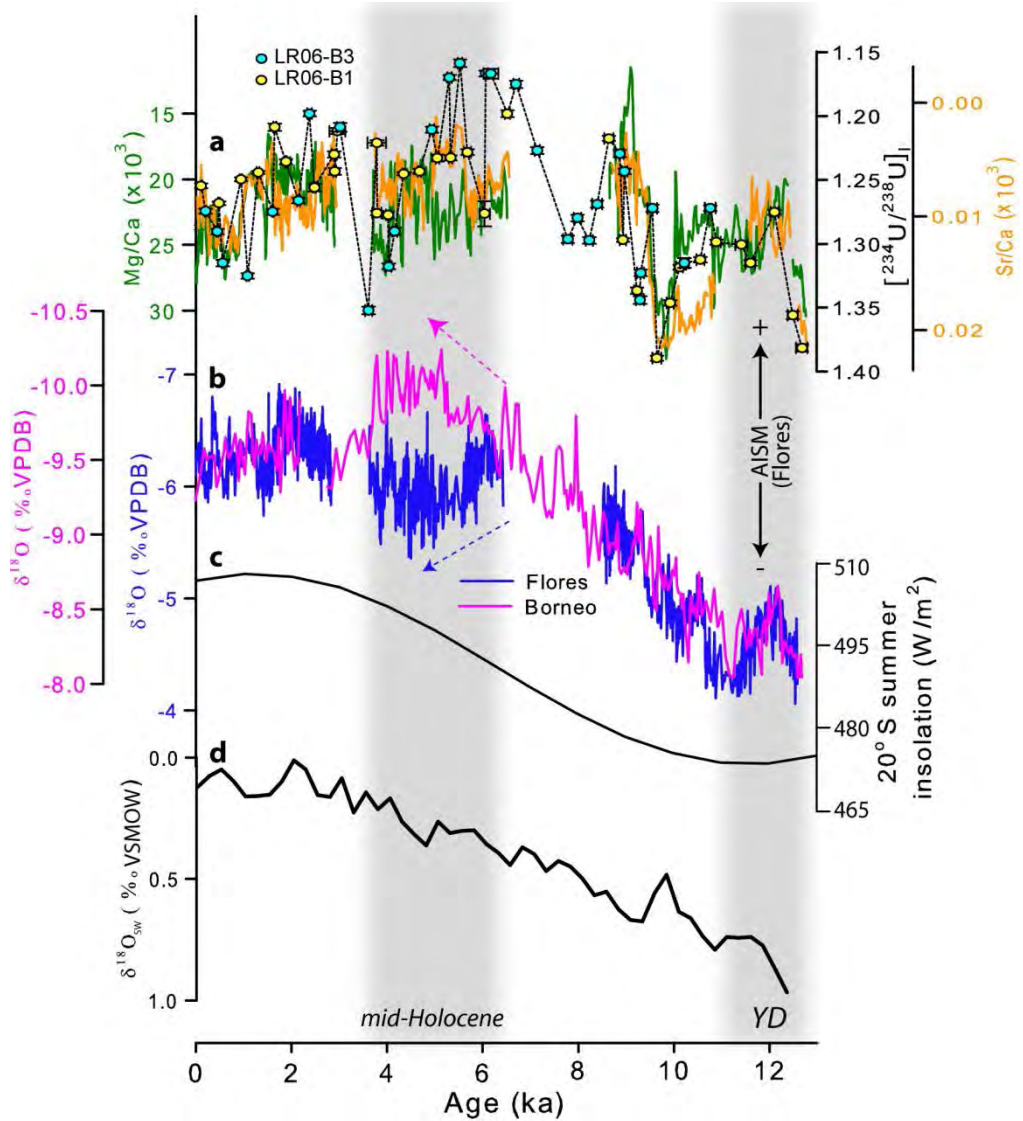


Figure 4.8 (a) Time-series of the LR06-B1 Mg/Ca (green), Sr/Ca (orange) and $[^{234}\text{U}/^{238}\text{U}]_I$ (yellow circles) records. Also shown are the $[^{234}\text{U}/^{238}\text{U}]_I$ values for a nearby stalagmite (LR06-B3) (cyan circles), which were previously reported in Griffiths et al. (2009). (b) Comparison of stalagmite $\delta^{18}\text{O}$ records from Liang Luar Cave (Flores) and Gunung Buda National Park (northern Borneo; Partin et al., 2007). There is a significant correlation between the two records [$r=0.50$ with 95% confidence interval (0.40; 0.58)]. The colour-coded arrows highlight the opposing $\delta^{18}\text{O}$ trends during the mid-Holocene interval from 4 to 6 ka. (c) Austral summer insolation at 20°S . (d) Average $\delta^{18}\text{O}_{\text{sw}}$ time-series for the IPWP reconstructed from stacked planktonic foraminifer $\delta^{18}\text{O}$ records (Stott et al., 2004). Grey shading highlights the timing of the Younger-Dryas climate anomaly ($\sim 12.8\text{--}11.5\text{ ka}$) and the mid-Holocene interval from 4 to 6 ka.

In Griffiths et al. (2009), we concluded that the precipitation $\delta^{18}\text{O}$ on Flores is likely a function of summer monsoon intensity, whereby higher (lower) rainfall amounts correspond with lower (higher) $\delta^{18}\text{O}$ values in the tropics. This $\delta^{18}\text{O}$ interpretation can now be confirmed by the strong coherence with the Mg/Ca ratios (and to a lesser extent the Sr/Ca ratios), which aforementioned reflect changes in the

degree of ventilation in the vadose zone controlled by the rate of meteoric water movement down through the soil-bedrock profile. Taken together, the results display a mode of east-Indonesian rainfall variability that is characterised by an overall reduction in AISM precipitation during the early Holocene (relative to modern), followed by a relatively rapid resumption during the period 9-10 ka. This pattern of monsoonal behaviour is interpreted to reflect a southward migration and/or intensification of the austral summer (AS)-ITCZ during the early-Holocene in response to the deglacial inundation of the Sunda Shelf and its inherent impact on source moisture availability for the monsoon (Griffiths et al., 2009); this abrupt monsoon shift is discussed in detail in the next chapter. Compounding this sea-level influence may have been a lower summer insolation during the early Holocene (Fig. 4.8c), which controlled continental heating over northern Australia and hence the thermal gradient between land and ocean; this land-sea thermal contrast has a major influence on modern monsoon activity.

Stott et al. (2004) noted findings similar to ours through their analysis of IWPW marine sediments, where the $\delta^{18}\text{O}$ of the planktonic foraminifer *Globigerinoides ruber* displayed a trend towards lower $\delta^{18}\text{O}$ values through the Holocene (Fig. 4.8d), which was interpreted to reflect variations in the tropical hydrological cycle associated with changes in the meridional position of the ITCZ. By contrast, lake-level reconstructions from interior Australia (e.g. Magee et al., 2004; Wyrwoll and Miller, 2001) indicate a rapid resumption of the monsoon as early as ~14 ka (more than 4-5 ka earlier than indicated by our speleothem record). Possible explanations for this apparent mismatch include: chronological constraints, differences in resolution, different climatic responses of lake versus cave systems, and site-specific differences in rainfall patterns over Indonesia relative to interior Australia during the early Holocene.

4.5.3 Centennial- to millennial-scale perturbations in the AISM-ITCZ

Superimposed upon the Holocene $\delta^{18}\text{O}$ and trace element profiles are a number of excursions that last from decades to millennia. Of these, the Younger Dryas (YD) climate anomaly appears to have been one of the more prominent. This event, which was previously reported in the $\delta^{18}\text{O}$ record of LR06-B1 (Griffiths et al., 2009; Fig. 4.8b), is characterised by a marked shift to lower trace element and $[\text{}^{234}\text{U}/\text{}^{238}\text{U}]_l$ ratios (Fig. 4.8a). In line with our previous interpretation, these results argue for an enhanced AISM during the YD event due to a periodic southward displacement of the AS-ITCZ. The common mechanism to explain this shift has been tied to the North Atlantic, where a periodic shutdown of the

Atlantic meridional overturning circulation [due to the large freshwater input from the drainage of proglacial lakes (McManus et al., 2004)], highly favoured the southward displacement of the ITCZ in the tropical Pacific (Zhang and Delworth, 2005). This finding is consistent with numerous monsoon records from the Asian (Dykoski et al., 2005; Fleitmann et al., 2003) and South-American monsoon domains (Cruz et al., 2005; Wang et al., 2006), which together demonstrate lower rainfall patterns to the north are mirrored by higher rainfall patterns to the south.

A major shortcoming in the understanding of tropical west-Pacific palaeoclimatology is the temporal and spatial homogeneity of centennial- to millennial-scale oscillations in the AISM-ITCZ throughout the monsoon affected region. This is largely because we currently lack sufficient accurately-dateable terrestrial records, of comparable resolution, from the northern and southern sectors of the AISM domain. I attempt to reduce this knowledge gap by comparing speleothem $\delta^{18}\text{O}$ profiles between Flores and Gunung Buda National Park, northern Borneo (Partin et al., 2007) (Figs 4.1 and 4.8b), with the overall intention of examining any regional fluctuations in the positioning and/or intensity of the AISM-ITCZ through the Holocene. Any common trends between the speleothem records should be due to orbital-scale changes which include both variations in the $\delta^{18}\text{O}$ of the ocean source and changes in the altitude of condensation with consequent variations in vapour/water isotope fractionation. Any differences between the $\delta^{18}\text{O}$ trends should then contain information about rainfall anomalies that occurred across a meridional transect in the western Pacific. Comparison of the $\delta^{18}\text{O}$ records between Flores and Borneo shows that they are highly covariant [$r=0.50$ with 95% confidence interval (0.40; 0.58); Fig. 4.8b] and share common trends through much of the Holocene. A notable exception to this, however, is the difference in $\delta^{18}\text{O}$ trends through the mid-Holocene interval between 4 and 6 ka: the decreasing Borneo trend from ~6-5 ka is mirrored by an increasing $\delta^{18}\text{O}$ trend (also evident in the Mg/Ca albeit not as pronounced) on Flores, while the opposite is true for the period 5-4 ka. While several factors may explain this discrepancy, the strong coherence through the remainder of the record argues for common or linked processes controlling $\delta^{18}\text{O}$ at both sites. Thus, other things being equal, this mid-Holocene anomaly most likely represents a real climatic perturbation, which had differential effects on the two regions.

A single coherent explanation for this mid-Holocene $\delta^{18}\text{O}$ anomaly [characterised by drier conditions over northern Australia (Turney et al., 2004) and wetter conditions over northern Borneo (Partin et al., 2007)] is a change in the zonal circulation over the region affected by the IOD and

associated contraction (or slight relocation) of the IPWP. $\delta^{18}\text{O}$ values of shallow marine foraminifera from the western tropical Pacific support an eastward relocation of atmospheric convection or a possible reduction in the size of the IPWP during the 4-6 ka interval. Moreover, they indicate a transition from predominantly “La Nina” conditions of the early Holocene to an intensification of ENSO activity starting at ~6 ka (Briker et al., 2007). Hence, a more easterly location of the IPWP would alter the centre of atmospheric convection and thus reduce the depth of the thermocline, resulting in a general decrease in temperature and precipitation in Indonesia.

Further evidence to support this interpretation involves the analysis of IPWP fossil corals from the Mentawai and Muschu/Koil Islands (Fig. 4.1), which implicate an approximate $1.2\text{ }^{\circ}\text{C} \pm 0.3\text{ }^{\circ}\text{C}$ cooling of the IPWP during the ~4 - 6 ka interval (Abram et al., 2009; Fig. 4.9c). Abram et al. (2009) inferred this mid-Holocene cooling to reflect a contraction of the southeast and southwest margins of the IPWP, which was linked to a more northerly displaced ITCZ and associated enhancement of the Asian summer monsoon (ASM) (e.g. Wang et al., 2005; Fig. 4.9a). Moreover, this mid-Holocene IPWP contraction was punctuated by an abrupt shift to warmer temperatures at ~6.6 - 6.3 ka and ~4.3 ka, which coincides with periods of stronger ASM intensity (Fig. 4.9b) and weaker Asian summer monsoon intensity (Fig. 4.9a) as a result of a southerly displaced ITCZ. Abram et al. (2009) noted a link between this mid-Holocene cooling of the IPWP and associated northward migration of the ITCZ, and the zonal configuration of the ocean-atmosphere across the Indian Ocean. Through the comparison of their coral records with $\delta^{18}\text{O}$ values from ice cores on Mt. Kilimanjaro (Thompson et al., 2002; Fig. 4.9d), they inferred the mid-Holocene to have a more positive Indian Ocean Dipole (IOD)-like mean state across the tropical Indian Ocean, which reduced precipitation over Flores and/or resulted in a change in seasonal atmospheric-circulation patterns (Fig. 4.9b). Modelling results have shown that a stronger, insolation-driven Asian monsoon (as was the case during the mid-Holocene) produces Indian Ocean SST anomalies that characterise a positive IOD mode (Abram et al., 2007). This suggests that a strengthened Asian monsoon may have been a precursor for the mid-Holocene positive-like mean IOD state, which in turn resulted in a reduction in monsoonal rainfall over east Indonesia due to a more northerly displaced ITCZ.

The ocean-atmosphere connections highlighted above emphasize the strong coupling of the AISM system with IPWP SSTs since the mid-Holocene. It is these SST variations that may have been a dominant driver of millennial- to centennial-scale changes in the AISM.

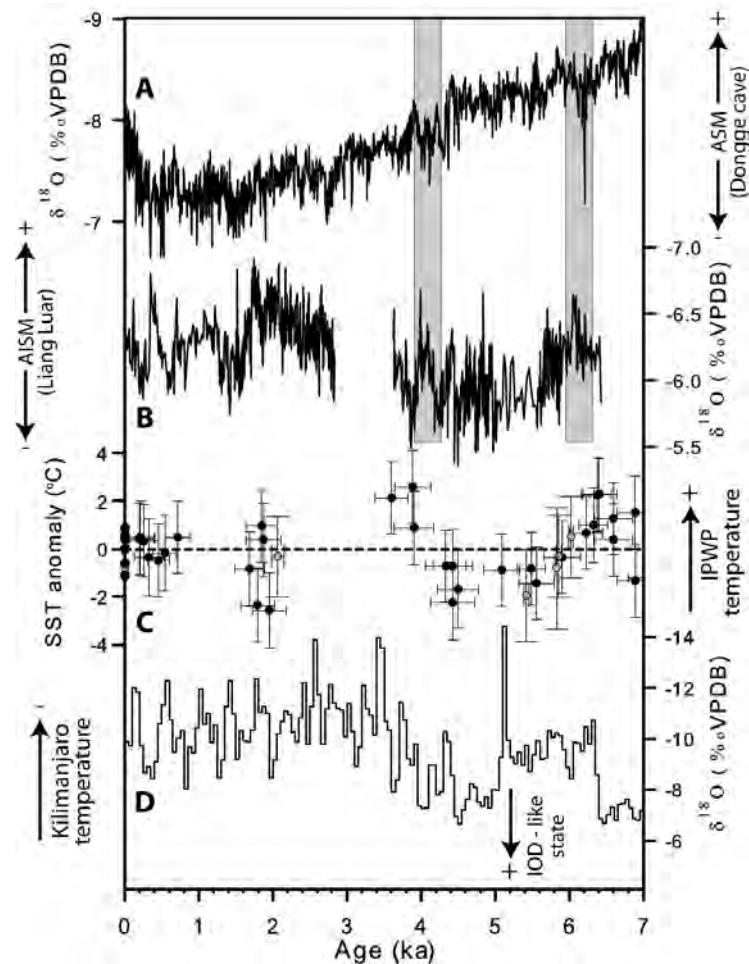


Figure 4.9 Comparison of Holocene palaeoclimate records from China, Indonesia, and east Africa. (a) Speleothem $\delta^{18}\text{O}$ records from Dongge cave, China (Wang et al., 2005), and (b) Liang Luar, Flores. (c) SST anomalies reconstructed from corals taken from the Mentawai (black circles) and Muschu/Koilo (grey circles) islands (Abram et al., 2009; Fig. 4.1). The grey bars highlight increases in IPWP SSTs and the ASM coincident (within dating error) with decreases in the ASM at ~6.3 and ~4.2 ka. This indicates a southward displacement of the ITCZ. (d) An ice-core $\delta^{18}\text{O}$ record from Mt. Kilimanjaro (Thompson et al., 2002) shows air temperature trends in east Africa. Periods of cooler (warmer) air temperatures in east Africa correspond with higher (lower) IPWP SSTs and a stronger (weaker) ASM, indicating that the IOD may have been responsible for much of the Holocene variability in the ASM.

4.6 Conclusions

Here I provide a precisely dated, high-resolution multi-proxy record of ASM variability over the Holocene. The close correspondence between Mg/Ca, Sr/Ca and $\delta^{13}\text{C}$ strongly suggests that the dominant mechanism controlling the trace element variability in stalagmite L R06-B1 is degassing associated with prior calcite precipitation. This mechanism also helps explain the relationship between the trace elements and $\delta^{18}\text{O}$, where higher Sr/Ca and Mg/Ca values correspond with higher $\delta^{18}\text{O}$ values. Thus, the Mg/Ca and Sr/Ca values reflect variations in the hydrology above the cave system in response to

changes in the intensity of the AISM during the Holocene. This trace elemental and isotopic signal, along with changes in the $[^{234}\text{U}/^{238}\text{U}]_i$ profile, confirms previous findings that the early Holocene was somewhat drier than the late Holocene in eastern Indonesia (Griffiths et al., 2009).

Comparison of stalagmite $\delta^{18}\text{O}$ records between Flores and northern Borneo (Partin et al., 2007) show that they are strongly covariant through much of the Holocene. However, there is a slight mismatch between the two records at ~ 6 to 4 ka, suggestive of a regional perturbation in ocean-atmosphere circulation patterns during this time. This interpretation finds qualitative support from the positive coherence of Flores $\delta^{18}\text{O}$ with IWPW coral SST records (Abram et al., 2009), and the antiphased relationship with Mt. Kilimanjaro ice-core records from east Africa (Thompson et al., 2002). Together, the results argue for a mid-Holocene IPWP climate pattern that is characterised by more positive IOD-like conditions and an associated northward shift of the ITCZ. These findings highlight the complex nature of the AISM system, with the indication that it does not behave in a simple linear fashion to southern summer insolation and sea-level change, but instead is dominated by a combination of internal and external forcing mechanisms operating at different spatial and temporal scales.

4.7 References

- Abram, N.J., Gagan, M.K., McCulloch, M.T., Chappell, J., Hantoro, W.S., 2003. Coral reef death during the 1997 Indian Ocean Dipole linked to Indonesian wildfires. *Science* 301, 952–955.
- Abram, N.J., Gagan, M.K., Liu, Z.Y., Hantoro, W.S., McCulloch, M.T. and Suwargadi, B.W., 2007. Seasonal characteristics of the Indian Ocean Dipole during the Holocene epoch. *Nature* 445, 299–302.
- Abram, N.J., Gagan, M.K., Cole, J.E., Hantoro, W.S., Mudelsee, M., 2008. Recent intensification of tropical climate variability in the Indian Ocean. *Nature Geoscience* 1, 849–853.
- Abram, N.J., McGregor, H.V., Gagan, M.K., Hantoro, W.S., Suwargadi, B.W., 2009. Oscillations in the southern extent of the Indo-Pacific Warm Pool during the mid-Holocene. *Quaternary Science Reviews* doi:10.1016/j.quascirev.2009.07.006.
- Aggarwal, P.K., Frohlich, K., Kulkarni, K.M. and Gourecy, L.L., 2004. Stable isotope evidence for moisture sources in the Asian summer monsoon under present and past climate regimes. *Geophysical Research Letters* 31, L08203, doi: 10.1029/2004gl019911.
- Ayalon, A., Bar-Matthews, M. and Kaufman, A., 1999. Petrography, strontium, barium and uranium concentrations, and strontium and uranium isotope ratios in speleothems as paleoclimatic proxies: Soreq Cave, Israel. *The Holocene* 9, 715–722.
- Borsato, A., Frisia, S., Fairchild, I.J., Somogyi, A. and Susini, J., 2007. Trace element distribution in annual stalagmite laminae mapped by micrometer-resolution X-ray fluorescence: Implications for incorporation of environmentally significant species. *Geochimica et Cosmochimica Acta* 71, 1494–1512.
- Brijker, J.M., Jung, S.J.A., Ganssen, G.M., Bickert, T. and Kroon, D., 2007. ENSO related decadal scale climate variability from the Indo-Pacific Warm Pool. *Earth and Planetary Science Letters* 253, 67–82.
- Brown, J., Simmonds, I. and Noone, D., 2006. Modeling delta O-18 in tropical precipitation and the surface ocean for present-day climate. *Journal of Geophysical Research-Atmospheres* 111, D05105, doi: 10.1029/2004jd005611.
- Burns, S.J., Matter, A., Frank, N. and Mangini, A., 1998. Speleothem-based paleoclimate record from northern Oman. *Geology* 26, 499–502.

- Burns, S.J., Fleitmann, D., Mudelsee, M., Neff, U., Matter, A. and Mangini, A., 2002. A 780-year annually resolved record of Indian Ocean monsoon precipitation from a speleothem from south Oman. *Journal of Geophysical Research-Atmospheres* 107 (D20), 4434, doi:10.1029/2001JD001281.
- Cruz, F.W., Burns, S.J., Karmann, I., Sharp, W.D., Vuille, M., Cardoso, A.O., Ferrari, J.A., Dias, P.L.S. and Viana, O., 2005. Insolation-driven changes in atmospheric circulation over the past 116,000 years in subtropical Brazil. *Nature* 434, 63-66.
- Cruz, F.W., Burns, S.J., Jercinovic, M., Karmann, I., Sharp, W.D. and Vuille, M., 2007. Evidence of rainfall variations in Southern Brazil from trace element ratios (Mg/Ca and Sr/Ca) in a Late Pleistocene stalagmite. *Geochimica et Cosmochimica Acta* 71, 2250-2263.
- Dai, A.G. and Wigley, T.M.L., 2000. Global patterns of ENSO-induced precipitation. *Geophysical Research Letters* 27, 1283-1286.
- Drysdale, R.N., Zanchetta, G., Hellstrom, J.C., Fallick, A.E. and Zhao, J.X., 2005. Stalagmite evidence for the onset of the Last Interglacial in southern Europe at 129 +/- 1 ka. *Geophysical Research Letters* 32, L24708, doi:10.1029/2005GL024658.
- Drysdale, R., Zanchetta, G., Hellstrom, J., Maas, R., Fallick, A., Pickett, M., Cartwright, I. and Piccini, L., 2006. Late Holocene drought responsible for the collapse of Old World civilizations is recorded in an Italian cave flowstone. *Geology* 34, 101-104.
- Drysdale, R.N., Zanchetta, G., Hellstrom, J.C., Fallick, A.E., McDonald, J. and Cartwright, I., 2007. Stalagmite evidence for the precise timing of North Atlantic cold events during the early last glacial. *Geology* 35, 77-80.
- Dykoski, C.A., Edwards, R.L., Cheng, H., Yuan, D.X., Cai, Y.J., Zhang, M.L., Lin, Y.S., Qing, J.M., An, Z.S. and Revenaugh, J., 2005. A high-resolution, absolute-dated Holocene and deglacial Asian monsoon record from Dongge Cave, China. *Earth and Planetary Science Letters* 233, 71-86.
- Fairchild, I.J., Borsato, A., Tooth, A.F., Frisia, S., Hawkesworth, C.J., Huang, Y.M., McDermott, F. and Spiro, B., 2000. Controls on trace element (Sr-Mg) compositions of carbonate cave waters: implications for speleothem climatic records. *Chemical Geology* 166, 255-269.
- Fairchild, I.J., Baker, A., Borsato, A., Frisia, S., Hinton, R.W., McDermott, F. and Tooth, A.F., 2001. Annual to sub-annual resolution of multiple trace-element trends in speleothems. *Journal of the Geological Society* 158, 831-841.

- Fairchild, I.J., Smith, C.L., Baker, A., Fuller, L., Spötl, C., Matthey, D., McDermott, F. and Eimp, 2006. Modification and preservation of environmental signals in speleothems. *Earth-Science Reviews* 75, 105-153.
- Fairchild, I.J. and Treble, P., 2009. Trace elements in speleothems as recorders of environmental change. *Quaternary Science Reviews* 28, 449-468.
- Fleitmann, D., Burns, S.J., Mudelsee, M., Neff, U., Kramers, J., Mangini, A. and Matter, A., 2003. Holocene forcing of the Indian monsoon recorded in a stalagmite from Southern Oman. *Science* 300, 1737-1739.
- Frisia, S., Borsato, A., Fairchild, I.J., Susini, J., 2005. Variations in atmospheric sulphate recorded in stalagmites by synchrotron micro-XRF and XANES analyses. *Earth and Planetary Science Letters* 235, 729–740.
- Gabitov, R.I., Watson, E.B., 2006. Partitioning of strontium between calcite and fluid. *Geochemistry, Geophysics, Geosystems* 7, Q11004. doi:10.1029/2005GC001216.
- Gascoyne, M., 1983. Trace-element partition coefficients in the calcite-water system and their paleoclimatic significance in cave studies. *Journal of Hydrology* 61, 213–222.
- Gascoyne, M., 1992. Paleoclimate Determination from Cave Calcite Deposits. *Quaternary Science Reviews* 11, 609-632.
- Goede, A. and Vogel, J.C., 1991. Trace element variations and dating of a late Pleistocene Tasmanian speleothem. *Palaeogeography, Palaeoclimatology, Palaeoecology* 88, 121-131.
- Griffiths, M.L., Drsydale, R.N., Gagan, M.K., Zhao, J.-x., Ayliffe, L.K., Hellstrom, J.C., Hantoro, W.S., Frisia, S., Feng, Y.-x., Cartwright, I., St. Pierre, E., Fischer, M.J., Suwargadi, B.W., 2009. Increasing Australian-Indonesian monsoon rainfall linked to early Holocene sea-level rise. *Nature Geoscience* 2, 636-639.
- Griffiths, M.L., Drsydale, R.N., Vonhof, H.B., Gagan, M.K., Zhao, J.-x., Ayliffe, L.K., Hantoro, W.S., Hellstrom, J.C., Cartwright, I., Frisia, S., Suwargadi, B.W., 2010. Younger Dryas-Holocene temperature and rainfall history of southern Indonesia from $\delta^{18}\text{O}$ in speleothem calcite and fluid inclusions. *Earth and Planetary Science Letters* 295, 30-36.
- Hellstrom, J.C. and McCulloch, M.T., 2000. Multi-proxy constraints on the climatic significance of trace element records from a New Zealand speleothem. *Earth and Planetary Science Letters* 179, 287-297.

- Hellstrom, J., 2003. Rapid and accurate U/Th dating using parallel ion-counting multi-collector ICP-MS. *Journal of Analytical Atomic Spectrometry* 18, 1346-1351.
- Hellstrom, J.C., 2006. U–Th dating of speleothems with high initial ^{230}Th using stratigraphical constraint. *Quaternary Geochronology* 1, 289-295.
- Hendy, C.H., 1971. The isotopic geochemistry of speleothems: The calculations of the effects of different modes of formation on the isotopic composition of speleothems and their applicability as palaeoclimate indicators. *Geochimica et Cosmochimica Acta* 35, 801-824.
- Huang, Y.M. and Fairchild, I.J., 2001. Partitioning of Sr^{2+} and Mg^{2+} into calcite under karst-analogue experimental conditions. *Geochimica et Cosmochimica Acta* 65, 47-62.
- Johnson, K.R., Hu, C.Y., Belshaw, N.S. and Henderson, G.M., 2006. Seasonal trace-element and stable-isotope variations in a Chinese speleothem: The potential for high-resolution palaeomonsoon reconstruction. *Earth and Planetary Science Letters* 244, 394-407.
- Kershaw, A.P., 1986. Climatic-Change and Aboriginal Burning in Northeast Australia during the Last 2 Glacial Interglacial Cycles. *Nature* 322, 47-49.
- Kershaw, A. P. and Nanson, G. C., 1993. The Last Full Glacial Cycle in the Australian Region. *Global Planetary Change* 7, 1-9.
- Kershaw, A. P., van der Kaars, S. and Moss, P. T., 2003. Late Quaternary Milankovitch-scale climatic change and variability and its impact on monsoonal Australasia. *Marine Geology* 201, 81-95.
- Kuczumow, A., Genty, D., Chevallier, P., Nowak, J., Ro, C., 2003. Annual resolution analysis of a SW-France stalagmite by X-ray synchrotron microprobe analysis. *Spectrochim. Acta Part B: Atomic Spectrometry* 58, 851–865.
- Kuczumow, A., Genty, D., Chavallier, P., Nowak, J., Florek, M., Bucynska, A., 2005. X-ray and electron microprobe investigation of the speleothems from Godarville tunnel. *X-ray Spectrometry* 34, 502–508.
- Li, H.C., Ku, T.L., You, C.F., Cheng, H., Edwards, R.L., Ma, Z.B., Tsai, W.S. and Li, M.D., 2005. Sr-87/Sr-86 and Sr/Ca in speleothems for paleoclimate reconstruction in Central China between 70 and 280 kyr ago. *Geochimica et Cosmochimica Acta* 69, 3933-3947.
- Magee, J.W., Miller, G.H., Spooner, N.A. and Questiaux, D., 2004. Continuous 150 ky monsoon record from Lake Eyre, Australia: Insolation-forcing implications and unexpected Holocene failure. *Geology* 32, 885-888.

- Mason, H.E., Frisia, S., Tang, Y., Reeder, R.J., Phillips, B.L., 2007. Phosphorus speciation in calcite speleothems determined from solid-state NMR spectroscopy. *Earth and Planetary Science Letters* 254, 313–322.
- McBride, J.L., Haylock, M., and Nicholls, N., 2003. Relationships between the Maritime Continent heat source and the El Niño–Southern Oscillation phenomenon. *Journal of Climate* 16, 2905–2914.
- McDonald, J., Drysdale, R. and Hill, D., 2004. The 2002–2003 El Niño recorded in Australian cave drip waters: Implications for reconstructing rainfall histories using stalagmites. *Geophysical Research Letters* 31, L22202, doi: 10.1029/2004GL020859.
- Meyers, G., McIntosh, P., Pigot, L., Pook, M., 2007. The years of El Niño, La Niña and interactions with the tropical Indian Ocean. *Journal of Climate* 20, 2872–2880.
- McManus, J.F., Francois, R., Gherardi, J.M., Keigwin, L.D. and Brown-Leger, S., 2004. Collapse and rapid resumption of Atlantic meridional circulation linked to deglacial climate changes. *Nature* 428, 834–837.
- Monk, K.A., De Fretes, V., and R eksodiharjo-Lilley, G., 1997. *The Ecology of Nusa Tenggara and Makulu. The Ecology of Indonesia Series, Volume V.* Periplus Editions, Singapore.
- Morse, J.W., Bender, M.L., 1990. Partition coefficients in calcite: examination of factors influencing the validity of experimental results and their application to natural systems. *Chemical Geology* 82, 265–277.
- Mudelsee, M., 2003. Estimating Pearson's Correlation Coefficient With Bootstrap Confidence Interval From Serially Dependent Time Series. *Mathematical Geology* 35, 651–665.
- Paquette, J., and Reeder, R. J., 1990. New type of compositional zoning in calcite: Insights into crystal-growth mechanisms. *Geology* 18, 1244–1247.
- Partin, J.W., Cobb, K.M., Adkins, J.F., Clark, B. and Fernandez, D.P., 2007. Millennial-scale trends in west Pacific warm pool hydrology since the Last Glacial Maximum. *Nature* 449, 452–455.
- Plagnes, V., Causse, C., Dominique, G., Paterne, M. and Blamart, D., 2002. A discontinuous climatic record from 187 to 74 ka from a speleothem of the Clamouse Cave (south of France). *Earth and Planetary Science Letters* 201, 87–103.
- Richards, D.A. and Dorale, J.A., 2003. Uranium-series chronology and environmental applications of speleothems. *Uranium-Series Geochemistry* 52, 407–460.

- Roberts, M. S., Smart, P. L. and Baker, A., 1998. Annual trace element variations in a Holocene speleothem. *Earth and Planetary Science Letters* 154, 237-246.
- Ropelewski, C.F., and Halpert, M. S., 1987. Global and regional scale precipitation patterns associated with the El Niño/Southern Oscillation. *Monthly Weather Review* 115, 1606-1626.
- Rozanski, K., Araguasaraguas, L. and Gonfiantini, R., 1992. Relation between Long-Term Trends of O-18 Isotope Composition of Precipitation and Climate. *Science*, 258, 981-985.
- Saji, N.H., Goswami, B.N., Vinayachandran, P.N., and Yamagata, T., 1999. A dipole mode in the Indian Ocean. *Nature* 401, 360-363.
- Siddall, M., Rohling, E.J., Almogi-Labin, A., Hemleben, C., Meischner, D., Schmelzer, I. and Smeed, D.A., 2003. Sea-level fluctuations during the last glacial cycle. *Nature* 423, 853-858.
- Stott, L., Cannariato, K., Thunell, R., Haug, G.H., Koutavas, A. and Lund, S., 2004. Decline of surface temperature and salinity in the western tropical Pacific Ocean in the Holocene epoch. *Nature* 431, 56-59.
- Thompson, L.G., Mosley-Thompson, E., Davis, M.E., Henderson, K.A., Brecher, H.H., Zagorodnov, V.S., Mashiotto, T.A., Lin, P.N., Mikhalenko, V.N., Hardy, D.R., Beer, J., 2002. Kilimanjaro ice core records: evidence of Holocene climate change in tropical Africa. *Science* 298, 589–593.
- Tooth, A.F. and Fairchild, I.J., 2003. Soil and karst aquifer hydrological controls on the geochemical evolution of speleothem-forming drip waters, Craig Cave, southwest Ireland. *Journal of Hydrology* 273, 51-68.
- Treble, P., Shelley, J.M.G. and Chappell, J., 2003. Comparison of high resolution sub-annual records of trace elements in a modern (1911-1992) speleothem with instrumental climate data from southwest Australia. *Earth and Planetary Science Letters* 216, 141-153.
- Treble, P.C., Chappell, J., Shelley, J.M.G., 2005. Complex speleothem growth processes revealed by trace element mapping and scanning electron microscopy of annual layers. *Geochimica et Cosmochimica Acta* 69, 4855–4863.
- Turney, C.S.M., Kershaw, A. P., Clemens, S.C., Branch, N., Moss, P.T. and Fifield, L.K., 2004. Millennial and orbital variations of El Niño/Southern Oscillation and high-latitude climate in the last glacial period. *Nature* 428, 306-310.

- Verheyden, S., Keppens, E., Fairchild, I.J., McDermott, F. and Weis, D., 2000. Mg, Sr and Sr isotope geochemistry of a Belgian Holocene speleothem: implications for paleoclimate reconstructions. *Chemical Geology* 169, 131-144.
- Vuille, M., Werner, M., Bradley, R.S., Chan, R.Y. and Keimig, F., 2005. Stable isotopes in east African precipitation record Indian ocean zonal mode. *Geophysical Research Letters* 32, L 21705, doi:10.1029/2005GL023876.
- Wang, X.F., Auler, A.S., Edwards, R.L., Cheng, H., Ito, E. and Solheid, M., 2006. Interhemispheric anti-phasing of rainfall during the last glacial period. *Quaternary Science Reviews* 25, 3391-3403.
- Wang, Y.J., Cheng, H., Edwards, R.L., He, Y.Q., Kong, X.G., An, Z.S., Wu, J.Y., Kelly, M.J., Dykoski, C.A. and Li, X.D., 2005. The Holocene Asian monsoon: Links to solar changes and North Atlantic climate. *Science* 308, 854-857.
- Webster, P.J., Magana, V.O., Palmer, T.N., Shukla, J., Tomas, R.A., Yanai, M. and Yasunari, T., 1998. Monsoons: Processes, predictability, and the prospects for prediction. *Journal of Geophysical Research-Oceans* 103, 14451-14510.
- Webster, P.J., Moore, M.D., Loschnigg, J.P., Leben, R.R., 1999. Coupled ocean-atmosphere dynamics in the Indian Ocean during 1997-98. *Nature* 401, 356-360.
- Williams, P.W., King, D.N.T., Zhao, J.X. and Collerson, K.D., 2005. Late pleistocene to holocene composite speleothem O-18 and C-13 chronologies from south island, new Zealand-did a global younger dryas really exist? *Earth and Planetary Science Letters* 230, 301-317.
- Wyrwoll, K.H. and Miller, G.H., 2001. Initiation of the Australian summer monsoon 14,000 years ago. *Quaternary International* 83-5, 119-128.
- Wyrwoll, K.H., Liu, Z.Y.S., Chen, G., Kutzbach, J.E. and Liu, X.D., 2007. Sensitivity of the Australian summer monsoon to tilt and precession forcing. *Quaternary Science Reviews* 26, 3043-3057.
- Yano, J.I. and McBride, J.L., 1998. An aquaplanet monsoon. *Journal of Atmospheric Science* 55, 1373-1399.
- Yu, K.F., Zhao, J.X., Shi, Q., Chen, T.G., Wang, P.X., Collerson, K.D. and Liu, T.S., 2006. U-series dating of dead Porites corals in the South China sea: Evidence for episodic coral mortality over the past two centuries. *Quaternary Geochronology* 1, 129-141.
- Zhang, R. and Delworth, T.L., 2005. Simulated tropical response to a substantial weakening of the Atlantic thermohaline circulation. *Journal of Climate* 18, 1853-1860.

5 Statistical “ramp-fitting” of Indonesian stalagmite record confirms early-Holocene resumption of monsoon system occurred within centuries

Abstract

A precisely dated, multi-proxy stalagmite record from Flores, Indonesia, shows a rapid onset of the Australian-Indonesian summer monsoon (AISM) ~9.5 thousand years before present (ka; present is defined as 1950 A.D.). The application of a “ramp-fitting” method (to detect statistically significant change-points in a time-series) to the $\delta^{18}\text{O}$, Mg/Ca, and Sr/Ca time-series indicate a relatively abrupt shift in the strength of the AISM during the early Holocene that lasted ~350 years. This finding is consistent with the steep rise in eustatic sea-level and an increase in coral-inferred sea-surface temperatures in the southwest Pacific, along with a rapid expansion of rainforest in northeast Australia. However, this result lies in stark contrast to previously reported monsoon lake-level records from interior Australia, which show the monsoon onset occurred ~4-5 ka earlier. Given the abrupt nature of this shift, and the absence of significant changes in insolation, it is suggested that this early Holocene increase in AISM intensity was controlled by the inundation of the Sunda Shelf during eustatic sea-level rise and/or the sharp increase in regional sea-surface temperatures, which would have increased evaporation over the moisture source regions.

5.1 Introduction

Palaeoclimate proxy records and climate model experiments show that the dominant mechanism controlling orbital-scale variations in tropical monsoon behaviour is changes in the intensity of summer insolation (Ruddiman, 2006). However, in the region affected by the Australian-Indonesian Summer Monsoon (AISM), there is still some disagreement. Evidence from lake-level records suggest that AISM activity was reduced during the last glacial maximum (LGM), and became re-established during the Late Glacial-to-Holocene transition (Magee et al., 2004; Miller et al., 2005; Wyrwoll and Miller, 2001). These authors attribute this change to Boreal-winter insolation and its influence on the AISM through the cross-equatorial flow of air from the semi-permanent Siberian high-pressure system. In contrast, some palaeoclimate model simulations have shown that increased local summer insolation can lead to stronger

monsoon activity over northern Australia (Chappell, 1996; Wyrwoll and Valdes, 2003). This divergence of views may indicate that the AISM does not behave in a simple linear fashion to variations in either northern or southern hemisphere insolation. Rather, it may be controlled by the complex interplay between these processes, and other known forcings such as sea-surface temperatures (Liu et al., 2004), sea-level (Griffiths et al., 2009), and land-cover change (Miller et al., 2005).

The lack of highly resolved, precisely dated records from the AISM domain means that questions regarding its variability in time and space remain unanswered. The aim of this study is to address some of these key questions, in particular the precise timing of the monsoon onset, using a suite of geochemical tracers from a previously published stalagmite record in western Flores, Indonesia (Griffiths et al., 2009, 2010). Quantitative assessment of this monsoon onset is facilitated by the use of a statistical “ramp-fitting” function, which detects a linear change from one steady state to another (Mudelsee, 2000).

5.2 Study site and methods

The stalagmite used in this study (LR06-B1) was collected from Liang Luar, a ~2 km-long cave developed in late-Miocene reef carbonates on the Indonesian island of Flores (Fig. 5.1). The local region has a mean annual temperature (MAT) of ~25 °C and receives an average rainfall of ~1200 mm annually. Most of the cave recharge (~69%) is delivered by the AISM between November and March, when the lower tropospheric winds shift from easterly (austral winter dry season) to northwesterly (austral summer wet season). The stalagmite, which measured 1.25 m in length, was active at the time of collection. It formed ~800 m from the cave entrance in a large chamber with a high humidity (close to 100%). Oxygen isotope ($\delta^{18}\text{O}$) values were determined from calcite powders, drilled at 1 mm increments, using a GV Instruments GV2003 continuous-flow isotope ratio mass spectrometer. Results are expressed as the deviation in per mil (‰) between the sample and the VPDB scale using an internal working standard of Carrara Marble (New1). The analytical uncertainty (2σ) of Carrara Marble (New1) was 0.08‰ for $\delta^{18}\text{O}$. Subsamples were analysed for Mg, Sr, and Ca on a Varian Liberty 4000 inductively coupled atomic emission spectrometer (ICP-AES) (see previous chapter and Griffiths et al., 2010 for a full description of the methods). The $\delta^{18}\text{O}$ and trace elements were tied to a previously published $^{230}\text{Th}/^{234}\text{U}$ depth-age model (Griffiths et al., 2009) constructed in two-stages using a Bayesian-Monte Carlo approach (Drysdales

et al., 2005, 2007). Principal Components Analysis (PCA) was performed on the $\delta^{18}\text{O}$, Mg/Ca, and Sr/Ca time-series to extract the dominant rainfall signal embedded within all three proxy time series.

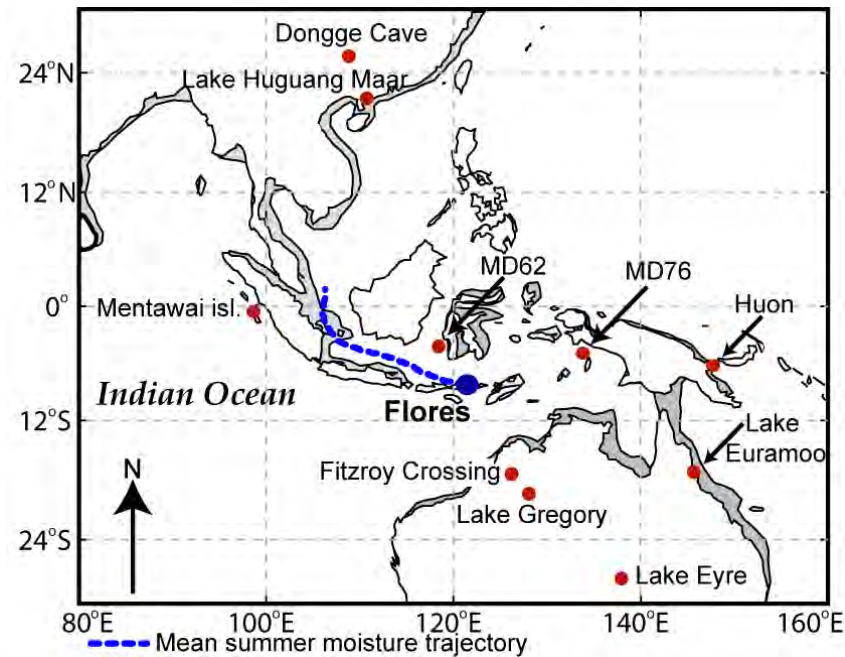


Figure 5.1 Location of Flores and other sites mentioned in the text. Mean summer (DJF) 96-hour back trajectory moisture path is shown (thick dashed line) for the period 1960-2000. HYSPLIT (Draxler and Rolph, 2003) was used to calculate moisture-source back-trajectories starting at an elevation of 1000 m (approximate cloud base height in the tropics). Gray shading shows the approximate position of the shoreline at 10 ka calculated from reconstructed gridded sea-level data (http://geochange.er.usgs.gov/pub/data/sea_level/).

5.3 Results and Discussion

5.3.1 Timing and structure of monsoon onset

The most striking feature common to all three stalagmite proxy time-series is the sharp decrease in values that began at ~ 9.5 ka (Fig. 5.2). The close coupling between all three variables at this time argues for a single environmental control on these stalagmite properties. Previous work on LR06-B1, supported by a replicated stalagmite record (LR06-B3) (from the same cave) through a partially overlapping segment has shown the $\delta^{18}\text{O}$ to largely reflect variations in the intensity of east Indonesian summer rainfall (Griffiths et al., 2009), with lower $\delta^{18}\text{O}$ values corresponding to higher rainfall amounts

and *vice versa*. The abrupt decrease of $\sim 0.5\%$ centred at ~ 9.5 ka therefore suggests an increase in rainfall at this time. This relationship can now be corroborated statistically by near-synchronous changes in the Sr/Ca and Mg/Ca of LR06-B1. In addition, initial uranium isotope activity ratios ($[^{234}\text{U}/^{238}\text{U}]_i$) from LR06-B1 — interpreted to reflect changes in palaeohydrology — display a dramatic transition to lower values (i.e. wetter conditions) at around 9.5 ka (Griffiths et al., 2010).

The Sr/Ca and Mg/Ca of LR06-B1 have a significant inter-correlation during the Holocene (Griffiths et al., 2010), suggesting that a single mechanism or set of mechanisms controlled their variability. Strong and systematic Mg/Ca and Sr/Ca co-variations in speleothems have been observed to reflect changes in seepage water chemistry during dry periods (Fairchild and Treble, 2009). Under this scenario, intervals of decreased rainfall recharge result in dewatering of fractures in the karst rock, which enhances ventilation and triggers CO_2 degassing. This promotes ‘prior calcite precipitation’ (PCP) along the fractures upstream of the drip site, resulting in higher Mg/Ca and Sr/Ca ratios of the meteoric water due to the preferential loss of the Ca^{2+} ion. The converse occurs during wetter phases. The effects of temperature (affecting the Mg/Ca ratio) and growth rate changes (affecting the Sr/Ca ratio) (Fairchild and Treble, 2009) can be discarded because air temperatures have remained relatively stable during the Holocene (see Chapters 3 and 4), and the growth rates only become significant when they exceed 0.5 mm year^{-1} (Fairchild and Treble, 2009), which is not the case for LR06-B1 (Griffiths et al., 2009).

A strong relationship is also observed between the $\delta^{18}\text{O}$, and both the Sr/Ca and Mg/Ca ratios (Fig. 5.2). This positive covariation provides additional evidence that the Sr/Ca and Mg/Ca trends reflect effective water excess due to changes in rainfall, with all proxies increasing during drier intervals. Slight discrepancies between the Mg/Ca and Sr/Ca ratios and the $\delta^{18}\text{O}$ profiles likely reflect the dependency of $\delta^{18}\text{O}$ values on factors other than rainfall amount, such as moisture trajectories (Cruz et al., 2007), whereas Mg and Sr variations are primarily controlled by hydrological processes acting upon time-constant geological sources. This may explain the $\sim 0.5\%$ negative $\delta^{18}\text{O}$ excursion at ~ 10.5 ka, which is absent from the Sr/Ca (owing to machine error of the ICP-AES) and much less pronounced in the Mg/Ca values.

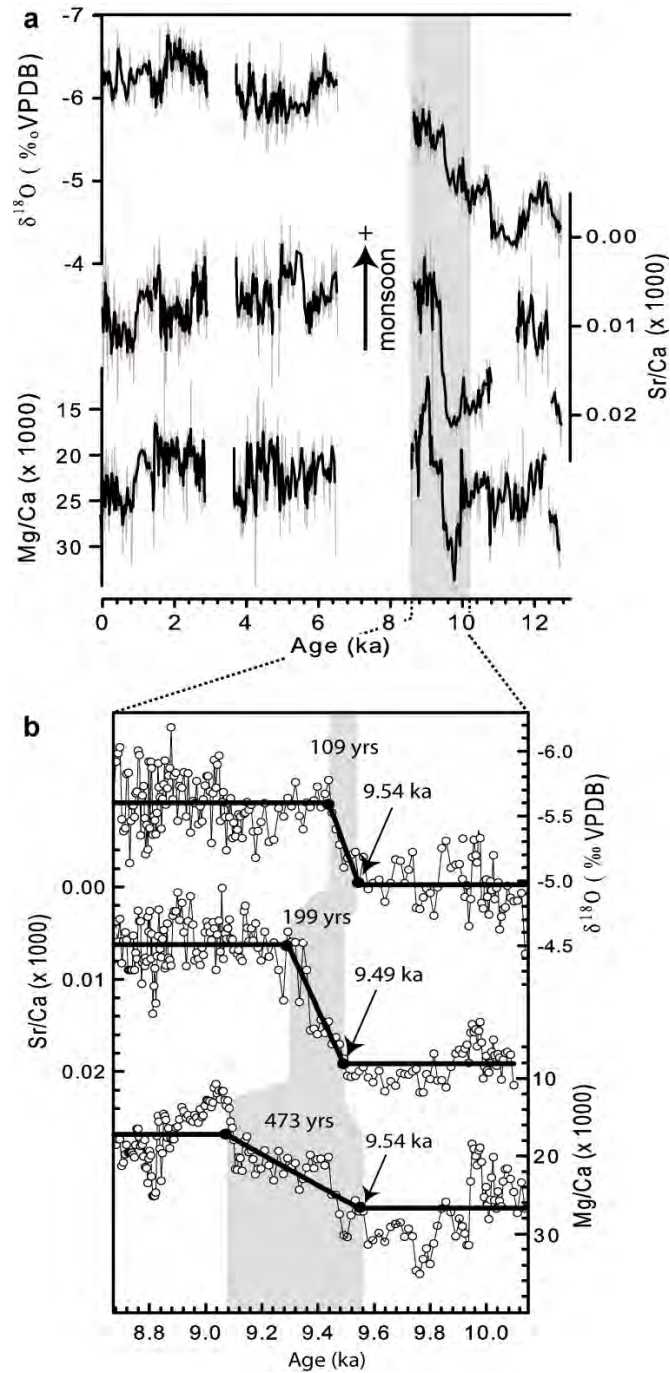


Figure 5.2 Multi-proxy records for stalagmite L R06-B1 over the period 0 to 12.7 ka B.P. (a) Time series of stalagmite $\delta^{18}\text{O}$, Sr/Ca, and Mg/Ca. (b) Rampfit regression model applied to the $\delta^{18}\text{O}$, Sr/Ca, and Mg/Ca time series over the period 8.65 ka to 10.15 ka. Gray shading highlights the duration of the shift in mean values for all three proxies.

Hydrological-controlled changes in all three proxies at ~ 9.5 ka points to a major increase in monsoon strength. However, such a climate shift can only be regarded as significant if the difference in the mean value either side of the inflection point is larger than the standard deviation of the noise over the

entire interval. To statistically quantify the timing and magnitude of the changes in the proxies, I applied a simple ramp-fitting function to the $\delta^{18}\text{O}$, Mg/Ca, and Sr/Ca time-series. This function detects the presence and timing of a linear change from one proxy state to another (Mudelsee, 2000). The mean proxy levels prior to and after the transition are determined by weighted least-squares regression over a 1500-year long interval (Fig. 5.2b) and the entire 0 to 12.64 ka period (Fig. 5.3). The length of the shorter interval was chosen to ensure an approximately even number of years (~600) either side of the transition (~300 year duration). The timing of the beginning and end points of the ramp were calculated by a brute-force search using a prescribed standard deviation of the data series (Mudelsee, 2000). The uncertainty, or standard error, of the ramp timing was calculated using 400 bootstrap simulations (Mudelsee, 2000). Data and fitted ramps for the individual Mg/Ca, Sr/Ca and $\delta^{18}\text{O}$ records over the 8.65 to 10.15 ka interval are shown in Fig. 5.2b. Further ramp-fitting was applied to the first principal component, calculated from the Mg/Ca, Sr/Ca and $\delta^{18}\text{O}$ time series over the 0 to 12.64 ka period; this is shown in Fig. 5.3. From Fig. 5.2b, it is evident that the onset of the stepwise transition in the Mg/Ca, Sr/Ca and $\delta^{18}\text{O}$ occurs (within statistical and analytical uncertainty) at about the same time. There are differences, however, in the duration of the ramps: the Mg/Ca ratio has a length of 473 years while the Sr/Ca ratio and $\delta^{18}\text{O}$ records have much shorter ramp lengths of 199 and 109 years, respectively.

5.3.2 Comparison with other records

The timing of the monsoon onset, inferred from the LR06-B1 AISM multi-proxy record, is in good agreement with tropical pollen records from northeast Australia. For example, comparison of LR06-B1 PCA1 (explains 67% of the variance) – interpreted to reflect the dominant rainfall signal among the three proxy time-series – with PCA1 (explains 63% of the variance) from rainforest pollen taxa at Lake Euramoo (Haberle, 2005; Fig. 5.1) reveals that the attainment of modern rainforest (interpreted to reflect an increase in effective rainfall) in northeastern Australia occurred (Fig. 5.3c) simultaneously (within dating uncertainty) with the sharp increase in monsoon rainfall in eastern Indonesia (Fig. 5.3b). Moreover, an almost synchronous decline in charcoal abundance from the same lake (Fig. 5.3a), indicative of decreased fire-frequency, further supports the notion of an enhanced rainfall signal over the monsoon belt during the early Holocene. In contrast, lake level records from (Lake Eyre, Lake Gregory, and Fitzroy Crossing; Fig. 5.1) the interior Australian continent (Magee et al., 2004; Wyrwoll and Miller, 2001) suggest monsoon initiation as early as 14 ka, more than 4–5 ky earlier than indicated by the LR06-

B1 multi-proxy record. Discrepancies between these proxy records may be due to: (1) different response times of lake-level records versus those from cave systems; (2) dating uncertainties; and (3) dissimilar local rainfall patterns under different orbital and sea-level configurations. For example, using the Fast Ocean Atmosphere Model (FOAM), Wyrwoll et al. (2008) showed pronounced anti-phasing between the northern monsoon region of Australia (higher rainfall) and the adjacent northeast Indian Ocean (lower rainfall) during the early Holocene when obliquity was high and insolation low.

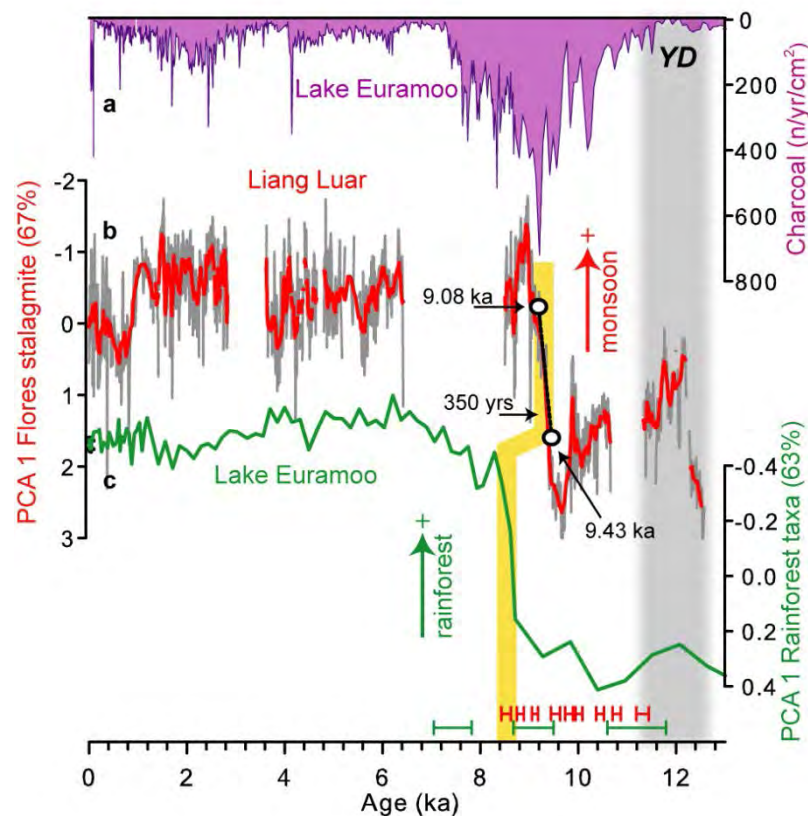


Figure 5.3 Comparison of the (b) first multi-proxy principal component (PCA1), extracted from the LR06-B1 $\delta^{18}\text{O}$, Sr/Ca, and Mg/Ca stalagmite records, with (a) charcoal and (c) PCA1 from rainforest pollen taxa from Lake Euramoo, Atherton Tablelands (Haberle, 2005). The red line shows a 10-point running mean. The open circles and dashed line in (b) shows the rampfit regression results, indicating the short duration of the monsoon transition which is also evident in the PCA1 of rainforest pollen taxa (yellow shading). Colour coded analytical uncertainties for the dates through the sharp transition in the stalagmite and pollen records are shown along the bottom. The gray shading highlights the timing of the Younger Dryas, which is characterised by increased AISM rainfall coeval with a periodic expansion of rainforest in northeast Australia.

The duration of the stepwise transition in LR06-B1 PCA1 occurs over a period of ~350 years (Fig. 5.3b), and demonstrates synchronicity with the expansion of rainforest taxa in northeast Australia (Haberle, 2005; Fig. 5.3c). These findings highlight the potential of the monsoon system to switch from one steady state to another over a period of centuries.

5.3.3 Possible mechanisms

Trends in the LR06-B1 PCA1 represent changes in rainfall characteristics at the cave site. Comparison with other regional and global climate archives (Fig. 5.4) allows an assessment of possible AISM controls during the Holocene. Using the $\delta^{18}\text{O}$ of two stalagmites from Flores (inferred to reflect rainfall amount and provenance), we have previously shown that the late-Glacial/early-Holocene rise in sea level had a dominant influence on the AISM (Griffiths et al., 2009). The value-added incorporation of the Mg/Ca and Sr/Ca profiles now provides robust support for a rapid monsoon increase during the early Holocene, with additional insights into the non-linear monsoon response to the inundation of the Sunda Shelf during rapid sea-level rise (Siddall et al., 2003; Fig. 5.4b); this pattern of behaviour is possibly related to a critical threshold in the depth of the IPWP which must be surpassed by the system. However, before conclusions can be drawn, other possible mechanisms must be considered.

Feedback mechanisms associated with sea-surface temperature (SST) variability have been shown to have a dominant influence on monsoon intensity over northern Australia during the Holocene (Liu et al., 2003, 2004; Wyrwoll et al., 2007). In an 11 ka climate model simulation, Liu et al. (2003) showed that, despite insolation being low, AISM precipitation was enhanced due to the presence of warm SSTs off northwest Australia. Their results indicated that monsoon variance over the northwest region of the continent could not be explained without feedbacks associated with SST changes. Comparison of our AISM record with SST proxies from corals and marine sediments gives contrasting views as to the role of SST feedbacks in palaeomonsoon behaviour. For example, SST reconstructions from marine sediment cores MD76 (Stott et al., 2004) and MD62 (Visser et al., 2003) – based on the planktonic foraminifer *Globigerinoides ruber* – from the IPWP (Fig. 5.1) show a relatively stable pattern through the interval, with no significant change at ~9.5 ka. However, SST reconstructions from southwest Pacific corals (Huon and Vanuatu) indicate a rather abrupt increase in temperatures (Beck et al., 1997; McCulloch et al., 1996) around this time (Fig. 5.4c), indicating that this climatic forcing may have played a more active role in the abrupt enhancement of the AISM during the early Holocene. A noteworthy caveat to this story, however,

is that this argument rests on the assumption that the fossil corals have not undergone any diagenetic alteration. The older coral data were generated over a decade ago, before we had a firm handle on the profound effects of diagenesis on fossil coral Sr/Ca. Hence, given modern understandings of aragonite crystallographic changes through time and ways of distinguishing it, this interpretation is purely speculative. Nevertheless, it is intriguing to note the almost synchronous changes in coral-inferred SSTs and the monsoon.

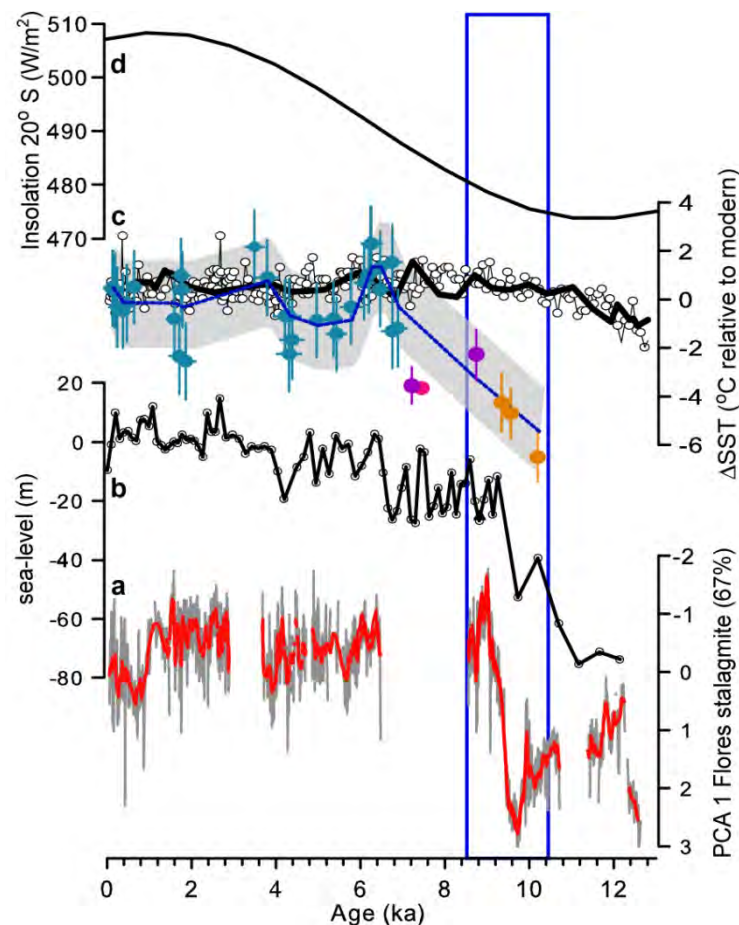


Figure 5.4 Comparison of the (a) LR06-B1 PCA1 record with other proxy data over the period 12.64 ka to present. Red line shows a 10-point running mean. (b) Sea-level reconstruction based on marine sediments from the Red Sea (Siddall et al., 2003). (c) Sea-surface temperature (SST) reconstructions from planktonic foraminifera marine cores MD76 (black circles; (Stott et al., 2004) and MD62 (solid line; (Visser et al., 2003), and coral records from the tropical west Pacific (blue, Abram et al., 2009; orange, Beck et al., 1997; pink, Castellaro et al., 1997; purple, McCulloch et al., 1996). Blue dashed line shows a 3-point running mean between all fossil coral records. Gray shading envelopes the 95% confidence interval around the running mean. (d) Summer (DJF) insolation at 20° S. The blue box surrounds the common change in the LR06-B1 PCA1, sea-level and coral-inferred SSTs.

The sharp transition in the AISM from one steady state to another occurs over a period of ~350 years (Fig. 5.3), and demands an explanation consistent with a rapid, rather than gradual, change in environmental variables. A contrasting view is the notion that the AISM is not controlled by southern hemisphere summer insolation *per se*, but by the strength of the East Asian winter monsoon (EAWM; Magee et al., 2004; Miller et al., 2005). Strong coupling of the AISM (Griffiths et al., 2009) and EAWM (Yancheva et al., 2007) was demonstrated during the Younger Dryas cooling. However, there is insufficient evidence to vindicate the EAWM as being the principal mechanism of the early Holocene AISM increase.

5.4 Conclusions

Overall, the trends in the LR06-B1 multi-proxy record provide compelling evidence for the onset and evolution of the AISM system in east Indonesia during the early Holocene. While mechanisms such as summer insolation have likely played a role in the circulation patterns over the Indonesia/northern Australia region, it is argued that sea-level over the Sunda region may have been a critical factor controlling AISM precipitation during the early Holocene. This influence may be explained as follows: a large proportion of the summer monsoon trajectory path would have been occupied by land surface or otherwise extremely shallow seas during the early Holocene, assuming moisture trajectories were broadly similar to the present day. Thus, a lower surface area over the mean trajectory would have limited the availability of source moisture and possibly altered the overall dynamics of the monsoon. Under this scenario, it was not until the source region became sufficiently large in a real extent that a critical threshold was surpassed and the AISM “switched on”. An alternative and somewhat complementary explanation for the abrupt monsoon change, invokes the monotonic increase in tropical west-Pacific SSTs (inferred from coral records) as being the more dominant forcing mechanism. Although, this latter explanation is not as robust as it relies on the assumption that the fossil corals have not undergone any diagenesis, which, given modern understandings of diagenesis, is unlikely.

5.5 References

- Abram, N.J., McGregor, H.V., Gagan, M.K., Hantoro, W.S., Suwargadi, B.W., 2009. Oscillations in the southern extent of the Indo-Pacific Warm Pool during the mid-Holocene. *Quaternary Science Reviews* 28, 2794-2803.
- Beck, J.W., R  cy, J., Taylor, F., Edwards, R.L., and Cabioch, G., 1997. Abrupt changes in early Holocene tropical sea surface temperature derived from coral records. *Nature* 385, 705-707.
- Castellaro, C., Ribaud-Laurenti, A., Claverie, K., Cabioch, G., Hamelin, B., Bard, E., Montaggioni, L., J. R  cy, 1997. Variabilit   de climat tropical    l'holoc  ne: Enregistrements Sr/Ca et U/Ca dans les coraux de Nouvelle-Cal  donia, de Tahiti, et des Seychelles (Indo-Pacifique). 6 Congr  s Fran  ais de la Chronologie Lion des Resumes, Publication ASF, Paris, 293 pp. 47-48.
- Chappell, J., and Syktus, J., 1996. Palaeoclimate modelling: a western Pacific perspective. In: *Climate Change: Developing Southern Hemisphere Perspectives*. Eds. Giamblluca, T.W., and Henderson-Sellers, A. Chichester, Wiley, pp. 175-194.
- Cruz, F.W., Burns, S.J., Jercinovic, M., Karmann, I., Sharp, W.D. and Vuille, M., 2007. Evidence of rainfall variations in Southern Brazil from trace element ratios (Mg/Ca and Sr/Ca) in a Late Pleistocene stalagmite. *Geochimica et Cosmochimica Acta* 71, 2250-2263.
- Draxler, R.R. and Rolph, G.D., 2003. HYSPLIT (Hybrid Single-Particle Lagrangian Integrated Trajectory) Model access via NOAA ARL R EADY Website (<http://www.arl.noaa.gov/ready/hysplit4.html>). NOAA Air Resources Laboratory, Silver Spring, MD.
- Drysdale, R.N., Zanchetta, G., Hellstrom, J.C., Fallick, A.E. and Zhao, J.X., 2005. Stalagmite evidence for the onset of the Last Interglacial in southern Europe at 129 +/- 1 ka. *Geophysical Research Letters* 32, L24708, doi: 10.1029/2005GL024658.
- Drysdale, R.N., Zanchetta, G., Hellstrom, J.C., Fallick, A.E., McDonald, J. and Cartwright, I., 2007. Stalagmite evidence for the precise timing of North Atlantic cold events during the early last glacial. *Geology* 35, 77-80.
- Fairchild, I.J. and Treble, P., 2009. Trace elements in speleothems as recorders of environmental change. *Quaternary Science Reviews* 28, 449-468.

- Griffiths, M.L., R.N. Drisdale, M.K. Gagan, J.-x. Zhao, L.K. Ayliffe, J.C. Hellstrom, W.S. Hantoro, S. Frisia, Y.-x. Feng, I. Cartwright, E. St. Pierre, M.J. Fischer, B.W. Suwargadi, 2009. Increasing Australian-Indonesian monsoon rainfall linked to early Holocene sea-level rise. *Nature Geoscience* 2, 636-639.
- Griffiths, M.L., Drisdale, R.N., Gagan, M.K., Ayliffe, L.K., Frisia, S., Zhao, J.-x., Hellstrom, J.C., Fischer, M.J., Hantoro, W.S., Feng, Y.-x., Suwargadi, B.W., 2010. Evidence for Holocene changes in Australian-Indonesian monsoon rainfall from stalagmite trace element and stable isotope ratios. *Earth and Planetary Science Letters* 292, 27-38.
- Haberle, S.G., 2005. A 23,000-yr pollen record from Lake Euramoo, Wet Tropics of NE Queensland, Australia, *Quaternary Research* 64, 343-356.
- Liu, Z., Otto-Bliesner, B., Kutzbach, J., Li, L. and Shields, C., 2003. Coupled climate simulation of the evolution of global monsoons in the Holocene. *Journal of Climate* 16, 2472-2490.
- Liu, Z., Harrison, S.P., Kutzbach, J. and Otto-Bliesner, B., 2004. Global monsoons in the mid-Holocene and oceanic feedback. *Climate Dynamics* 22, 157-182.
- Magee, J.W., Miller, G.H., Spooner, N.A. and Questiaux, D., 2004. Continuous 150 ky monsoon record from Lake Eyre, Australia: Insolation-forcing implications and unexpected Holocene failure. *Geology* 32, 885-888.
- McCulloch, M.T., Mortimer, G., Esat, T., Xianhua, L., Pillans, B., Chappell, J., 1996. High resolution windows into early Holocene climate: Sr/Ca coral records from the Huon Peninsula. *Earth and Planetary Science Letters* 138, 169-178.
- Miller, G., Mangan, J., Pollard, D., Thompson, S., Felzer, B. and Magee, J., 2005. Sensitivity of the Australian Monsoon to insolation and vegetation: Implications for human impact on continental moisture balance. *Geology* 33, 65-68.
- Mudelsee, M., 2000. Ramp function regression: a tool for quantifying climate transitions. *Computers & Geosciences* 26, 293-307.
- Ruddiman, W.F., 2006. What is the timing of orbital-scale monsoon changes? *Quaternary Science Reviews* 25, 657-658.
- Siddall, M., Rohling, E.J., Almogi-Labin, A., Hemleben, C., Meischner, D., Schmelzer, I. and Smeed, D.A., 2003. Sea-level fluctuations during the last glacial cycle. *Nature* 423, 853-858.

- Stott, L., Cannariato, K., Thunell, R., Haug, G.H., Koutavas, A. and Lund, S., 2004. Decline of surface temperature and salinity in the western tropical Pacific Ocean in the Holocene epoch. *Nature* 431, 56-59.
- Visser, K., Thunell, R. and Stott, L., 2003. Magnitude and timing of temperature change in the Indo-Pacific warm pool during deglaciation. *Nature* 421, 152-155.
- Wyrwoll, K.H. and Miller, G.H., 2001. Initiation of the Australian summer monsoon 14,000 years ago. *Quaternary International* 83-5, 119-128.
- Wyrwoll, K.H. and Valdes, P., 2003. Insolation forcing of the Australian monsoon as controls of Pleistocene mega-lake events. *Geophysical Research Letters* 30, 2279, doi:10.1029/2003GL018486.
- Wyrwoll, K.H., Liu, Z.Y.S., Chen, G., Kutzbach, J.E. and Liu, X.D., 2007. Sensitivity of the Australian summer monsoon to tilt and precession forcing. *Quaternary Science Reviews* 26, 3043-3057.
- Yancheva, G., Nowaczyk, N.R., Mingram, J., Dulski, P., Schettler, G., Negendank, J.F.W., Liu, J.Q., Sigman, D.M., Peterson, L.C. and Haug, G.H., 2007. Influence of the intertropical convergence zone on the East Asian monsoon. *Nature* 445, 74-77.

6 Abrupt Indo-Pacific climate response to high-latitude warming during MIS 5a/b

Abstract

Uranium-series dating of two stalagmites (LR07-A8 and LR07-A9) collected from Liang Luar Cave (Flores, Indonesia), show that they grew from 91 to 88 ka and 89 to 84 ka respectively. High-resolution stable-isotope and trace-element measurements from them record the history of Indo-Pacific climate through marine isotope stage 5a/b. The detrended $\delta^{18}\text{O}$ and $\delta^{13}\text{C}$ series significantly co-vary, suggestive that they were probably driven by similar forcing mechanisms at the decadal- to centennial-scale. In addition, the $\delta^{13}\text{C}$ record displays a significant positive correlation with the Mg/Ca (and to a lesser extent the Sr/Ca) ratios, suggesting that the high-frequency variability in these proxies was dominated by prior calcite precipitation and/or enhanced selective leaching associated with extended water-rock contact times. These phase relationships corroborate our previous interpretation of Liang Luar stable isotopes that higher-frequency $\delta^{13}\text{C}$ and $\delta^{18}\text{O}$ variability represents changes in rainfall amount above the cave. Trace elements Y and P display similar patterns to the Mg and Sr and likely reflect the strong influence of soil hydrology on the colloidal transport of these elements into the cave system.

Examination of the lower-frequency $\delta^{18}\text{O}$ and $\delta^{13}\text{C}$ trends reveals quite different patterns between the two proxies. Whilst the $\delta^{18}\text{O}$ record exhibits a trend that closely matches southern hemisphere summer insolation at 20° S, the $\delta^{13}\text{C}$ profile bears a closer resemblance to the $\delta^{18}\text{O}_{\text{ice}}$ and CH_4 recorded in Greenland ice cores. Specifically, the abrupt decrease in $\delta^{18}\text{O}_{\text{ice}}$ (i.e. increased temperatures) and CH_4 during the onset of Greenland interstadial (GIS) 21 is paralleled by an abrupt decrease in Liang Luar $\delta^{13}\text{C}$ values. It is argued that this link is best explained by a temperature-controlled increase in soil microbial activity above the cave as a result of the strong meridional teleconnection with Greenland during GIS 21. This interpretation is supported by the synchronous rise in atmospheric CH_4 , indicative of higher tropical temperatures.

6.1 Introduction

Abrupt perturbations in ocean-air temperature were a regular occurrence over the North Atlantic region during the last glacial period (Rahmstorf 2002, 2006). Of these, the Greenland interstadials (GIS) [(otherwise referred to as ‘Dansgaard-Oeschger’ events (Dansgaard, 1993)], which are manifested in the oxygen-isotope ($\delta^{18}\text{O}$) ratios of Greenland ice cores (Grootes et al., 1993) and North Atlantic marine sediments (Bard et al., 2000; Bond et al., 1993), were the most prominent. Each GIS is characterised by an abrupt (within approximately a decade) and large (8-16 °C) warming followed by gradual cooling (Severinghaus et al., 2003). Associated with these oscillations are ‘Heinrich Events’ (Heinrich, 1988): periods of major iceberg discharge into the North Atlantic, thought to be the result of ice sheet instability (Rahmstorf, 2006) and characterised by widespread cooling in the high latitudes of the Northern Hemisphere (Broecker, 1992). Two main hypotheses have been put forth to explain these extreme shifts in climate: the first invokes the ocean’s thermohaline circulation shifting from one state to another due to fluctuations in the freshwater input into the North Atlantic; the second calls for changes in the configuration of the tropical ocean-atmosphere system (e.g. ENSO) (Broecker, 2003). Although these proposed mechanisms have been tested extensively through climate model simulations, there is still some doubt as to the precise origin of these events. This is because climate proxies from around the globe lack a robust universal chronology, which precludes an entirely convincing theory on the trigger of these changes (Hinnov et al., 2002).

A counterpart to these Northern Hemisphere cycles are more subdued oscillations in Antarctic temperatures, which occurred over longer time-scales (centennial- to millennial-scale) and were out of phase with the high northern latitudes (Blunier and Brook, 2001). A single coherent explanation for these opposing warm and cold transitions between the hemispheres, termed the ‘bi-polar see-saw’ (Broecker, 1998), is variations in the Atlantic Meridional Overturning Circulation (AMOC), which controls meridional heat transport between the North and South Atlantic (Broecker, 1998). Although variations in the AMOC offer a mechanism for the anti-phasing between the northern and southern high-latitudes, they do not explain why the Antarctic displays a gradual rather than abrupt change during a GIS. The common explanation for this difference has been linked to the large heat storage of the Southern Ocean and its inherently slower reaction time (Stocker and Johnsen, 2003).

The extent to which these high latitude climate swings extend into the tropics has been, until recently, an unsolved puzzle for scientists. Although many studies documenting these meridional

teleconnections have emerged over the years, there is still a great degree of uncertainty in the nature and timing of the tropical-climate response to these events (especially over the terrestrial Southern Hemisphere). North of the equator, stalagmite records from the Indian (Burns et al., 2003) and East-Asian (Wang et al., 2001; Wang et al., 2008; Yuan et al., 2004) monsoon domains exhibit abrupt negative shifts in $\delta^{18}\text{O}$ values (i.e. stronger monsoon) that are synchronous with the timing of North Atlantic GIS; similar patterns, but of opposite sign, are observed during Heinrich events. Moreover, marine sediment records from the tropical Indian Ocean (Altabet et al., 2002; Schulz et al., 1998), the tropical northeast (Leduc et al., 2007) and northwest (Stott et al., 2002) Pacific Ocean, and the Cariaco Basin (Peterson et al., 2000) demonstrate similar excursions that are synchronous with those observed in Greenland ice. By contrast, speleothem and travertine deposits from tropical/sub-tropical Brazil (Cruz et al., 2005; Wang et al., 2004) and lake sediments from East Africa (Brown et al., 2007) indicate higher (lower) rainfall patterns over the region during Heinrich events (GIS). Modeling experiments have linked these north-south phase relationships to periodic shifts in the meridional positioning of the ITCZ due to changes in the AMOC (Zhang and Delworth, 2005). The large freshwater input to the North Atlantic during Heinrich events induced a reduction in the AMOC, which led to an asymmetric geometry of tropical SSTs and a subsequent southward shift of the Hadley circulation (Broccoli et al., 2006; Zhang and Delworth, 2005).

While these aforementioned proxy records demonstrate an intimate connection between North Atlantic climate and rainfall patterns over Asia, Africa and South America, the high-latitude link with western Pacific hydrology [namely the Australian-Indonesian Summer Monsoon (AISM)] still remains enigmatic. Previous studies of surface-dwelling planktonic foraminifera from the IPWP (Stott et al., 2002; Visser et al., 2003) indicate a strong Mg/Ca-inferred SST signal that is coherent with high-latitude temperature fluctuations. Moreover, terrestrial proxies from peat sediments in northeastern Australia (Muller et al., 2008; Turney et al., 2004) highlight millennial-scale rainfall oscillations that are in concert with the GISP2 ice-core record (Stuiver and Grootes, 2000) and portray pronounced dry (wet) episodes during GIS (Heinrich events). These studies, however, lack the temporal resolution and age constraints capable of testing the timing and magnitude of these observed hydrological changes. The aim of this study is to analyse the Indo-Pacific climate response during GIS 21 and constrain the precise timing of this response in the southern tropics during part of the last glacial.

GIS 21 was arguably the most unique and pertinent North Atlantic climate anomaly during the last glacial period because it coincides with the transition from Marine Isotope Stage (MIS) 5b to MIS

5a—a shift in Northern Atlantic climate from a stadial (“cool”) to interstadial (“warm”) state—when Northern Hemisphere summer insolation (Berger and Loutre, 1991) (60° N) peaked at ~ 84 ka, the highest insolation intensity prior to the start of the Holocene (Fig. 6.1). Moreover, this event, the longest and warmest according to the GISP2 ice-core record (Grootes and Stuiver, 1997), was characterised by an ~ 300 parts per billion (p.p.b.v.) increase in atmospheric CH_4 , the largest excursion prior to Termination I (Fig. 6.1). The timing of GIS 21 is uniquely positioned within the later stages of the last interglacial, and as such, presents a time when global boundary conditions were not at all that different from the pre-industrial era. Hence, focusing in on this interval provides an excellent opportunity to examine the impact of a abrupt Northern Hemisphere warming on the southern tropics when Earth’s climate was still in a relatively warm state. Thus, this period may ultimately serve as an analogue for future climate changes due to Greenhouse warming.

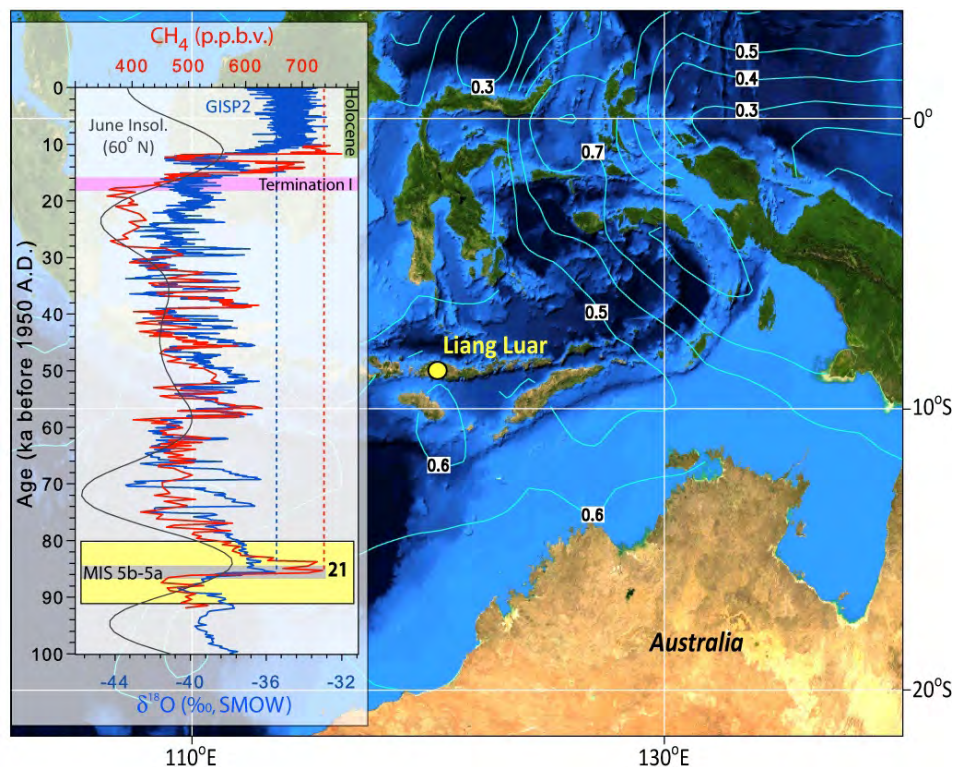


Figure 6.1 The location of Liang Luar Cave, Flores, Indonesia, from where stalagmites LR07-A8 and LR07-A9 were collected. Contour lines show average SST anomalies during the 1975/76, 1988/89 and 1998/99 La Niña events (Smith et al., 2008). Inset: The GISP2 $\delta^{18}\text{O}$ (blue) (Grootes and Stuiver, 1997) and CH_4 (red) (Blunier and Brook, 2001) profiles plotted against Northern Hemisphere summer insolation (gray) (Berger and Loutre, 1991). The yellow shading is the time period of interest, with GIS 21 labelled. The gray box indicates the approximate timing of the MIS5a-5b transition. The GISP2 records were synchronised to the most recent EPICA time-scale (Lemieux-Dudon et al., 2010).

Assessing teleconnections between the tropics and high latitudes requires proxies that are sensitive to environmental change and datable with a high level of precision; speleothems (i.e. stalagmite and flowstones) have the potential of providing such detail (McDermott, 2004). Previously, we have shown that speleothems from Flores (east Indonesia) are sensitive to atmospheric conditions, namely air-mass transport via the summer monsoon, which is recorded in the $\delta^{18}\text{O}$ composition of the calcite (Griffiths et al., 2009). Furthermore, we have demonstrated the ability to produce high precision $^{230}\text{Th}/^{234}\text{U}$ dates [due to low concentrations of detrital thorium (^{232}Th)], thus enabling the construction of accurate age models back to at least marine isotope stage (MIS) 5. Here, a continuous, high-resolution reconstruction of IPWP climate during the period 91 ka to 84 ka is provided from two speleothems from Liang Luar Cave. A suite of geochemical proxies were employed to examine climatic changes in east Indonesia during the MIS 5a/b transition. The record provides the first precisely dated reconstruction of IPWP climate beyond the limits of radiocarbon dating (~ 50 ka), thus enabling the testing of new hypotheses regarding changes in the AISM through glacial-interglacial cycles without *a priori* assumptions of leads/lags among different regions.

6.2 Site description and climate setting

The speleothems used in this study were recovered from Liang Luar, a ~ 2 km long cave situated on the east Indonesian island of Flores ($8^{\circ} 32'\text{N}$, $120^{\circ} 26'\text{E}$; Fig. 6.1). The island extends over a length of ~ 360 kilometres and lies to the northwest of Australia. The island is flanked to the north by the Flores Basin and to the south by the Savu Basin, and has at least 13 active volcanoes. Liang Luar is situated ~ 550 m above mean sea level within a wide river valley cut into reefal (coral reef) carbonates of Miocene-Early Pliocene age.

Stalagmites LR07-A8 and LR07-A9 were collected *in situ* from a large block of cave breakdown which had rotated approximately 45° some time after growth had stopped. The specimens were located in a chamber situated ~ 600 m from the cave entrance and beneath ~ 30 - 50 m of soil and bedrock. The deep chamber is cut off from the outside world by a series of narrow passage-ways and rock falls, inhibiting air flow and thus inducing a high relative humidity (close to 100%). Mean annual temperature (MAT) at the collection site is a stable $\sim 25^{\circ}\text{C}$, which closely resembles the MAT of the surface (Griffiths et al., 2009).

Flores provides an ideal locality from which to study palaeoclimate because it resides in the climatically sensitive, seasonally-dry southern sector of the IPWP: the largest source of heat on Earth and thus a major driver of the global atmosphere circulation. This “heat-source” is influenced by ENSO variability, with modern La Niña events bringing higher than average sea-surface temperatures (SSTs) for the region (Fig. 6.1) while the opposite occurs during El Niño events (Smith et al., 2008). Regional rainfall is dominated by the AISM system, which accounts for ~69% (~800 mm) of the precipitation that is deposited annually. The highly seasonal pattern of rainfall is characterised by a replacement of the dry southeasterly trade winds with the convective northwesterly monsoonal winds for the months December through March. Similar to other monsoon systems, the AISM is largely driven by the land-sea thermal contrast between the north Australian land-mass and adjacent Indian Ocean. During the summer months, insolation-driven continental heating sets up a zone of low-pressure over northwest Australia, anchoring the equatorial trough and drawing in moisture laden air-masses from the north (Magee et al., 2004). The peak of the monsoon occurs from January to February where the region occupying Indonesia and northern Australia is dominated by strong westerly winds with speeds of up to $\sim 9 \text{ m s}^{-1}$. During this time, the easterly trade winds south of $\sim 15^\circ \text{ S}$ also strengthen, which sets up a line of strong cyclonic shear (termed the ‘monsoon shear line’) that divides the higher latitude easterly trades from the lower latitude monsoonal westerlies (Wheeler and McBride, 2005).

Although the land-sea thermal gradient is the dominant mechanism controlling the inter-annual variability, there are other factors which control the strength and timing of the monsoon at annual to orbital time-scales, including: (i) the strength of cross-equatorial air-flow from the Siberian High during the Asian winter monsoon and its associated control on the position of the ITCZ (Miller et al., 2005; Suppiah and Wu, 1998); (ii) Southern Hemisphere summer insolation (Wyrwoll and Valdes, 2003); (iii) Indian Ocean SST fluctuations (Liu et al., 2004); (iv) eustatic sea-level (Griffiths et al., 2009); (v) variations in modes of ocean-atmosphere circulation, such as the El Niño/Southern Oscillation and Indian Ocean Dipole (Griffiths 2010a; Wu and Kirtman, 2007); and (vi) land-cover changes (Miller et al., 2005).

The strong seasonality of precipitation on Flores is also manifested in the isotopic composition of the rainfall. Previously we have shown that seasonal variations in rainfall amount are characterised by a distinctive oxygen isotope signature: an assessment of local daily-rainfall $\delta^{18}\text{O}$ values for the 2006-2007 wet/dry season and their respective source moisture trajectories using back-trajectory analyses indicate that northwesterly sourced monsoon moisture is isotopically depleted ($\sim 7\text{‰}$) relative to easterly-sourced

air masses (Griffiths et al., 2009). Because source moisture variations within the IPWP are too small to account for this difference (Brown et al., 2006), the seasonal isotopic discrepancy is likely due to the intense vertical uplift and distillation of water vapour during the summer monsoon. Climate model simulations of rainfall $\delta^{18}\text{O}$ variability within the wider Asian monsoon domain, using the ECHAM-4 Atmospheric General Circulation Model fitted with stable isotope tracers, show that local precipitation amounts are anti-correlated with rainfall $\delta^{18}\text{O}$ anomalies throughout the tropical west Pacific. This is consistent with observations from the International Atomic Energy Agency-Global Network of Isotopes in Precipitation (IAEA-GNIP) (International Atomic Energy Agency/World Meteorological Organization, 2004), whereby higher rainfall periods are characterised by more depleted $\delta^{18}\text{O}$ values while drier phases have a more enriched isotopic signature (Vuille et al., 2005).

6.3 Materials and methods

6.3.1 Sample description and preparation

LR07-A8 and LR07-A9 (Fig. 6.2) are relatively thin, elongated stalagmites measuring 300 mm and 400 mm in length, respectively. Both specimens were cut longitudinally down the centre and set in clear casting resin prior to analysis. Interior surfaces were polished to accommodate visual inspection of individual growth laminae. They consist of slightly opaque, compact calcite with highly parallel, tabular laminations with no sign of diagenetic alteration or growth hiatuses. Sample LR07-A8 shows little overall deviation of the central growth axis. By contrast, LR07-A9 growth was slightly more complicated, with the stalagmite-forming drip point shifting laterally and episodically throughout the growth period.

6.3.2 Chronology

A total of 19 pieces of calcite, each weighing ~50 mg, were extracted from the central growth axis of LR07-A8 and LR07-A9 (Fig. 6.2). Top and basal samples were extracted using a carbide dental burr fitted to an air drill while the remaining samples were extracted using a more precise micromilling lathe. ^{230}Th – ^{234}U measurements were performed on these sub-samples using a Nu Instruments Plasma multi-collector inductively coupled plasma mass-spectrometer (MC-ICP-MS) at the University of Melbourne, Australia; see Hellstrom (2003) for a full description of the MC-ICP-MS protocol used to calculate the ages.

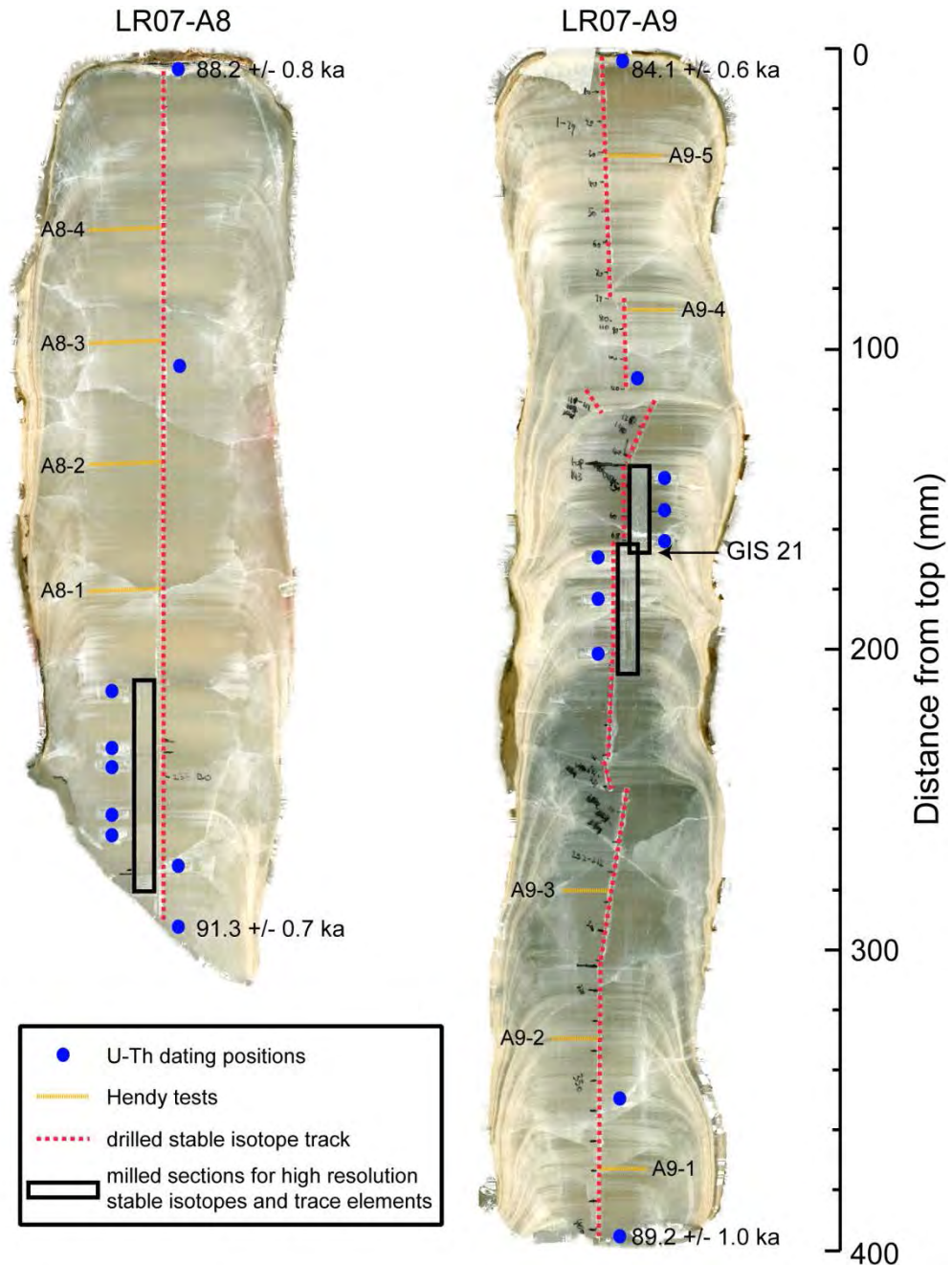


Figure 6.2 Scanned images of stalagmites LR07-A8 and LR07-A9. Blue dots indicate the positions of the 19 U/Th ages. Yellow dashed lines show the positions and names of the nine Hendy tests conducted along individual laminae. Red dashed lines show the 1-mm resolution drill-hole tracks used for the stable isotopes. Black boxes indicate the micro-milled sections used for high-resolution (0.25 mm) analysis of stable isotopes and trace elements. Also indicated is the approximate mid-point position of GIS 21.

6.3.3 Oxygen and carbon isotope measurements

Sample powders for stable isotope analyses were drilled at continuous 1-mm increments along the vertical axis of LR07-A8 and LR07-A9. Each slab was mounted to a moving stage where it was

drilled using a Taig CNC micromilling lathe using a 1-mm carbide drill bit. Higher resolution micromilling (250 μm increments) was conducted along two target time-slices — between 85.7 - 86.3 ka (TS1) and 89.4 - 90.2 ka (TS2) — to resolve finer-scale details through two major isotopic excursions (Fig. 6.2). Owing to the highly tabular laminations, both specimens were ideally suited for high-resolution microsampling.

The stable isotope ratios of the low (1 mm increments) and high resolution (250 μm increments) samples (total of 1190 $\delta^{18}\text{O}$ and $\delta^{13}\text{C}$ analyses for both LR07-A8 and LR07-A9) were analysed from CO_2 gas produced by reaction of ~ 1 mg powders with 105% phosphoric acid at 70 °C. The measurements were performed on a GV Instruments GV 2003 continuous-flow isotope ratio mass spectrometer at the University of Newcastle, Australia. The results are expressed as parts per mil (‰) relative to the Vienna Pee Dee Belemnite (VPDB) standard using an internal working standard of Carrara Marble (NEW1), which was calibrated against the international standards NBS18 and NBS19. Mean analytical uncertainty of the standards was 0.06‰ for $\delta^{18}\text{O}$ and 0.03‰ for $\delta^{13}\text{C}$.

Additional stable isotopes were run on powders extracted from nine individual growth laminae throughout LR07-A8 and LR07-A9 (Fig. 6.2). Each layer was drilled horizontally at 1-mm increments from the central growth axis outwards. The isotopes were then analysed in an effort to assess whether the stalagmites had been deposited in isotopic equilibrium [i.e. the so-called “Hendy Test” (Hendy, 1971)]. The measurements (total of 81 $\delta^{18}\text{O}$ and $\delta^{13}\text{C}$ analyses) were performed on an automated individual-carbonate reaction Kiel device coupled to a Finnigan MAT-251 dual-inlet stable isotope mass spectrometer at the Research School of Earth Sciences at The Australian National University. Calcite subsamples weighing 180-220 μg were reacted with anhydrous 103% H_3PO_4 at 90 °C to liberate CO_2 for isotopic analysis. The results were normalised to the VPDB scale such that NBS19 yields $\delta^{18}\text{O}$ VPDB (-2.20‰) and $\delta^{13}\text{C}$ VPDB (+1.95‰), and NBS18 yields $\delta^{18}\text{O}$ VPDB (-23.0‰) and $\delta^{13}\text{C}$ VPDB (-5.0‰). Analytical precision of the standards was ± 0.06 ‰ for $\delta^{18}\text{O}$ and ± 0.03 ‰ for $\delta^{13}\text{C}$.

6.3.4 Trace elements

Replicate trace element analyses were conducted on several sections of LR07-A8 and LR07-A9 (Fig. 6.2). These subsections, identical to those used for the high-resolution stable-isotope analysis, were cut into small slabs, embedded in clear casting resin, and polished prior to analysis. Trace elements were measured parallel to the growth axis using excimer laser-ablation inductively coupled mass spectrometry

(LA-ICP-MS) within the School of Earth Sciences, The University of Melbourne, Australia. A suite of elements were analysed (Ca, Mg, Sr, Ba, P, Y, La, Al, S, Mn, Fe, Cu, Zn, Pb, U, and Th) using a Varian 810 quadrupole ICP-MS equipped with a Lambda Physik Compex 110 ArF excimer pulsed laser ablation system of wavelength 193 nm; see Woodhead et al. (2007) for a more detailed description of the technique. Here I focus on those elements that have the highest correlations with each other (i.e. Mg, Sr, P, and Y).

Prior to analysis, each sample was pre-cleaned in a teflon beaker of double de-ionised water inserted in an ultrasonic bath for 15 minutes to remove any surface impurities. Replicates were carried out for each section along two parallel laser scans spaced 3 mm apart to check for spatial homogeneity and reproducibility. To ensure analyses were conducted on a clean surface, each scan line was pre-ablated twice at 10 Hz using a rectangular spot size of $250\text{ }\mu\text{m} \times 50\text{ }\mu\text{m}$ and a scan speed of 20 mm min^{-1} . Actual measurements were conducted by pulsing the laser beam again at 10 Hz, but with a reduced spot size of $150\text{ }\mu\text{m} \times 25\text{ }\mu\text{m}$ and slower scan speed of 1.2 mm min^{-1} . Sample intensities were converted to parts per million (ppm) using the NIST612 glass standard, which was ablated before, during, and after each sample run. The software program “Iolite” (<http://iolite.earthsci.unimelb.edu.au/>) was used to process the data, which amongst other things involves background subtraction, calibration and drift correction.

6.4 Results

6.4.1 Chronology

The stable isotope and trace element time-series for stalagmites LR07-A8 and LR07-A9 were anchored by nine and ten $^{230}\text{Th} - ^{234}\text{U}$ dates, respectively. With the exception of two samples, the ages for both stalagmites lie in stratigraphic order (within dating uncertainty) and show that LR07-A8 grew from 91.3 ± 0.7 to 88.2 ± 0.8 ka and LR07-A9 from 89.2 ± 1.0 to 84.1 ± 0.6 ka. The measured U and Th isotope ratios used to calculate the ages are shown in Table 6.1. The U concentration of LR07-A8 ranges between 7.5 and 28.5 ng g^{-1} with an average of 15.5 ng g^{-1} while the U for LR07-A9 ranges between 8.0 and 26.3 ng g^{-1} with an average of 13.2 ng g^{-1} . The $^{230}\text{Th}/^{232}\text{Th}$ ratios are relatively high (1272 - 15719), indicative of negligible detrital thorium contamination within majority of samples. All ages have been corrected for initial thorium contamination.

Table 6.1 Summary of MC-ICP-MS U-Th age data (ka) for stalagmites LR07-A8 and LR07-A9 from Liang Luar Cave. “U ng g⁻¹” is uranium content of the sample. Activity ratios were determined by the methods described in Hellstrom (2003) and the supplementary materials of Drysdale et al. (2005). The corrected (corr.) ²³⁰Th ages were calculated using equation 1 of Hellstrom (2006) using half-lives specified in Cheng et al., 2000.

Sample I.D.	U ng g ⁻¹	Depth (mm)	[²³⁰ Th/ ²³⁸ U]	±2σ	[²³⁴ U/ ²³⁸ U]	±2σ	[²³² Th/ ²³⁸ U]	±2σ	[²³⁰ Th/ ²³² Th]	Corr. ²³⁰ Th age	±2σ	Corr. initial [²³⁴ U/ ²³⁸ U]	±2σ
LR07-A8/1	7.5	5.0	0.6131	0.0032	1.0925	0.0024	0.000067	0.000002	9183.8	88.167	0.775	1.1185	0.0030
LR07-A8/2	28.5	105.0	0.6057	0.0031	1.0810	0.0026	0.000287	0.000002	2107.9	87.963	0.784	1.1040	0.0032
LR07-A8/3	24.3	187.0	0.6190	0.0024	1.0887	0.0024	0.000039	0.000002	15719.0	90.020	0.630	1.1145	0.0030
LR07-A8/4	14.7	203.8	0.6176	0.0018	1.0920	0.0021	0.000087	0.000001	7087.4	89.218	0.487	1.1185	0.0026
LR07-A8/5	8.1	223.8	0.6208	0.0024	1.0935	0.0027	0.000229	0.000002	2707.7	89.625	0.654	1.1206	0.0033
LR07-A8/6	22.9	245.5	0.6228	0.0029	1.0983	0.0022	0.000084	0.000002	7419.5	89.495	0.702	1.1267	0.0028
LR07-A8/7	10.2	262.0	0.6279	0.0016	1.1021	0.0022	0.000151	0.000001	4154.8	90.049	0.470	1.1318	0.0027
LR07-A8/8	14.1	273.0	0.6315	0.0026	1.1066	0.0021	0.000050	0.000003	12583.6	90.284	0.629	1.1377	0.0026
LR07-A8/9	9.2	285.0	0.6375	0.0028	1.1088	0.0018	0.000089	0.000001	7182.5	91.269	0.659	1.1407	0.0022
LR07-A9/1	13.1	5.0	0.6111	0.0026	1.1210	0.0026	0.000053	0.000001	11472.1	84.067	0.620	1.1535	0.0031
LR07-A9/2	8.0	110.0	0.6131	0.0044	1.1224	0.0029	0.000460	0.000018	1331.8	84.071	0.964	1.1554	0.0035
LR07-A9/3	5.2	145.0	0.6223	0.0027	1.1224	0.0029	0.000221	0.000002	2812.7	86.109	0.675	1.1563	0.0035
LR07-A9/4	26.3	156.0	0.6166	0.0026	1.1147	0.0023	0.000484	0.000003	1272.8	85.724	0.633	1.1463	0.0029
LR07-A9/5	8.1	167.0	0.6184	0.0032	1.1200	0.0021	0.000065	0.000001	9563.5	85.708	0.711	1.1530	0.0026
LR07-A9/6	14.4	170.5	0.6143	0.0019	1.1120	0.0023	0.000044	0.000001	14034.7	85.883	0.485	1.1429	0.0028
LR07-A9/7	11.3	187.5	0.6157	0.0017	1.1133	0.0025	0.000094	0.000001	6563.5	85.973	0.477	1.1446	0.0030
LR07-A9/8	21.0	203.8	0.6125	0.0020	1.1059	0.0020	0.000307	0.000009	1997.5	86.110	0.499	1.1352	0.0025
LR07-A9/9	13.0	355.0	0.6140	0.0039	1.0903	0.0028	0.000159	0.000003	3873.0	88.615	0.942	1.1161	0.0035
LR07-A9/10	12.0	399.0	0.6272	0.0044	1.1075	0.0022	0.000387	0.000007	1621.5	89.167	1.008	1.1382	0.0028

The age-depth models were calculated using a Bayesian-Monte Carlo approach implemented in two stages using Wavemetrics Igor Pro software. A full description of the technique can be found in Drysdale et al. (2005, 2007). From the age models (Fig. 6.3), it is evident that both speleothems grew continuously throughout their growth history. Noteworthy, two spurious ages were excluded from the age-model calculations on the grounds that, although given the 95% error bars could possibly be valid ages, they are somewhat anomalous relative to the sequence of ages around them. Moreover, on the day these samples were being analysed the MC-ICP-MS instrument was not running particularly well (the other ages were run on a different day); at the time of submission these ages were being reanalysed. Inclusion of the two anomalous ages in the age-model calculations would mean that the growth rates between ~110 and 180 mm for LR07-A8 and between ~110 and 160 mm for LR07-A9 would be exceptionally rapid.

There is no physical evidence in the growth layer pattern of either speleothem (i.e. the visible layers have been determined to be annual based on physical laminae counting and trace-element peaks) nor their shape (they do not increase in diameter, which would happen if there was more drip water entering the cave) to indicate this.

The age models indicate that the rate of extension for stalagmite LR07-A8 ranges between 11 and 138 mm ka⁻¹ throughout the 91-88 ka interval. This pattern is characterised by a slower extension rate of ~13 mm ka⁻¹ during initial growth, followed by an abrupt increase at ~90 ka where the extension rate averaged ~135 mm ka⁻¹. This abrupt increase may represent a perturbation in the infiltration rate above the stalagmite due to a change in the climate. However, the slow growth preceding this may indicate that the speleothem grew over a surface that was not perpendicular to the drip angle [as appears to be the case judging by the inclined base of LR07-A8 (Fig. 6.2)], which would have inhibited vertical extension during the early stages of formation. In contrast, LR07-A9 appears to have had a much more consistent growth rate (Fig. 6.3), with much less overall variability. For example, the growth rate ranged from 48 to 80 mm ka⁻¹ and averaged 61 mm ka⁻¹ through the 89-84 ka interval, much slower than LR07-A8.

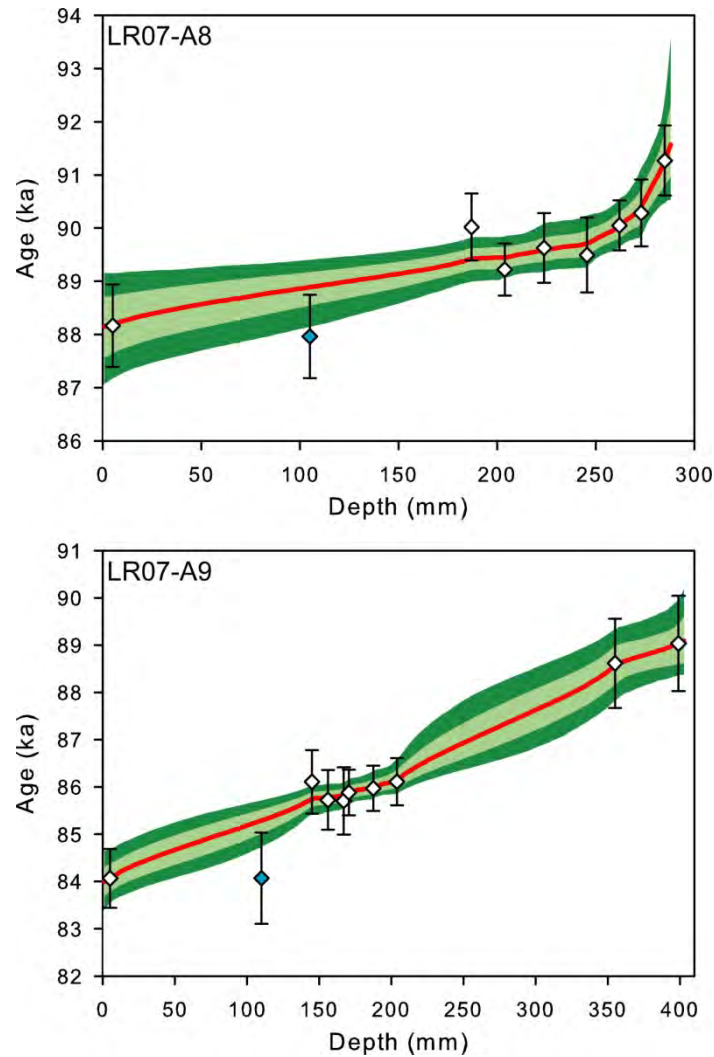


Figure 6.3 Age-depth models for stalagmites LR07-A8 (upper) and LR07-A9 (lower). The symbols indicate each date along with its respective 2σ uncertainty. The red line indicates the derived age model, while the green shading represents 1σ and 2σ error envelopes. The two anomalous ages (blue diamonds) were not included in the age-model calculations.

6.4.2 Isotopic equilibrium precipitation

An essential prerequisite for environmental-climate based interpretations of the speleothem $\delta^{18}\text{O}$ is assessing whether or not the calcite was deposited in isotopic equilibrium with respect to the cave dripwaters. Non-equilibrium calcite fractionation can occur if the degassing of CO_2 is too rapid for the stable isotopes to equilibrate with the water and bicarbonate ion (Hendy, 1971). This can lead to Rayleigh fractionation of the isotopes, generating higher values than those expected from equilibrium precipitation

at the same temperature and same $\delta^{18}\text{O}$ of drip-water. I have employed a number of tests and observations to assess the possibility of these processes contaminating the signal.

First, both specimens were collected from deep within the cave passage (~600 m from the entrance) where humidity was high (close to 100%) and air-flow low; hence, non-equilibrium deposition of the calcite due to evaporative processes would be negligible (Fairchild et al., 2006). Second, a series of ‘Hendy tests’ were conducted on nine individual growth laminae located throughout the longitudinal axes of stalagmites LR07-A8 and LR07-A9 (Fig. 6.1). Isotopic values are plotted as distance (in mm) away from the central growth axis. Results of the Hendy tests reveal that the majority of tested growth laminae do not vary by more than 0.5‰—the maximum threshold value used to infer isotopic equilibrium deposition as defined by Hendy (1971)—away from the central growth axis (Fig. 6.3). Third, another means of determining equilibrium deposition is the replication of $\delta^{18}\text{O}$ profiles from different stalagmites within the same cave: it is highly unlikely that two (or more) speleothems would produce similar isotopic profiles if both formed under non-equilibrium conditions. The $\delta^{18}\text{O}$ profiles for stalagmites LR07-A8 and LR07-A9 show remarkable similarities for the periods of overlap (Fig. 6.4). Lastly, there is a significant relationship between the $\delta^{18}\text{O}$ and trace-element time-series (namely Mg, Sr, Y, and P) through the two time-slices (Fig. 6.5). Because these trace elements are primarily controlled by hydrological processes acting upon time-constant geological sources within the karst system, the strong coherence with the $\delta^{18}\text{O}$ suggests that the isotopes are dominated by climatic processes external to the cave environment.

The above discussion argues for the precipitation of stalagmites LR07-A8 and LR07-A9 under (or close to) isotopic equilibrium conditions. Hence, the $\delta^{18}\text{O}$ of the two stalagmites may be interpreted in terms of variations in the $\delta^{18}\text{O}$ of the drip water (and hence rainfall) from which the speleothem grew.

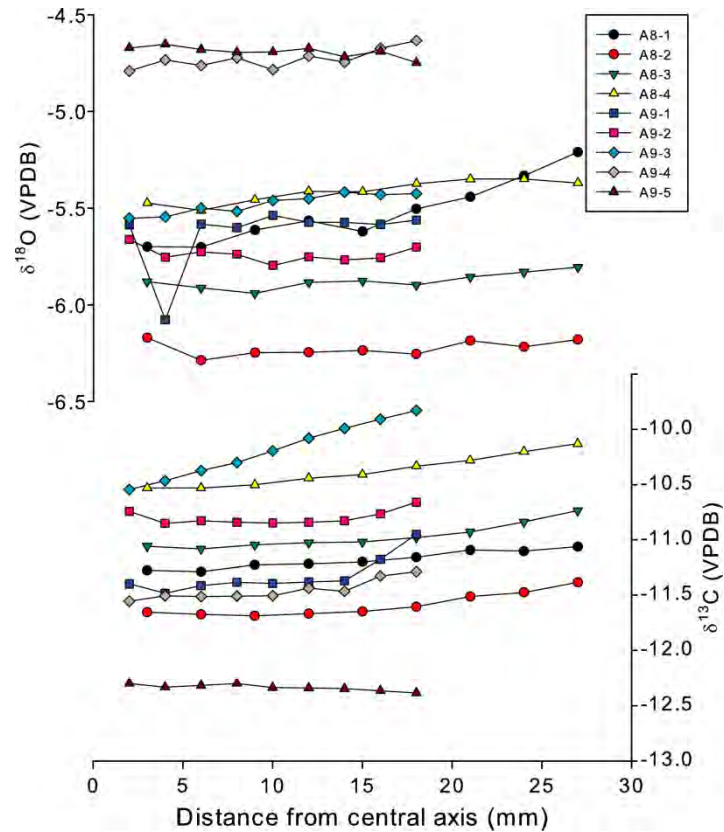


Figure 6.4 Hendy tests conducted on nine individual growth laminae throughout stalagmites LR07-A8 and LR07-A9. Colour coded symbols represent the names of each laminae corresponding to their longitudinal positions indicated in Fig. 6.2. Laminae with $\delta^{18}\text{O}$ variability $\leq 0.5\%$ are assumed to have been deposited in isotopic equilibrium where the $\delta^{18}\text{O}$ reflects that of the drip-water, rather than non-equilibrium fractionation (Hendy, 1971).

6.4.3 Stable isotopes

Based on the age models calculated for both stalagmites (Fig. 6.3), the average resolution of the stable isotope measurements for the entire length of LR07-A8 and LR07-A9 was 5 and 7 years, respectively (Fig. 6.5). In addition, the high-resolution sampling through TS1 and TS2 yielded isotopic measurements spaced every ~ 2 -3 years. Throughout the 91 to 84 ka period the spliced² $\delta^{18}\text{O}$ record averages -5.4‰ and ranges from -7.0‰ to -4.2‰ , while the spliced $\delta^{13}\text{C}$ record averages -10.9‰ and ranges from -12.6‰ to -8.8‰ .

The lower-resolution $\delta^{18}\text{O}$ and $\delta^{13}\text{C}$ profiles display differences in the long-term trends (Fig. 6.5) while showing remarkable similarities at the decadal to centennial scale (Fig. 6.6a). The detrended spliced

² The spliced records were constructed by averaging the stable isotopes of stalagmites LR07-A8 and LR07-A9 for the period of overlap. Before averaging, the LR07-A8 record (~ 5 year resolution) was interpolated to the lower temporal resolution record of LR07-A9 (~ 17 year resolution) for the period of overlap. The $\pm 2\sigma$ deviation for the overlapping section was used as an error envelope around the spliced record.

records have a positive covariance over the 91 to 84 ka interval ($r = 0.43$; $n = 570$; $p < 0.01$). The higher-resolution records also display strong covariance (through 85.7 – 86.3 ka: $r = 0.41$, $n = 260$, $p < 0.01$, Fig. 6.6b; through 89.4 – 90.2 ka: $r = 0.71$, $n = 256$, $p < 0.01$, Fig. 6.6c) (Table 6.2).

The combined LR07-A8 and LR07-A9 $\delta^{18}\text{O}$ time series demonstrates a slight decreasing trend from 91 to ~89.6 ka followed by a ~2‰ monotonic increase throughout the remainder of the record (Fig. 6.5). The combined $\delta^{13}\text{C}$ records demonstrate a similar pattern from 91 to ~85.8 ka. However, in contrast to the $\delta^{18}\text{O}$ record, which continues to increase, the $\delta^{13}\text{C}$ record displays an abrupt ~2‰ shift to a new mean state where values thereafter remain relatively constant (Fig. 6.5). Superimposed upon the $\delta^{13}\text{C}$ trends (and, to a lesser extent, the $\delta^{18}\text{O}$) are a number of decadal- to centennial-scale isotopic excursions, the most prominent of which are the two large (~2-3‰) and abrupt negative shifts in the carbon isotopes centred at ~85.8 ka and ~89.6 ka (Fig. 6.5).

The U/Th-inferred growth rates of LR07-A8 and LR07-A9 portray a distinct similarity to the stable isotopes, particularly through the two prominent isotope excursions (Fig. 6.5). For example, the growth rate of LR07-A8 increased rapidly from ~30 mm ka⁻¹ to ~150 mm ka⁻¹ at ~89.6 ka, with the transition occurring over a period comparable (within dating uncertainty) to that of the isotopes. A similar but lower magnitude change in growth rate of LR07-A9 is also observed: from ~50 mm ka⁻¹ to ~80 mm ka⁻¹ at ~85.8 ka.

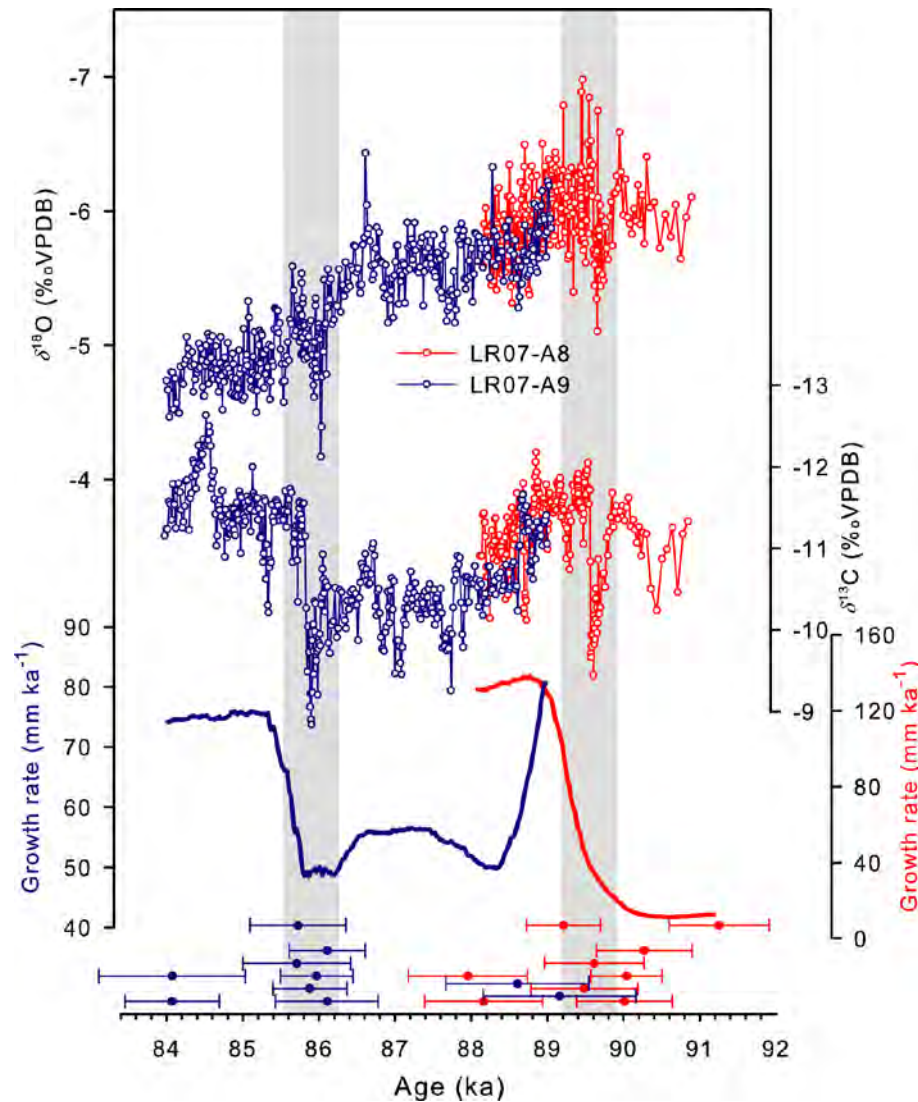


Figure 6.5 Comparison of the combined $\delta^{18}\text{O}$ and $\delta^{13}\text{C}$ records with the growth rate curves for stalagmites LR07-A8 (red) and LR07-A9 (blue). The positions of the U/Th ages used to construct the age models and growth rates are shown along the bottom. The gray shading highlights two isotopic excursions that coincide with start of increased growth rates. These intervals are examined in finer detail in the next section.

6.4.4 Trace elements

The LA-ICP-MS trace-element analyses through the TS1 and TS2 are plotted in Figures 6.6b and 6.6c and correlation statistics are summarised in Table 6.2. Statistically significant correlations are revealed between the trace elements and the stable isotopes through TS2 (Table 6.2b), with the highest coefficient occurring for Mg vs. $\delta^{18}\text{O}$ (+0.64) and Mg vs. $\delta^{13}\text{C}$ (+0.86). In contrast, the relationships between the stable isotopes and trace elements through TS1 (Table 6.2a), while still significant (with the exception of $\delta^{13}\text{C}$ vs. both P and Sr), are not as strong. Amongst the trace elements, the strongest

correlation coefficients through TS2 are observed between Sr and P (-0.71), P and Mg (-0.68), and Mg and Y (-0.66). Weaker correlations include Sr vs. Mg (+0.56), P vs. Y (+0.56) and Sr vs. Y (-0.51). The strongest correlations through the TS1 interval are observed between Sr and Mg (+0.53), P and Y (+0.49) and Sr and P (-0.38), whilst weaker correlations are found for Sr vs. Y (-0.33), Mg vs. Y (-0.30) and P vs. Mg (-0.09). A noteworthy point is that, while the correlation coefficient for P vs. Mg is one of the highest through TS2 (-0.68), it is the lowest during TS1 interval (-0.09). The high correlation coefficients between the trace elements and stable isotopes strongly argue for a similar or linked causal mechanism controlling the concentration of all elements within the speleothems.

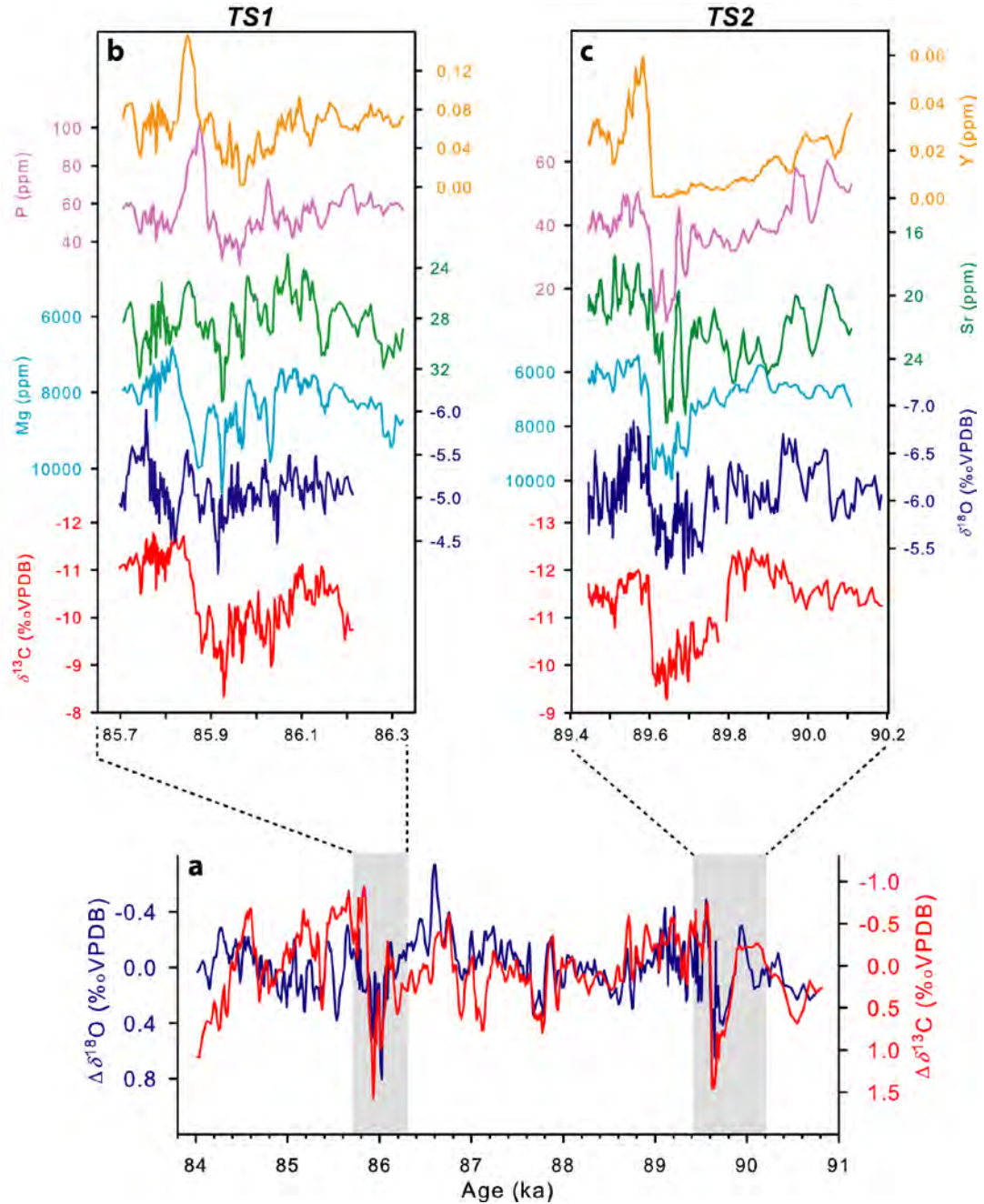


Figure 6.6 (a) Comparison of the $\delta^{18}\text{O}$ and $\delta^{13}\text{C}$ records for the spliced time-series of talagmites LR07-A8 and LR07-A9. The spliced record was obtained by averaging the stable-isotope values for the period of overlap (i.e. ~88–89 ka). Both records were also detrended to highlight the decadal- to centennial-scale coherence between the two records. The detrended $\delta^{18}\text{O}$ ($\Delta\delta^{18}\text{O}$) and $\delta^{13}\text{C}$ ($\Delta\delta^{13}\text{C}$) records have a significant correlation coefficient ($r = 0.43$). (b) High-resolution analysis of stable isotopes and trace elements through TS1 (85.7–86.3 ka) and (c) TS2 (89.4–90.2 ka). Trace elements have been smoothed with a 5-point running mean.

Table 6.2 Correlation matrix of the stable isotope and trace element transects through (a) TS1 (89.4 – 90.2 ka; $n=260$) and (b) TS2 (89.4 – 90.2 ka; $n=252$). Prior to analysis, trace element profiles were interpolated to the same depth scale (0.25 mm resolution) as the stable isotopes. All series were detrended prior to analysis. Bold values are significant at the $P < 0.01$ level.

Element	$\delta^{18}\text{O}$	$\delta^{13}\text{C}$	Mg	Y	P	Sr
(a) Transect through TS1 (85.7 – 86.3 ka)						
$\delta^{18}\text{O}$	–	0.41	0.24	-0.31	-0.21	0.18
$\delta^{13}\text{C}$		–	0.54	-0.49	-0.15	0.07
Mg			–	-0.30	-0.09	0.53
Y				–	0.49	-0.33
P					–	-0.38
Sr						–
(b) Transect through TS2 (89.4 – 90.2 ka)						
$\delta^{18}\text{O}$	–	0.71	0.64	-0.59	-0.52	0.39
$\delta^{13}\text{C}$		–	0.86	-0.63	-0.62	0.35
Mg			–	-0.66	-0.68	0.56
Y				–	0.56	-0.51
P					–	-0.71
Sr						–

Through TS2, the Mg, Y, P, and Sr time-series all show structural similarities with each other and the stable-isotope profiles (Fig. 6.6c). Most notably, beginning at ~ 90.2 ka, all elements display a slight trend which terminates with an abrupt step-change at ~ 89.6 ka. The average Mg and Sr values for the interval post-dating this transition were $\sim 24\%$ and $\sim 15\%$, respectively, lower than the interval preceding it, while the P and Y values were 47% and 683% , respectively, higher.

The trace elements through TS1 (Fig. 6.6b) also show similar structural coherence with each other and the stable isotopes. Similar to TS2, the trace element profiles (with the exception of Sr) are characterised by a slow-ramping trend followed by a rapid change, coincident with the change in stable isotopes at ~ 85.8 ka. However, the transition of the elements in TS1 is not as large and abrupt as it is during TS2. For example, P and Y show an 8% and 56% increase, respectively, through the transition while Mg only shows a 9% decrease; there is no significant change in Sr ($<3\%$).

6.5 Discussion

6.5.1 Interpretation of the stable isotopes

6.5.1.1 $\delta^{18}\text{O}$

The slow increase in $\delta^{18}\text{O}$ values over the combined LR07-A8 and LR07-A9 record (Fig. 6.7a) reflects the coupled influence of cave air-temperature and cave drip-water composition. Based on previous studies of Liang Luar stalagmites (Griffiths et al., 2009, 2010a, 2010b), I interpret the $\delta^{18}\text{O}$ composition of the drip-water to reflect that of the recharge rainfall, which is controlled by rainfall amount, global ice-volume (and hence sea-level), seasonality, and vapour-condensation temperatures (McDermott, 2004).

The relationship between air temperature and $\delta^{18}\text{O}$ of precipitation is highly non-linear (i.e. the fractionation factor for $^{18}\text{O}/^{16}\text{O}$ changes constantly with changing temperature). At the poles, the thermometer works nicely because the change in $\delta^{18}\text{O}$ of snow per $^{\circ}\text{C}$ is large ($\sim +0.7\text{‰ }^{\circ}\text{C}^{-1}$) (Dansgaard, 1964), while in the tropics it is much harder to extract because the temperature component is small ($\sim +0.1\text{‰ }^{\circ}\text{C}^{-1}$) (Gat and Gonfiantini, 1981) and is typically masked by other factors (such as air-mass transport). Nevertheless, it still has some influence on the rainfall- $\delta^{18}\text{O}$ signal preserved in tropical speleothems. Opposing this effect is the negative relationship between $\delta^{18}\text{O}$ of calcite and drip-water temperature ($\sim -0.24\text{‰ }^{\circ}\text{C}^{-1}$) (Craig, 1965) during calcite precipitation. Taken together, the two opposing effects have a net temperature influence on speleothem $\delta^{18}\text{O}$ of $\sim -0.14\text{‰ }^{\circ}\text{C}^{-1}$ for this region. Thus, if the $\delta^{18}\text{O}$ of LR07-A8 and LR07-A9 were solely driven by temperature, the observed $\sim 2\text{‰}$ increase through MIS 5a/b would require a temperature decrease of $\sim 14^{\circ}\text{C}$, which is approximately seven times the estimated $\sim 2^{\circ}\text{C}$ SST range from nearby marine records during the last glacial (Stott et al., 2002). Worth noting, however, is that recent Liang Luar temperature reconstructions (during the Holocene) from stalagmite fluid inclusions (Griffiths et al., 2010b) suggest that tropical air-temperature anomalies during high-latitude climate events (e.g. the Younger Dryas) may have in fact been larger than previously estimated from IPWP marine sediments (e.g. Stott et al., 2004). Therefore, it is quite difficult to remove the exact temperature component from the stalagmite $\delta^{18}\text{O}$ given the current lack of accurately-dated and high-resolution temperature records from the IPWP during MIS 5a/b. At this stage, the best I can do is to estimate a $\sim 2^{\circ}\text{C}$ temperature influence which explains $\sim 14\text{‰}$ ($\sim +0.28\text{‰}$) of the $\sim 2\text{‰}$ shift.

In light of the above discussion, I attribute most of the Liang Luar $\delta^{18}\text{O}$ variability to other factors associated with regional rainfall, which are controlled by ocean-source changes (related to the

“global ice-volume effect”) and variations in air-mass transport (i.e. amount, intensity, and/or seasonality). Fluctuations in the $\delta^{18}\text{O}$ composition of ocean-source waters can likely be ruled out as a dominant influence given the relatively minor changes in global ice-volume during this time (Shackleton et al., 2000). Therefore, most of the 91 ka to 84 ka speleothem $\delta^{18}\text{O}$ record must represent mean changes in isotope fractionation between the site of evaporation and the cave site.

Previously, we have shown that the average composition of annual rainfall- $\delta^{18}\text{O}$ in Flores represents the balance of moisture between the summer-wet (more depleted in ^{18}O) and winter-dry (more enriched in ^{18}O) seasons and/or the intensity of the summer monsoon system (Griffiths et al., 2009). Strong correspondence of $\delta^{18}\text{O}$ and trace elements in a Holocene stalagmite (Griffiths et al., 2010a) argues for a rainfall amount-dominated $\delta^{18}\text{O}$ signal preserved in the calcite. This finding is now confirmed in this study (see Fig. 6.6 and Table 6.2). However, it must be noted that a smaller fraction of the variance may represent changes in the contribution of summer versus winter rainfall, which would have had an impact on the $\delta^{18}\text{O}$ composition of the speleothems. Notwithstanding the above, I interpret the steady increase in $\delta^{18}\text{O}$ during the 91 to 84 ka period to primarily reflect a gradual decrease in the AISM system.

In contrast to previous interpretations, in which we call for eustatic sea-level being the dominant AISM climate forcing in the region (Griffiths et al., 2009, 2010a, 2010b), the pattern of AISM variability during MIS 5a/b closely matches the summer insolation curve at 20°S (i.e. over the north Australian continent) (Fig. 6.7a), with higher insolation corresponding with lower $\delta^{18}\text{O}$ values and *vice versa* with lower insolation. A possible reason for this discrepancy is that the magnitude of sea-level change through MIS 5a/b (Shackleton et al., 2000) was much smaller compared to that of the last deglaciation. Hence, in the absence of a major sea-level shift insolation took over as the prime forcing mechanism. Modeling simulations (e.g. Marshall and Lynch, 2008) have shown that higher summer insolation results in the AISM-ITCZ being pulled further south than would otherwise be the case during periods of lower insolation because of greater continental heating (and hence a greater land-sea thermal contrast) during the summer months. Under this scenario, a more southerly displaced ITCZ would result in the incursion of more depleted $\delta^{18}\text{O}$ rainfall in Flores because of higher summer rainfall amounts and thus a greater contribution of summer (lower $\delta^{18}\text{O}$) versus winter (higher $\delta^{18}\text{O}$) rainfall. This pattern of variability is in-phase with monsoon records from southern Brazil (Cruz et al., 2005; Wang et al., 2007; Fig. 6.7b) but anti-phased with those from East-Asia (Fig. 6.7c).

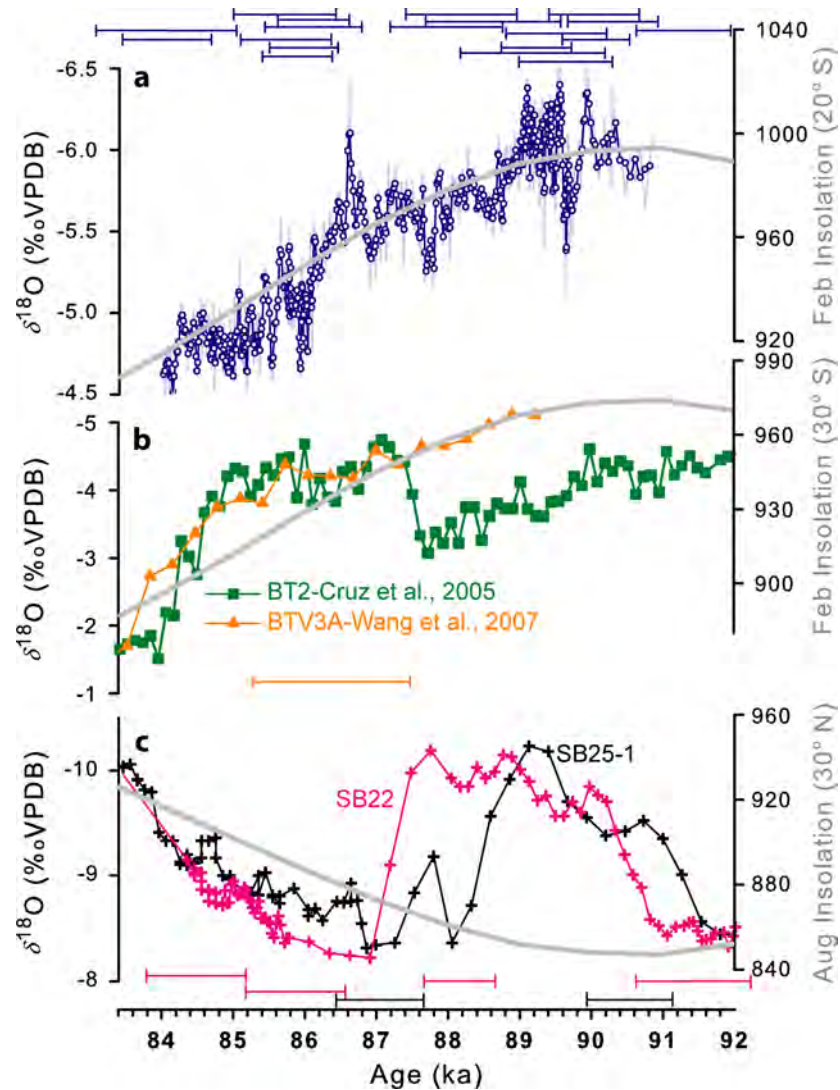


Figure 6.7 Comparison of stalagmite $\delta^{18}\text{O}$ records between (a) Liang Luar Cave, Flores, (b) Boutevera Cave, Brazil (Cruz et al., 2005; Wang et al., 2007), and (c) Sanbao Cave, China (Wang et al., 2008). The gray curves represent summer insolation at the respective cave latitudes. The y-axis for the $\delta^{18}\text{O}$ curves in (a) and (b) have been inverted for clarity. The open circles in (a) show a 3-point running mean. Colour-coded error bars for the U/Th ages used to constrain the isotopes for each record are also shown.

6.5.1.2 $\delta^{13}\text{C}$

Assuming calcite precipitation in isotopic equilibrium, the $\delta^{13}\text{C}$ of the carbonate should be the same as that of the dissolved inorganic carbon (DIC) of the parent solution as per the fractionation factor. Possible factors controlling the dissolved inorganic carbon (DIC) of the Liang Luar cave drips include: (i) the intensity of bedrock carbonate (CaCO_3) dissolution during seepage flow (Fairchild et al., 2006; Genty et al., 2003); and (ii) changes in the isotopic composition of CO_2 sourced from the soil and atmosphere (Genty et al., 2001). The $\delta^{13}\text{C}$ composition of the cave calcite, however, may also be affected by

degassing processes at equilibrium (Scholz et al., 2009) or in-cave kinetics, when degassing is forced by ventilation (Spötl et al., 2005). This issue cannot be completely ruled out for Liang Luar as it has not been possible to carry out annual monitoring of cave air CO₂ fluxes (e.g. Baldini et al., 2008; Spötl et al., 2005) because of the logistical constraints. However, the macromorphology of the speleothems suggest that variations in the drip rate have not been large enough to modify the shape of the specimens (from candle to cone-shaped), thus precluding the inference that the DIC $\delta^{13}\text{C}$ ratios were affected by prolonged degassing caused by an increase in elapsed time between successive drips (e.g. see Mühlinghaus et al., 2007). The micromorphology and fabric characteristics of the speleothems also suggest that the speleothems were always wetted by a thin film of fluid that spread evenly from the impact point to the equilibrium diameter. Hence, the $\delta^{13}\text{C}$ composition at any point of the stalagmite surface should be the same, or slightly heavier towards the external margin of the stalagmite; with the exception of a few laminae, the Hendy tests demonstrate that this assumption is valid. One last important factor which can control the $\delta^{13}\text{C}$ of cave calcite is fluctuations in the rates of CO₂ degassing caused by shifts in cave atmospheric circulation (Spötl et al., 2005). However, this process is unlikely to be significant given that the $\delta^{13}\text{C}$ and growth rates do not positively covary (Fig. 6.5); if this process were significant, one would expect a positive relationship between the $\delta^{13}\text{C}$ and growth rates because increased CO₂ degassing enhances the supersaturation of the solution, promoting faster calcite precipitation and leading to higher ^{13}C enrichment of the speleothem (Cruz et al., 2006). Therefore, it can be assumed that the speleothem calcite was precipitated in equilibrium with respect to the $\delta^{13}\text{C}$ ratios and, as a consequence, assume that the $\delta^{13}\text{C}$ directly reflects that of the parent-water DIC.

Preliminary ^{14}C activities measured in a Holocene stalagmite (Griffiths et al., unpublished data) indicate that most of the carbon (80-90%) in Liang Luar stalagmites comes from the soil, a result that bears similarities with temperate cave systems (e.g. Genty et al., 2001). A small percentage (10% to 20%) pertains to old carbon, which may come from old organic matter in the soil zone or from the host rock dissolution, possibly contributing to the shifts in DIC C isotope ratios to more positive values. Overall, the $\delta^{13}\text{C}$ content of LR07-A8 and LR07-A9 is interpreted to be mostly controlled by soil (microbial activity) processes above the cave system, and in-part by physicochemical processes affecting percolation waters along the karst flow-path.

The Liang Luar $\delta^{13}\text{C}$ record (Fig. 6.8c) displays a broad similarity with the GISP2 ice-core CH₄ (Grachev et al., 2007) (Figs 6.8a) and $\delta^{18}\text{O}$ (Grootes and Stuiver, 1997) (Fig. 6.8b) values, as well as the

atmospheric CO₂ concentrations of the Byrd ice core (Ahn and Brook, 2008) (Fig. 6.8d). Most notably, there is a large (~3‰) and abrupt negative $\delta^{13}\text{C}$ excursion [also present in the $\delta^{18}\text{O}$ and trace elements, albeit not as pronounced (Fig. 6.6b)] centred on ~85.8 ka that coincides with a period of increased speleothem growth (Fig. 6.5c). This matches the timing (within dating uncertainty) of GIS 21. The nature of this abrupt $\delta^{13}\text{C}$ shift bears a strong resemblance to the rapid increase in Greenland ice-core CH₄ (Fig. 6.8a) and $\delta^{18}\text{O}$ (Fig. 6.8b) values during the onset of GIS 21, in contrast to the monotonic temperature trends observed in Antarctic ice cores (Fig. 6.8e and 6.8f). Therefore, it is evident that Liang Luar $\delta^{13}\text{C}$ values reflect phenomena that were tightly coupled with North Atlantic temperature oscillations and atmospheric CH₄ variability during the MIS 5a/b transition. In terms of placing the carbon isotopes into a climatological framework, the question then becomes: what is (are) the dominant climate-driven parameter(s) controlling the $\delta^{13}\text{C}$ in stalagmites LR07-A8 and LR07-A9?

Previously we have shown that the decadal- to centennial-scale $\delta^{13}\text{C}$ variability of a Liang Luar stalagmite was controlled by degassing of percolation waters and prior calcite precipitation (PCP) (Griffiths et al., 2010a), a conclusion drawn from the strong positive covariance of the carbon isotopes with the Mg/Ca ratios (Fairchild et al., 2000). This geochemical process, which results in ^{13}C enrichment of the drip-waters and hence stalagmites, also appears to be a dominant driver of the shorter-term isotopic changes in LR07-A8 and LR07-A9, again because of the high $\delta^{13}\text{C}$ vs. Mg correlation through both TS1 and TS2 (Table 6.2; Figs 6.6b and 6.6c). Alternatively, $\delta^{13}\text{C}$ values may be controlled by water-rock interaction times whereby periods of prolonged water residence time (i.e. drier intervals) may result in a greater contribution of $\delta^{13}\text{C}$ -enriched C being incorporated into the seepage water and thus into the speleothem calcite. Notwithstanding this, both of these explanations [which are compounded by the strong correlation of the $\Delta\delta^{13}\text{C}$ and $\Delta\delta^{18}\text{O}$ records (Table 6.2; Fig. 6.6a)] imply that shorter-term fluctuations in $\delta^{13}\text{C}$ are influenced by hydrological processes in the epikarst, which are dominated by the amount of effective recharge at the surface. Noteworthy is the lack of long-term coherence between the $\delta^{18}\text{O}$ and $\delta^{13}\text{C}$ trends (Fig. 6.5) through the 84 to 91 ka interval, suggesting that while hydrological processes may have dominated the higher-frequency variability, the millennial-scale trends were controlled by factors other than effective recharge (e.g. temperature).

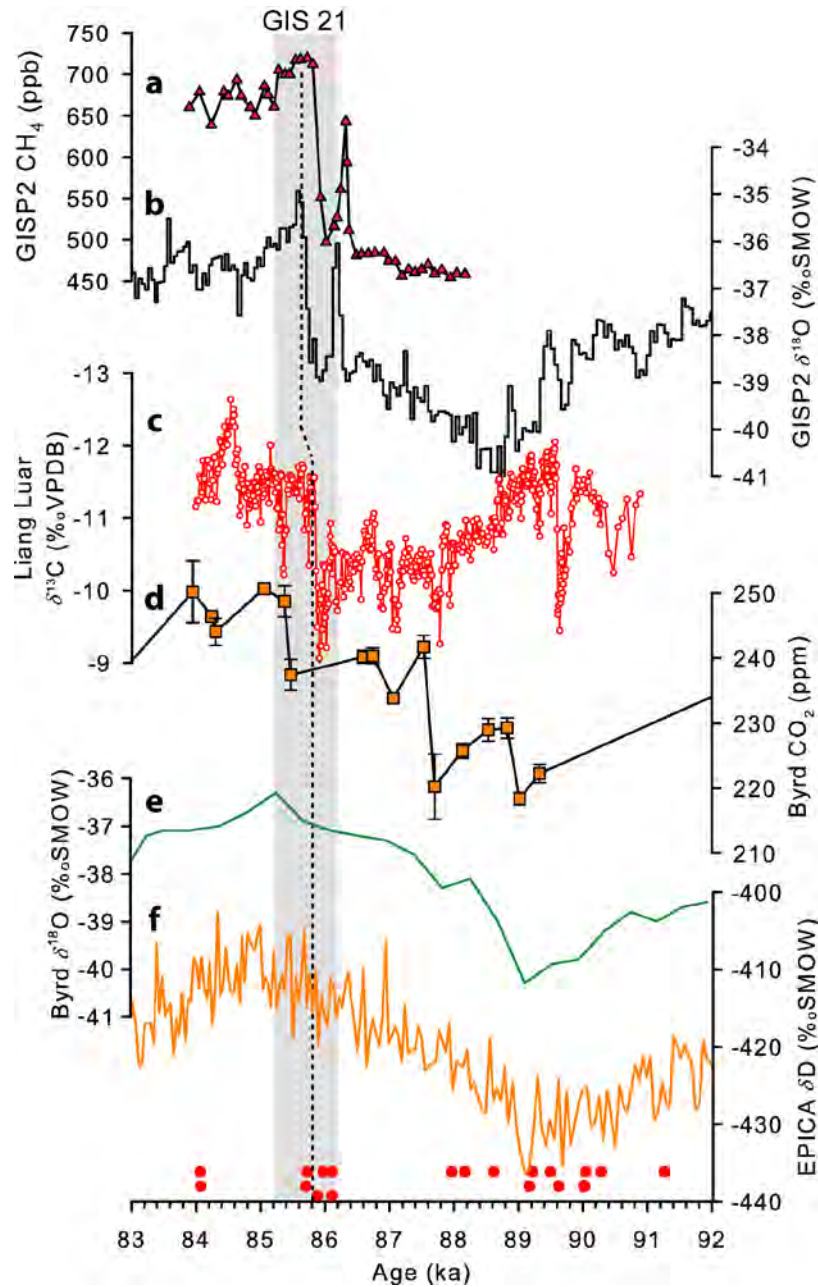


Figure 6.8 Comparison of the Liang Luar stalagmite $\delta^{13}\text{C}$ record (c), with (a) CH_4 (Grachev et al., 2007) and (b) $\delta^{18}\text{O}$ (Grootes and Stuiver 1997) concentrations from the GISP2 ice-core, (d) CO_2 (Ahn and Brook, 2008) and $\delta^{18}\text{O}$ records from the Byrd ice core, and (f) dD from the EPICA ice core record (Members, 2006). The gray shading highlights the abrupt negative shift in stalagmite $\delta^{13}\text{C}$ values coincident with the abrupt CH_4 and $\delta^{18}\text{O}$ excursions during the onset of GIS 21. The positions of the speleothem radiometric ages are shown along the bottom (red dots). All ice-core records have been placed on the most up-to-date EPICA time-scale (Lemeux-Dudon et al., 2010), which employed a stratigraphic marker (i.e. a tephra layer) at 92.5 ± 2 ka. All ice-core records were subsequently synchronised to the new EPICA time-scale by linearly interpolating between the 'old' and 'new' EPICA time-scale and then applying these adjustment factors to the GISP2 CH_4 and $\delta^{18}\text{O}$ ice-core records and the Byrd CO_2 and $\delta^{18}\text{O}$ ice-core records. This resulted in all records being shifted back in time by ~ 2 ka. The Byrd time-scale was on the GISP2 time-scale prior to adjustment.

Similar to interpretations of speleothem carbon isotopes from subtropical (Cruz et al., 2006) and temperate cave systems (Genty et al., 2006; Hellstrom et al., 1998), it is argued that the most likely explanation for the millennial-scale $\delta^{13}\text{C}$ trends is variations in the amount of biogenic CO_2 supply to the soil waters from plant respiration and microbial activity, which are influenced by both temperature and precipitation (McDermott, 2004). Increased temperatures and/or precipitation above the cave would enhance the production of soil CO_2 , resulting in a greater proportion of isotopically depleted carbon being incorporated into the groundwater and consequently leading to a lower $\delta^{13}\text{C}$ signature preserved in Liang Luar stalagmites. For example, the onset of abrupt warming in Greenland during GIS 2.1 may have increased the average temperature and/or precipitation in Flores, triggering an upsurge of soil microbial activity and vegetation density, and hence a greater proportion of ^{13}C -depleted biogenic CO_2 being dissolved into the seepage water. The synchronous $\delta^{18}\text{O}$ and trace element anomalies support this contention (Figs 6.6b). However, the magnitudes of the shifts are somewhat more subdued with respect to the $\delta^{13}\text{C}$. Thus, while precipitation changes likely had some influence on carbon cycling above Liang Luar, it was changes in temperature that probably had the more dominant effect on soil processes during this time.

An alternative, and somewhat complementary, factor influencing the soil CO_2 and hence speleothem $\delta^{13}\text{C}$ is the CO_2 concentration of the atmosphere. Similar centennial-scale patterns observed between the Liang Luar $\delta^{13}\text{C}$ record (Fig. 6.8b) and the CO_2 of air-bubbles entrapped in the Byrd ice core (Fig. 6.8c; Ahn and Brook, 2008), suggest a possible link between the isotopic composition of the soil and atmospheric CO_2 during the last glacial. However, establishing a direct causal link between atmospheric- and soil- CO_2 is quite complex because it is difficult to ascertain whether the atmospheric CO_2 is an indirect driver of biogenic CO_2 due to its influence on global temperatures or whether it plays a more active forcing role on the soil CO_2 . The strong connection between higher growth rates and lower $\delta^{13}\text{C}$ values suggests that temperature variations dominated carbon cycling above Liang Luar because higher temperatures promote microbial activity and hence biogenic CO_2 supply to the seepage waters. This would increase bedrock dissolution and hence drip water Ca^{2+} concentrations, a major controller of speleothem growth rates (Genty et al., 2001). Growth rates may also be influenced by effective recharge at the surface because periods of higher rainfall can result in faster drip rates and hence higher growth rates (Kaufmann and Dreybrodt, 2004). Cruz et al. (2006) found a similar link between the $\delta^{13}\text{C}$ of a Late-

Pleistocene stalagmite and atmospheric CO_2 , with higher $\delta^{13}\text{C}$ values corresponding with lower CO_2 concentrations in the Vostok ice core (Petit et al., 1999) and *vice versa*.

6.5.2 Environmental controls on the trace elements

The synchronous behaviour observed between the trace-element and stable-isotope ratios through TS1 and TS2 provides robust support for all proxies being driven by similar or linked forcing factors, most likely of which is the climate. The processes controlling the incorporation of trace elements into the speleothem CaCO_3 are extremely complex (Borsato et al., 2007; Fairchild and Treble, 2009). Most studies have focused on elements which form divalent cations in solution and that substitute for Ca in the crystal lattice, such as Mg and Sr. The degree to which these elements exist in the calcite phase relative to that of solution is referred to as the partition coefficient (Gascoyne, 1983), which may vary according to changes in temperature, precipitation rate, crystal surface structure, or other aspects of solution composition (e.g. Paquette and Reeder, 1990, 1995; Staudt et al., 1994; Temman et al., 2000). In contrast, other elements (such as Y, P, U, and Th) may be incorporated in CaCO_3 via fine detrital particles or sub-micron-sized colloids transported by water (Borsato et al., 2007). Higher concentrations of such elements in speleothems would thus correspond with higher infiltration rates (Fairchild and Treble, 2009). Below, I describe in detail the environmental factors controlling the incorporation of several trace-element species into stalagmites LR07-A8 and LR07-A9 through the two ~1 ka time-slices.

6.5.2.1 Magnesium and Strontium

Previous studies have linked variations in trace elements, particularly Mg and Sr, to changes in source water composition, cave air temperature and growth rate (e.g. Borsato et al., 2007; Fairchild et al., 2000; Gascoyne, 1992). By comparing the Mg/Ca ratios from stalagmite tips between temperate and tropical cave systems, Gascoyne (1983) demonstrated a positive relationship between the partition coefficient of Mg (D_{Mg}) and temperature. Huang and Fairchild (2001) subsequently confirmed this D_{Mg} -temperature relationship through laboratory testing of inorganic calcite precipitated under karst-analogue conditions. However, they noted that the temperature dependence of D_{Mg} is rather small and would typically be masked by the much larger variations in the Mg/Ca of the drip-water (Huang and Fairchild, 2001); this has previously been linked with fluctuations in karst hydrology (Fairchild et al., 2000; Fairchild and Treble, 2009; Roberts, 1998). In contrast, the partition coefficient for Sr (D_{Sr}) is influenced

by the speleothem growth rate, with faster growth rates corresponding to higher Sr/Ca ratios and *vice versa* (Borsato et al., 2007; Huang and Fairchild, 2001). Although, the Sr/Ca variability cannot be solely driven by calcite crystal growth kinetics because changes in Sr/Ca are generally too large to be explained by growth rate alone (Fairchild et al., 2006). Consequently, previous studies have also linked Sr variability to changes in effective palaeohydrology (Cruz et al., 2007; Fairchild et al., 2000; Treble et al., 2003).

The strong positive covariation between the Sr and Mg (Fig. 6.9; Table 6.2) implies similar or linked forcing processes controlled their concentration. As previously mentioned, the highly significant positive correlation between the Mg and $\delta^{13}\text{C}$ is a strong indicator for both elements being controlled by PCP (Fairchild and Treble, 2009), a process that involves percolation waters becoming supersaturated in CaCO_3 from degassing within the vadose aquifer and thus leading to calcite precipitation ‘upstream’ of the drip site. PCP has been used to infer dry conditions because reduced water flow through the karst fracture network can enhance ventilation and trigger CO_2 degassing, leaving the waters enriched in the trace element with respect to Ca. Because the D_{Mg} and D_{Sr} values are typically much less than one, the result is a much larger reduction in Ca compared to the trace element and thus a higher trace element to Ca ratio during drier conditions (Fairchild and Treble, 2009). Previous studies have shown that a strong Mg-Sr covariation is a good indicator that shorter-term (i.e. seasonal to annual) fluctuations in the elements are driven by PCP (Johnson et al., 2006; McMillan et al., 2005; Verheyden et al., 2000). Moreover, Cruz et al. (2007) and Griffiths et al. (2010a) demonstrated that these systematic covariations can indicate that PCP also occurred over much longer time-scales (i.e. centennial to orbital).

On the other hand, the much higher concentrations of Mg relative to Sr in the Liang Luar stalagmites, and also the much larger amplitude shifts through TS1 and TS2, suggests that alternative processes may have been more dominant. For example, selective leaching of Mg and Sr from the host-rock (Fairchild et al., 2000), modulated by the karst aquifer switching between an open and closed system during different hydrological states, may have controlled the elemental variability. Drier intervals would favour closed system conditions, causing enrichment in $\delta^{13}\text{C}$ values (due to a greater contribution of isotopically enriched C from the host-rock being incorporated into the seepage water) and parallel enrichment in Mg and Sr via a higher water/rock interaction. Further, lower Sr concentrations in the speleothem may point to the fact that the reefal facies above the cave have been diagenised and as such a large proportion of the Sr is gone, relative to the Mg.

Despite the various possible mechanisms controlling the Mg and Sr in LR07-A8 and LR07-A9, their strong covariation with the $\delta^{13}\text{C}$ and $\delta^{18}\text{O}$ values strongly argues for them being predominantly driven by hydrological processes above the cave via PCP and/or selective leaching effects with prolonged water-rock contact times (Fairchild et al., 2000). There are, however, additional factors (such as cave air-temperature and speleothem growth-rate) which must also be considered. For example, one possible reason for the lack of a significant mean shift in the Sr (as compared with the Mg) during TS1 (Fig. 6.6a) may be that the increased speleothem growth rate through this transition had a buffering effect on the Sr: increased growth rates can increase the Sr concentration of speleothems, and the sharp rise in growth rate of LR07-A9 through the transition into GIS 21 may have inhibited the Sr from following the same pattern as the Mg. Further, some of the observed Mg variability through the two intervals, particularly GIS 21, may be explained by fluctuations in cave air temperature. However, the effect of temperature on D_{Mg} is minor compared to typical changes in drip-water composition (Fairchild and Treble, 2009).

6.5.2.2 Phosphorous and Yttrium

Electronegative P and trivalent Y concentrations within LR07-A8 and LR07-A9 are likely to be associated with the transport of these elements from the soil to the cave system. In tropical soils, P may be present as inorganic orthophosphate and/or within phosphate and phosphonate groups occupying humic substances (Myneni, 2002). Phosphate sorption in soils is minimised between pH 4 and 6 (Giesler et al., 2005), implying that desorption may occur in the upper soil horizon where similar pH values are found during warmer/humid conditions. A significant amount of the bioavailable soil P can be leached, with the amount depending on soil hydrology (Pote et al., 1999). The incorporation of P into speleothem calcite depends on the relative proportion of free ions versus inorganic and organic colloidal-forms, which is currently unknown at Liang Luar. For the free ion, high pH in the cave waters (i.e. when degassing or dissolution of the host rock is maximised, depending on the cave system) would promote adsorption by maximizing the concentration of PO_4^{3-} ions (see for example Burton and Walter (1990)).

Numerous studies have linked lower speleothem P concentrations to colder and drier conditions when both vegetation and soil activity is reduced (Fairchild and Treble 2009). Heathwaite (1997) demonstrated that dissolved P (at concentrations of 80-1700 ppb) became dominant following the first autumnal storm events because soluble P was flushed from the soils where P-uptake may have been restricted by water availability. P supply in caves also appears to be related to higher water infiltration

rates (and vegetation activity die-back or slow down). For example, at Grotta di Ernesto (NE Italy), Huang et al. (2001) discovered an annual P cycle in the speleothem calcite, which they attributed to a seasonal flush of the soil from heavy autumnal rains. More recently, Borsato et al. (2007) confirmed this annual P cycle in speleothems from the same cave, which they associated with the autumnal period of maximum soil infiltration and vegetation die-back. P concentrations measured in speleothems from Moondyne Cave (southwest Australia) displayed a close relationship with the instrumental rainfall record (Treble et al., 2003), with lower P coinciding with periods of lower rainfall and *vice versa*.

I interpret the patterns of P variability in LR07-A8 (Fig. 6.9b) and LR07-A9 (Fig. 6.9a) to be consistent with the above studies, whereby increases in P concentration reflect higher infiltration rates and hence higher rainfall. This finding is supported by the strong correspondence of the P with the other trace elements. However, this relationship is much weaker in LR07-A9 (TS1) compared with LR07-A8 (TS2), which may be due to site-specific differences in the hydrological pathways between the two stalagmites and/or differences in the climate-driven parameters controlling the P concentration between both intervals. This discrepancy is mirrored in the calcite fabric: LR07-A9 displays a clear change from translucent to more opaque calcite through the large negative P anomaly while LR07-A8 does not.

Y has similar characteristics to heavy rare earth elements (REE) in that it forms strong complexes with electronegative organic ligands (Tyler, 2004), which facilitate its leaching from soils. Desorption of Y is significantly reduced in alkaline rather than acidic soils (Wen et al., 2002). Furthermore, Y leaching from soils under alkaline conditions will strongly depend on the mobility of organic substances to which Y is bound. Hence, acidic soil conditions favour Y desorption.

In terms of Y transport into cave systems, and hence speleothems, Borsato et al. (2007) found that Y was preferentially transported into Grotta di Ernesto during intense infiltration events. The authors reported an increase in the abundance of Y during the early 20th century, which they interpreted to reflect a period of deforestation rather than a climatic anomaly. Hence, enhanced infiltration may be due to both higher rainfall and/or deforestation because both processes can promote more active bacterial degradation and efficient infiltration. Based on the significant correlation of the Y with the other trace elements and stable isotopes (Table 6.2), I interpret the speleothem Y concentration to reflect infiltration episodes related to rainfall variability at the surface. Higher Y values thus correspond with higher rainfall periods and *vice versa*. Therefore, Y can provide an additional palaeoclimate proxy with which to confirm the stable isotope patterns in Liang Luar speleothems.

6.5.3 Summary of stable-isotope and trace-element results

In summary, the overall strong covariation between the stable isotopes and trace elements through TS1 and TS2 suggests that the higher-frequency variability in all proxies is dominated by hydrological processes above the cave system. The positive correlation between the $\delta^{13}\text{C}$, Mg and Sr values is a strong indicator that all three were controlled by PCP during drier periods when dewatered conduits above the cave favoured CO_2 degassing and hence calcite precipitation of seepage waters upstream of the drip-site (Fairchild and Treble, 2009). However, the significant difference in concentration between Mg and Sr may indicate that other processes, such as selective leaching related to enhanced water-rock contact times, may have been more dominant. Either way, higher $\delta^{13}\text{C}$, Mg and Sr values are indicative of drier conditions and *vice versa*. This pattern of variability is supported by the strong positive relationship of these proxies with the atmosphere-controlled $\delta^{18}\text{O}$. As mentioned above, I interpret the $\delta^{18}\text{O}$ to be controlled by the strength of the AISM such that a weaker monsoon (i.e. reduced amount and/or intensity of rainfall during the Austral summer) corresponds with higher $\delta^{18}\text{O}$ values. Hence, the fact that all four proxies move in the same direction robustly argues for all of them being driven by the same environmental processes, namely the climate.

The Y and P are interpreted to reflect infiltration rates of water down through the soil-bedrock profile, because both of these elements are primarily transported into the cave via soil colloids. Hence, during higher recharge events a greater proportion of colloidal movement facilitates the transport of Y and P into the speleothems. Therefore, higher Y and P concentrations reflect higher rainfall periods and *vice versa*. Whilst this pattern is opposite to that observed in the stable-isotope and Mg and Sr records, there is a significant anti-correlation between them, adding further support to a climate-controlled signal preserved in all the proxy records.

6.5.4 Influence of GIS 21 in the southern Indo-Pacific

The advancement of knowledge regarding climatic links between the Indo-Pacific and high latitudes during the last glacial has been hindered by the lack of radiometrically dated high-resolution records from the tropical region. Hence, there is still a great degree of uncertainty into the possible teleconnections between Indonesia/northern Australia and the polar latitudes during known climate turning points (e.g. GISs and Heinrich events).

The high concentration of U/Th dates through speleothem LR07-A9, added with the high-resolution ($\sim 1\text{--}3$ year) stable-isotope and trace-element measurements, has permitted the timing and structure of GIS 21 to be established with great precision (Figs 6.9 and 6.10). Based on our age model, the commencement of GIS 21 in Flores occurred at 85.9 ± 0.3 ka, coincident with the $\delta^{18}\text{O}_{\text{ice}}$ and CH_4 excursions preserved in the GISP2 ice core (Grachev et al., 2007; Grootes and Stuiver, 1997). From the LR07-A9 $\delta^{13}\text{C}$ record it is apparent that the duration of the shift from stadial to interstadial conditions (i.e. through GIS 21) occurred over a period of ~ 100 years (Fig. 6.10c), similar to that of the GISP2 CH_4 (Fig. 6.10a). In contrast, the GISP2 $\delta^{18}\text{O}_{\text{ice}}$ appears to have taken ~ 300 years to reach full stadial conditions following its commencement. However, this increased response-time may reflect the differences in sampling resolution between the different proxies. Nevertheless, it is interesting to note the rapid response of the Australasian climate system to perturbations far-afield. Noteworthy, is the large gap in the age model post-dating the GIS 21 transition (i.e. between ~ 110 and 160 mm) in LR07-A9. While further dating to improve the age model through this interval is desirable, it will not alter the timing of the climate excursion in the speleothem, and hence the overall conclusions of this chapter. This is because the position of the large $\delta^{13}\text{C}$ excursion is bounded by a total of 6 U/Th ages, resulting in an age uncertainty that exceeds the Greenland record by a factor of three (Fig. 6.9).

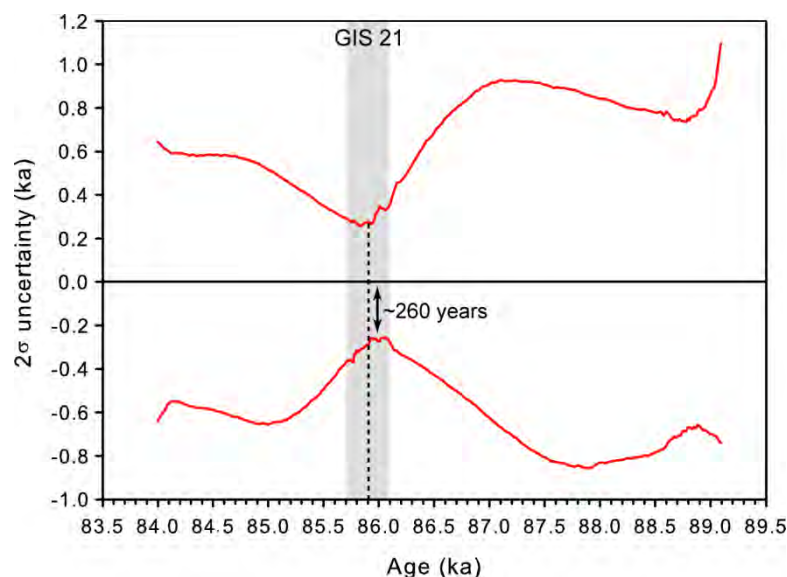


Figure 6.9 Age-uncertainty-versus-age plot for stalagmite LR07-A9 calculated from the U/Th age-model - see Drysdale et al. (2005, 2007) for details of the methods used to calculate this plot. The gray bar brackets GIS 21 in Liang Luar while the dashed line shows the commencement of this event as highlighted in Figure 6.10. Note the minimal uncertainty in the speleothem chronology during GIS 21 owing to the high concentration of U/Th ages through this interval. The timing of the event is thus extremely well constrained.

As noted above, the stable isotopes and trace elements display strong synchronicity throughout TS1 (i.e. 85.7 – 86.3 ka). However, whilst all elements exhibit a marked change at 85.9 ka, the $\delta^{18}\text{O}$ (Fig. 6.9d) and trace-element (Fig. 6.9e) perturbations are short lived and are followed by a retraction towards the mean state prior to the shift. In contrast, the $\delta^{13}\text{C}$ values post-dating the shift are on average $\sim 2\%$ lower than those values preceding it. Hence, despite the fact that the $\delta^{18}\text{O}$ and trace-element profiles display a brief negative anomaly, the $\delta^{13}\text{C}$ record exhibits a significant step-change in values from one steady state to another. This disparity may suggest that a temperature-controlled shift in $\delta^{13}\text{C}$ was not accompanied by the same degree of variation in monsoon strength through GIS 21. Further evidence to support this contention is the abrupt increase in speleothem growth rate through the GIS 21 transition (6.10d). As previously mentioned, growth rate is highly dependent upon surface temperature because of its impact on soil microbial activity and hence biogenic CO_2 supply to the seepage waters (Genty et al., 2001). Thus, the fact that the $\delta^{18}\text{O}$ and trace elements do not portray a similar magnitude shift to the growth rate is a strong indicator that the $\delta^{13}\text{C}$ change represents a shift in temperature rather than rainfall.

The absence of a major ASM swing through GIS 21 is quite surprising given the large perturbation in $\delta^{13}\text{C}$, indicative of a change in vegetation and temperature. It is also surprising given the sensitivity of other monsoon systems to high-latitude temperature anomalies. For example, speleothem records from the East-Asian land-mass have documented a strong physical link between the strength of the East-Asian summer monsoon (EASM) and North Atlantic climate fluctuations. Wang et al. (2001) showed that abrupt negative shifts in calcite $\delta^{18}\text{O}$ (indicative of a more intense summer monsoon) from Hulu Cave (China) resembled similar positive excursions in the GISP2 ice core (indicative of warmer conditions) from Greenland. Hence, this clearly shows that there were almost synchronous teleconnection patterns linking the Asian monsoon system with North Atlantic temperature oscillations over the past ~ 75 ka. Conversely, monsoon records from South American speleothems show weaker monsoon conditions during high-latitude warm periods (Wang et al., 2007), suggestive of a strong anti-phasing between these northern and southern low-latitude sites. Periodic shifts in the ITCZ has been the favoured explanation for these opposing signals; for example, higher North Atlantic temperature anomalies correspond with a northerly displaced ITCZ while lower temperatures correspond with a more southern ITCZ position.

Based on the above discussion, it is apparent that southern Indo-Pacific temperature swings may not govern regional atmospheric circulation patterns, at least over longer time-scales. This is in concert with the findings of Oppo et al. (2009) who showed, using geochemical tracers from IWPW marine

sediments, that cooler SSTs during the ‘Little Ice Age’ were paralleled by higher precipitation, the opposite of what one would expect if SSTs were a controlling factor on rainfall. Moreover, we previously reported a decrease in Liang Luar temperatures during the Younger Dryas cold stage, which was mirrored by an increase in the AISM. Therefore, while an annual- to decadal-scale coupling of temperature and precipitation in the southern Indo-Pacific is clear from the strong covariation between the $\Delta\delta^{18}\text{O}$ and $\Delta\delta^{13}\text{C}$ records (Fig. 6.5) (and also evident in modern settings), millennial-scale perturbations in IPWP precipitation may not be driven by local SSTs (and thus air temperatures), but rather by larger scale circulation patterns associated with the position of the ITCZ.

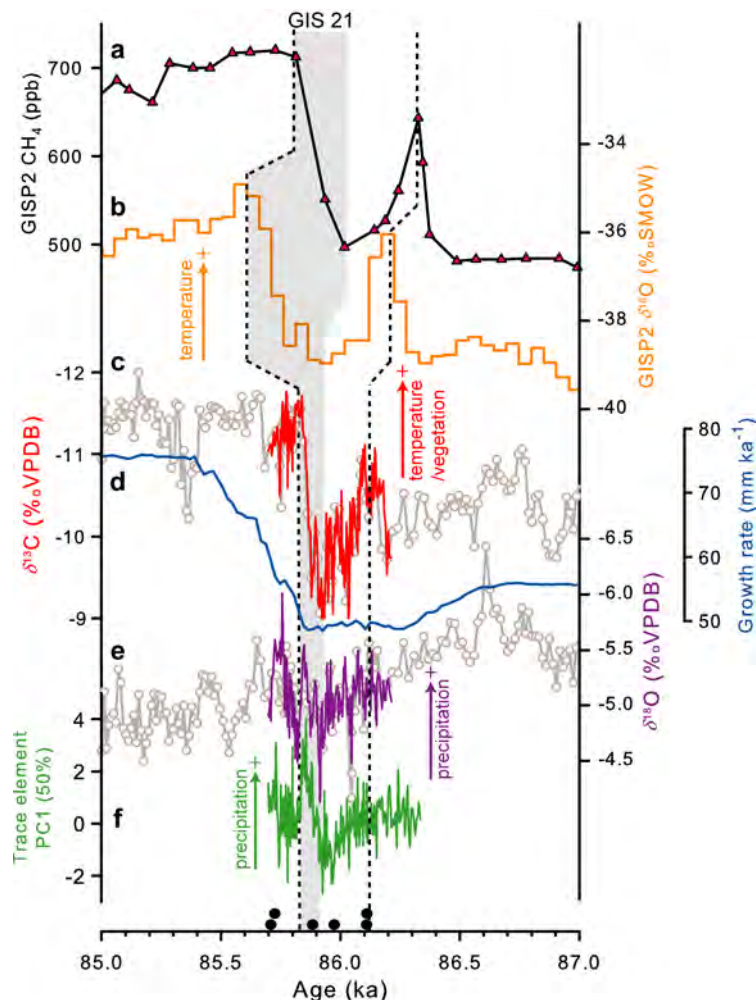


Figure 6.10 Comparison of GISP2 (a) CH_4 (Grachev et al., 2007) and (b) $\delta^{18}\text{O}_{\text{ice}}$ (Grootes and Stuiver 1997) with (c) $\delta^{13}\text{C}$, (d) growth rate (e) $\delta^{18}\text{O}$ and (f) the first principal component (PC1) of the trace elements from stalagmite LR07-A9 for the period 85-87 ka. PC1 was obtained from the elements Mg, Sr, Y, and P and explains 50% of the variance. The coloured lines in (c) and (e) represent the high-resolution (0.25 mm) stable-isotope measurements while the gray circles show the lower resolution (1 mm) analyses. The gray shading highlights the duration of the transition of each proxy into GIS 21. The dashed vertical lines indicate the approximate timing of GIS 21, and the isotopic anomaly just prior-to, in the CH_4 , $\delta^{18}\text{O}_{\text{ice}}$, and stalagmite $\delta^{13}\text{C}$. Black dots at the bottom of the figure show radiometric ages for LR07-A9.

The evidence presented suggests that there was a strong teleconnection between the northern hemisphere and Indo-Pacific during GIS 21. This is also supported by regional sea-surface conditions during GISs. SST reconstructions from the Mg/Ca concentration of planktonic foraminifera — *Globigerinoides ruber*— in marine core MD2181 (Stott et al., 2002), shows systematic increases in IPWP SSTs and corresponding decreases in salinity during GISs. Moreover, a recent decadal-resolved continuous SST reconstruction from numerous marine cores in the Makassar Strait, Indonesia (Oppo et al., 2009), showed that IPWP SSTs were in concert with a Northern Hemisphere temperature reconstruction over the past two millennia (Mann et al., 2008). We noted a similar connection between Flores and the North Atlantic during the Younger Dryas cold stage (Griffiths et al., 2010b; see Chapter three), where the combined $\delta^{18}\text{O}$ of speleothem calcite and fluid inclusions showed a drip-water temperature anomaly of $\sim 5^\circ\text{C}$ during this event. Given these regional consistencies throughout the Indo-Pacific, the findings verify that southern IPWP temperatures had a predominant North Atlantic signal during the last glacial, compared to other Southern Hemisphere sites (e.g. Cruz et al., 2006) which indicate a more southern high-latitude signal.

The strong linkage between the Liang Luar $\delta^{13}\text{C}$ excursion (Fig. 6.10c) and the spike in GISP2 CH_4 (Fig. 6.10a) during GIS 21 adds further support to the inference that the carbon isotopes represent an abrupt increase in tropical air temperatures. The primary source of preindustrial CH_4 during glacial times was tropical soils, whereby interstadials were characterised by increased CH_4 concentrations and the opposite during stadials (Blunier and Brook, 2001). Tropical climate can control atmospheric CH_4 emissions because warmer conditions in tropical-boreal forests can stimulate methanogenesis in wetlands, which is the major natural source of methane (Grachev and Brook, 2007).

A direct causal mechanism linking the Indo-Pacific with the North Atlantic invokes perturbations in the thermohaline circulation and its inherent impact on ocean heat transport. Sudden increases in North Atlantic temperatures during GISs, resulting from the penetration of warm, salty Atlantic waters into the Nordic Seas (van Kreveld et al., 2000), may have triggered warming in the tropics, promoting soil microbial activity and subsequent outbursts of CH_4 . Consequently, the CH_4 increase may have provided a positive feedback that amplified the increase in temperatures. Exactly how North Atlantic warming triggered an abrupt temperature increase over the Indo-Pacific is not entirely clear, but may be related to oceanic circulation within the IPWP. I speculate that during GISs, the meridional temperature gradient between the equator and high northern latitudes was more subdued,

weakening the NH Hadley cell because of its lower dependency on the transport of heat northward. By contrast, the SH Hadley cell would have strengthened, resulting in the enhancement of the SH trade winds. Strengthening of the trades would have allowed a greater build up of warm ocean water over the western tropical Pacific, leading to warmer temperatures over the region (because ocean and air temperatures are tightly coupled), conditions analogous to modern La Niña events (Fig. 6.1). However, it must be recognized that this pattern may also be a local affect, given the heterogeneity of the ocean-atmosphere system. For example, an alternative, and somewhat complementary, explanation invokes local upwelling as the dominant mechanism. During modern La Niña events, the trade winds over eastern Indonesia become weakened due to the incursion of the semi-stationary low-pressure system over northern Australia (Smith et al., 2008). Weakening of the local trades would have reduced oceanic upwelling west of PNG and hence warmer sea-surface conditions would have prevailed. Support for these explanations is provided by climate model simulations (e.g. Yang et al., 2005; Zhang et al., 2005), which show that the remote impact of the extratropics can influence tropical atmosphere-ocean circulation. For example, Zhang et al. (2005) demonstrated that extratropical warming can be conveyed to the equator via the mean subduction current, resulting in a warming of the tropical thermocline. Further, this warming was shown to weaken the Hadley cells and the trade-wind induced upwelling, which in turn slowed down the meridional overturning circulation in the upper Pacific, reducing the equatorward supply of cold water. These ocean dynamical processes would act to stabilise the equatorial coupled system and result in a weaker and longer ENSO cycle.

On the other hand, some authors (e.g. Cane and Clement, 1999; Clement and Cane, 1999) have attributed these interstadial cycles to shifts in atmospheric planetary-wave patterns, controlled remotely from the tropics. This is based on the strong control that tropical SSTs exert on global atmospheric heat-transport. While this hypothesis presents an attractive alternative, it is difficult to discern whether the trigger for these events lay in the high-latitudes and the tropics merely acted as a feedback or whether the latter played a more important role.

6.6 Conclusions

Carbon and oxygen isotope ratios have been used to reconstruct the temperature and rainfall history of the Indo-Pacific region through MIS 5a/b. The detrended $\delta^{18}\text{O}$ and $\delta^{13}\text{C}$ records, which extend over the period 91 to 84 ka, have a significant positive correlation with each other, suggesting that they

were controlled by similar or linked processes over decadal to centennial time-scales. Strong positive covariation between the $\delta^{13}\text{C}$, Mg, and Sr values suggests that the higher-frequency variability in all three are driven by hydrological processes above the cave via PCP and/or selective leaching effects related to prolonged water-rock contact times. Both of these processes are enhanced during drier periods when increased degassing and/or water-rock interaction times above the cave results in higher $\delta^{13}\text{C}$, Mg, and Sr values; the converse occurs during wetter phases. Because of the strong covariation of these elements with the $\delta^{18}\text{O}$, these patterns lend strong support to the inference that the oxygen isotopes were largely driven by rainfall amounts with higher (lower) $\delta^{18}\text{O}$ values corresponding with lower (higher) rainfall.

The strong covariation of the Y and P concentrations with the other elemental and stable-isotope ratios, suggests that they are also dominated by hydrological conditions above the cave. Based on previous interpretations of Y and P transport into cave systems (e.g. Borsato et al., 2007), it is argued that both Y and P were flushed into Liang Luar via colloidal transport during high infiltration events (e.g. higher rainfall). Hence, during more intense rainfall periods (e.g. stronger monsoon) there was a greater tendency for the movement of these elements down through the soil-bedrock profile. Therefore, higher Y and P values are interpreted to reflect higher recharge events and thus provide an additional rainfall proxy with which to support the stable isotopes.

The lower-frequency variability of the $\delta^{18}\text{O}$ record displays a monotonic increase through the 91 to 84 ka interval and resembles the trend in summer insolation over the north-Australian land mass. In contrast, the $\delta^{13}\text{C}$ record portrays a long-term pattern that has a closer match to the $\delta^{18}\text{O}_{\text{ice}}$ preserved in Greenland ice cores. Most notably, the large increase in the GISP2 $\delta^{18}\text{O}_{\text{ice}}$ and CH_4 values during GIS 21 is characterised by a large and abrupt negative shift in Liang Luar $\delta^{13}\text{C}$, suggestive of a strong high northern-latitude connection with the southern Indo-Pacific during MIS 5a/b. Given the lack of significant change in the $\delta^{18}\text{O}$ and trace elements through this period, I attribute this climate link to fluctuations in the meridional temperature gradient, which controlled microbial activity in the soil zone and hence the carbon isotope concentration of the DIC in the drip-water. The close $\delta^{13}\text{C}$ -methane link adds further support to a temperature controlled carbon signal in Flores because air temperatures can strongly influence CH_4 emissions from tropical wetlands. However, it is difficult to ascertain whether the tropical temperatures and thus CH_4 increases during GIS 21 were triggered by high-latitude temperature anomalies or whether the tropics played a more active forcing role. This question will not be resolved

until further radiometric-dated and high-resolution palaeoclimate records are obtained from the Indo-Pacific.

6.7 References

- Ahn, J. and Brook, E.J., 2008. Atmospheric CO₂ and climate on millennial time scales during the last glacial period. *Science* 322, 83-85.
- Altabet, M.A., Hoggins, M.J. and Murray, D.W., 2002. The effect of millennial-scale changes in Arabian Sea denitrification on atmospheric CO₂. *Nature* 415, 159-162.
- Baldini, J.U.L., McDermott, F., Hoffmann, D.L., Richards, D.A., Clipson, N., 2008. Very high frequency and seasonal cave atmosphere *p*CO₂ variability: implications for stalagmite growth and oxygen isotope-based paleoclimate records. *Earth and Planetary Science Letters* 272, 118-129.
- Bard, E., Rostek, F., Turon, J.L. and Gendreau, S., 2000. Hydrological impact of Heinrich events in the subtropical northeast Atlantic. *Science* 289, 1321-1324.
- Berger, A., and Loutre, M.F., 1991. Insolation values for the climate of the last 10 Million Years. *Quaternary Science Reviews* 10, 297-317.
- Blunier, T. and Brook, E.J., 2001. Timing of millennial-scale climate change in Antarctica and Greenland during the last glacial period. *Science* 291, 109-112.
- Bond, G., Broecker, W., Johnsen, S., McManus, J., Labeyrie, L., Jouzel, J. and Bonani, G., 1993. Correlations between climate records from the Atlantic sediments and Greenland ice. *Nature* 365, 143-147.
- Borsato, A., Frisia, S., Fairchild, I.J., Somogyi, A. and Susini, J., 2007. Trace element distribution in annual stalagmite laminae mapped by micrometer-resolution X-ray fluorescence: Implications for incorporation of environmentally significant species. *Geochimica et Cosmochimica Acta* 71, 1494-1512.
- Broccoli, A.J., Dahl, K.A. and Stouffer, R.J., 2006. Response of the ITCZ to Northern Hemisphere cooling. *Geophysical Research Letters* 33, L01702, doi:10.1029/2005GL024546.
- Broecker, W., Bond, G., Klas, M., Clark, E. and McManus, J., 1992. Origin of the northern Atlantic's Heinrich events. *Climate Dynamics* 6, 265-273.
- Broecker, W.S., 1998. Paleocirculation during the last deglaciation: A bipolar seesaw? *Paleoceanography* 13, 119-121.
- Broecker, W., 2003. Does the trigger for abrupt climate change reside in the ocean or in the atmosphere? *Science* 300, 1519-1522.

- Brown, J., Simmonds, I. and Noone, D., 2006. Modeling delta O-18 in tropical precipitation and the surface ocean for present-day climate. *Journal of Geophysical Research-Atmospheres* 111, D05105, doi: 10.1029/2004jd005611.
- Brown, E.T., Johnson, T.C., Scholz, C.A., Cohen, A.S. and King, J.W., 2007. Abrupt change in tropical African climate linked to the bipolar seesaw over the past 55,000 years. *Geophysical Research Letters* 34, L20702, doi:10.1029/2007GL031240.
- Burns, S.J., Fleitmann, D., Matter, A., Kramers, J. and Al-Subbary, A.A., 2003. Indian Ocean climate and an absolute chronology over Dansgaard/Oeschger events 9 to 13. *Science* 301, 1365-1367.
- Burton, E.A. and Walter, L.M., 1990. The Role of Ph in Phosphate Inhibition of Calcite and Aragonite Precipitation Rates in Seawater. *Geochimica et Cosmochimica Acta* 54, 797-808.
- Cane, M. A. and Clement, A. C., 1999. In: *Mechanisms of Global Climate Change at Millennial Time Scales*, eds. Clark, P. U., Webb, R. S. & Keigwin, L. D. American Geophysical Union, Washington DC. pp. 373–383.
- Clement, A. C. and Cane, M. A., 1999. In: *Mechanisms of Global Climate Change at Millennial Time Scales*, eds. Clark, P. U., Webb, R. S. & Keigwin, L. D. American Geophysical Union, Washington DC. pp. 363–371.
- Cheng, H., Edwards, R.L., Hoff, J., Gallup, C.D., Richards, D.A. and Asmerom, Y., 2000. The half-lives of uranium-234 and thorium-230. *Chemical Geology* 169, 17-33.
- Craig, H., 1965. The measurement of oxygen isotope palaeotemperatures. In: *Stable isotopes in oceanographic studies and palaeotemperatures*, Ed. E. Tongiorgi. Consiglio Nazionale delle Ricerche Laboratorio di Geologia Nucleare, Pisa. pp. 166–182.
- Cruz, F.W., Burns, S.J., Karmann, I., Sharp, W.D., Vuille, M., Cardoso, A.O., Ferrari, J.A., Dias, P.L.S. and Viana, O., 2005. Insolation-driven changes in atmospheric circulation over the past 116,000 years in subtropical Brazil. *Nature* 434, 63-66.
- Cruz, F.W., Burns, S.J., Karmann, I., Sharp, W.D., Vuille, M. and Ferrari, J.A., 2006. A stalagmite record of changes in atmospheric circulation and soil processes in the Brazilian subtropics during the Late Pleistocene. *Quaternary Science Reviews* 25, 2749-2761.
- Cruz, F.W., Burns, S.J., Jercinovic, M., Karmann, I., Sharp, W.D. and Vuille, M., 2007. Evidence of rainfall variations in Southern Brazil from trace element ratios (Mg/Ca and Sr/Ca) in a Late Pleistocene stalagmite. *Geochimica et Cosmochimica Acta* 71, 2250-2263.

- Dansgaard, W., 1964. Stable Isotopes in Precipitation. *Tellus* 16, 436-468.
- Dansgaard, W., Johnsen, S. J., Clausen, H. B., Dahl-Jensen, D., Gundestrup, N. S., Hammer, C. U., Hvidberg, C. S., Steffensen, J. P., Sveinbjörnsdóttir, A. E., Jouzel, J. and Bond, G., 1993. Evidence for general instability of past climate from a 250-kyr ice-core record. *Nature* 364, 218-220.
- Desmarchelier, J. M., Hellstrom, J. C. and McCulloch, M. T., 2006. Rapid trace element analysis of speleothems by ELA-ICP-MS. *Chemical Geology* 231, 102-117.
- Drysdale, R. N., Zanchetta, G., Hellstrom, J. C., Fallick, A. E. and Zhao, J. X., 2005. Stalagmite evidence for the onset of the Last Interglacial in southern Europe at 129 +/- 1 ka. *Geophysical Research Letters* 32, L24708, doi:10.1029/2005GL024658.
- Drysdale, R., Zanchetta, G., Hellstrom, J., Maas, R., Fallick, A., Pickett, M., Cartwright, I. and Piccini, L., 2006. Late Holocene drought responsible for the collapse of Old World civilizations is recorded in an Italian cave flowstone. *Geology* 34, 101-104.
- Drysdale, R. N., Zanchetta, G., Hellstrom, J. C., Fallick, A. E., McDonald, J. and Cartwright, I., 2007. Stalagmite evidence for the precise timing of North Atlantic cold events during the early last glacial. *Geology* 35, 77-80.
- EPICA Members, 2006. One-to-one coupling of glacial climate variability in Greenland and Antarctica. *Nature* 444, 195-198.
- Fairchild, I. J., Borsato, A., Tooth, A. F., Frisia, S., Hawkesworth, C. J., Huang, Y. M., McDermott, F. and Spiro, B., 2000. Controls on trace element (Sr-Mg) compositions of carbonate cave waters: implications for speleothem climatic records. *Chemical Geology* 166, 255-269.
- Fairchild, I. J., Smith, C. L., Baker, A., Fuller, L., Spötl, C., Matthey, D., McDermott, F. and Eimp, 2006. Modification and preservation of environmental signals in speleothems. *Earth-Science Reviews* 75, 105-153.
- Fairchild, I. J. and Treble, P., 2009. Trace elements in speleothems as recorders of environmental change. *Quaternary Science Reviews* 28, 449-468.
- Gascoyne, M., 1983. Trace-element partition coefficients in the calcite-water system and their paleoclimatic significance in cave studies. *Journal of Hydrology* 61, 213-222.
- Gascoyne, M., 1992. Paleoclimate Determination from Cave Calcite Deposits. *Quaternary Science Reviews* 11, 609-632.

- Gat, J.R., Gonfiantini, R., 1981. Stable isotope hydrology: Deuterium and oxygen-18 in the water cycle. IAEA Technical Report Series No. 210, International Atomic Energy Agency, Vienna, pp. 339.
- Genty, D., Baker, A. and Vokal, B., 2001. Intra- and inter-annual growth rate of modern stalagmites. *Chemical Geology* 176, 191-212.
- Genty, D., Blamart, D., Ouahdi, R., Gilmour, M., Baker, A., Jouzel, J. and Van-Exter, S., 2003. Precise dating of Dansgaard-Oeschger climate oscillations in western Europe from stalagmite data. *Nature* 421, 833-837.
- Genty, D., Blamart, D., Ghaleb, B., Plagnes, V., Causse, C., Bakalowicz, M., Zouari, K., Chkir, N., Hellstrom, J., Wainer, K. and Bourges, F., 2006. Timing and dynamics of the last deglaciation from European and North African delta C-13 stalagmite profiles - comparison with Chinese and South Hemisphere stalagmites. *Quaternary Science Reviews* 25, 2118-2142.
- Giesler, R., Andersson, T., Lovgren, L. and Persson, P., 2005. Phosphate sorption in aluminum- and iron-rich humus soils. *Soil Science Society of America Journal* 69, 77-86.
- Grachev, A.M., Brook, E.J. and Severinghaus, J.P., 2007. Abrupt changes in atmospheric methane at the MIS 5b-5a transition. *Geophysical Research Letters* 34, L20703, doi:10.1029/2007GL029799.
- Griffiths, M.L., Drysdale, R.N., Gagan, M.K., Zhao, J.X., Ayliffe, L.K., Hellstrom, J.C., Hantoro, W.S., Frisia, S., Feng, Y.X., Cartwright, I., Pierre, E.S., Fischer, M.J. and Suwargadi, B.W., 2009. Increasing Australian-Indonesian monsoon rainfall linked to early Holocene sea-level rise. *Nature Geoscience* 2, 636-639.
- Griffiths, M.L., Drysdale, R.N., Gagan, M.K., Ayliffe, L.K., Frisia, S., Zhao, J.-x., Hellstrom, J.C., Fischer, M.J., Hantoro, W.S., Feng, Y.-x., Suwargadi, B.W., 2010a. Evidence for Holocene changes in Australian-Indonesian monsoon rainfall from stalagmite trace element and stable isotope ratios. *Earth and Planetary Science Letters* 292, 27-38.
- Griffiths, M.L., Drysdale, R.N., Vonhof, H.B., Gagan, M.K., Zhao, J.-x., Ayliffe, L.K., Hantoro, W.S., Hellstrom, J.C., Cartwright, I., Frisia, S., Suwargadi, B.W., 2010b. Younger Dryas-Holocene temperature and rainfall history of southern Indonesia from $\delta^{18}\text{O}$ in speleothem calcite and fluid inclusions. *Earth and Planetary Science Letters* 295, 30-36.
- Grootes, P.M., Stuiver, M., White, J.W.C., Johnsen, S. and Jouzel, J., 1993. Comparison of Oxygen-Isotope Records from the GISP2 and GRIP Greenland Ice Cores. *Nature* 366, 552-554.

- Grootes, P.M. and Stuiver, M., 1997. Oxygen 18/16 variability in Greenland snow and ice with 10(-3)- to 10(5)-year time resolution. *Journal of Geophysical Research-Oceans* 102, 26455-26470.
- Heathwaite A. L., 1997. Sources and pathways of phosphorus loss from agriculture. In: *Phosphorus Loss From Soil to Water*, eds. H. Tunney, O.T. Careton, P.C. Brookes and A.E. Johnstone, pp. 205–223. CAB International, Wallingford, UK.
- Heinrich, H., 1988. Origin and Consequences of Cyclic Ice Rafting in the Northeast Atlantic-Ocean during the Past 130,000 Years. *Quaternary Research* 29, 142-152.
- Hellstrom, J., McCulloch, M. and Stone, J., 1998. A detailed 31,000-year record of climate and vegetation change, from the isotope geochemistry of two New Zealand speleothems. *Quaternary Research* 50, 167-178.
- Hellstrom, J.C. and McCulloch, M.T., 2000. Multi-proxy constraints on the climatic significance of trace element records from a New Zealand speleothem. *Earth and Planetary Science Letters* 179, 287-297.
- Hellstrom, J., 2003. Rapid and accurate U/Th dating using parallel ion-counting multi-collector ICP-MS. *Journal of Analytical Atomic Spectrometry* 18, 1346-1351.
- Hendy, C.H., 1971. The isotopic geochemistry of speleothems: The calculations of the effects of different modes of Formation on the isotopic composition of speleothems and their applicability as palaeoclimate indicators. *Geochimica et Cosmochimica Acta* 35, 801-824.
- Hinnov, L.A., Schulz, M. and Yiou, P., 2002. Interhemispheric space-time attributes of the Dansgaard-Oeschger oscillations between 100 and 0 ka. *Quaternary Science Reviews* 21, 1213-1228.
- Huang, H.M., Fairchild, I.J., Borsato, A., Frisia, S., Cassidy, N.J., McDermott, F. and Hawkesworth, C.J., 2001. Seasonal variations in Sr, Mg and P in modern speleothems (Grotta di Ernesto, Italy). *Chemical Geology* 175, 429-448.
- Huang, Y.M. and Fairchild, I.J., 2001. Partitioning of Sr^{2+} and Mg^{2+} into calcite under karst-analogue experimental conditions. *Geochimica et Cosmochimica Acta* 65, 47-62.
- International Atomic Energy Agency/World Meteorological Organization, 2004. Global Network of Isotopes in Precipitation: The GNIP Database, <http://isohis.iaea.org>, Vienna.
- Johnson, K.R., Hu, C.Y., Belshaw, N.S. and Henderson, G.M., 2006. Seasonal trace-element and stable-isotope variations in a Chinese speleothem: The potential for high-resolution paleomonsoon reconstruction. *Earth and Planetary Science Letters* 244, 394-407.

- Kaufmann, G. and Dreybrodt, W., 2004. Stalagmite growth and palaeo-climate: an inverse approach. *Earth and Planetary Science Letters* 224, 529-545.
- Leduc, G., Vidal, L., Tachikawa, K., Rostek, F., Sonzogni, C., Beaufort, L. and Bard, E., 2007. Moisture transport across Central America as a positive feedback on abrupt climatic changes. *Nature* 445, 908-911.
- Lemieux-Dudon, B., Blayo, E., Petit, J.-R., Waelbroeck, C., Svensson, A., Ritz, C., Barnola, J.-M., Narcisi, B., Parrenin, F., 2010. Consistent dating for Antarctic and Greenland ice cores. *Quaternary Science Reviews* 29, 8-20.
- Liu, Z., Harrison, S.P., Kutzbach, J. and Otto-Bliesner, B., 2004. Global monsoons in the mid-Holocene and oceanic feedback. *Climate Dynamics* 22, 157-182.
- Magee, J.W., Miller, G.H., Spooner, N.A. and Questiaux, D., 2004. Continuous 150 ky monsoon record from Lake Eyre, Australia: Insolation-forcing implications and unexpected Holocene failure. *Geology* 32, 885-888.
- Mann, M.E., Zhang, Z.H., Hughes, M.K., Bradley, R.S., Miller, S.K., Rutherford, S. and Ni, F.B., 2008. Proxy-based reconstructions of hemispheric and global surface temperature variations over the past two millennia. *Proceedings of the National Academy of Sciences of the United States of America* 105, 13252-13257.
- Marshall, A.G. and Lynch, A.H., 2008. The sensitivity of the Australian summer monsoon to climate forcing during the late Quaternary. *Journal of Geophysical Research-Atmospheres* 113, D11107, doi:10.1029/2007JD008981.
- McDermott, F., 2004. Palaeo-climate reconstruction from stable isotope variations in speleothems: a review. *Quaternary Science Reviews* 23, 901-918.
- McMillan, E.A., Fairchild, I.J., Frisia, S., Borsato, A. and McDermott, F., 2005. Annual trace element cycles in calcite-aragonite speleothems: evidence of drought in the western Mediterranean 1200-1100 yr BP. *Journal of Quaternary Science* 20, 423-433.
- Miller, G., Mangan, J., Pollard, D., Thompson, S., Felzer, B. and Magee, J., 2005. Sensitivity of the Australian Monsoon to insolation and vegetation: Implications for human impact on continental moisture balance. *Geology* 33, 65-68.

- Muller, J., Kylander, M., Wust, R.A.J., Weiss, D., Martinez-Cortizas, A., LeGrande, A.N., Jennerjahn, T., Behling, H., Anderson, W.T. and Jacobson, G., 2008. Possible evidence for wet Heinrich phases in tropical NE Australia: the Lynch's Crater deposit. *Quaternary Science Reviews* 27, 468-475.
- Mühlinghaus, C., Scholz, D., Mangini, A. 2007. Modelling stalagmite growth and $\delta^{13}\text{C}$ as a function of drip interval and temperature. *Geochimica et Cosmochimica Acta* 71, 2780-2790.
- Myneni S. C. B., 2002. Soft X-ray spectroscopy and spectromicroscopy studies of organic molecules in the environment. In: *Application of Synchrotron Radiation in Low-Temperature Geochemistry and Environmental Science*, eds. P.A. Fenter, M.L. Rivers, N.C. Surchio and S.R. Sutton, Mineralogical Society of America, Washington. vol. 49, pp. 485–579.
- Oppo, D. W., Rosenthal, Y. and Linsley, B.K., 2009. 2,000-year-long temperature and hydrology reconstructions from the Indo-Pacific warm pool. *Nature* 460, 1113-1116.
- Paquette, J., Reeder, R.J., 1990. New type of compositional zoning in calcite: Insights into crystal-growth mechanisms. *Geology* 18, 1244-1247.
- Paquette, J., Reeder, R.J., 1995. Relationship between surface structure, growth mechanism and trace element incorporation in calcite. *Geochimica et Cosmochimica Acta* 59, 735–749.
- Peterson, L.C., Haug, G.H., Hughen, K.A. and Rohl, U., 2000. Rapid changes in the hydrologic cycle of the tropical Atlantic during the last glacial. *Science* 290, 1947-1951.
- Petit, J.R., Jouzel, J., Raynaud, D., Barkov, N.I., Barnola, J.M., Basile, I., Bender, M., Chappellaz, J., Davis, M., Delaygue, G., Delmotte, M., Kotlyakov, V.M., Legrand, M., Lipenkov, V.Y., Lorius, C., Pepin, L., Ritz, C., Saltzman, E. and Stievenard, M., 1999. Climate and atmospheric history of the past 420,000 years from the Vostok ice core, Antarctica. *Nature* 399, 429-436.
- Pote, D.H., Daniel, T.C., Nichols, D.J., Moore, P.A., Miller, D.M. and Edwards, D.R., 1999. Seasonal and soil-drying effects on runoff phosphorus relationships to soil phosphorus. *Soil Science Society of America Journal* 63, 1006-1012.
- Rahmstorf, S., 2002. Ocean circulation and climate during the past 120,000 years. *Nature* 419, 207-214.
- Rahmstorf, S., 2006. Glacial Climates: Thermohaline Circulation. In: *Encyclopedia of Quaternary Science*, ed. S.A. Elias. Elsevier, Amsterdam. pp. 739-750.
- Roberts, M.S., Smart, P.L. and Baker, A., 1998. Annual trace element variations in a Holocene speleothem. *Earth and Planetary Science Letters* 154, 237-246.

- Scholz, D., Mühlinghaus, C., Mangini, A. Modelling $\delta^{13}\text{C}$ and $\delta^{18}\text{O}$ in the solution layer on stalagmite surfaces. *Geochimica et Cosmochimica Acta* 73, 2592-2602.
- Schulz, H., von Rad, U. and Erlenkeuser, H., 1998. Correlation between Arabian Sea and Greenland climate oscillations of the past 110,000 years. *Nature* 393, 54-57.
- Severinghaus, J.P., Grachev, A., Luz, B. and Caillon, N., 2003. A method for precise measurement of argon 40/36 and krypton/argon ratios in trapped air in polar ice with applications to past firn thickness and abrupt climate change in Greenland and at Siple Dome, Antarctica. *Geochimica et Cosmochimica Acta* 67, 325-343.
- Shackleton, N.J., Hall, M.A. and Vincent, E., 2000. Phase relationships between millennial-scale events 64,000-24,000 years ago. *Paleoceanography* 15, 565-569.
- Smith, T.M., Reynolds, R.W., Peterson, T.C. and Lawrimore, J., 2008. Improvements to NOAA's historical merged land-ocean surface temperature analysis (1880-2006). *Journal of Climate* 21, 2283-2296.
- Spötl, C., Fairchild, I.J. and Tooth, A.F., 2005. Cave air control on dripwater geochemistry, Obir Caves (Austria): Implications for speleothem deposition in dynamically ventilated caves. *Geochimica et Cosmochimica Acta* 69, 2451-2468.
- Staudt W. J., Reeder R. J., and Schoonen M. A. A. 1994. Surface structural controls on compositional sector zoning of SO_4^{2-} and SeO_4^{2-} in synthetic calcite crystals. *Geochimica et Cosmochimica Acta* 58, 2087-2098.
- Stocker, T.F. and Johnsen, S.J., 2003. A minimum thermodynamic model for the bipolar seesaw. *Paleoceanography* 18, 1087, doi:10.1029/2003PA000920.
- Stott, L., Poulsen, C., Lund, S. and Thunell, R., 2002. Super ENSO and global climate oscillations at millennial time scales. *Science* 297, 222-226.
- Stott, L., Cannariato, K., Thunell, R., Haug, G.H., Koutavas, A. and Lund, S., 2004. Decline of surface temperature and salinity in the western tropical Pacific Ocean in the Holocene epoch. *Nature* 431, 56-59.
- Stuiver, M. and Grootes, P.M., 2000. GISP2 oxygen isotope ratios. *Quaternary Research* 53, 277-283.
- Suppiah, R. and Wu, X.G., 1998. Surges, cross-equatorial flows and their links with the Australian summer monsoon circulation and rainfall. *Australian Meteorological Magazine* 47, 113-130.

- Temmam M., Paquette J., and Vali H. 2000. Mn and Zn incorporation into calcite as a function of chloride aqueous concentration. *Geochimica et Cosmochimica Acta* 64, 2417–2430.
- Treble, P., Shelley, J.M.G. and Chappell, J., 2003. Comparison of high resolution sub-annual records of trace elements in a modern (1911-1992) speleothem with instrumental climate data from southwest Australia. *Earth and Planetary Science Letters* 216, 141-153.
- Turney, C.S.M., Kershaw, A. P., Clemens, S.C., Branch, N., Moss, P.T. and Field, L.K., 2004. Millennial and orbital variations of El Nino/Southern Oscillation and high-latitude climate in the last glacial period. *Nature* 428, 306-310.
- Tyler, G., 2004. Rare earth elements in soil and plant systems—A review. *Plant Soil* 267, 191–206.
- van Kreveld, S., Sarnthein, M., Erlenkeuser, H., Grootes, P., Jung, S., Nadeau, M.J., Pflaumann, U. and Voelker, A., 2000. Potential links between surging ice sheets, circulation changes, and the Dansgaard-Oeschger cycles in the Irminger Sea, 60-18 kyr. *Paleoceanography* 15, 425-442.
- Verheyden, S., Keppens, E., Fairchild, I.J., McDermott, F. and Weis, D., 2000. Mg, Sr and Sr isotope geochemistry of a Belgian Holocene speleothem: implications for paleoclimate reconstructions. *Chemical Geology* 169, 131-144.
- Visser, K., Thunell, R. and Stott, L., 2003. Magnitude and timing of temperature change in the Indo-Pacific warm pool during deglaciation. *Nature* 421, 152-155.
- Vuille, M., Werner, M., Bradley, R.S. and Keimig, F., 2005. Stable isotopes in precipitation in the Asian monsoon region. *Journal of Geophysical Research-Atmospheres* 110, D23108, doi:10.1029/2005JD006022.
- Wang, Y.J., Cheng, H., Edwards, R.L., An, Z.S., Wu, J.Y., Shen, C.C. and Dorale, J.A., 2001. A high-resolution absolute-dated Late Pleistocene monsoon record from Hulu Cave, China. *Science* 294, 2345-2348.
- Wang, X.F., Auler, A.S., Edwards, R.L., Cheng, H., Cristalli, P.S., Smart, P.L., Richards, D.A. and Shen, C.C., 2004. Wet periods in northeastern Brazil over the past 210 kyr linked to distant climate anomalies. *Nature* 432, 740-743.
- Wang, X.F., Auler, A.S., Edwards, R.L., Cheng, H., Ito, E., Wang, Y.J., Kong, X.G. and Solheid, M., 2007. Millennial-scale precipitation changes in southern Brazil over the past 90,000 years. *Geophysical Research Letters* 34, L23701, doi:10.1029/2007GL031149.

- Wang, Y.J., Cheng, H., Edwards, R.L., Kong, X.G., Shao, X.H., Chen, S.T., Wu, J.Y., Jiang, X.Y., Wang, X.F. and An, Z.S., 2008. Millennial- and orbital-scale changes in the East Asian monsoon over the past 224,000 years. *Nature* 451, 1090-1093.
- Wen, B., Shan, X.Q., Lin, J.M., Tang, G.G., Bai, N.B. and Yuan, D.A., 2002. Desorption kinetics of yttrium, lanthanum, and cerium from soils. *Soil Science Society of America Journal* 66, 1198-1206.
- Wheeler, M.C. and McBride, J.L., 2005. Australian-Indonesian monsoon. In: *Intraseasonal variability in the atmosphere-ocean climate system*, eds. W.K. Lau and D.E. Waliser. Praxis Publishing. pp. 125-172.
- Woodhead, J.D., Hellstrom, J., Hergt, J.M., Greig, A., Maas, R., 2007. Isotopic and Elemental Imaging of Geological Materials by Laser Ablation Inductively Coupled Plasma-Mass Spectrometry. *Geostandards and Geoanalytical Research* 31, 331-343.
- Wu, R. and Kirtman, B.P., 2007. Roles of the Indian Ocean in the Australian summer monsoon-ENSO relationship. *Journal of Climate* 20, 4768-4788.
- Wyrwoll, K.H. and Valdes, P., 2003. Insolation forcing of the Australian monsoon as controls of Pleistocene mega-lake events. *Geophysical Research Letters* 30, 2279, doi:10.1029/2003GL018486.
- Yang, H., Zhang, Q., Zhong, Y., Vavrus, S., Liu, Z., 2005. How does extratropical warming affect ENSO? 32, L01702, doi: 10.1029/2004GL021624.
- Yuan, D.X., Cheng, H., Edwards, R.L., Dykoski, C.A., Kelly, M.J., Zhang, M.L., Qing, J.M., Lin, Y.S., Wang, Y.J., Wu, J.Y., Dorale, J.A., An, Z.S. and Cai, Y.J., 2004. Timing, duration, and transitions of the Last Interglacial Asian Monsoon. *Science* 304, 575-578.
- Zhang, Q., Yang, H., Zhong, Y., Wang, D., 2005. An idealized study of the impact of extratropical climate change on El Niño–Southern Oscillation. *Climate Dynamics* 25, 869-880.
- Zhang, R. and Delworth, T.L., 2005. Simulated tropical response to a substantial weakening of the Atlantic thermohaline circulation. *Journal of Climate* 18, 1853-1860.

7 Conclusions

7.1 Summary of thesis

This thesis has been presented as a compilation of manuscripts, each aimed at addressing a specific set of palaeoclimate questions. The overall goal was to gain insights into how tropical climates within the Indo-Pacific region have evolved and the underlying mechanisms controlling their variability over different time-scales. The following sections summarise the outcomes of the four specific objectives outlined in Chapter 1.

7.1.1 *Reconstruct the Holocene history of the AISM from $\delta^{18}\text{O}$ of coeval speleothems*

In Chapter 2, oxygen isotopes from two precisely-dated stalagmites were used to explore the history of the AISM during the YD-Holocene. From the isotopes it was concluded that, in contrast to other monsoon systems (e.g. Asian and South-American monsoons), local summer insolation was not the most important driver of AISM variability during the Holocene. Rather, the abrupt increase in monsoon intensity (inferred from the sharp decline in $\delta^{18}\text{O}$) coincided with a sharp eustatic sea-level rise (Bard, 1996; Peltier and Fairbanks, 2006; Siddall et al., 2003), which increased moisture availability over the Sunda Shelf (the moisture source region fuelling the monsoon). Additionally, it was demonstrated that the summer monsoon precipitation increased during the YD climate anomaly, when Atlantic meridional overturning circulation was relatively weak (McManus et al., 2004). A direct causal mechanism linking the North Atlantic Ocean circulation with tropical monsoon intensity was enhanced surface-outflow from the Asian winter monsoon (Yancheva et al., 2007) and a consequent southward shift in the AISM-ITCZ.

7.1.2 *Assessing the feasibility of using stable isotopes from speleothem fluid-inclusions to extract tropical palaeotemperatures*

Chapter 3 explored the use of oxygen and hydrogen isotopes from speleothem fluid-inclusions to reconstruct the temperature and rainfall history of the Indo-Pacific through the Holocene. The results demonstrated that the fluid-inclusion oxygen-isotope ($\delta^{18}\text{O}_f$) record varied in parallel with the $\delta^{18}\text{O}$ of the calcite ($\delta^{18}\text{O}_c$), thus confirming that the $\delta^{18}\text{O}$ of the speleothem calcite reflects that of the recharge

rainfall. Given this, the synchronous $\delta^{18}\text{O}_f$ and $\delta^{18}\text{O}_c$ records, which trend towards lower values through the early-to-mid Holocene, reaffirm the gradual intensification of the AISM system in response to deglacial sea-level rise. In addition, it was shown that coupled measurements of $\delta^{18}\text{O}_f$ and $\delta^{18}\text{O}_c$ could be used to reconstruct cave palaeotemperatures (and by inference external temperatures in the tropics) based on the relationship between $\delta^{18}\text{O}$ of calcite and drip-water temperature (O'Neil et al., 1969). Reconstructed cave temperatures indicate a relatively stable pattern over the Indo-Pacific during the Holocene, in good agreement with the SST history for the IPWP (Briker et al., 2007; Lea et al., 2000; Stott et al., 2004; Visser et al., 2003). By contrast, the YD cold event was characterised by a marked cooling in cave temperatures by $\sim 5^\circ\text{C}$. This pattern is in good agreement with YD SST anomalies inferred from fossil-coral Sr/Ca ratios (Castellaro et al., 1997; Corrège et al., 2004; Gagan et al., 2000) and $\delta^{18}\text{O}$ of tropical ice cores (Thompson et al., 1995; Thompson et al., 1998), but not of foraminiferal Mg/Ca records from the IPWP (Stott et al., 2004; Visser et al., 2003), which only indicate a $\sim 1^\circ\text{C}$ cooling during this time; as noted in Chapter 3, this disparity may be, amongst other things, due to: (i) diagenetic alteration of fossil corals and/or marine sediment foraminifera; and/or (ii) differences in climate sensitivity of air versus sea-surface temperatures. A final important finding from the fluid-inclusion $\delta^{18}\text{O}_f$ record was that local SSTs (and air temperatures) had little influence on the positioning of the ITCZ because cooling of the southern IPWP during the YD was accompanied by higher rainfall in the AISM climate domain. A similar finding has recently been shown from a foraminiferal Mg/Ca reconstruction for the IPWP showing cool SSTs and high rainfall in the IPWP during the “Little Ice Age” (Oppo et al., 2009).

7.1.3 Utilising trace elements from a Holocene speleothem to validate oxygen isotope interpretations and provide additional palaeoenvironmental information

Chapters 4 and 5 presented a high-resolution reconstruction of Indo-Pacific hydrology from stable isotopes ($\delta^{18}\text{O}$ and $\delta^{13}\text{C}$), trace elements (Mg/Ca and Sr/Ca), and initial $^{234}\text{U}/^{238}\text{U}$ activity ratios. The strong coherence between the Mg/Ca, Sr/Ca and $\delta^{13}\text{C}$ strongly argued for the trace elements being driven by changes in the flow rate of percolation water passing through the limestone rock mass above the cave, which are dependent primarily on evapotranspiration and rainfall amounts. Given this, intervals of decreased recharge result in dewatering of fractures in the karst rock, which enhances ventilation and triggers CO_2 degassing. This promotes ‘prior calcite precipitation’ along the fractures upstream of the

drip site, resulting in higher Mg/Ca and Sr/Ca ratios of the meteoric water due to the preferential loss of the Ca^{2+} ion (Fairchild and Treble, 2009). The converse occurs during wetter phases. The trace element profiles display a strong correspondence to the $\delta^{18}\text{O}$, thus confirming previous interpretations that lower $\delta^{18}\text{O}$ values reflect higher rainfall recharge and *vice versa*. Chapter 4 also employed the use of initial $^{234}\text{U}/^{238}\text{U}$ activity ratios, a derivative of the U/Th age determinations, to assess cave palaeohydrology. Comparison between these activity ratios and the trace-element and stable-isotope profiles corroborate the findings of Chapters 2 and 3 that the early Holocene was somewhat drier than the late Holocene in eastern Indonesia.

Another unique aspect of Chapter 4 involved the comparison of speleothem $\delta^{18}\text{O}$ records between Flores and northern Borneo (Partin et al., 2007), which demonstrated that they are highly covariant for much of the Holocene. However, a notable disparity was evident during the mid-Holocene (i.e. 4 - 6 ka) suggestive of a regional perturbation in ocean-atmosphere circulation patterns during this time. The positive coherence of Flores $\delta^{18}\text{O}$ with IPWP coral SST records (Abram et al., 2009), and the antiphased relationship with Mt. Kilimanjaro ice-core records from east Africa (Thompson et al., 2002) during this interval adds further weight to this perturbation occurring over a large region. Together, the findings imply that the mid-Holocene climate anomaly was characterised by more positive IOD-like conditions and an associated northward shift of the ITCZ. This is quite a significant finding, as it demonstrates that modes of climate variability, such as the IOD, were in full operation and had some bearing on Indonesian rainfall during the Holocene.

Chapter 5 was built upon the results of Chapter 4, by focusing on the abrupt change in $\delta^{18}\text{O}$ and trace elements (i.e. Mg/Ca and Sr/Ca) during the early Holocene (i.e. ~9.5 ka) in finer detail. By integrating all three climate-sensitive proxies, it was revealed that the resumption of the monsoon during the early Holocene may have in fact occurred much faster than previously interpreted from the $\delta^{18}\text{O}$ alone. The timing and structure of this sharp monsoon increase in Indonesia is in phase (within dating uncertainty) with the rainforest expansion in northeastern Australia (Haberle, 2005).

7.1.4 Explore a “snapshot” of Flores climate through MIS 5a/b and assess possible teleconnection patterns between the Indo-Pacific and high latitudes

In Chapter 6, the carbon and oxygen isotopes of two well-dated speleothems were used to examine the temperature and rainfall history of east Indonesia through the interval 84 to 91 ka. The detrended $\delta^{18}\text{O}$ and $\delta^{13}\text{C}$ records display a significant correlation with one another, suggesting that they were driven by similar processes through the MIS 5a/b interval over decadal to centennial time-scales. Similar to the trace element results presented in Chapter 4, a significant positive correlation between the $\delta^{13}\text{C}$ and Mg and Sr concentrations through the two target time-slices, suggests that the higher frequency variability in both proxies was controlled by PCP and/or enhanced selective leaching with extended water-rock contact times. Hence, higher $\delta^{13}\text{C}$ and Mg and Sr values are indicative of drier conditions and *vice versa*. Moreover, the strong covariation of the trace elements with the $\delta^{18}\text{O}$ again confirms that the isotopes are dominated by rainfall amounts. Significant correlations between Y and P and the stable isotopes and other trace elemental values, implies that they are also governed by hydrological conditions above the cave. Based on previous interpretations of Y and P (e.g. Borsato et al., 2007), it is argued that both elements were transported into Liang Luar via colloids during higher infiltration events (e.g. higher rainfall). Therefore, higher (lower) Y and P values are interpreted to reflect higher (lower) recharge events. The lower-frequency $\delta^{18}\text{O}$ record displays an increasing trend through the 84 to 91 ka interval and matches the summer insolation curve over northern Australia. By contrast, the $\delta^{13}\text{C}$ profile displays a closer resemblance to the $\delta^{18}\text{O}_{\text{ice}}$ of Greenland ice cores. Specifically, the abrupt increase in GISP2 $\delta^{18}\text{O}_{\text{ice}}$ (Groote and Stuiver, 1997) and CH_4 (Grachev et al., 2007) at GIS 21 is synchronous with an abrupt negative shift in $\delta^{13}\text{C}$ values in Flores speleothems. This suggests that there was a strong Northern Hemisphere teleconnection with the tropics during GISs. Owing the lack of a similar shift in the $\delta^{18}\text{O}$ and trace elements, it was argued that this climate link can best be explained by an increase in tropical air temperatures during GISs, which controlled microbial activity in the soil zone and hence the carbon isotope concentration of the DIC in the drip-water. Further, the synchronous shift in atmospheric CH_4 adds weight to a temperature-controlled $\delta^{13}\text{C}$ signal in the Flores speleothems because air temperatures can strongly influence CH_4 emissions from tropical wetlands.

7.2 Future directions

Below I discuss a sample of many fruitful research opportunities available within the Indo-Pacific region.

7.2.1 *Exploring water-carbonate systematics in tropical cave systems*

Establishing the oxygen isotopic composition and trace element (e.g. Mg, Sr, Ba, P, U, Na) concentration of modern-water carbonate systematics has increasingly become an important tool for validating speleothem-based palaeoclimate reconstructions. Whilst the relationship between tropical rainfall- $\delta^{18}\text{O}$ and regional atmospheric circulation patterns has been well studied (e.g. Aggarwal et al., 2004; LeGrande et al., 2009; Vuille et al., 2005), a full understanding of the tropical $\delta^{18}\text{O}$ signal-transfer between the surface recharge and cave interior, including Liang Luar, is still lacking. This is largely because of the complexities of karst hydrology, involving groundwater mixing in the epikarst, variable hydrological flow-paths and possible evaporative fractionation (Cobb et al., 2007).

To address this shortcoming, it would be extremely useful to carry out daily to seasonal drip-water monitoring campaigns in Flores (or other potential cave sites from Indonesia and/or northern Australia) to better understand the relationship between the $\delta^{18}\text{O}$ of the rainfall and drip-water, and also establish cave recharge-trace element calibrations. For example, it would be interesting to examine the stable-isotope and trace-element composition of drip waters following major modes of climate variability (e.g. following El Niño and/or positive IOD events), similar to that of McDonald et al., (2004) in SE Australia, which would thus help to place modern climate-karst processes into a palaeoclimatological context.

7.2.2 *Extending the instrumental record back two millennia*

Flores and northern Australia contain some high resolution instrumental records for both temperature and precipitation. However, these records rarely extend back beyond the 20th century, greatly limiting our understanding of the longer-term variability. Although coral (e.g. Gagan et al., 1998; Hendy et al., 2002) and marine sediment (Oppo et al., 2009) records have provided some insights into the palaeotemperature and palaeosalinity of the Indo-Pacific Warm Pool, a huge void is yet to be filled in continental northern Australia/southern Indonesia. Consequently, there is a distinct lack of information regarding decadal- to centennial-scale monsoon variability, especially during important climate intervals

such as the “Medieval Climate Anomaly” (A.D. ~900-1350) and the “Little Ice Age” (A.D. ~1350-1850). Moreover, it is extremely critical to place recent drought history in Australia into a longer-term perspective because several important unknowns are still at large; for example:

- Is the recent drought history of central Australia anomalous with respect to the past two millennia, or is it quite typical over this time-scale?
- How often do these ‘one-in-a-100 year’ floods occur in northern-central Australia (currently occurring in parts of interior Australia due to a large 2009/2010 summer monsoon season)?
- What influence have modes of climate variability (e.g. ENSO, IOD) played in the monsoon behaviour over decadal to centennial time-scales?

The main focus would be to gain a high resolution record of monsoon variability, thereby extending the instrumental time-series back to at least 0 A.D. through the calibration of geochemical tracers with modern instrumental data. This would be achieved by sampling actively growing stalagmites from several cave systems in southern Indonesia/northern Australia, and utilising stable isotopes ($\delta^{18}\text{O}$ and $\delta^{13}\text{C}$), climate sensitive trace elements (Mg, P, U, Sr, Ba and Na) and, if present, thickness of annual laminae, to reconstruct summer monsoon variability on a monthly to annual time scale. These time series would then be compared with nearby meteorological stations and, over longer time scales, with reconstructed sea-surface temperatures (Oppo et al., 2009), hemispheric air-temperature averages (e.g. Mann et al., 2008), and climate indices such as the ENSO (Cobb et al., 2003) and IOD (Abram et al., 2008).

7.2.3 *Glacial/interglacial monsoon evolution*

Due to the current lack of high-resolution, terrestrial palaeoclimate records from the Indo-Pacific, it is largely unknown how the climate has varied throughout the region on glacial/interglacial time-scales. Hence, it is clear that a future objective is to develop continuous, decadal-resolved climate time-series through a ‘stacked’ compilation of numerous stalagmite records back through glacial terminations. In addition to stable isotopes and trace elements, it would be interesting to examine (if present) the isotopes of fluid-inclusions, particularly through terminations, with the hope of reconstructing cave palaeotemperatures through glacial/interglacial cycles. This may help shed new light onto the role of the tropics in global climate change.

As previously mentioned, GISs were characterised by abrupt changes in ocean and air temperatures over the North Atlantic and occurred quite regularly during the last glacial period. Although

many studies from around the globe have documented these climate anomalies, there is still a great degree of uncertainty into the nature and timing of the tropical climate response to these events, especially over the terrestrial southern tropics. Hence, this objective would aim to build upon the findings of Chapter 6 by examining tropical climate behaviour through GIS cycles.

7.2.4 *Integration of AISM reconstructions and palaeoclimate model simulations*

One of the largest uncertainties in global climate model projections is the responses of the Earth's monsoon systems to global warming (IPCC, 2007). This is because current climate models do not have a firm handle on the underlying physics governing monsoon variability, and hence the model output is ambiguous amongst the many different climate models. As such, there is an urgent need for the integration of palaeo-data with quantitative model simulations in order to improve their predictive capabilities under enhanced greenhouse-gas forcing.

Interpretation of palaeoclimate records is vastly improved when there is cross-disciplinary collaboration between palaeoclimatologists, climate dynamicists, and climate modelers. Because climate variability is governed by an array of interacting processes, it is extremely difficult to interpret single-site palaeo-records without a sense of the larger physical setting; integrating stalagmite palaeo-data with physical model simulations will improve our understanding of the physical mechanisms governing past climate variability and allow our results to be placed into a global context. Moreover, merging these research fields together will ensure that our understanding of past climate variability is far more quantitative and concise than it could possibly be if the fields worked at it alone.

7.3 Final comments

The research presented in this thesis has documented, for the first time, the nature of AISM variability and soil activity during two climatically significant time intervals: the Holocene and MIS 5a/b. By utilising several geochemical tracers from active and fossil cave speleothems, I have provided an insight into the dominant mechanisms controlling monsoon variability and highlighted the strong teleconnections observed between the tropics and high latitudes during climate turning points (e.g. GISs).

One of the most important findings of this research has been the realisation that, in contrast to other monsoon systems, the AISM was not dominated by summer insolation during the Holocene. While insolation likely played a role, it was the infilling of the Sunda Shelf during deglacial sea-level rise that

was the more important driver given its strong influence on monsoon source-moisture. Another unique finding was that inferred from oxygen-isotope ratios of speleothem calcite and fluid inclusions, which indicate that decreased tropical air-temperatures during the YD cold stage were not accompanied by a similar reduction in rainfall, rather quite the opposite (i.e. more rainfall). This pattern was also observed during MIS 5a/b, where an abrupt temperature-controlled decrease in $\delta^{13}\text{C}$ values (indicative of warmer conditions) during GIS 21 was not paralleled by a significant shift in rainfall, as inferred from the $\delta^{18}\text{O}$ and trace elements. Hence, while annual- to decadal-scale coupling of temperature and rainfall over the southern IPWP is evident from the strong covariation between detrended $\delta^{18}\text{O}$ and $\delta^{13}\text{C}$ records (also evident in modern settings), millennial-scale variations in IPWP hydrology may not be controlled by local SSTs (and hence air temperature) but by larger scale circulation patterns associated with the position of the ITCZ. Therefore, long-term air-temperature variability was likely controlled by local oceanic upwelling associated with changes in trade-wind strength, while long-term precipitation patterns were driven by larger, more regional circulation patterns associated with eustatic sea-level and summer insolation.

7.4 References

- Abram, N.J., Gagan, M.K., Cole, J.E., Hantoro, W.S., Mudelsee, M., 2008. Recent intensification of tropical climate variability in the Indian Ocean. *Nature Geoscience* 1, 849–853.
- Abram, N.J., McGregor, H.V., Gagan, M.K., Hantoro, W.S., Suwargadi, B.W., 2009. Oscillations in the southern extent of the Indo-Pacific Warm Pool during the mid-Holocene. *Quaternary Science Reviews* doi:10.1016/j.quascirev.2009.07.006.
- Aggarwal, P.K., Frohlich, K., Kulkarni, K.M. and Gourey, L.L., 2004. Stable isotope evidence for moisture sources in the Asian summer monsoon under present and past climate regimes. *Geophysical Research Letters* 31, L08203, doi: 10.1029/2004gl019911.
- Bard, E., Hamelin, B., Arnold, M., Montaggioni, L., Cabioch, G., Faure, G., and Rougerie, F., 1996. Deglacial sea-level record from Tahiti corals and the timing of global meltwater discharge. *Nature* 382, 241-244.
- Borsato, A., Frisia, S., Fairchild, I.J., Somogyi, A. and Susini, J., 2007. Trace element distribution in annual stalagmite laminae mapped by micrometer-resolution X-ray fluorescence: Implications for incorporation of environmentally significant species. *Geochimica et Cosmochimica Acta* 71, 1494-1512.
- Brijker, J.M., Jung, S.J.A., Ganssen, G.M., Bickert, T. and Kroon, D., 2007. ENSO related decadal scale climate variability from the Indo-Pacific Warm Pool. *Earth and Planetary Science Letters* 253, 67-82.
- Castellaro, C., Ribaud-Laurenti, A., Claverie, K., Cabioch, G., Hamelin, B., Bard, E., Montaggioni, L., J. Recy, 1997. Variabilité du climat tropical à l'holocène: Enregistrements Sr/Ca et U/Ca dans les coraux de Nouvelle-Calédonie, de Tahiti, et des Seychelles (Indo-Pacifique). 6 Congrès Français de la Chronologie Lion des Resumes, Publication ASF, Paris, 293 pp. 47-48.
- Climate Change 2007: The Physical Science Basis. Contribution of Working Group I to the Fourth Assessment Report of the Intergovernmental Panel on Climate Change. Eds. Solomon, S., D. Qin, M. Manning, Z. Chen, M. Marquis, K.B. Averyt, M. Tignor and H.L. Miller. Cambridge University Press, Cambridge.
- Cobb, K.M., Charles, C.D., Cheng, H. and Edwards, R.L., 2003. El Niño/Southern Oscillation and tropical Pacific climate during the last millennium. *Nature* 424, 271-276.

- Cobb, K.M., Adkins, J.F., Partin, J.W., Clark, B., 2007. Regional-scale climate influences on temporal variations of rainwater and cave dripwater oxygen isotopes in northern Borneo. *Earth and Planetary Science Letters* 263, 207-220.
- Corrége, T., Gagan, M.K., Beck, J.W., Burr, G.S., Cabioch, G. and Le Cornec, F., 2004. Interdecadal variation in the extent of South Pacific tropical waters during the Younger Dryas event. *Nature* 428, 927-929.
- Fairchild, I.J. and Treble, P., 2009. Trace elements in speleothems as recorders of environmental change. *Quaternary Science Reviews* 28, 449-468.
- Gagan, M.K., Ayliffe, L.K., Hopley, D., Cali, J.A., Mortimer, G.E., Chappell, J., McCulloch, M.T., Head, M.J., 1998. Temperature and surface-ocean water balance of the mid-Holocene tropical western Pacific. *Science* 279, 1014-1018.
- Gagan, M.K., Ayliffe, L.K., Beck, J.W., Cole, J.E., Druffel, E.R.M., Dunbar, R.B., Schrag, D.P., 2000. New views of tropical paleoclimates from corals. *Quaternary Science Reviews* 19, 45-64.
- Grachev, A.M., Brook, E.J. and Severinghaus, J.P., 2007. Abrupt changes in atmospheric methane at the MIS 5b-5a transition. *Geophysical Research Letters* 34, L20703, doi:10.1029/2007GL029799.
- Grootes, P.M., Stuiver, M., White, J.W.C., Johnsen, S. and Jouzel, J., 1993. Comparison of Oxygen-Isotope Records from the GISP2 and GRIP Greenland Ice Cores. *Nature* 366, 552-554.
- Haberle, S.G., 2005. A 23,000-yr pollen record from Lake Euramoo, Wet Tropics of NE Queensland, Australia, *Quaternary Research* 64, 343-356.
- Hendy, E.J., Gagan, M.K., Alibert, C.A., McCulloch, M.T., Lough, J.M. and Isdale, P.J., 2002. Abrupt decrease in tropical Pacific Sea surface salinity at end of Little Ice Age. *Science* 295, 1511-1514.
- Lea, D.W., Pak, D.K. and Spero, H.J., 2000. Climate impact of late Quaternary equatorial Pacific sea surface temperature variations. *Science* 289, 1719-1724.
- LeGrande, A.N., and Schmidt, G.A., 2009. Sources of Holocene variability of oxygen isotopes in paleoclimate archives. *Climate of the Past* 5, 441-455.
- Mann, M.E., Zhang, Z.H., Hughes, M.K., Bradley, R.S., Miller, S.K., Rutherford, S. and Ni, F.B., 2008. Proxy-based reconstructions of hemispheric and global surface temperature variations over the past two millennia. *Proceedings of the National Academy of Sciences of the United States of America* 105, 13252-13257.

- McDonald, J., Drysdale, R., Hill, D., 2004. The 2002-2003 El Niño recorded in Australian cave drip waters: Implications for reconstructing rainfall histories using stalagmites. *Geophysical Research Letters* 31, L22202, doi: 10.1029/2004GL020859.
- McManus, J.F., Francois, R., Gherardi, J.M., Keigwin, L.D. and Brown-Leger, S., 2004. Collapse and rapid resumption of Atlantic meridional circulation linked to deglacial climate changes. *Nature* 428, 834-837.
- O'Neil, J.R., Clayton, R.N., Mayeda, T.K., 1969. Oxygen isotope fractionation in divalent metal carbonates. *Journal of Chemical Physics* 51, 1-10.
- Oppo, D.W., Rosenthal, Y. and Linley, B.K., 2009. 2,000-year-long temperature and hydrology reconstructions from the Indo-Pacific warm pool. *Nature* 460, 1113-1116.
- Partin, J.W., Cobb, K.M., Adkins, J.F., Clark, B. and Fernandez, D.P., 2007. Millennial-scale trends in west Pacific warm pool hydrology since the Last Glacial Maximum. *Nature* 449, 452-455.
- Peltier, W.R. and Fairbanks, R.G., 2006. Global glacial ice volume and Last Glacial Maximum duration from an extended Barbados sea level record. *Quaternary Science Reviews* 25, 3322-3337.
- Siddall, M., Rohling, E.J., Almogi-Labin, A., Hemleben, C., Meischner, D., Schmelzer, I. and Smeed, D.A., 2003. Sea-level fluctuations during the last glacial cycle. *Nature* 423, 853-858.
- Stott, L., Cannariato, K., Thunell, R., Haug, G.H., Koutavas, A. and Lund, S., 2004. Decline of surface temperature and salinity in the western tropical Pacific Ocean in the Holocene epoch. *Nature* 431, 56-59.
- Thompson, L.G., Mosley-Thompson, E., Davis, M.E., Henderson, K.A., Brecher, H.H., Zagorodnov, V.S., Mashiotto, T.A., Lin, P.N., Mikhalev, V.N., Hardy, D.R., Beer, J., 2002. Kilimanjaro ice core records: evidence of Holocene climate change in tropical Africa. *Science* 298, 589-593.
- Visser, K., Thunell, R. and Stott, L., 2003. Magnitude and timing of temperature change in the Indo-Pacific warm pool during deglaciation. *Nature* 421, 152-155.
- Vuille, M., Werner, M., Bradley, R.S. and Keimig, F., 2005. Stable isotopes in precipitation in the Asian monsoon region. *Journal of Geophysical Research-Atmospheres* 110, D23108, doi:10.1029/2005JD006022.

Yancheva, G., Nowaczyk, N.R., Mingram, J., Dulski, P., Schettler, G., Negendank, J.F.W., Liu, J.Q., Sigman, D.M., Peterson, L.C. and Haug, G.H., 2007. Influence of the intertropical convergence zone on the East Asian monsoon. *Nature* 445, 74-77.